UNIVERSITY OF SOUTHAMPTON

FACULTY OF ENGINEERING, SCIENCE & MATHEMATICS

OPTOELECTRONICS RESEARCH CENTRE

Novel Direct UV Written Devices

by

Gregory Daniel Emmerson

Thesis submitted for the degree of Doctor of Philosophy

30th September 2003

UNIVERSITY OF SOUTHAMPTON

Abstract

FACULTY OF ENGINEERING, SCIENCE & MATHEMATICS

OPTOELECTRONICS RESEARCH CENTER

Doctor of philosophy

NOVEL DIRECT UV WRITTEN DEVICES

By Gregory Daniel Emmerson

This thesis reports a series of developments based on UV writing of novel waveguide structures. The first section is an investigation into the production of Direct UV-written channel waveguides on the perimeter of a cylindrical substrate. Cylindrical waveguides were produced using variants of the Modified Chemical Vapour Deposition (MCVD) and Flame Hydrolysis Deposition for the fabrication of thin films on either surface of the cylinder. Three layer, buried waveguide structures were produced using three techniques, and channel waveguides Directly UV-written into one of the samples.

The second section concerns the simultaneous definition of channel waveguides and Bragg grating structures in planar substrates. This new process used two overlapped, tightly focused UV laser beams to generate a ~3μm writing spot with an interference pattern within the intensity profile. Translation of the writing spot with the power set to a continuous value averages out the effect of the interference pattern, defining channel waveguides. Modulation of the intensity of the writing spot in the fabrication process results in the definition of channel waveguides and Bragg gratings at the same time. The structure of the grating is defined by the precise motion and modulation of the writing spot, a function controlled by a computer and is not an absolute function of the interference pattern. Using this Direct Grating Writing technique, grating and channel structures were written into blank photosensitive 3-layer silica-on-silicon samples producing gratings with peak reflection intensities between 0dB and >30dB. Bragg gratings with peak centre wavelength reflections spanning 488nm were written in a single fabrication run, all with equalised grating strengths. Direct Grating Writing was also used to produce a range of 2-dimensional planar structures including y-splitters and directional couplers. The gratings produced using this new technique were used to investigate sample photosensitivity and waveguide dispersion. Other results include; superimposed gratings, the superposition of a grating onto an etched structure and a Bragg grating based sensor.

Acknowledgments

First of all I would like to thank my supervisor Dr Peter Smith for his help, guidance and patience (and the chance to do the PhD!) over the past years. I would also like to thank the excellent team of post-docs that I have worked with over the years, Dr Richard Williams, Dr Sam Watts and Dr Corin Gawith. I would particularly like to thank Corin for beating the UV laser into submission over the last couple of months, your help has been invaluable.

I would also like to thank the members of the research group, Vassilios, Denis and Ian for working so well together as a team. Cheers. I would also like to thank others in the department, Stuart, Ed, Anna S, Anna P and Justin for keeping me sane with the intellectual lunch time discussions.

Thanks to the technical staff, Dave, Ed and Mark, for keeping this place running. I would also like to thank the secretaries for all their help behind the scenes.

The Engineering and Physical Sciences Research Council must be thanked for providing the funding and chance to experience the rollercoaster of a PhD.

Finally I must thank my family, for all their support, motivation and prodding, just when I needed it. Thank you.

Greg Emmerson

Table of Contents

Chapter 1: Introduction

1.1 Talking with light

Optical fibres were first proposed as a high bandwidth transmission line in 1966 by Kao et al., with the first practical 'low' loss ($20dBkm^{-1}$) fibre produced in 1970 at Corning. Optical networks were implemented from that point on, however it was not until 1982, when the United Sates government deregulated the telecommunications industry, that the large-scale adoption of optical fibre networks truly took off. Initially network traffic was dominated by voice transmission, however, today the revolution of the internet dominates network use. Rapidly developing and always increasing, the bandwidth requirement from the internet is tremendous. A significant advancement to the bandwidth of optical systems resulted from the development of the erbium fibre amplifier (EDFA) in the 1990's. The EDFA is an all optical device allowing signals to be amplified without conversion to electrical signals, avoiding the electronic bandwidth bottleneck and increasing the length of the transmission links. One of the strengths of the EDFA is the ability to provide gain to signals with different wavelengths, or channels simultaneously. This allows various signals to be transmitted down the same fibre encoded with a different wavelength, a process know as Wavelength Division Multiplexing (WDM) and provides much of the future capacity of the optical networks. However, with increasing complexity of optical fibre networks the component infrastructure becomes more sophisticated with rapidly expanding numbers of components necessary.

Integrated optics was first suggested in 1969 by S. E. Miller. He proposed that multiple optical elements could be integrated together into a block of glass, combining the multiple functions into a single element. The development of integrated optics is not as advanced as that of fibres, but fuelled by the increasing complexity of the optical systems, research has rapidly been catching up. Currently, Planar Lightwave Circuits (PLC) have started to be employed for a variety of functions for WDM applications, the most common of which is the Array Waveguide Grating (AWG) allowing the separation of WDM channels. However as the requirements of optical systems increase, the use of Bragg gratings as wavelength selective filters on a planar base is becoming more common. Bragg gratings, popular in

fibre form, can be applied to wide range of applications. The ability to flexibly incorporate these Bragg grating structures into planar devices is of huge potential.

1.2 The optics of burst bubbles

Since the 'bubble' burst for the optical communication industry in 2000 the market landscape has changed, perhaps forever. In the '90s when use of the internet was expanding at an unprecedented rate, the pressure for more bandwidth meant the optical telecommunications field was seen as an industry guaranteed to grow. The investment in the field was massive, and so the technology and infrastructure improved to a point that capacity outstripped the demand. The telecoms carriers found they had a surplus of unused bandwidth, caused primarily by the imbalance of network development. The long haul optical fibre capacity had rapidly expanded though the innovation of the work in the field, however at the local network level, the development and distribution of broadband and DSL was rolled out too slowly to utilise the bandwidth. Thus, when the markets re-aligned themselves, the investment stopped coming in, and many companies geared up for the production of thousands of components were no longer able to survive. But the demand for bandwidth is there, still rising and the current network systems constantly need replacing and repairing. The model for companies now is to avoid the massive investments tying up capital, but to be cost efficient. Thus, flexible, low cost fabrication techniques with rapid turnaround are becoming more attractive. In such a market, single-step fabrication processes have much potential.

1.3 Aim of research

One such fabrication process is Direct UV writing, a technique analogous to the computer numerical control (CNC) milling used in mechanical workshops. A milling machine executes a control program, producing a finished, machined work-piece in a single fabrication process. The program can be different for each work-piece or repeated to produce multiple, identical pieces with no effect on the fabrication time or cost. The Direct UV writing technique is a similar process, defining channel waveguide structures in blank substrates under a CNC process. This avoids the costly, and time consuming infrastructures of multi-step fabrication techniques.

The work presented in this thesis investigates two variants to the traditional planar Direct UV writing process. The first variation allows the production of long channel waveguide structures suitable for PLC integration. The second technique is a variation of the Direct UV writing technique incorporating the ability to define Bragg grating structures with the same CNC flexibility as the channel waveguide structures.

Within the field of waveguide optics there are two discrete system types, planar and fibre. Both system types are very different in implementation, even though they operate on the same fundamental physics. In general, the two technologies cover different applications, the strength of fibre is its low loss propagation, covering distances up to 50km in a single component. Planar devices, typically less than 10cm long obviously cannot propagate signals long distances, but large numbers of components can be incorporated into a single device (Planar Lightwave Circuits). The advantage of planar technology is clear in terms of complex devices, however the total length of a structure is limited, thus for components that require long interaction lengths, traditional planar structures are not suitable. Such devices include for example; rare-earth doped amplification sections (lasers, amplifiers), poled silica switches and dispersion compensating Bragg gratings. These structures all require long interaction lengths for efficient operation and as such, typically have remained in the fibre geometry.

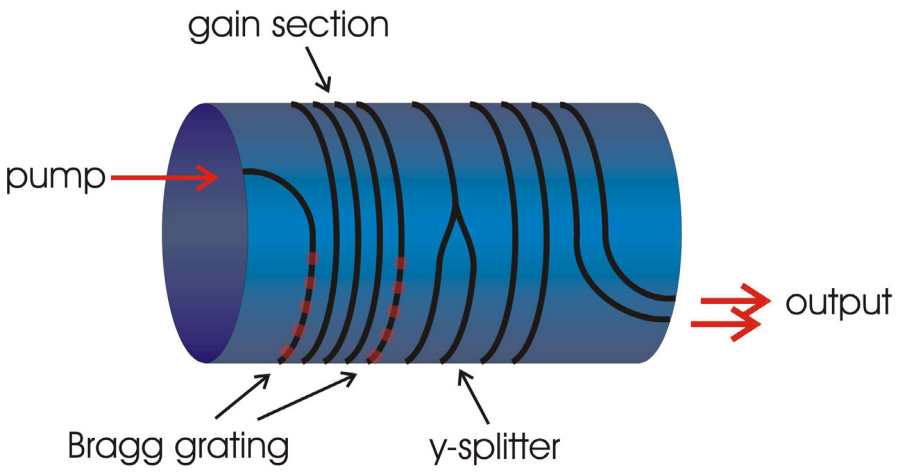

Figure 1.1: Illustration of the cylindrical waveguide concept

The first aim of the work presented in this thesis is the combination of the advantages of the fabrication techniques for Planar Lightwave Circuits with the benefits from the long interaction lengths in fibre. This is proposed to be implemented through use of cylindrical

substrates with planar waveguide layers deposited on the surface. The 2-dimensional nature of the surface will remain, allowing the fabrication of planar structures, but if required the waveguide can form a helix around the perimeter of the cylinder for long path-length structures (figure 1.1). The work presented investigates and develops the fabrication techniques for the definition of such helical channel waveguides.

The second aim of the thesis is the development of a Bragg grating writing technique compatible with the Direct UV writing process. By defining the Bragg grating structures at the same time as the channel waveguides, the number of fabrication steps, and thus complexity should be reduced (figure 1.2). The ability to define both structures through a computer controlled process would result in a very flexible technique for the definition of Planar Lightwave Circuits.

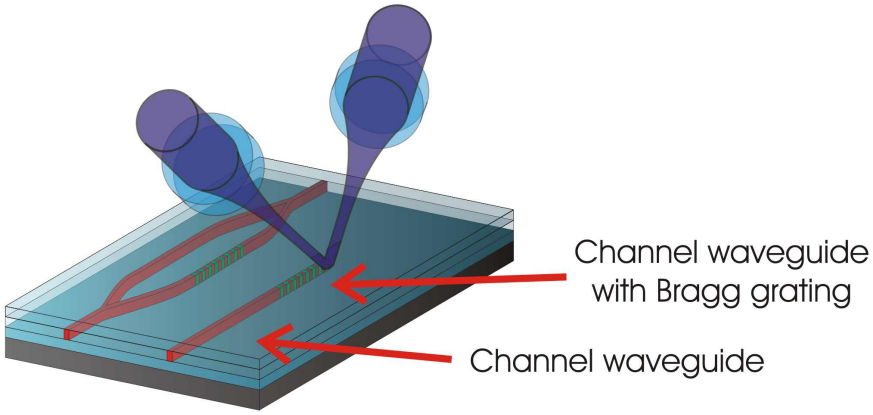

Figure 1.2: Concept of simultaneous channel and Bragg grating definition

1.4 Thesis synopsis

The project effectively had two aims; the fabrication of cylindrical photosensitive substrates for Direct UV writing and the development of a technique for simultaneous definition of channel waveguides and Bragg grating structures. As such, the following material is split into two sections, chapters 3 to 5 relate to the theory of waveguides and the fabrication of cylindrical waveguides. Chapters 6 to 9 relate to the development of the simultaneous channel waveguide and Bragg grating writing process and the applications thereof.

Chapter 2 is a brief introduction to photosensitivity, the history and concept. The phenomenon of photosensitivity is well exploited throughout the work presented in this thesis and is pertinent to virtually all aspects of the experimental work undertaken. As such it is presented at the start of the thesis. Chapter 3 is based on waveguide theory, and provides a derivation of the various guidance conditions. This background on the field distribution of the waveguides structures is essential to the function of the sensor devices presented later in the thesis. The chapter also provides the background to a channel waveguide mode-solver produced by the author allowing for non-symmetrical waveguide dimensions and refractive index distributions. This program is used at various stages throughout the rest of the thesis. Chapter 4 is a review of various fabrication techniques with a view to the cylindrical substrate geometry. Chapter 5 describes the fabrication of the cylindrical structures using three fabrication techniques. It covers the modifications to the existing fabrication processes (FHD and MCVD) to allow deposition onto cylindrical geometry and the results from each technique. The set-up built by the author for cylindrical Direct UV writing is presented with the results from the channel writing into the cylinders.

Cylindrical substrates with layers suitable for waveguiding were produced using all three deposition techniques. Layers produced on the inside of the cylinder, although high quality, suffered from high bend loss and difficulty in defining channel waveguides. Using the FHD based technique, layers were successfully deposited on the outside of a cylinder, however they were prone to cracking. Using a variant of the MCVD process layers were deposited on the outside of a cylinder and channels directly UV written down the length. However the layer was only lightly Germanium doped and the strength of the waveguides was not sufficient to cope with the bend loss associated with the cylindrical geometry. The principle of the cylindrical waveguides was proven however, and at that point a decision to focus on the second technique presented in the thesis, resulting in the Direct Grating Writing system.

In chapter 6 the Bragg grating is introduced. The theory to predict the grating response is presented along with descriptions of the different types of grating structures. Various applications for the Bragg grating structure are presented. In chapter 7 there is a historical review of the development of Bragg grating fabrication techniques. This demonstrates the evolution of the technology before introducing the technique the author has pioneered, Direct Grating Writing (figure 1.3). The principles behind DGW are presented, before the fabrication set-up and process is described. A simulation of the writing process is described

and used to investigate the effects of various writing parameters. In chapter 8, the first ever demonstration of Direct Grating Writing is presented, with the channel and Bragg grating defined in a blank substrate. The chapter describes the optimisation of the writing process in various samples before demonstrating the first ever production of Bragg grating structures with responses covering the entire ITU spectrum from a fixed setup. Chapter 9 describes the use of DGW to fabricate complex structures suitable for planar light wave circuits. Direct grating writing was also used as a tool for the investigation of the more subtle effects in the UV writing process as well as the production of Bragg gratings later used as sensor structures. The thesis is concluded in chapter 10, summarising the two projects within the thesis and suggesting possible future developments for the project.

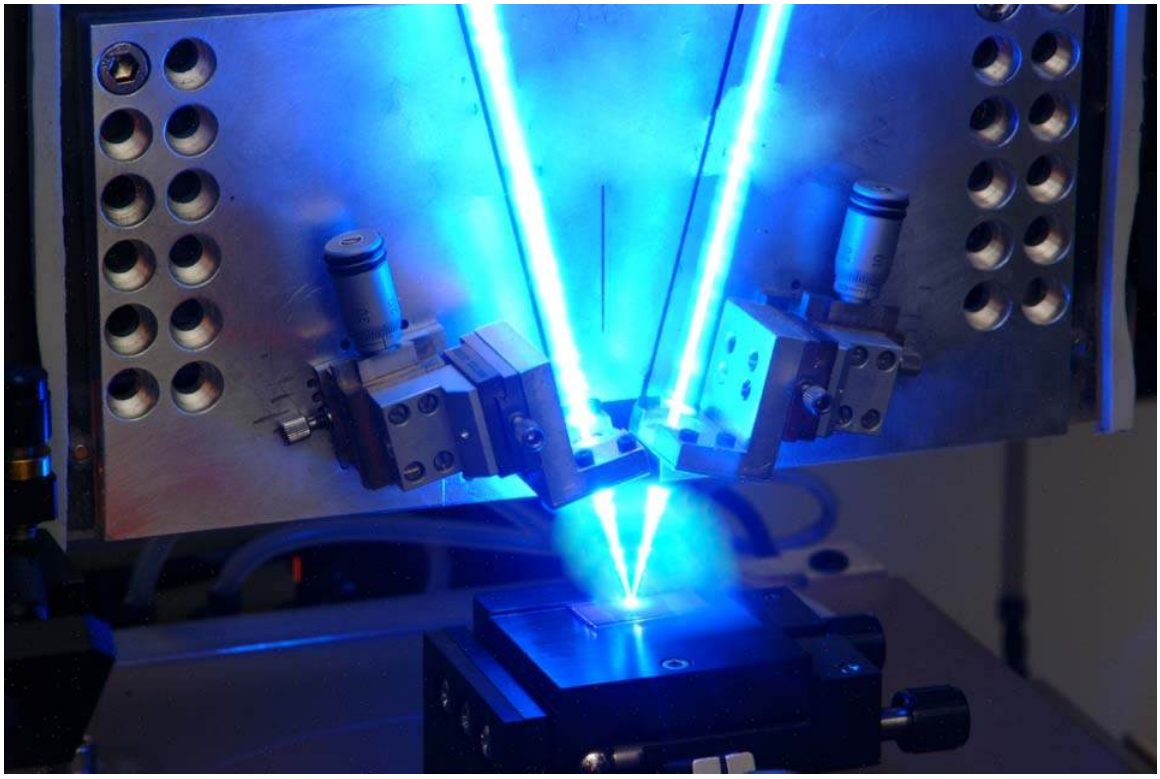

Figure 1.3: Realisation of Direct Grating Writing.

Chapter 2: Photosensitivity

2.1 Abstract

In this material a brief summary of photosensitivity is provided. The history of its discovery is reviewed, together with some of the significant developments leading to the 10^{-2} UV induced index changes observed in current processes. Some of the proposed defect sites responsible for the index change are described before the Hydrogen loading technique for the increasing the photosensitivity of the glass is described.

2.2 Introduction

The work contained in this thesis relies strongly on the characteristic property of many glasses known as 'photosensitivity' and which is required for both the channel definition and the grating inscription in our technique. Since it is applicable to both sections of the thesis, the concept is reviewed here so as to avoid unnecessary repetition. There are various review papers and other sources based on this topic, including (Svalgaard 1997; Othonos and Kalli 1999; Riziotis 2002) which form the basis for this chapter.

Photosensitivity is the phrase used to define the quasi-permanent change in a material's refractive index after exposure to light of a specific wavelength. This is not to be confused with the photo-refractive effect which arises through charge migration due to gradients of light intensity. The photorefractive effect is a different mechanism observed in materials that are photoconductive or photovoltaic in nature, most commonly, ferroelectric crystals. There is some confusion in the literature over the use of the two terms, and whilst photorefractive materials can demonstrate photosensitivity, throughout the rest of this thesis the term photosensitivity will relate to the refractive index change described in the following sections.

2.3 Photosensitivity

The first realisation of photosensitivity involved the fabrication of Bragg gratings in 1978(Hill, Fujii et al. 1978), with the same experiment leading to the serendipitous discovery of both grating structures and glass photosensitivity. An intense beam from a high power Ar-ion laser was launched down a germanium-doped optical fibre. After a period of minutes the power emanating from the fibre was observed to drop to almost zero. Upon subsequent inspection of the fibre's spectral response a narrow reflection band was observed at the wavelength of the Ar-ion laser (488nm). This marked the first production of a fibre Bragg grating using a technique later known as self-organised grating formation, a discovery that at the time elicited little interest in the field of optical fibre research.

2.3.1 Self-organised grating formation

The self-organised grating formation process was, as the name implies due to the response of the waveguide itself. When the light transmitted down the fibre was incident on the output facet there was a small partial back reflection forming a weak counter-propagating wave (figure 2.1). This reflected light formed an initially weak, standing-wave pattern with the incident light. At the anti-nodes of the standing wave the maximum intensity was such that it triggered a photosensitive response of the germanium doped core (previously unseen), increasing the refractive index at the high field strength locations. The refractive index increase pattern formed through the standing wave automatically satisfied the Bragg resonance condition, generating the refractive index perturbation required to couple light into a counter-propagating mode. As the strength of the refractive index modulation increased the grating structure coupled more power into the counter-propagating wave, thus increasing the strength of the standing wave, and hence resulting in a stronger refractive index change in the material. This process of self-reinforcement continued until virtually all the incident light at the Bragg wavelength was reflected back to the incident facet while light not satisfying the phase matching condition was transmitted. Overall, the strength of the index modulation was relatively weak, of the order 10^{-6} to 10^{-5}, and occurred over a length of 1m. This grating formation process subsequently became known as self-induced grating formation but has the disadvantage that it can only write gratings of a fixed period as defined by wavelength of the writing beam.

These structures became known as 'Hill gratings' although they were initially viewed with little interest as the period of the grating structure is fixed to the wavelength of the writing radiation and the photosensitive effect was only observed at 488nm (and at high power).

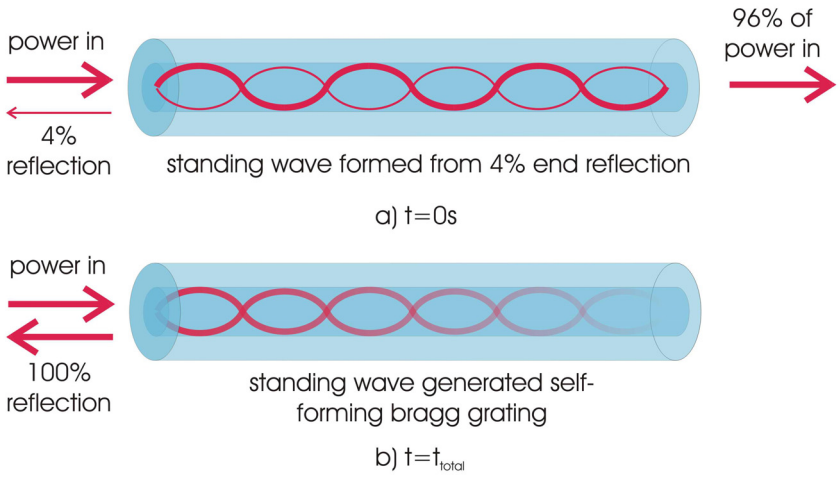

Figure 2.1: Schematic of the self-organising process in the formation of a Bragg grating

It was later discovered that the refractive index change was not occurring at 488nm, but through a 2-photon process occurring in the 240nm absorption band (Lam and Garside 1981). By directly stimulating the 240nm absorption the refractive index increase was much more efficient for any given power. However, due to the losses of the material in the 240nm band and the lack of practical applications of a 244nm reflection grating there was a general lack of interest in this form of grating, and indeed photosensitivity in the optics community.

In 1989, about a decade after the first self-written gratings, Meltz *et al.* first demonstrated the transverse exposure method of defining a controllable periodic index modulation as required for a Bragg grating (Meltz, Morey et al. 1989). In this process the periodic intensity pattern of UV light was generated by the intersection of two laser beams, incident through the side of the fibre. The intersection of the two beams created an interference pattern in the overlapping region, the period of which was defined by the intersection angle. Using this transverse exposure technique gratings of any period could be written, irrespective of the wavelength of the laser used for the inscription. Side exposure coupled with direct stimulation of the 240nm absorption band changed the production of gratings

from scientifically curious structures to realistic devices with significant index modulations in the order of 10^{-3} resulting in practical interaction lengths.

In 1991 Lemaire *et al* demonstrated that the photosensitivity of Germanosilicates typically used as the core of fibres could be significantly enhanced through hydrogenation prior to the UV exposure (Lemaire 1991). The photosensitivity could routinely be enhanced resulting in index modulations an order of magnitude greater (10^{-2}) than previously achieved in silica.

2.3.2 Mechanism of Photosensitivity

There has been a large effort by many different research groups in the last 20 years to try to understand the process of photosensitivity, and yet the exact process giving rise to this effect is still a much debated topic. Many of the findings within the different research groups differ and are often contradictory. This has lead to the general consensus that there are several different processes that result in the refractive index change of the glass. The exact process, or processes, appear to be dependent on many factors including the material composition, the thermal history of the material, and the wavelength and power density of light used to induce the photosensitive change in the glass. The index change is referred to as a quasi-permanent change because although it has a long lifetime it is possible, in many instances, to reverse the change in index through annealing at temperatures below that required to re-flow the glass.

Of particular interest are the refractive index changes caused by exposure to intense ~240nm laser irradiation in Germanosilicate glasses. For many years now the photosensitivity of germanium doped cores in telecoms fibres has been utilised to produce grating structures within the waveguide. Recently this technology has been developed for use in planar structures in the hope of producing planar lightwave circuits without the need for the more complicated multi-step processes commonly used (see chapter 7). Germanosilicate glasses are not the only material to demonstrate photosensitivity, indeed in the course of this work many materials have been irradiated, and almost all show some form of material or index change resulting from the exposure. However the following sections will focus on Germanosilicates since there been much research on this material in

the course of fibre Bragg grating development. Moreover this material system is compatible with existing fibre materials (Refractive index, thermal expansion, etc). For an excellent general resource on photosensitivity readers are directed towards (Othonos and Kalli 1999).

2.3.3 Types of Photosensitivity

As stated above, there are believed to be many mechanisms resulting in refractive index change but the resultant effects are often classed into three types(Douay, Xie et al. 1997). Type 1 is the most commonly used photosensitive effect, the characteristic resulting in an increase in the refractive index of the material approximately proportional to the writing power used to produce the index change. This is the class of photosensitivity that many of the fibre Bragg gratings that are produced use, with the characteristic of a moderate index change ($<10^{-3}$) which remains stable up to temperatures of 200-300°C.

The Type 2 process, while resulting in an increase in the refractive index, appears to be dependent on the formation of damage in the boundary between the absorbing and non-absorbing layers of a waveguide. This mechanism results in large positive index changes ($>10^{-3}$) but also produces an increase in the loss of the waveguide. However the refractive index change is very thermally stable requiring very high temperatures (approx. >800˚C) for the erasure of the index increase.

The third mechanism (Type 2A) results in a negative index change. This effect occurs in the regime of prolonged exposure after the Type 1 and is associated with overexposure. This mechanism is more prominent in systems with an UV emission of 193nm rather than 240nm, although it does occur in both writing systems. The reaction that provides the index change is slower than that of the Type 1, resulting in an overlap between the two effects. Increasing the power after the saturation of the Type 1 effect leads to the onset of the Type 2A process which starts to erase the previous index increase before creating the negative index change.

2.3.4 The Structure of Silica

Pure silica consists of a tetrahedral structure of Si atoms bonded to four oxygen atoms, each bonded to two silicon atoms. The tetrahedral arrangement forms a quasi-periodic lattice typical of amorphous structures. The material structure of silica contains defects that can typically be classified into two types. *Distributed* defects caused by variations in the glass structure over large area, these are typically related to the glasses bulk characteristics such as strength. The second type, *point* defects, are caused by missing atoms or 'wrong' atomic bonds. It is generally accepted that point defects cause the enhanced absorption in the UV region, and hence the resultant photosensitivity of the material.

2.3.5 Germanium co-doped Silica

It is now well known that by co-doping pure silica glass with germanium the observed photosensitivity is significantly increased. Typical doping levels of Germanium tend to be a few mole percent. At these levels the germanium is incorporated into the silica matrix with little disruption. This incorporation is possible without massive disruption since germanium has the same valence as silicon (4) and so can readily be incorporated. The resulting Germanosilicate glass has a refractive index slightly greater than that of pure silica, this index increase can be described through the Kramers – Kronig relation (2.1). The KK relation relates resonant absorption in the UV region to the refractive index change at longer wavelengths.

$$\Delta n(\lambda) = \frac{1}{2\pi^2}\int_0^\infty \frac{\Delta\alpha(\lambda')d\lambda'}{1-(\lambda'/\lambda)^2} \qquad [2.1]$$

The inclusion of germanium in a pure silica glass also affects the glass' mechanical properties, namely the mechanical strength and thermal expansion of the material. This is covered more extensively in the fabrication chapter of this thesis.

Germanosilicates, while containing the point defects associated with pure silica also contain germanium specific defects. These defects are typically grouped into two categories;

diamagnetic defects where the electron spins are paired and *paramagnetic* defects with unpaired electron spin (Sulimov, Sokolov et al. 1996).

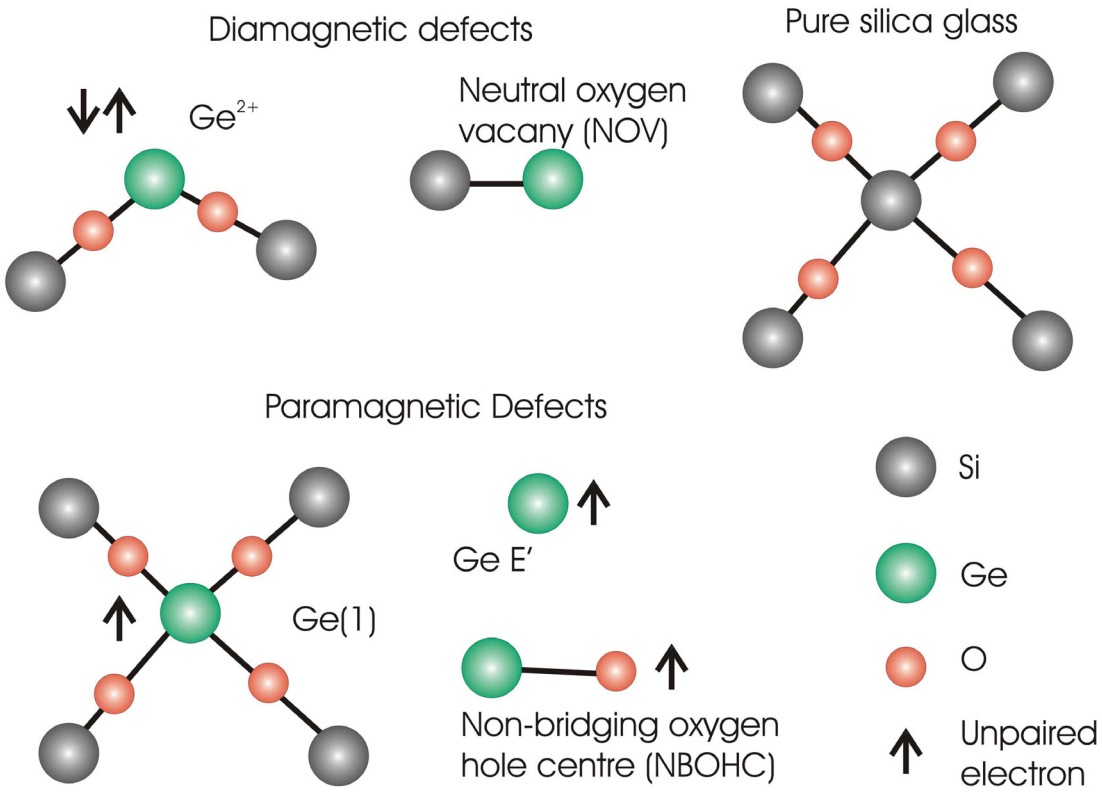

Figure 2.2: Examples of common point defects in Germanosilicate

2.3.6 Diamagnetic Defects

Diamagnetic defects generally are formed in the glass formation process when there is a lack of sufficient oxygen, these defects are classed as Germanium Oxygen Deficient Centre (GODC's). The lack of sufficient oxygen prevents the formation of the typical tetrahedral glass structure.

The most prevalent GODC is the Ge^{2+} defect, the germanium atom is in the 2+ oxidisation state rather than the normal 4+ oxidisation state. The second most prevalent and investigated GODC is the Neutral Oxygen Vacancy (NOV). In a NOV a germanium atom bonds directly to a adjacent silicon atom rather than the normal oxygen. Typically, approximately 0.1-1% of the germanium incorporated into the glass that results in the

creating of GODC's with the Ge^{2+} defects 1-2 orders of magnitude more dominant than NOV's.

2.3.7 Paramagnetic Defects

Since paramagnetic defects contain an unpaired electron there has been much study into them using electron spin resonance. The paramagnetic defects can take several forms. The Ge(1) defects consists of a fully bonded germanium atom with a trapped free electron, the GeE' defect where the germanium is bonded to three oxygen atoms and the Non-Bridging Oxygen Hole Centre (NBOHC) where the oxygen atom is bonded to only one atom.

2.3.8 Photosensitisation

It is thought that the process of photosensitive refractive index increase is caused through the absorption of the UV photon energy by the GODC's resulting in the disassociation of an electron creating a paramagnetic defect. This change in the structure of the defects again changes the absorption of UV, hence changing the refractive index of the exposed area. The localised effect of the exposure changes the defect distribution from the homogenous background resulting in the localised index change observed in photosensitivity.

The inherent photosensitivity of a glass layer can be increased through several processes. One method is to increase the germanium concentration in the glass. However the incorporation of germanium also increases the refractive index of the glass. In order to maintain compatibility with industry standard telecoms fibre, co-doping with boron reduces the refractive index of the glass, allowing for increased germanium doping levels. However the incorporation of boron not only decreases the index but significantly increases the photosensitivity of the glass beyond that of germanium alone. There has since been much investigation into the effects of other co-dopants on photosensitivity including europium, cerium, tantalum, aluminium and tin. Of particular interest is tin that demonstrates enhanced photosensitivity and can withstand greater temperatures before reversal of the index change.

Whatever materials are used to enhance the photosensitivity of the host glass there is normally a limit to the maximum level of doping possible before negative effects are observed. Sometimes these limits are placed by the fundamental deposition technique, but ultimately these limits often arise from the properties of the glass produced. Ultimately, high doping levels will produce greater levels of loss within the waveguide, with effects ranging from absorption and scattering to phase separation and clustering. Frequently it is not only the optical properties of the glass that are adversely affected, the mechanical strength and susceptibility to external environment (e.g. humidity) can likewise be significantly reduced.

The other method of enhancing the photosensitivity of a host Germanosilicate glass is to increase the percentage of the germanium incorporated that forms defect sites. The degree of germanium defect creation is heavily influenced by the processing history of the glass, with the fabrication atmosphere and the thermal processing critical to the extent of the defect formation.

2.3.9 Hydrogen/Deuterium Loading

As mentioned in the history of photosensitivity, in 1992 it was discovered that the diffusion of hydrogen into the matrix of a Germanosilicate glass enhanced the photosensitivity change observed in a material. The hydrogen loading process was rapidly adopted and is still used to increase the photosensitivity of a glass, essentially reducing the doping levels required for a given index change. The process was originally developed using hydrogen, however, as will be explained in the following section hydrogen loading results in the formation of extra OH molecules. Due to the absorption resonance at 1.38μm this increases the loss in the typical telecoms window. An alternative is to use deuterium, that has almost the same diffusion characteristics as hydrogen but the molecule OD has a different bond resonance, shifting the absorption window away from the 1.38μm window. In general the rest of this chapter unless stated otherwise the use and effects of deuterium and hydrogen loading are interchangeable.

Like photosensitivity, there is much conjecture resulting in several different theories expressed in the literature as to the cause of the photosensitive enhancement, the resultant

process is likely to be combination of several effects. The initial stage in all the proposed mechanisms is the diffusion of the hydrogen into the silica matrix with the hydrogen molecules occupying any voids or vacancies in the silica matrix. This diffusion process occurs due to the high diffusivity of hydrogen and is a mechanism that has had much investigation. From the Fickian/Arrhenius equations for plate geometry, the diffusivity can be simply expressed as an exponential expression dependent on the thermal energy of the system;

$$D = A \cdot \exp\left(-\frac{E}{RT}\right) \qquad [2.2]$$

where D is the diffusivity, A is a scaling factor, E is the activation energy of gas diffusion in the glass, R is the gas constant and T is the temperature of the system in Kelvin. The constant values for hydrogen and deuterium are given in table 2.1, showing that the two gases exhibit very similar behaviour.

	A	E (KJ/mole)
Hydrogen	5.65×10^{-4}	43.55
Deuterium	5.0×10^{-4}	43.96

Table 2.1: Comparison of activation energy for Hydrogen and Deuterium

Ultimately, it is the level of hydrogen contained within the silica matrix that is of interest. At room temperature the equilibrium point of hydrogen has been experimentally measured at;

$$c_{eq(H_2)} = 116\, ppm / bar \qquad [2.3]$$

where ppm is part per million. The loading should be performed at low temperatures since the solubility of hydrogen in silica is;

$$sol \propto \exp\left(\frac{8.67 KJ / mole}{RT}\right) \qquad [2.4]$$

and thus reduces with temperature, although this is a relatively weak dependence. For the case of planar layers (effectively 1-D) the time over which a molecule traverses a distance l is;

$$\frac{l^2}{4D} \qquad [2.5]$$

where D is the diffusivity (2.2). By assuming a thin film thickness d the time for approximately 95% of the equilibrium density to be reached is;

$$\tau_{0.95} \approx \frac{0.8 \cdot d^2}{D} \qquad [2.6]$$

From equation (2.4) the time for the hydrogen to diffuse out to a pre-determined level can be described as;

$$\tau = -\ln(\alpha)\tau_0 \exp\left(\frac{E}{RT} - \frac{E}{RT_0}\right) \qquad [2.7]$$

where τ is the decay time at temperature T, α is the relative concentration of H_2, τ_0 is an empirically determined decay time at temperature T_0. Relating the empirically determined out-diffusion rate (11.8h @ 23˚C) at a given temperature allows the diffusion rate in or out of the material for any other temperature, allowing the selection of different temperatures during the various stages of the loading/writing process for optimal performance.

One of the more investigated photosensitivity enhancement mechanisms occurs because of the interaction of the hydrogen with local GeO_2 sites. The proposed reaction occurs at the germanium sites as the oxygen bonds are slightly weaker than those of silica. The enhancement occurs through either thermal or photololytic triggering, essentially imparting energy into the system so that the hydrogen breaks the bond between the germanium and oxygen, resulting in the formation SiOH (or SiOD) silica matrix termination, and hence a GODC. Therefore, in the presence of sufficient hydrogen every germanium site could be converted into GODC, resulting in the maximum sensitivity observed in the system.

A secondary photosensitivity enhancement has been observed in which the presence of hydrogen (or deuterium) in the glass matrix acts as a catalyst for the photobleaching GODC associated with the transition from diamagnetic to paramagnetic defects and results in an increase in refractive index.

2.3.10 Thermally Induced Density Change

A mechanism that results in refractive index change but is not photosensitivity as such, although is sometimes labelled as such is a density or stress change of the material arising from local heating. This process normally arises from direct UV writing or variants of such a technique and is an artefact of the very high power density produced in these processes. Absorption of the laser power is obviously converted into thermal energy and due to the

power densities involved in direct writing this can result in a strong local heating effect. The temperatures reached can be very high and easily result in sintering, melting or even ablation in most materials. In bulk materials there is normally a point below the ablation threshold where the material at the writing spot has enough energy to flow, in this regime there is often a material density change, increasing or decreasing depending on the exact power level and the properties of the material. As the heat source is removed by the laser traversing, the material is rapidly quenched, freezing in a different density state. The refractive index of a material is directly related to the density, thus this process results in a refractive index change as a result of irradiation. This is a thermally driven process rather than a photo-induced defect modification.

2.4 Summary

A description of the accidental discovery of photosensitivity is presented. The key points that changed photosensitivity from a subject of little practical value to a commonly used fabrication technique are presented. The different types of photosensitivity that have been observed are included, summarising some of the key characteristics of the refractive index response. The structure of silica is investigated with a particular consideration of the defects created by Germanium doping of silica. These defects are believed to be one of the main sources of refractive index changes through UV irradiation. Techniques for increasing the sensitivity of a glass are discussed with a look at the use of Deuterium loading to enhance the process. The considerations and techniques involved in Deuterium loading are discussed with a view to its out-diffusion with time.

Chapter 3: Waveguide Theory

3.1 Abstract

An understanding of the process of modal confinement within a waveguide structure is essential for the efficient production of such structures. In the following material the theory of modal confinement is presented, starting from Maxwell's equations, and ending with the development of a technique for evaluating the effective index of a channel structure comprising of a non-symmetrical index distribution. This standard technique for evaluating the channel structures is a useful tool that has been implemented by the author for this work, allowing various parameters to be adjusted within the waveguide structure and the subsequent modal properties predicted. The various steps are defined in some detail as each step in the derivation has relevance to the specific material in the following chapters, in particular the existence of evanescent fields and the phase shift encountered in reflection from a dielectric boundary.

3.2 Introduction

The theory of guided waves is well covered in a wide range of publications that vary in their approaches. In this following chapter the process for the assessment of the guiding properties of channel waveguides is presented in a coherent derivation originating from Maxwell's equations and ultimately ending in the assessment of asymmetric channel waveguides. The theoretical assessment of the properties of a channel waveguide is frequently used in the following chapters of this thesis and so it is important that the origins and associated limitations of the evaluation techniques are well understood. For more information on waveguide theory the reader is directed to the wide range of good resources available on the topic (Snyder and Love 1983; Lee 1986; Ghatak and Thyagarajan 1998) upon which this chapter is heavily based.

Initially, the wave equation for the propagation of an electro-magnetic wave in a uniform isotropic media is presented, derived from Maxwell's equations, although many of the steps involved are purely mathematical in nature but it is necessary to understand the nature of the

manipulations. One of the fundamental aspects of wave guiding that needs to be clearly understood is the effect a boundary between two materials of differing refractive indices on the power and phase of the propagating wave, as this fundamentally defines the nature of the standing wave that is built up within a waveguide. The derivation process then continues on to a two dimensional structure known as a planar, or 'slab' waveguide with an index variation in one dimension but uniform index in the other two. These structures confine the guided mode in the one axis and as such are relatively easy to evaluate and clearly demonstrate the concept of modes and their relative field distributions. From the derivation of the slab waveguide a general evaluation process is demonstrated in terms of *normalised waveguide parameters*. These terms are expressions for the frequency and wavevector components that are normalised against themselves into dimensionless quantities that are applicable to a wide range of structures allowing quick evaluation of structure at various wavelengths.

Finally the process of evaluating a channel waveguide, a structure with index variation in two dimensions is discussed with the relative merits of two of the different techniques that are often applied. The *effective index* method is ultimately used to create a program, evaluating channel waveguide structures with profiles similar to those presented in later chapters.

3.3 Maxwell's Equations

Maxwell's equations are well known and normally form the basis from which the wave equation is derived. The equations essentially define the relationships between the magnetic and electric field in a source free, isotropic media. The magnetic flux density $\boldsymbol{B}(\mathrm{Am}^{-2})$ and the magnetic field $\boldsymbol{H}(\mathrm{Am}^{-1})$ are related by;

$$B = \mu H \qquad [3.1]$$

where μ is the permeability of the medium and is defined by;

$$\mu = \mu_0 \mu_r \qquad [3.2]$$

where μ_0 is the permeability of a vacuum and μ_r is the relative permeability of the medium. However, the relative permeability of anything other than magnetic materials is 1, therefore $\mu = 4\pi \mathrm{x} 10^{-7}$ in the case of silica based materials.

The electric flux density $\boldsymbol{D}$(Cm^{-2}) and electric field $\boldsymbol{E}$(Vm^{-1}) are similarly related through;

$$D = \varepsilon E \quad [3.3]$$

where ε is the permittivity and given by (3.4) and the subscripts have the same meaning as for the permeability.

$$\varepsilon = \varepsilon_0 \varepsilon_r \quad [3.4]$$

Finally, to be thorough, in the general case of these equations the current density $\boldsymbol{J}$(Am^{-2}) in a conductive material is given by;

$$J = \sigma E \quad [3.5]$$

where σ is the conductivity. Using these field relations the well known Maxwell's equations are defined as;

$$\nabla \times E = -\frac{\partial B}{\partial t} \quad [3.6]$$

$$\nabla \times H = \frac{\partial D}{\partial t} + J \quad [3.7]$$

$$\nabla \cdot B = 0 \quad [3.8]$$

$$\nabla \cdot D = \rho \quad [3.9]$$

3.3.1 The wave equation

The above Maxwell's equations are dependent on both space and time, a common simplification is to take the case of time-harmonic fields. In time harmonic fields the fields vary with a sinusoidal frequency ω so the general form of equations (3.6)-(3.9) can be replaced with:

$$\nabla \times E = -j\omega\mu H \quad [3.10]$$

$$\nabla \times H = j\omega E \quad [3.11]$$

$$\nabla \cdot H = 0 \quad [3.12]$$

$$\nabla \cdot (\varepsilon E) = 0 \quad [3.13]$$

Taking the curl of equation (3.10) results in:

$$\nabla \times (\nabla \times E) = -j\omega\mu \nabla \times H \quad [3.14]$$

Applying the vector identity $\nabla \times (\nabla \times A) = \nabla(\nabla \cdot A) - \nabla^2 A$ to the LHS of equation (3.14) allows it to be expressed as:

$$LHS = \nabla \cdot (\nabla \cdot E) - \nabla^2 E \qquad [3.15]$$

Whilst separating out equation (3.13) allows the expression of the ***E*** field:

$$\nabla \cdot (\varepsilon E) = \nabla \varepsilon . E + \varepsilon \nabla \cdot E = 0 \Rightarrow \therefore \nabla \cdot E = -\frac{\nabla \varepsilon}{\varepsilon} \cdot E \qquad [3.16]$$

Therefore by combining equations (3.11), (3.15) and (3.16) into equation (3.14) results in;

$$\nabla^2 E + \nabla\left(\frac{\nabla \varepsilon}{\varepsilon} \cdot E\right) + \omega^2 \mu \varepsilon E = 0 \qquad [3.17]$$

But assuming ε is constant, $\nabla \varepsilon \to 0$ thus equation (3.17) reduces to the Helmholtz, or wave equation. It represents the three components of E and the solutions allow insight into the behaviour of material in certain circumstances.

$$\nabla^2 E + \omega^2 \mu \varepsilon E = 0 \qquad [3.18]$$

Where, for later use we define the wave number *k* as;

$$k^2 = k_x{}^2 + k_y{}^2 + k_z{}^2 = \omega^2 \mu \varepsilon \qquad [3.19]$$

3.3.2 Effects of dielectric boundaries

The solution of equation (3.17) describes the propagation of light in a uniform medium, and as such is a very general statement. By convention the general description of fields in the materials are defined using both the permeability and permittivity. However in the case of optical waves guided within a glass or non-magnetic material, commonly the materials are described in terms of refractive index. The relationship between the refractive index of a material (*n*) and the permittivity of a medium is related through:

$$n = \sqrt{\varepsilon_r} \qquad [3.20]$$

The behaviour of electromagnetic waves propagating through a medium upon reaching a boundary with a material of differing refractive index is of key importance to several effects both in bulk optics and guided waves. Of these effects, arguably one of the most interesting and certainly the one that has had the greatest effect in the field of long distance communication is the case of guided modes. Guided modes occur in structures of non-uniform refractive index profile in which a material of 'higher' refractive index is

surrounded by material of 'lower' refractive index in at least one dimension. The propagation of light within this structure is defined by its wavelength and the size/strength of the waveguide, particularly at the boundaries between different mediums.

It is well known that light waves are both refracted and reflected at a boundary between differing refractive indices and that the nature of the reflection and transmission is dependent on the refractive index difference, the angle of intersection and the polarization of the incident beam. In the following section the behaviour of these parameters is described with particular reference to total internal reflection (TIR) that is critical to the understanding of the behaviour of optical waveguides.

Consider an incident wave, propagating with a given wave vector in a uniform medium encountering a plane interface with a medium of differing refractive index which has a component that is reflected (*r*) and a component which is transmitted (*t*) as shown in figure 3.1.

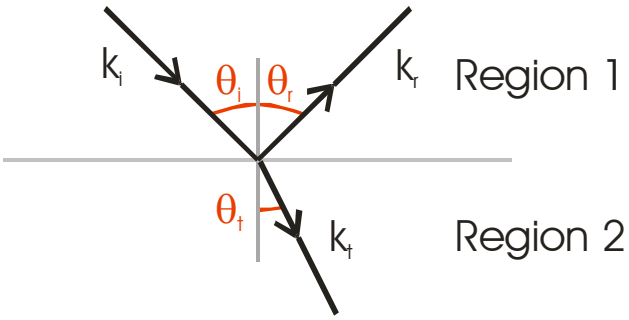

Figure 3.1: Diagram of a wave incident to a boundary between two regions with differing refractive indices, indicating the refracted and reflected waves. *i* denotes the incident wave, *r* is the reflected wave and *t* is the transmitted wave. The refractive indices of the two regions are defined as n_1 and n_2 respectively.

From Maxwell's equation it can be shown that across a boundary between the two media the tangential components of **E** and **H** along with the normal components of **D** and **B** are continuous. From these boundary condition the *phase matching condition* is arrived at, essentially stating that the reflected and transmitted waves all lie in the same plane.

$$k_{iy} = k_{ry} = k_{ty} \equiv k_y$$
$$k_{iz} = k_{rz} = k_{tz} \equiv k_z \qquad [3.21]$$

If the wave vectors are expressed as angles in figure 1 then the components in (3.21) can equally be expressed as;

$$\begin{aligned} k_{ix} &= k_1 \cos\theta_i & k_{iz} &= k_1 \sin\theta_i \\ k_{rx} &= k_1 \cos\theta_r & k_{rz} &= k_1 \sin\theta_r \\ k_{tx} &= k_2 \cos\theta_t & k_{tz} &= k_2 \sin\theta_t \end{aligned} \qquad [3.22]$$

where $k_1 = n_1 k_0$ and likewise for k_2, where k_0 is the magnitude of the wave vector $\boldsymbol{k}$ in free space $\left(\omega/c\right)$. From the above requirement that the tangential components of the reflected and transmitted waves are the same we get the well known results of the $\theta_i = \theta_r$ and Snell's Law for the refracted wave;

$$\frac{\sin\theta_i}{\sin\theta_t} = \frac{n_2}{n_1} \qquad [3.23]$$

The phase matching concept can readily be illustrated by a diagram in *k*-space. The components of the wave vectors obey $k_x^{\,2} + k_z^{\,2} = k^2$ in regions 1 and 2 respectively, therefore all the possible wave vectors are described as arcs in the two regions as shown in figure 3.2.

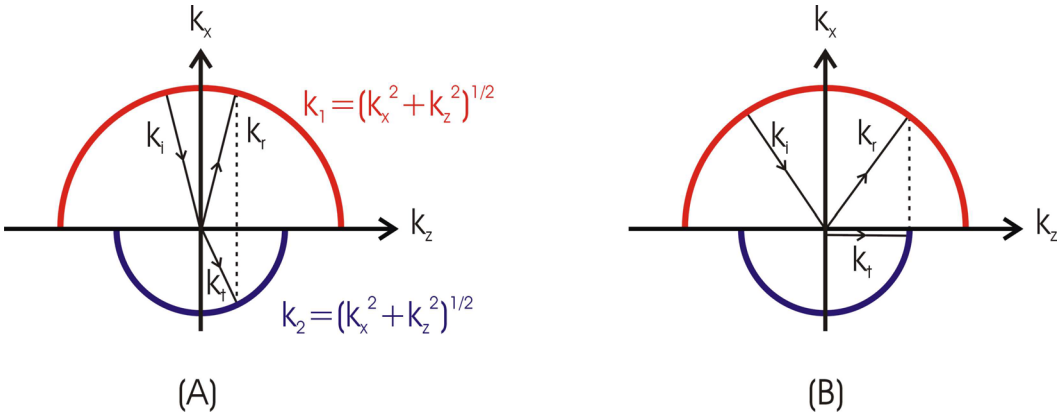

Figure 3.2: graphical representation of the phase matching at a boundary between two media. (a) when the incident angle is less than the critical angle and the transmitted wave can propagate in region 2, (b) the angle of incidence is the critical angle with the transmitted wave vector propagating along the boundary of the two mediums.

From figure 3.2 it is clear that the critical angle can be expressed as $\sin\theta_c = k_2/k_1$, the point where total internal reflection occurs, classically regarded as the reflection of all the incident light, however it is important to understand the nature of the transmitted wave vector in the cases of $\theta_i > \theta_c$ as it has a large impact on the behaviour of the reflected waves. The *x*

component of the transmitted wave vector can be expressed in terms of the incident angle resulting in the expression (3.24).

$$k_{tx} = \sqrt{k_2^{\,2} - k_1^{\,2} \sin^2 \theta_i} \qquad [3.24]$$

It should be noted that at the critical angle and the term in the square root is negative and the therefore the x-component in the transmitted wave is purely an imaginary term and as such can be expressed as:

$$k_{tx} = \pm j\sqrt{k_1^{\,2} \sin^2 \theta_i - k_2^{\,2}} = \pm j\alpha_{tx} \qquad [3.25]$$

As the solution must be bound as $x \to -\infty$ then the solution $k_{tx} = -j\alpha_{tx}$ is selected thus the fields decrease exponentially as they penetrate into region 2 resulting in the *evanescent* 'tail' in the region. It is worth noting that although the guided mode field penetrates into region 2, in this case there is no net power flow into this region and thus all the incident power is still reflected.

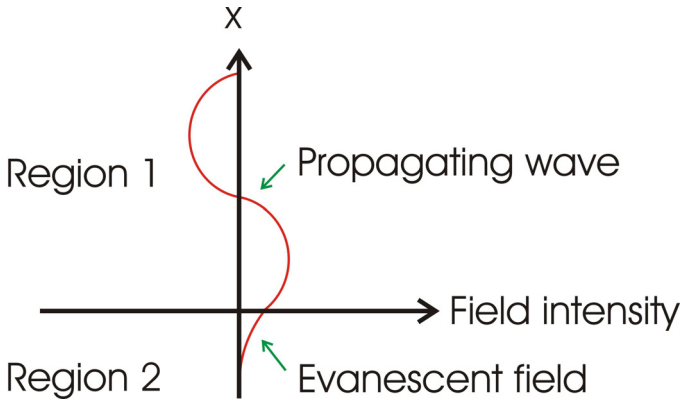

Figure 3.3: Illustration of electric field intensity over a boundary of differing mediums resulting in the total internal reflection of the incident wave and the resulting evanescent 'tail' penetrating into the lower index region 2.

The power and phase of the reflected and transmitted waves depends not only on the angle of incidence but on the polarization of the incident wave. By considering the two polarizations of the incident light and applying the requirements of continuous **E** and **H** fields at the boundary yield the two sets of reflection and transmission coefficients (3.26):

$$\begin{aligned} R^{TE} &= \frac{k_{ix} - k_{tx}}{k_{ix} + k_{tx}} & R^{TM} &= \frac{k_{ix} n_2^2 - k_{tx} n_1^2}{k_{ix} n_2^2 + k_{tx} n_1^2} \\ T^{TE} &= \frac{2k_{ix}}{k_{ix} + k_{tx}} & T^{TM} &= \frac{2k_{ix} n_1 n_2}{k_{ix} n_2^2 + k_{tx} n_1^2} \end{aligned} \qquad [3.26]$$

The reflection and transmission ratios in (3.26) are expressed individually for the TE and TM polarisations respectively demonstrating the polarization dependence. It is worth noting that the reflection and transmission coefficients in general, are complex quantities, and so not only the relative powers in the reflected and transmitted waves vary with the incident beam state, but the phase of the reflected and transmitted waves also vary.

If we consider the vector triangles shown in figure 3.2 we obtain the relationships:

$$k_{ix}^2 = n_1^2 k_0^2 - k_z^2 \qquad [3.27]$$

$$k_{tx}^2 = n_2^2 k_0^2 - k_z^2 \qquad [3.28]$$

From the definition of the wavevector in medium1 we get;

$$k_z = n_1 k_0 \sin\theta_i \qquad [3.29]$$

that by substituting back into (3.28) provides:

$$(k_{tx})^2 = \left(n_2^2 - n_1^2 \sin^2\theta_i\right) k_0^2 \qquad [3.30]$$

Once again the imaginary nature of k_{tx} is evident when $\sin\theta_i > \frac{n_2}{n_1}$. So from equation (3.25) where $k_{tx} = -j\alpha_{tx}$ the resultant reflected wave amplitude can now be expressed as;

$$R^{TE} = \frac{k_{ix} + j\alpha_{tx}}{k_{ix} - j\alpha_{tx}} = 1e^{j2\phi^{TE}} \qquad [3.31]$$

$$R^{TM} = \frac{k_{ix} n_2^2 + j\alpha_{tx} n_1^2}{k_{ix} n_2^2 - j\alpha_{tx} n_1^2} = 1e^{j2\phi^{TM}} \qquad [3.32]$$

where the phase of the waves are:

$$\phi^{TE} = \tan^{-1}\left(\frac{\alpha_{tx}}{k_{ix}}\right) \qquad [3.33]$$

$$\phi^{TM} = \tan^{-1}\left(\frac{\alpha_{tx} n_1^2}{k_{ix} n_2^2}\right) \qquad [3.34]$$

By combining equations (3.25), (3.27) and (3.30) the phase change is readily expressed in terms of incidence angle and refractive index difference. Illustrations of the results are plotted in figures 3.4 and 3.5 for the case of air/glass interface demonstrating the TE and TM response respectively.

$$\phi^{TE} = \tan^{-1}\sqrt{\frac{n_1^2 \sin^2\theta_i - n_2^2}{n_1^2 \cos^2\theta_i}} \qquad [3.35]$$

$$\phi^{TM} = \tan^{-1}\left(\frac{n_1^2}{n_2^2}\sqrt{\frac{n_1^2 \sin^2\theta_i - n_2^2}{n_1^2 \cos^2\theta_i}}\right) \qquad [3.36]$$

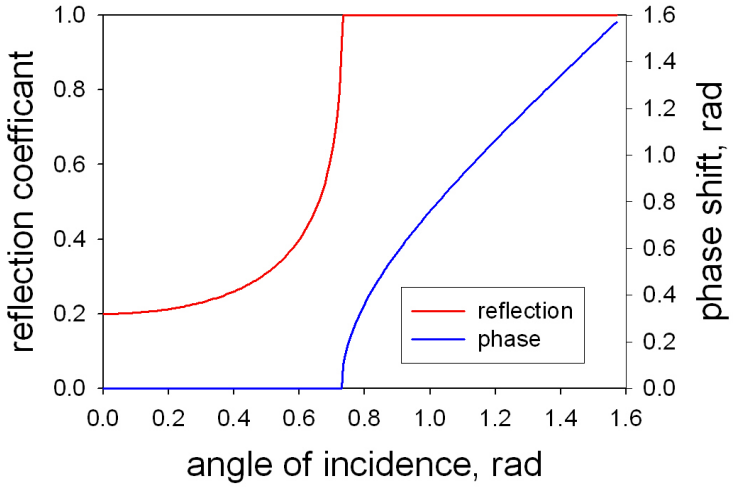

Figure 3.4: Diagram showing the magnitude and phase of a TE polarised reflected wave with respect to angle of incidence at a boundary into a material with a greater refractive index (n_1=1.5, n_2=1.0).

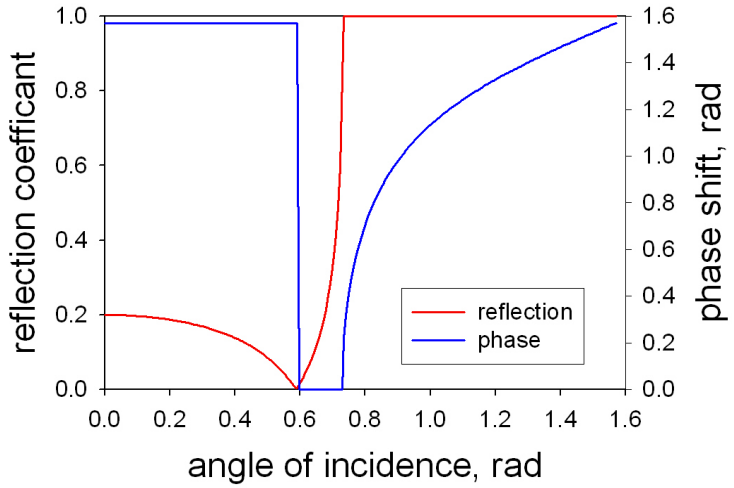

Figure 3.5: Diagram showing the magnitude and phase of a TM polarised reflected wave with respect to angle of incidence at a boundary into a material with a greater refractive index (n_1=1.5, n_2=1.0) highlighting the dependence on polarisation between the two cases.

3.4 The asymmetric slab waveguide

The wave equation (3.18) allows for general solutions to be found describing the propagation of a wave in a uniform, isotropic medium. Analytical solutions for guided

modes in waveguide structures are, except for some special cases, hard to find especially in non-symmetric planar channel structures. One of the solutions that can be relatively simply defined is the asymmetric slab waveguide, which in itself can be used as a tool for solving more complicated structures. In this case it is assumed that the refractive index of the structure varies only in the *x* axis, and is continuous in both the *y* and *z* axis (see figure 3.6).

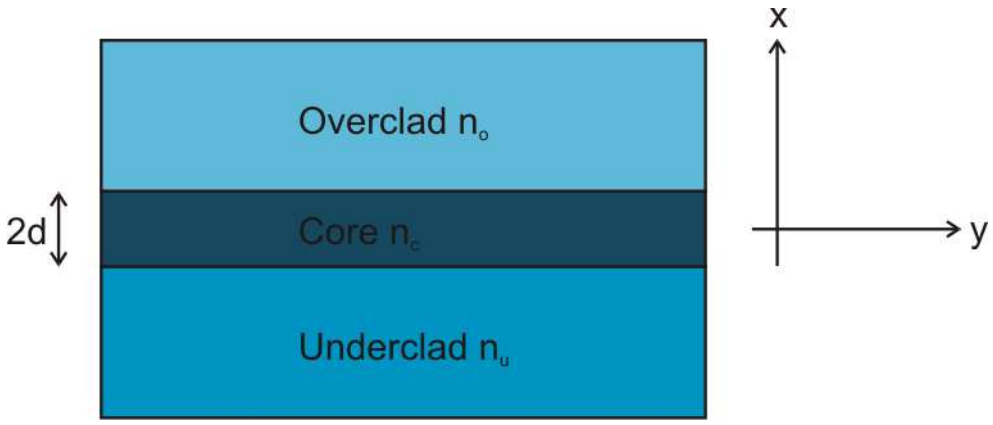

Figure 3.6: Structure of the asymmetric slab waveguide. The structure is continuous in the *y* and *z* axis with the refractive index varying in the *x* direction. The refractive indices of the structure are n_o, n_c and n_u where $n_c > n_o, n_u$ and the thickness of the core is 2*d*.

The 'slab' refers to the core structure, a layer of higher refractive index sandwiched between two materials of lower index. If light propagating down the core of the structure experiences total internal reflection each time it encounters the boundary between the core and a cladding then the light is effectively trapped in the core layer, unable to propagate in the *x* axis. In this rather simplified approximation the form of the electric field in the respective regions is known. In the core of the structure we expect the wave to be a superposition of reflected waves from the two boundaries resulting in a guided wave with real propagation constant. In the cladding regions the field is evanescent in nature due to the total internal reflection and so the propagation constant is purely imaginary. Thus the form of the light ray path can be considered as shown in figure 3.7.

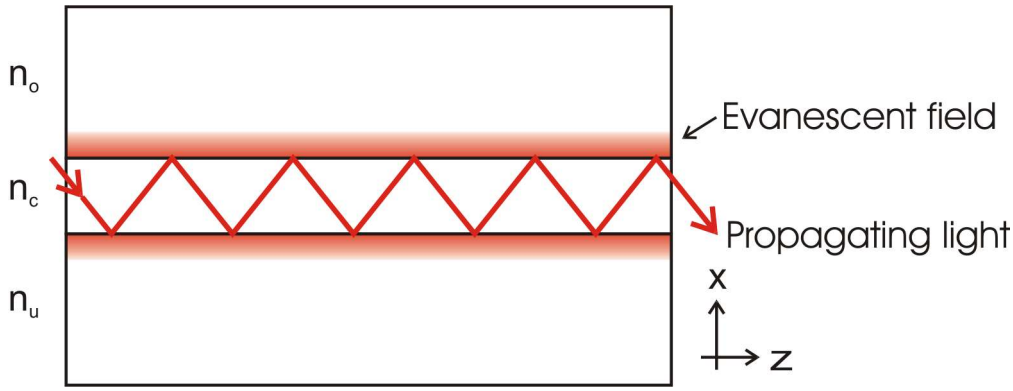

Figure 3.7: Light propagation in a slab waveguide with evanescent fields extending into the cladding layers

The waveguide mode is, by definition, a set of electromagnetic fields which maintain their transverse spatial distribution (standing wave) while propagating along the z axis. In this case it is assumed that that the **E** and **H** are of the form;

$$\begin{Bmatrix} E(x,y,z) \\ H(x,y,z) \end{Bmatrix} = \begin{Bmatrix} E(x,y) \\ H(x,y) \end{Bmatrix} e^{-jk_z} \qquad [3.37]$$

maintaining the nomenclature from before. As always the TE and TM modes have to be considered separately when finding the guidance conditions, especially when considering the effect of the polarisation on the phase of the reflected fields as demonstrated in figures 3.4 and 3.5.

From the above assumptions about the form of the wave in the guiding cases and the evanescent field we can use the following expressions for the electric fields in the respective regions:

$$E_y(x,z) = \begin{Bmatrix} A_o e^{-\alpha_{1x}x} & x > d \\ A_c \cos(k_{2x}x + \psi) & |x| < d \\ A_u e^{\alpha_{3x}x} & x < -d \end{Bmatrix} e^{-jk_z z} \qquad [3.38]$$

where the form of the wave in the core can either be even or odd depending on the value of ψ. The constants A_o, A_c and A_u are the field intensity constants in each of the regions. The

wave numbers in the respective regions are provided by the dispersion relationship and are expressed as:

$$\alpha_{ox} = \sqrt{k_z^2 - n_o^2 k_0^2} \qquad [3.39]$$

$$k_{cx} = \sqrt{n_c k_0^2 - k_z^2} \qquad [3.40]$$

$$\alpha_{ux} = \sqrt{k_z^2 - n_u k_0^2} \qquad [3.41]$$

The magnetic component is obtained from Maxwell's curl equation;

$$H_z(x,z) = \frac{j}{\omega\mu_m}\frac{\partial}{\partial x}E_y(x,z) \qquad [3.42]$$

and hence knowing the electric field components (3.38) the magnetic field can therefore be expressed as:

$$H_z(x,z) = \left\{ \begin{array}{c} \dfrac{-j\alpha_{ox}}{\omega\mu_o} A_o e^{-\alpha_{ox}x} \\ \dfrac{-jk_{cx}}{\omega\mu_c} A_c \sin(k_{cx}x + \psi) \\ \dfrac{j\alpha_{ux}}{\omega\mu_u} A_u e^{\alpha_{ux}x} \end{array} \right\} e^{-jk_z z} \qquad \begin{array}{l} x > d \\ |x| \le d \\ x < -d \end{array} \qquad [3.43]$$

The boundary conditions arising at the interface between the different mediums now allows the evaluation of the relative field strengths given in (3.38) and (3.43). The tangential components of **E** and **H** fields are required to be continuous in these boundary regions and thus allow comparison of the relative field magnitudes of the fields strengths in the various regions (A_o, A_c *and* A_u). Thus from the boundary between the over-clad (o) and the core (c) at $x = d$ we get:

$$E_{\tan} : A_o e^{-\alpha_{ox}\frac{d}{2}} = A_c \cos\left(k_{cx}\frac{d}{2} + \psi\right) \qquad [3.44]$$

$$H_{\tan} : A_o e^{-\alpha_{ox}\frac{d}{2}} = \frac{\mu_1 k_{cx}}{\mu_c k_{ox}} A_c \sin\left(k_{cx}\frac{d}{2} + \psi\right) \qquad [3.45]$$

and thus by dividing equation (3.45) by (3.44) we can eliminate the constants A_o and A_c giving:

$$\tan\left(k_{cx}\frac{d}{2} + \psi\right) = \frac{\alpha_{ox}}{k_{cx}} \qquad [3.46]$$

The core to under-clad boundary conditions likewise yield the relationship (3.47), although obviously if the structure is symmetric this is unnecessary.

$$\tan\left(k_{cx}\frac{d}{2}-\psi\right)=\frac{\alpha_{ux}}{k_{cx}} \qquad [3.47]$$

The repeating nature of the *tan* function $\left[\tan x=\tan(x\pm n\pi)\right]$ and introducing the phase functions allow equations (46) and (47) to be expressed as:

$$k_{cx}\frac{d}{2}+\psi=\phi_o^{TE}\pm n\pi \qquad [3.48]$$

$$k_{cx}\frac{d}{2}-\psi=\phi_u^{TE}\pm m\pi \qquad [3.49]$$

with the familiar phase function from equation (3.33) for the two individual boundaries $\phi_g^{TE}=\tan^{-1}\left(\frac{\alpha_{gx}}{k_{cx}}\right)$ where g = o or u. By combining (3.48) and (3.49) to eliminate the function ψ we get the *guidance condition* for an asymmetric planar waveguide:

$$4k_{cx}d-2\phi_o^{TE}-2\phi_u^{TE}=2p\pi \quad p=0,1,.... \qquad [3.50]$$

The guidance condition equation can be solved to yield the number of modes permitted to guide within a structure at a given frequency (p corresponds to the mode) and the propagation constants for those modes. The guidance condition is an eigenvalue equation which cannot directly be solved, however solutions can be found through numerical or graphical techniques. Rearranging equation (3.50) and taking the tangent of both sides results in:

$$\tan\left(k_{cx}d-\frac{n\pi}{2}\right)=\tan\left(\frac{\phi_o+\phi_u}{2}\right) \qquad [3.51]$$

By using the relation (3.22) of $k_{cx}=n_1k_0\cos\theta$ and the forms of ϕ_o^{TE} and ϕ_u^{TE} given in (3.35) both the LHS and RHS of equation (3.51) can be plotted as functions of $\cos\theta$. The intersection points between the two functions correspond to solutions of the guidance

condition indicating the number of modes able to propagate down the structure and the propagation constant for each one.

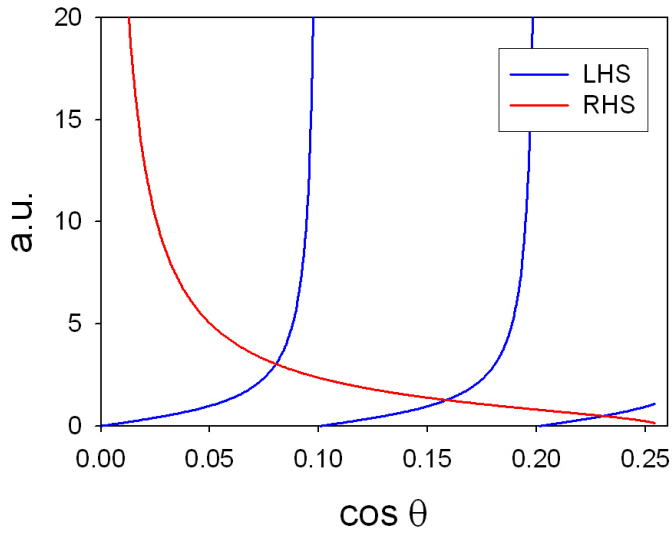

Figure 3.8: Demonstration of the graphical solution of the guidance condition (TE) for a symmetrical waveguide. In this example the cladding refractive index is 1.44, the core index 1.49 with a core width of 5μm resulting in three modes corresponding to k_{1x}=5.0, 9.9 and 14.4 x10^{5}m^{-1} respectively.

The solutions for TM polarised light can be derived through an analogous process obtained directly through use of the duality relation.

The magnetic field as described as:

$$H_y(x,z) = A_c \begin{cases} \cos\left(k_{cx}\frac{d}{2}+\psi'\right)e^{-\varepsilon_{ox}\left(x-\frac{d}{2}\right)} & x > d \\ \cos(k_{cx}+\psi') & |x| \le d \\ \cos\left(k_{cx}\frac{d}{2}-\psi'\right)e^{\alpha_{ux}\left(x+\frac{d}{2}\right)} & x < -d \end{cases} e^{-jk_z z} \qquad [3.52]$$

The guidance condition becomes:

$$4k_{cx}d - \phi_o^{TM} - \phi_u^{TM} = 2p\pi \qquad [3.53]$$

again with reference to equation (3.34) defining the phase shift at the dielectric boundary $\phi_g^{TM} = \tan^{-1}\left(\frac{\alpha_{gx} n_1^2}{k_{gx} n_2^2}\right)$ where g = o or u. Knowing the phase shift experienced at the boundaries and the x component of the wave vector we can determine the distribution of the electric field within the waveguide for each of the guided modes. Given the standing wave pattern formed by a guided mode in the waveguide structure the y component of the electric field (3.38) can be expressed as;

$$E_y = A_c \cos\left(k_{cx} x - \frac{p\pi}{2}\right) \qquad [3.54]$$

where the mode number p defines if the function is an even function ($A_c \cos(k_{cx} x)$) or an odd function ($A_c \sin(k_{cx} x)$). In a symmetric waveguide the 'phase centre' of the wave is located midway between the two interfaces (x=0). In the more complicated case of the asymmetric waveguide structure the effective phase centre will be displaced away towards the interface with the lower index difference. From the guidance condition the total phase change for a standing wave starting from the phase centre, reflecting off the two boundaries and back to the centre is $(-4\pi m)$ where n is an integer. This phase change is a combination of the distance the wave propagates $(-4k_{cx} d)$ and the phase shift from the TIR at the boundary (ϕ_o^{TE} and ϕ_u^{TE}). By considering the phase centre to be offset by a distance (Δ) from the spatial centre and by considering the propagation of the waves from the phase centre to each boundary and back to the phase centre individually then the displacement distance can be expressed as:

$$\Delta = \frac{\phi_u - \phi_o}{2k_{cx}} \qquad [3.55]$$

and the distance x in equation (3.55) is considered to be the distance from the centre of the waveguide plus Δ. The field is normalised (A_c=1) and the constants for the evanescent fields (A_o and A_u) are set at the boundaries relative to the normalised constant A_c with the magnitude of α_{ox} and α_{ux} set by equation (3.39) and (3.41) respectively.

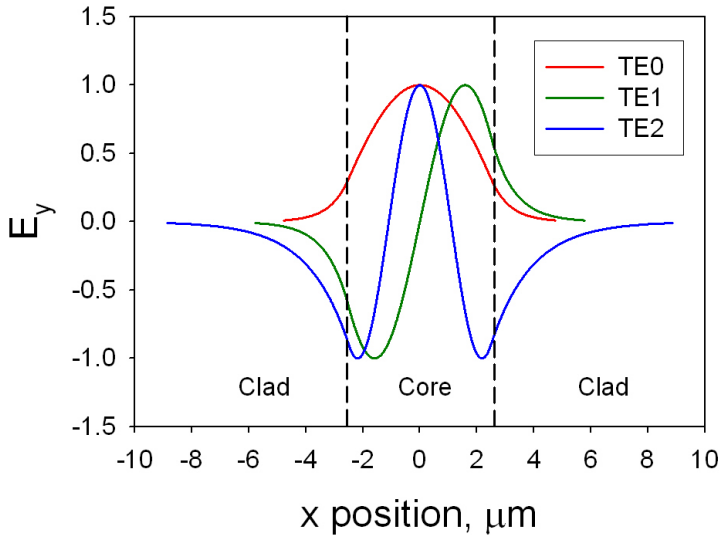

Figure 3.9: Demonstration of the electric field intensity of three modes identified in figure 3.3. Clearly visible is the greater penetration of the evanescent field as the mode order increases (i.e. weaker bound).

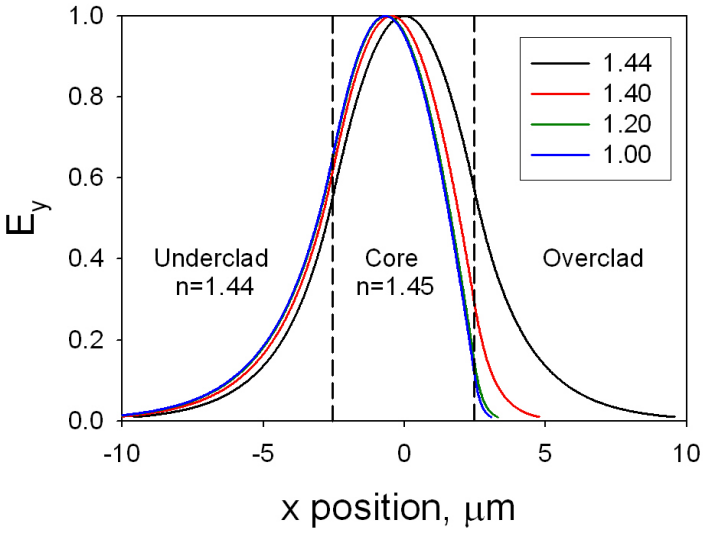

Figure 3.10: Effect of asymmetry on the electric field distribution in a 3-layer waveguide. The different traces correspond to varying over-clad refractive indices.

3.4.1 Normalised parameters

To calculate the wave-guiding properties of various structures at a given wavelength the solutions to the guidance condition has to be found in each instance. In order to reduce the calculation overhead for each of these situations the specifics of wave-guiding problems are expressed in terms of *normalised parameters*. These parameters are dimensionless and allow the solution of a wide range of slab waveguides from a single computation. The first

parameter is the *normalised frequency* or *v-number* that is related to the free-space wave-number, waveguide width and strength in the following relationship:

$$v = k_0 d \sqrt{\left(n_c^2 - n_u^2\right)} \qquad [3.56]$$

The *v* number can be considered as an expression for how strong the guide is for any given frequency. The next parameter is the normalised propagation constant *b* as expressed in equation (3.57) and this can be considered an expression concerning the propagation of the light relative to that in the core and cladding layers;

$$b = \frac{\left(n_{eff}^2 - n_u^2\right)}{\left(n_c^2 - n_u^2\right)} \qquad [3.57]$$

where n_{eff} is the effective refractive index observed by the guided light. As the effective dielectric constant can take a value between the core and cladding constants, the value varies from 0 to 1 with cut-off occurring ($b \rightarrow 0$) as the effective refractive index tends towards that of the under clad.

If the refractive index profile is symmetric then the normalised frequency and propagation constant are sufficient to describe the guidance condition, however as given in the above examples and as frequently occurs in practical situations the profile is not symmetric and so we introduce an *asymmetry* factor *a* (polarisation dependant) to address the refractive index difference between the two cladding layers (3.58).

$$a^{TE} = \frac{\left(n_u^2 - n_o^2\right)}{\left(n_c^2 - n_u^2\right)} \qquad [3.58]$$

The possible values of *a* varying between 0 for a symmetric waveguide and ∞ for a very asymmetric waveguide structure.

Incorporating these normalised parameters the guidance condition (3.53) allows a general description of the properties of a slab waveguide;

$$v\sqrt{1-b} = p\pi + \tan^{-1}\sqrt{\frac{b}{(1-b)}} + \tan^{-1}\sqrt{\frac{(b+a)}{(1-b)}} \qquad [3.59]$$

where again *p* denotes the various modes that can propagate within the structure. When evaluated, equation (3.59) provides a normalised ω vs. k_z diagram as shown in figure 3.11.

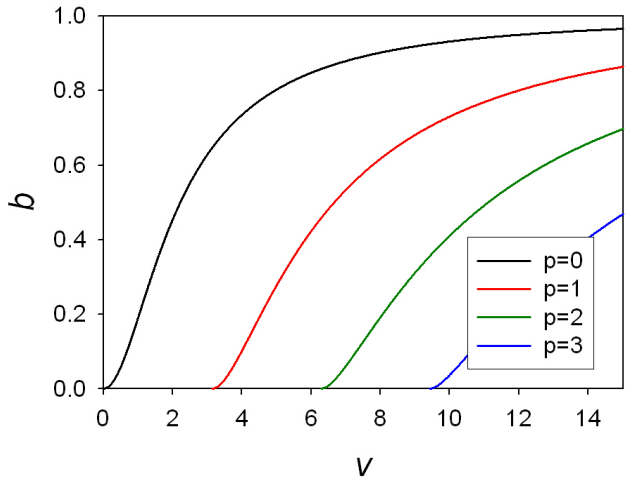

Figure 3.11: Normalised waveguide parameter diagram showing the first 4 modes of a symmetric slab waveguide.

These normalised parameters readily allow for the modal properties of a structure to be determined. The interpretation of b as it tends to 0 is that the effective refractive index becomes that of the cladding, the mode is no longer bound into the core of the waveguide, and hence, not a guided mode. So in the symmetric case shown in figure 3.11 it is clear that for the first mode cut-off occurs at v=0, i.e. there is always a fundamental mode, but the second mode experiences a cut-off at $v \approx 3.1$, so for 'v' numbers below this cut-off the structure can support only a single mode, above this the structure is multi-mode, a key distinction in modern optical systems.

As can be seen in figure 3.12 by considering the fundamental mode of an asymmetric waveguide with a range of asymmetry factors the cut-off and propagating properties of the guided mode are significantly affected through the imbalance of the cladding layers refractive indices. With strong waveguides (high v number) the mode is confined primarily to the core of the waveguide and the effect of the asymmetry decreases with the effective index tending to that of the symmetrical case. As the strength of the waveguide decreases the mode becomes less confined to the core with greater penetration of the evanescent fields into the cladding layers, therefore the mode is more susceptible to the refractive index difference. The boundary with the smallest index difference becomes the dominant factor in the occurrence of cut-off, therefore unlike the symmetric case, fundamental cut-off can occur at values of the normalised frequency >0.

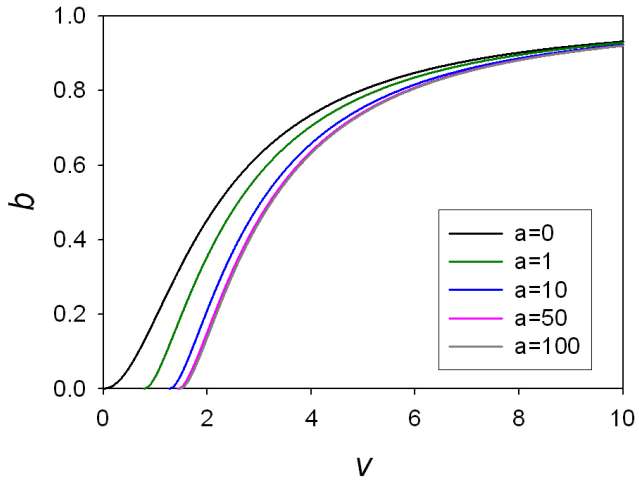

Figure 3.12: Effect of asymmetry on the *b-v* diagram for the fundamental mode of a slab waveguide with the cut-off shifting due to the lower refractive index of one of the cladding layers.

3.5 Channel Waveguides

Channel waveguides are structures that have index variations in two dimensions and in general cannot be analytically evaluated for the guidance condition except for a few special situations involving waveguide structures with simple, symmetrical index distributions. In reality channel waveguides rarely fit into these cases and as such cannot be analytically solved.

However, there remains a need for understanding the guidance properties of these structures and to this end there are a wide range of techniques to approximate the situations ranging from the simple but inflexible Marcatili's method, Effective index method, to the more complicated but versatile techniques of Finite elements methods (scalar and vectorial) and finite difference methods. Given the practical nature of this thesis it was decided that one of the cruder analysis techniques for channel waveguides would provide enough information on the behaviour of the waveguides. Of the simpler 'analytical' methods the commonly used techniques are the Marcatili Method and the Effective Index Method.

Marcatili's method was first proposed in 1969 and despite its age it is still a commonly utilised technique for approximate solutions. The limitation of the technique is the relative crudity and symmetrical nature of the channel waveguide that can be analysed as shown in figure 3.13. The structure is a buried waveguide, with index n_1, $2a$ wide and a height of $2b$.

The index of the surrounding layers is always n_2 and it is assumed that the mode is contained only in the core, thus the effect of the material in the four corners of the grid (grey squares in figure 3.13) is discounted. Although this method is readily applicable to many buried waveguide structures, due to the nature of the fabrication techniques employed in the production of the structures actually implemented, it is not necessarily an accurate representation of the structure we are interested in and so the more flexible *effective index* method was used.

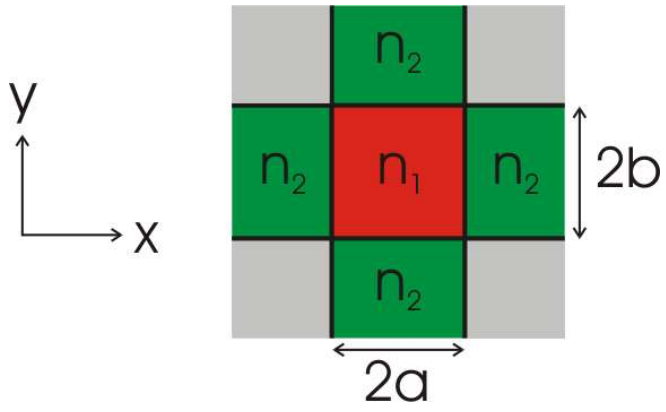

Figure 3.13: Structures that can be analysed utilising Marcatili's method. The field is confined entirely in the core, not existing in the four corners (grey). It is further assumed the index difference is the same in both the *x* and *y* axis.

3.5.1 The Effective Index Method

The effective index method is essentially an extension of the slab waveguide solving technique described in detail in section 3.4. To evaluate a channel structure it effectively separates the 2-d grid of indices into three planar waveguides. These waveguides are solved and the three resultant effective indices are then used to create an orthogonal planar waveguide that is in turn solved to give an estimate of the channel waveguide. The structure and process is illustrated in figure 3.14.

This technique allows for a matrix of 9 independent refractive indices to be entered and yet requires minimal processing power for the computation of the resulting guided modes. The flexibility of implementing a matrix of refractive indices allows the simulation of fabrication techniques that will allow horizontal index structure not only relative to the core but relative to the cladding layers as well. A custom program was implemented as a low cost simulation technique ensuring transparency in the calculation method. A second

advantage to the custom program is that it permits any of the waveguide parameters to be varied in a systematic process and the effect to be plotted. More information on the program written to solve these problems is included in Appendix B, avoiding the inclusion of code in the body of this thesis.

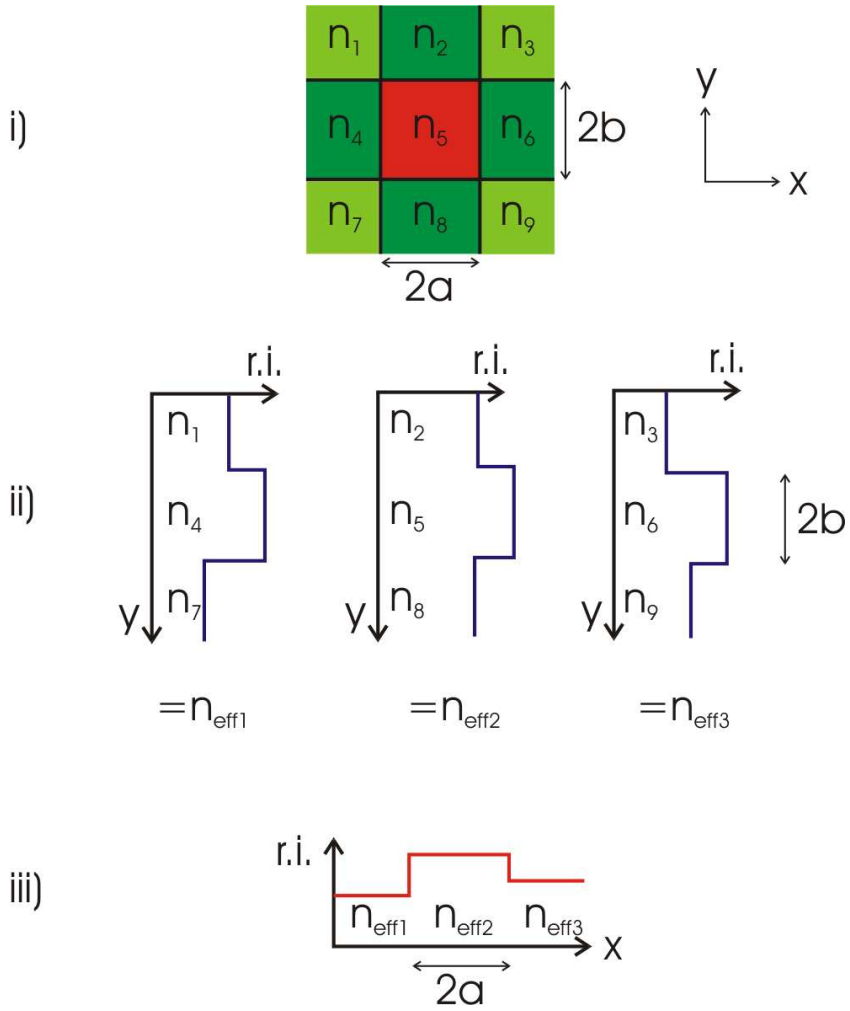

Figure 3.14: Effective Index Method evaluating a channel waveguide. i) defining the structure as a grid of 9 separate refractive indices ii) Separate the grid into three 'slab' waveguides down the *y* axis, evaluating each to give a effective index. iii) Create a 'effective slab' from the results of step (ii) the width of the original channel and evaluate to give the results for the channel waveguide.

The program allows for simulation of slab structures as shown in figure 3.6, symmetric channels as shown in figure 3.13 and the 9 cell arrangement as described in figure 3.14. It provides the determination of the number of modes of a given structure, the effective index of those modes and the field distribution of the given modes.

In figure 3.15 a channel waveguide is evaluated for the number of modes and the effective index of the modes as the index of the channel waveguide is varied from the background index to $3x10^{-2}$. As can be clearly seen that the effective index tends towards that of the core as the index difference gets greater and the point at which the channel becomes multimode is clearly evident.

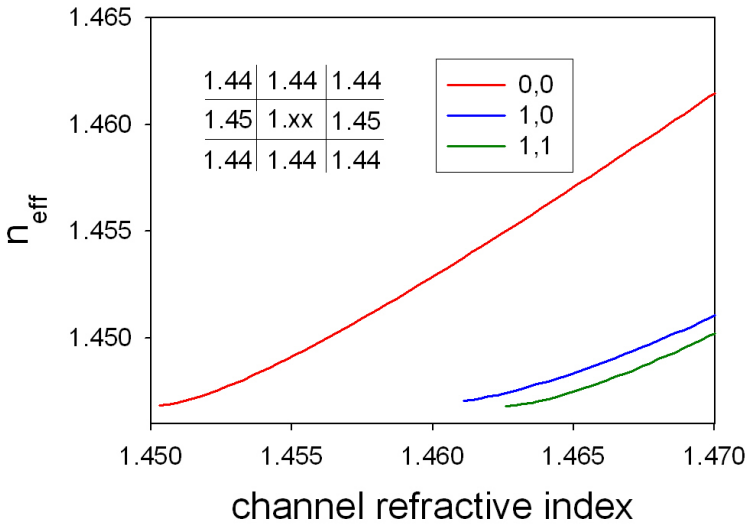

Figure 3.15: Effective index of guided mode in a channel waveguide structure 5µm x 5µm vs. the index of the core of the waveguide. The index matrix is in the top LHS of the figure and the plots represent the 3 modes possible in the structure.

3.6 Summary

This section dealt with the theory and derivation of a computer program to estimate the wave-guiding properties of channel waveguides constructed from a nine element matrix of refractive indices. This program has been used repeatedly in the following chapters to provide insight of the various structures and devices fabricated.

The derivation originated from Maxwell's equations, from which the wave equation was derived. From this, the effect of discontinuities in the refractive index of a glass with the resultant reflected and refracted waves was shown. Particular attention was paid to the additional phase shift induced to waves undergoing total internal reflection and the presence of evanescent fields into the region where typically there is no transmitted wave.

An asymmetric slab waveguide structure was then considered, resulting in confinement of the light between two material layers with a low refractive index. The process of the solving the guidance condition for such structures was demonstrated with the field distribution calculation for each of the waveguide modes. Alternative, normalised parameters were introduced, allowing the expression of various waveguide structures using a single parameter.

The problems with solving channel waveguides solutions were discussed, with mention of two techniques for the types of channel structures implemented throughout this thesis. The limitations of the commonly used Marcatili method are described before the Effective Index Method is introduced. The EIM technique is described and implemented into a simulation for the solving of the guidance condition of structures with non-symmetrical index distributions. This simulation is used throughout later sections of this thesis to provide an estimate of the guided mode response to a range of waveguide structures.

Chapter 4: Fabrication techniques

4.1 Abstract

A brief summary of some of the common fabrication techniques is presented in this section. A historical progression of the CVD process from thermal oxidisation through to plasma enhanced chemical vapour deposition is presented, highlighting the similarities and differences between the techniques. Included are two fibre fabrication processes; modified chemical vapour deposition and outside vapour deposition, as these are fundamental to the techniques presented in chapter 5. Two channel definition techniques are introduced; Reactive Ion Etching and Direct UV writing, the two techniques are compared, emphasising the different foundry applications of the processes.

4.2 Introduction

In the following material a review is given of the deposition techniques based on the Chemical Vapour Deposition process, used for the fabrication of planar or thin-film layers suitable for optical waveguide fabrication. There are many variants and sub-variants of the techniques that are not mentioned, the following covers the family of techniques that are applicable to the material presented later in this thesis. There is much information available on the production of planar lightwave circuits, however readers are directed towards (Sze 1988; Li and Henry 1996; Okamoto 1999; Hibino, Maruno et al. 2001) for excellent background information on the techniques.

The CVD based deposition techniques deposit layer structures, defined as uniform 2-dimensional planes of material. To define a channel waveguide subsequent processing is required. Presented are two techniques that allow the definition of channel waveguides using significantly different methods. One of the techniques is the de-facto industry standard and the other technique is a very flexible process and forms the basis for much of the work in this thesis. This summary is not exhaustive; it is worth noting that there are many other techniques such as ion-exchange, direct electron beam writing and ion milling that are not discussed.

4.3 Material deposition

In all the techniques described, the deposition process is directed to produce a silica-based amorphous layer suitable for optical waveguides. As described in the previous section to define a waveguide structure the refractive index of the material is required to be a function of position, with a core layer surrounded by material with a lower refractive index. In terms of fabricating these structures, as in the fabrication of optical fibres the properties of pure silica are modified by the introduction of small levels of dopants to change the properties of the glass. Originally, the function of the dopants was to control the refractive index of the material, thus allowing the definition of the guided mode confinement structure. However with the discovery of photosensitivity co-doping with photosensitisers is essential, since pure silica is not sufficiently photosensitive for most applications (chapter 2). Common dopants include Germanium, Phosphorous and Boron, each resulting in a different influence on the glass' refractive index, glass transition temperature and thermal expansion.

Typically in the fabrication of planar structures there is a host substrate. With silica based material systems the substrate tends to be either bulk silica or silicon wafers. Silica or silicon tend to be the industry standard as they are both mechanically strong, can be very high quality and most importantly can resist the temperatures involved in most of the fabrication processes. Silica is a robust material, has a high melting temperature and is very compatible with the silica-based structures deposited onto the substrates. One of the disadvantages of silica substrates is that they are not mass produced and so are more expensive than alternatives. Silica has a tendency to crystallise with time in the fabrication process if held at temperatures below the glass transition temperature(Varshneya 1994), and at temperatures significantly lower than the melting point silica becomes malleable, often deforming. The alternative, silicon wafers are mass produced, readily available and fully understood and compatible with the equipment and techniques developed by the microelectronics industry. However, there is a significant difference in refractive index, expansion coefficient and melting point.

4.3.1 CVD derived processes

One of the most commonly employed classes of fabrication technique for the fabrication of silica-based waveguides is that of Chemical Vapour Deposition processes (CVD). Chemical Vapour Deposition is the name given to a general process type, involving halide or hydride vapours (contained within a transport gas, typically nitrogen or oxygen) that undergo a heterogeneous reaction on, or above the substrate. This results in either a glass film deposited or an intermediary particle form that is subsequently sintered into a solid film. A few of the CVD derived processes are detailed below, illustrating the relationships between the differing techniques.

- Thermal Oxidation
- Low Pressure Chemical Vapour Deposition (LPCVD)
- Plasma Enhanced Chemical Vapour Deposition (PECVD)
- Modified Chemical Vapour Deposition (MCVD)
- Outside Vapour Deposition (OVD)
- Flame Hydrolysis Deposition (FHD)

The majority of the techniques above describe planar definition processes; however the MCVD and the OVD fibre fabrication processes have been included as they are the foundations for some of the fabrication techniques used in the fabrication of the samples presented in chapter 5.

4.3.1.1 Thermal Oxidisation

Thermal oxidisation is a process involving the thermal dissociation of the reagents and the subsequent growth of the solid compound composed of the constituents of the initial reagents. The reagents are of a gaseous nature with the resulting compound forming a solid layer upon any surfaces within the deposition chamber.

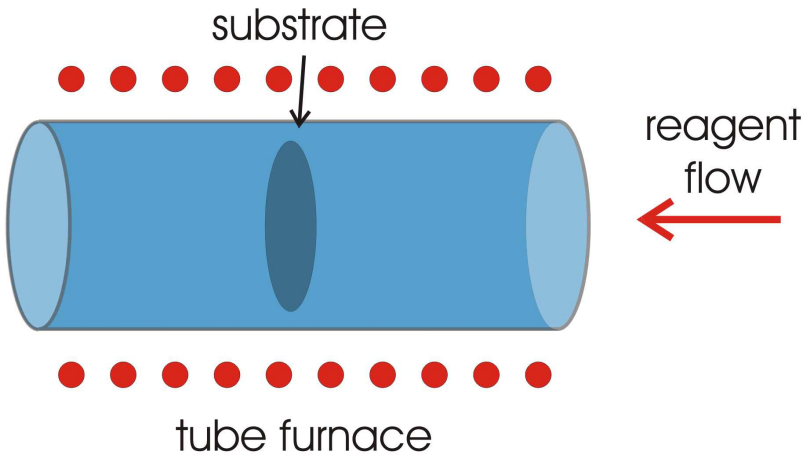

Figure 4.1: Basic CVD process, reagent flow through a tube furnace triggering the thermal decomposition of the reagent gas onto the substrate

Basic thermal oxidisation occurs within a furnace in which the substrate to be deposited is placed, the reagents are passed through in a laminar flow. The temperature within the furnace is selected to allow the thermal decomposition of the halide molecules resulting in deposition on the sample and the production of the associated waste gas (example see equation 4.1). The vapour form of the reagents allows safe, remote production of the source material. The oxide deposition occurs as a direct transition from the gas phase to the solid glass film onto the substrate. The rate of the deposition is a function of the flow rate and the temperature of the substrate, with typical operating temperatures of the order of 700 – 900°C, promoting a slow but controlled growth of the oxide layer.

$$SiCl_{4(v)} + O_{2(g)} \rightarrow SiO_{2(s)} + 2Cl_{2(g)} \qquad [4.1]$$

Even though the temperatures involved are relatively low for thermal processing the long time scales involved for this fabrication method often triggers problems with the unwanted diffusion of dopant molecules between layers of different compositions of the sample.

The steps of thermally driven CVD process are shown below:

- Transport of the reactants to the growth region
- Mass transport of reactants to wafer surface
- Absorption of reactants
- Physical-Chemical reactions yielding the solid film reaction by-products

- Desorption of by-products
- Mass transport of by-products to the main gas stream
- Transport of by-products away from growth region

4.3.1.2 Low Pressure Chemical Vapour Deposition (LPCVD)

As the name implies this is the same thermally driven process as described above however in a controlled environment. The reaction chamber is under a vacuum (30 to 250 Pa) with the substrate at the base of the chamber. The substrate is heated to the same temperature as before (700 to 900^{o}C) to trigger the thermal decomposition. As the deposition chamber is under vacuum with only the reagent gas flowing through the vessel the contamination of the sample due to atmospheric contamination is significantly reduced. This provides greater control over the composition of the layers and significantly lower loss, allowing the production of higher quality films.

4.3.1.3 Plasma Enhanced Chemical Vapour Deposition (PECVD)

Possibly the most applied thin film deposition technique employed in production of planar structures in the current market is the Plasma Enhanced Chemical Vapour Deposition process. PECVD is a development of the low pressure chemical vapour deposition process with the environment in the deposition chamber strictly controlled. However, unlike the previous techniques the dissociation of the reagents is not only thermally triggered but promoted through electron impact. Conceptually, the parallel plate reactor is the simplest implementation to demonstrate the process. The deposition chamber is comprised of two parallel conductive plates that form the electrodes required to strike the plasma. The sample is placed on the bottom electrode, typically heated through use of resistive elements thus allowing the temperature of the sample to be controlled during the deposition. The two electrodes are in close proximity and with the deposition chamber pumped down, a plasma is struck between the electrodes by applying a RF signal across the electrodes. During deposition the reagent gas is introduced to the plasma, the resulting energetic electrons strike providing the energy for the dissociation of the reagents. As the plasma triggers the decomposition the substrate can be held at much lower temperatures (250 to 350^{o}C) significantly reducing the diffusion of dopants.

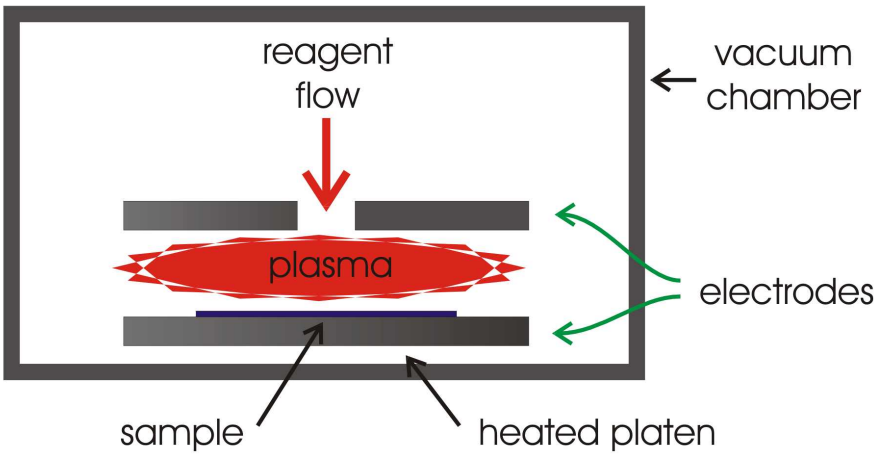

Figure 4.2: PECVD deposition process.

The process of layer growth in PECVD is the same as that for LPCVD (2.2.2) with the notable exception of additional processes between steps 2 – 6. A fraction of the reactants are in a highly reactive state due to electron impact dissociation and excitation by the plasma. Due to the excited state of the reactants, the activation energies of the oxidization reactions are lower resulting in a low process temperature.

This technique is often quoted as a single step fabrication technique, however the layers produced are not fully dense. To produce low-loss optical layers the sample require a subsequent annealing stage to fully compact the layer at temperatures >1000^{o}C (Hoffmann, Kopka et al. 1997). Although generally short, this step can again induce migration of dopants. Before the layer is annealed, there is an observed increase in the photosensitivity in germanosilicate layers.

4.3.2 Fibre fabrication techniques

4.3.2.1 Modified Chemical Vapour Deposition (MCVD)

Modified Chemical Vapour Deposition is a technique for fabricating fibre preforms. A silica tube is rotated in a lathe with an oxy-hydrogen torch played along the outside of the tube. Inside the tube, a laminar flow of a carrier gas (often oxygen) containing the halide vapour. During each traversal of the burner, within the heated region the temperature is such that a homogenous reaction creates fine oxidized particles (thermal oxidization, see

equation 4.1) referred to as 'soot' within the tube vapour stream. The particles deposit down-stream from the burner on the internal walls of the silica tube. The temperature of the torch (1500 – 2050°C) raises the temperature of the tube such that the oxidised particles sinter within the tube to form a glassy film. After the desired glass film thickness has been reached, slower translation of the torch heats the tube such that the silica became soft and surface tension causes the collapse of the tube, thus forming a rod. Fibres are subsequently produced from the rod (fibre preform) in a thermal drawing process.

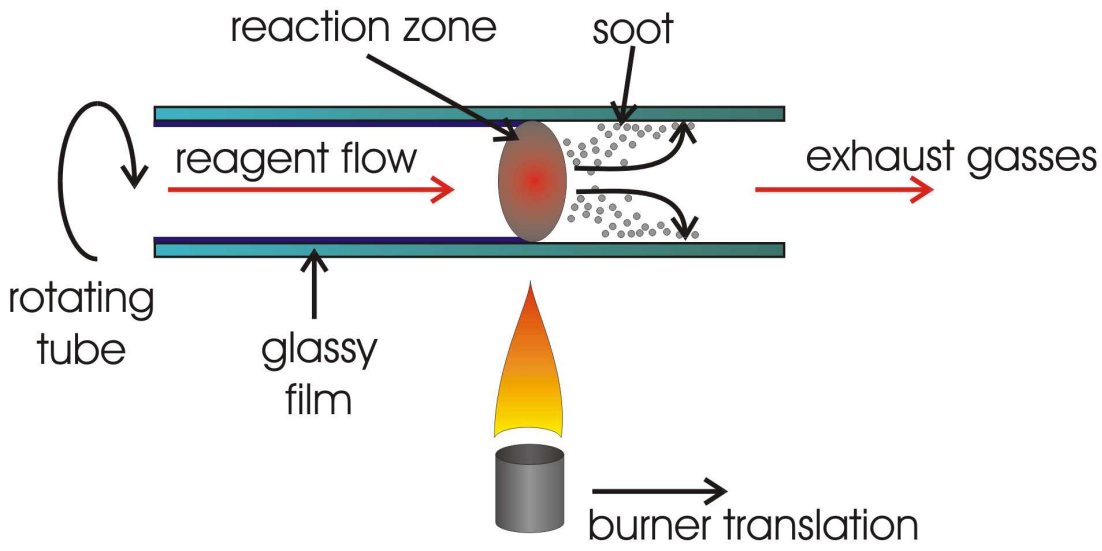

Figure 4.3: MCVD fabrication process for production of fibre preforms.

4.3.2.2 Outside Vapour Deposition (OVD)

Outside vapor deposition is a deposition technique based on flame hydrolysis rather than thermal oxidization. A metal mandrel is mounted in a lathe, along which an oxy-hydrogen burner is traversed. The oxy-hydrogen flame burns in an exothermic reaction producing heat and H_2O, Halide vapors within a transport gas are subsequently introduced into the burner to produce the oxide. The subsequent hydrolysis reaction (see equations 4.3-4.4 for typical dopants) creates a glass 'soot' (oxide particles) that is deposited onto the mandrel. A by-product of the hydrolysis reaction is hydrochloric acid.

$$SiCl_{4(v)} + 2H_2O \rightarrow SiO_{2(s)} + 4HCl_{(v)} \quad [4.2]$$

$$2POCl_{3(v)} + 3H_2O \rightarrow P_2O_{5(s)} + 6HCl_{(v)} \quad [4.3]$$

$$4BBr_{3(v)} + 6H_2O \rightarrow 2B_2O_{3(s)} + 12HBr_{(v)} \quad [4.4]$$

Typical halide reagents used are $SiCl_4$, $POCl_3$, BCl_3, and $GeCl_4$ thus producing SiO_2, P_2O_3, B_2O_3 and GeO_2 particles along with HCl in vapour phase. The temperature of the burner is set to partially sinter the silica particles and create a robust porous silica soot layer over the mandrel. The dopant concentration in the deposited soot is defined by the halide concentration supplied to the burner and the incorporation efficiency of each reagent. After deposition, the soot layer is removed from the mandrel and subsequently consolidated to form a preform, before drawing into a fibre.

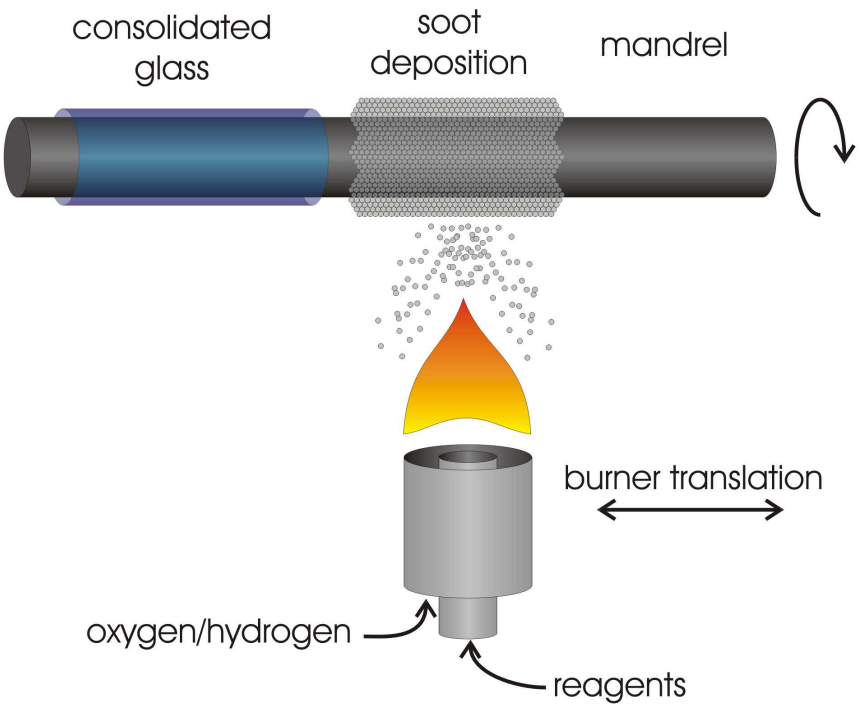

Figure 4.4: Schematic of the OVD deposition process

Although the description above ascribes the oxide formation to hydrolysis, the exact process of oxide particle formation in an OVD burner depends on the burner parameters used. Research has shown that even in a wet atmosphere, as in the case of an oxy-hydrogen flame the particle formation could be due to thermal oxidation rather than hydrolysis (Bautista and Atkins 1991). If the heat from the oxy-hydrogen flame is sufficient that the temperature of the reagents in an oxygen carrier gas is above 1200°C before contact with H_2O then the oxidation effects will dominate. If the temperature is less than 1200°C then the hydrolysis

reaction will dominate. Thus depending on the characteristics of the burner (size, flow and dilution of the gases either or both oxidation processes could be occurring).

4.3.2.3 FHD (Flame Hydrolysis Deposition)

Flame hydrolysis deposition is a variation of OVD for the deposition of thin silica films in a planar geometry (Watts 2002). Unlike OVD where the soot is deposited onto a mandrel that is removed later in the processes, the substrate is retained and provides the mechanical base for the silica layers. As with OVD, the soot particles are created in a hydrolysis (or thermal oxidation) reaction in an oxy – hydrogen burner to which halide reagents are supplied on a carrier gas. The burner and substrate are translated relative to each other to create an even film of oxide particles over the substrate. The layer is subsequently sintered in a furnace to consolidate the soot into an amorphous layer. As before, the composition of the thin glass film is defined by the ratio of Silicon Tetrachloride to dopant reagent in the carrier gas and the incorporation ratio for the deposition and consolidation process.

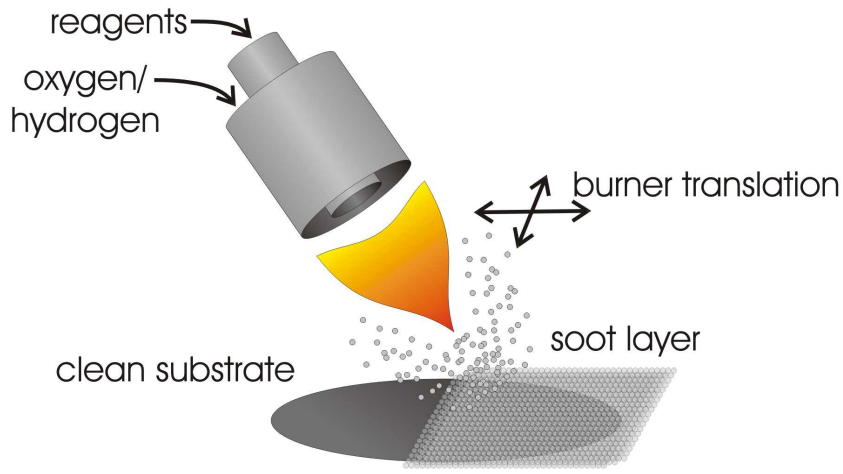

Figure 4.5: Schematic of the deposition step of the flame hydrolysis deposition procedure. The soot is subsequently sintered in a furnace to form a glassy layer.

4.4 Channel definition

The previous section described the commonly applied fabrication processes used to produce planar thin films (or fibres) in silica based material systems. However, for guided wave optics the light needs to be confined in two axes by defining a channel waveguide structure. In the following section two techniques are described, the first is reactive ion etching,

effectively the industry standard, and a well developed technique ideal for the mass production of similar devices. The second technique, Direct UV writing, is a relatively new alternative fabrication method offering a high degree of flexibility in the structures that can be defined.

4.4.1 Photolithography and Reactive Ion Etching

Photolithography (or optical lithography) is a technique that has been used for many years in the manufacture of semiconductor integrated circuits and has made the transition into the field of planar waveguide fabrication. It is the processes of transferring geometric shapes from a transmission mask into a 'photographic' layer spun onto a substrate. The photographic layer, known as photoresist can work in either positive or negative mode depending on the subsequent processing. It is a polymer sensitive to UV light, causing the exposed polymer to crosslink. The photoresist is spun onto the sample creating a thin film that is exposed to the mask pattern through a mask-aligner. The mask aligner exposes the sample through the mask to a weak UV source imprinting the mask structure into the resist. The resist can consequently be developed and the un-exposed resist washed away.

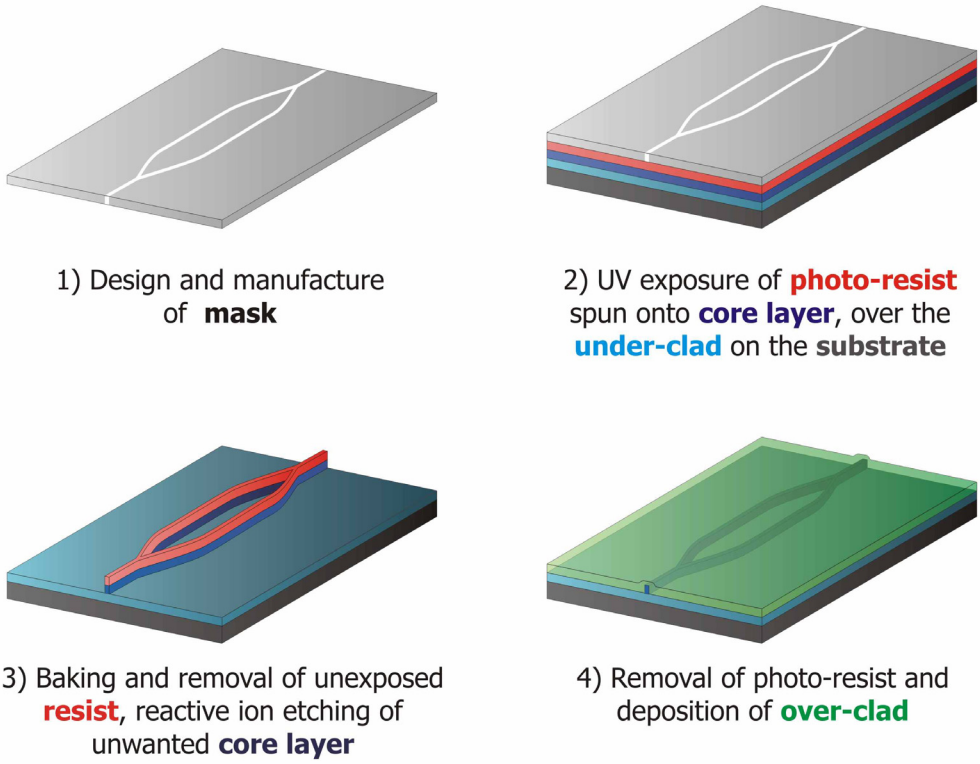

Figure 4.6: Processing steps involved in the photolithographic and reactive ion etching, manufacturing a buried Mach-Zehnder structure

The subsequent structure is then used either as an etch mask itself, or to fabricate a metal etch mask, depending on the composition of the material to be etched and the process used. Once the mask has been defined the structure is then etched to turn the pattern into a surface relief profile in the layer. There are two types of etching processing used, wet etch and dry etch.

Wet etching is the application or immersion of the sample into the etching solution. For silica based materials the etching solution is typically Hydrofluoric acid (HF) with the strength used depending on the application. If the photo-resist or metal mask has a slower etch rate than the glass then the covered areas of the sample are protected while only the exposed regions are etched away. The advantage of wet-etching is the simplicity of the process and low cost. The disadvantage of the technique is the isotropic nature of the etch, once within the etch material the etching process occurs in all directions, resulting in non straight etching features. Whilst this makes the technique not directly applicable to the definition of channel structures it is very good at bulk material removal (see section 9.13).

The alternative is Reactive Ion Etching (RIE), a dry etch technique aided by plasma. RIE is a combination of physical sputtering and chemical activity of the reactive species. The etchants are in a gaseous form and excited through the striking of plasma enhancing the material removal. This etch process maintains the material selectivity through the tailoring of the etch composition. Physical sputtering is the bombardment of a material with non-reactive ions, physically knocking atoms off of the material. This process results in a high degree of anisotropy but no selectivity of the composition of the material removal. The combination of the two etch effects result in a process with a high degree of anisotropy and etch selectivity.

The primary characteristic of photolithography combined with RIE lie in the multi-stage nature of the process (and figure 4.6):

- An optical mask needs to be created for any given design
- The sample is coated in photoresist, exposed and developed
- The relevant sections of photoresist need to be removed (depending on the lithography method used – could be many steps)

- Reactive ion etching of the sample
- Deposition of any cladding layers

This is a long and expensive process for defining small numbers of devices. The cost both in finance and time of fabricating a mask alone is considerable and not worth the investment if only a few devices are to be produced from it. The disadvantage of such a multistage process is each fabrication step increases the possibility of fabrication mistakes, thus decreasing the device yield per fabrication run.

The advantage of the combined photolithographic and reactive ion etch fabrication techniques lies in its ability to produce very large numbers of identical devices, and in parallel. By producing very large numbers of identical devices the cost per unit should be very low, following the trend demonstrated in the electronics industry. Given the large quantities of devices produced, relatively poor yields are acceptable with minimal impact on the cost of individual devices.

4.4.2 Direct UV Writing

Direct UV writing as a technique for defining channel waveguides is a relatively new fabrication process(Svalgaard 1997). It is based on the refractive index increase of a photosensitive material when exposed to ultraviolet light (section 2.3) however unlike most previous cases of photosensitivity the index change is not used to inscribe a grating into an existing channel waveguide but to define the channel waveguide itself. A laser with an emission around the 240nm absorption window (commonly frequency doubled Ar-ion or Excimer lasers) is focused down to a circular writing spot ~4μm diameter that is translated relative to a suitable sample. A suitable sample contains a photosensitive layer the thickness of the desired channel waveguides uniformly across the substrate and a non-photosensitive cladding layer if required. No other material structuring is required, therefore all initial unprocessed wafers are the same. The ‘blank’ sample is then translated relative to the writing spot, with the path of translation defining the channel waveguide structure.

Both the material characteristics and the power exposed during the writing process define the strength of the channel waveguides induced in this technique. To allow comparisons

between the different exposure values used during the writing process an expression for the average power exposed to the material in the channel waveguide. The *fluence* of the exposure can be defined as(Svalgaard and Kristensen 1997):

$$F = \frac{I_{UV} \cdot a}{v_{scan}} \qquad [4.1]$$

where F is the fluence in KJcm^{-2}, I_{uv} is the average power density of the writing spot in KWcm^{-2}, a is the spot diameter in cm and v_{scan} is the translation speed in cms^{-1}. This expression does not describe the entire writing process (see section 8.5) but is an approximate expression allowing the comparison of like writing powers.

The advantages of Direct UV writing lie in the flexibility of the process, unlike the previous etch based process there is only a single fabrication step between the design of a structure and the completed device. The structure is coded as a series of translations of the substrate, the blank sample is mounted on the stages with the fixed position writing spot defining the channel structure. There are no further processing steps to produce a device.

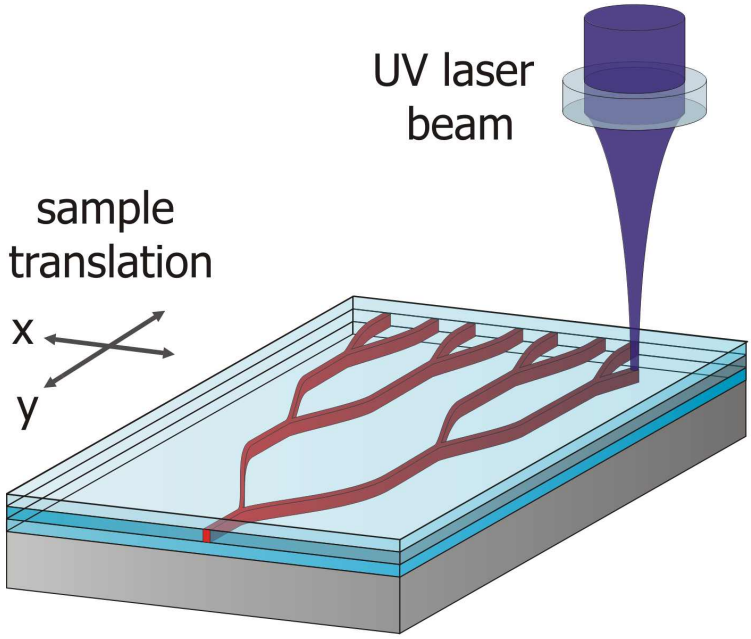

Figure 4.7: Direct UV writing fabrication process

Other advantages associated with this technique is the ability to change the channel waveguide parameters as the structure is defined. For example, by defocusing the writing spot as the sample is translating a tapered channel structure can be defined. Alternatively by changing the power of the writing spot as the sample is translated, a structure with a tapered

index change can be defined, a device virtually impossible to achieve with etching techniques.

There are two disadvantages associated with Direct UV writing, the refractive index change, and hence the channel strength is dependent on the photosensitivity of the material. Initially the waveguide material must have some form of photosensitive response which limits the choice of material composition. In general the refractive index changes defined through UV exposure is of a maximum of $1x10^{-2}$, and often lower compared to the wide range of indices possible from the deposition and etching of waveguide material. To obtain the largest UV induced index changes the material's photosensitivity must be enhanced through loading with Deuterium or Hydrogen. The gases are very mobile, and will diffuse out of the planar sample at room temperature, thus inducing time dependant sensitivity, and hence index change on the sample. There are ways around this problem, such as keeping the sample cold during UV writing (Svalgaard 1999)or enhancing the photosensitivity in a non-time dependent manner (Emmerson, Gawith et al. 2003), but nevertheless these effects must be considered.

The other disadvantage is the serial nature of the process, each channel waveguide is defined individually, at a finite speed. Unlike the etching technique where many structures and devices are formed in parallel, to define multiple structures they need to be defined sequentially. It is the author's opinion that the technique is ideally suited to the definition of one-off prototypes or small to medium batch production up to 100's of units due to the single-step fabrication. If there is ever a requirement for 1000's of identical structures then the etching process is undoubtedly the preferred technique.

4.5 Summary

In this section a brief development of the fabrication techniques used to produce thin film optical layers was presented. All the techniques involve source reagent in a gaseous or vapour form transported to the reaction site via a carrier gas. The initial and by far simplest technique was the thermal decomposition of the reagent species directly onto the substrate inside a heated furnace. However this technique was slow and the high temperatures triggered the diffusion of the glass dopants between material layers. The technique was

particularly sensitive to contamination, both particulate and elemental. The contamination was reduced by placing the reaction chamber under vacuum (Low Pressure CVD). This significantly reduced the contamination but did not prevent the diffusion of dopants. Introducing a plasma in the deposition chamber (Plasma Enhanced CVD) promotes the decomposition of the reagents at much lower temperatures, preventing the diffusion of the dopants during the deposition process. However, the layers are not fully dense and require a subsequent annealing step at high temperatures to produce low loss waveguides.

The fabrication techniques then branch out into fibre fabrication processes. These techniques, rather than the above described planar techniques, decompose the reagents in the vapour stream at very high temperatures forming particulates, or soot, of the glass to be deposited. In the modified chemical vapour deposition process (MCVD) the reaction occurs within a silica tube subsequently to form the cladding of the fibre. The process is triggered by a high temperature torch causing the thermal oxidation of the reagents in the vapour stream. The soot is deposited 'down stream' of the reaction zone and is subsequently sintered into glass as the touch passes over the tube. The second technique deposits the glass on the outside of a mandrel (OVD). The reagents are introduced into an oxy-hydrogen flame that triggers the formation of soot through a hydrolysis reaction. The soot is sprayed onto the mandrel and subsequently consolidated into glass using the same torch. The planar variation of the OVD is presented (Flame Hydrolysis Deposition) allowing the deposition of glass layers on planar substrates.

Two channel definition techniques are presented, the first is a combination of photolithography and reactive ion etching (RIE). This technique was developed for the semiconductor industry and later transferred to optical waveguide fabrication. It is a process that turns a design on an optical mask into a material or surface relief structure. It is a multi-step process allowing the parallel production of many identical waveguide devices but has minimal flexibility in the fabrication process. Direct UV writing in contrast is a technique where a channel structure is directly defined in a suitable photosensitive material by the translation of a tightly focused UV laser beam. The fabrication is a single step process with the structures designed on computer and then directly fabricated with no interim stages. This technique is ideal for production of one-off structures or small lot fabrication, but due to the serial nature of the process is not well suited to the fabrication of thousands of identical devices.

Chapter 5: Cylindrical structures

5.1 Abstract

In the following material the deposition processes for the fabrication of thin-film waveguide layers on cylinders is presented. Equipment, procedures and characterisation steps developed to produce such structures are presented. Layers were deposited on the surface of a cylinder using a Flame Hydrolysis Deposition based technique and a variant of the Modified Chemical Vapour Deposition process. Channels were directly UV written into the CVD layers. Waveguide films were also deposited using the normal MCVD process in the on side of a cylinder.

5.2 Introduction

In the material contained within the following sections I will give a brief overview into the various techniques applied to the fabrication of cylindrical structures. It is worth noting that there are very few systems that allow for the fabrication of large diameter cylindrical waveguides. Therefore, to deposit thin film layers suitable for 'planar' waveguides on cylindrical substrates required a range of modifications and compromises to be made to the fabrication systems.

The following chapter can be split into two sections, the 'planar' waveguide layer deposition and the channel definition process. For the channel fabrication process only one technique, Direct UV writing was used to define the channel as it is a versatile technique for defining complex structures which is further developed in the later chapters of this thesis. However the equipment again required substantial alteration to allow channel definition in a non-planar geometry. Over the course of the work, several techniques for the deposition of planar waveguide layers suitable for direct UV writing were investigated, with varying degrees of success.

5.3 Considerations of cylindrical layers

5.3.1 Cylindrical substrate

As discussed previously, the aim of this project was the deposition of thin, planar quality films onto non-planar geometries. Although not the only geometry to fit this description, the parallel cylinder is amongst the simplest implementation of such a structure. Parallel to the axis of the structure the surface is essentially planar, allowing straight channels to be defined with simplicity. Waveguides with path-lengths longer than the length of the cylinder can be defined by channel structures spiralling around the perimeter of the cylinder.

In considering the material for the cylindrical substrate, the silica tubes used as pre-forms for the MCVD process appear ideal. The tubes are readily available in a range of sizes and are manufactured out of high-grade (F300) silica. One significant consideration is the location of the planar layer, in the cylindrical geometry it can be manufactured on the inside of the cylinder or on the outside surface. The inside of a cylinder is in general harder to process for the definition of channel structures, has a smaller radius and may interfere with mounting systems for a cylindrical geometry. A layer on the perimeter of a cylinder would be easier to define channels in, but is more prone to mechanical or environmental damage. During this study various fabrication techniques and layer structures were implemented.

5.3.2 Cylinder diameter

In the transition between planar and cylindrical planar geometry there are several considerations to take into account. The size of the substrate is very relevant to the design of the devices; if the diameter of the cylinder is small then bend loss has a greater effect on the power of the guided mode. Bend losses are caused by the power in the confined mode being radiated away due to macroscopic changes in the propagation direction of the waveguide. An expression for the bend loss can be obtained by considering a situation where the evanescent ‘tail’ of the mode cannot propagate with sufficient velocity in the cladding to stay in phase with the guided mode. The light from the ‘tail’ radiates away and the power required to maintain the evanescent field is drained from the guided mode, hence

the guided mode experiences attenuation. The attenuation due to bend loss can be expressed as:

$$P(z) = P(0)e^{-\alpha z} \qquad [5.1]$$

where α is the exponential decay constant and $P(z)$ is the power at any point along the waveguide. It can be shown (Lee 1986) that the attenuation is of the form:

$$\alpha = C_1 e^{-C_2 R} \qquad [5.2]$$

$$C_1 = \frac{\alpha_x^{\,2}}{k_1} \qquad C_2 = \frac{2}{3}\frac{\alpha_x^{\,3}}{k_1^{\,2}} \qquad [5.3]$$

$$\alpha_x = \frac{\sqrt{v^2+1}-1}{d} \qquad [5.4]$$

where R is the bend radius, α_x is the attenuation constant for the evanescent field, k_1 is the propagation constant in the cladding, d the waveguide width and v the normalised frequency (section 3.4.1). In figure 5.1, the bend loss as a function of bend radius is plotted for a core/cladding index difference $1\text{x}10^{-2}$ and a layer thickness of 5µm.

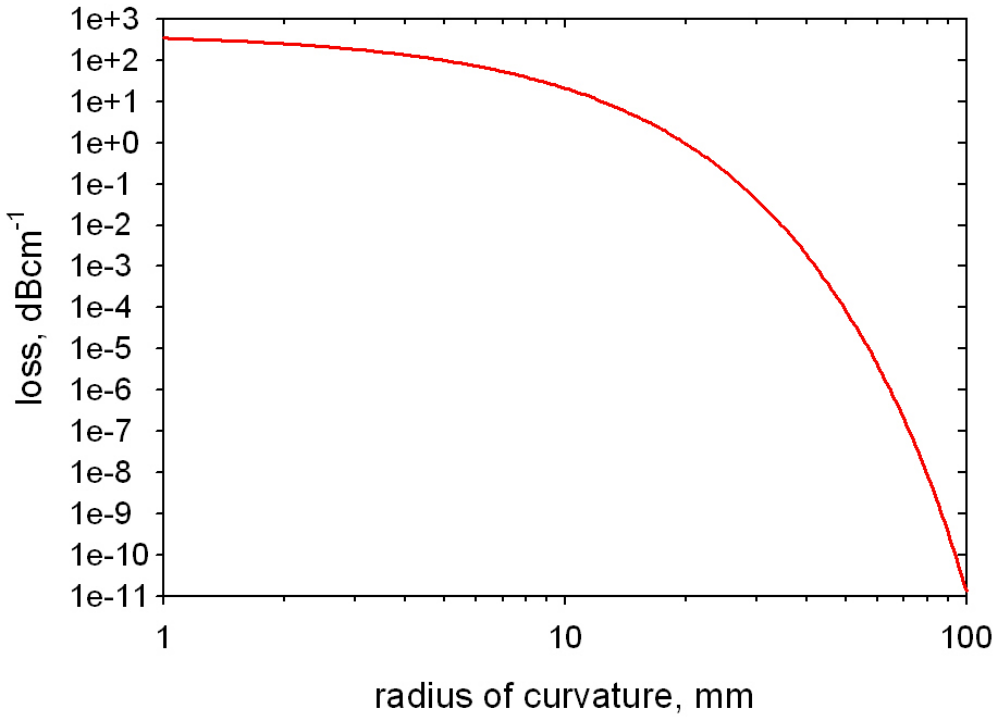

Figure 5.1: Bend loss as a function of bend radius, for a index difference of $1\text{x}10^{-2}$ between the core and cladding interface and a layer thickness of 5µm.

As illustrated in figure 5.1, the loss of the waveguide due to radius of curvature is a significant factor for bend radii less than 20mm in structures with a typical index difference between core and cladding. The bend loss for radii less than 20mm could be reduced somewhat by increasing the index difference between the core and cladding.

5.4 Cylindrical channel definition

The process of channel definition is described initially because only one fabrication method was employed. Direct UV writing was chosen as it does not require any surface contact on the substrate and is not dependent on a flat substrate. One of the considerations with the process was the focusing effect from the curved nature of the cylinder, however as long as the radius of cylinder is considerably larger than the distance between the air/silica interface and the photosensitive layer then there should be minimal effect on the writing beam focus.

There is a planar Direct UV writing set-up already in existence within the ORC. This setup is very flexible and has been used to demonstrate UV induced channel waveguides in a range of planar materials (Contardi, Taylor et al. 2001; Mairaj, Fu et al. 2001; Koo, Williams et al. 2003; Mailis, Riziotis et al. 2003), with a two dimensional linear translation stage allowing the motion of the samples tangentially to the incident writing beam. In the case of cylindrical geometry one axis of motion is linear and other rotational and as such are not readily compatible with the existing planar UV writing system. Much effort has gone into the stabilisation of the planar stages and as such they are not really suitable for re-configuring into a linear and rotational setup. Thus an alternative cylindrical setup was implemented to allow the testing of the Direct UV writing on cylinders without disturbing the planar setup.

The planar Direct UV writing setup is described in detail in section 7.5.4, however both the planar and cylindrical set-up share the same laser source, acousto-optic modulator and spatial filter. After the spatial filter the beam path could be directed towards the cylindrical Direct UV writing set-up. This set-up was designed and implemented specifically for the proof-of-principle work in this thesis. At the onset of the project there were two possible routes to the development of the equipment, a set of high precision stages compatible with the existing planar solution or a low-cost in-house fabricated system to investigate the

concept. Given the nature of the system and the cost involved in the high precision stages it was decided initially to work with a prototype system.

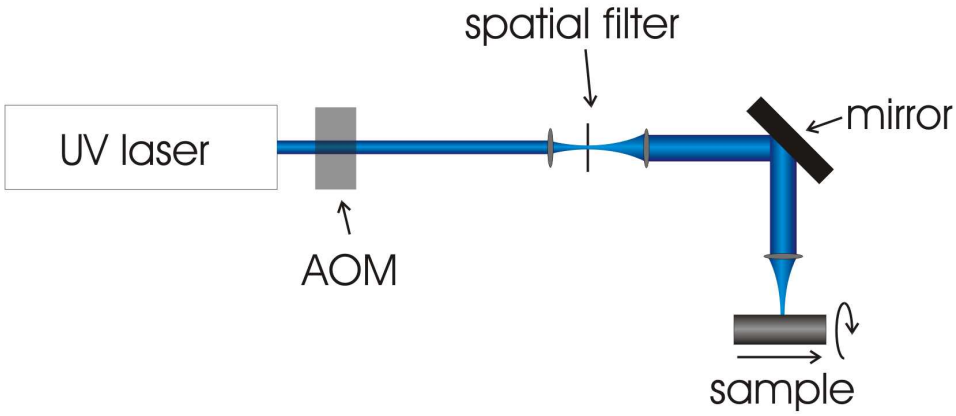

Figure 5.2: Schematic of the cylindrical Direct UV writing system

The cylindrical setup (figure 5.2) stages consisted of a linear translation stage upon which the rotational unit was mounted. Translation was powered by a stepper motor geared down with a ratio of 500:1 driving a belt fixed to the rotational unit. The belt was constantly tensioned using a sprung arm. The rotational unit consisted of a second stepper motor geared down to either 500:1 or 1000:1, coupled via a tensioned belt to the sample roller. The sample roller was a hardened steel bearing shaft, mounted on two roller bearings for support. It could be used as a drive roller of two sprung arms inside the cylinder for the large 40mm diameter samples or as a single spindle for the smaller diameter samples (figure 5.3). Surrounding the rollers, there was a Perspex enclosure with a narrow slot allowing access to the UV laser beam. The enclosure was purged with nitrogen passed through a copper coil in liquid nitrogen to cool the sample down to temperature less than -100°C preventing Deuterium out-diffusion during the writing process. The enclosure also limits the UV scatter from the sample.

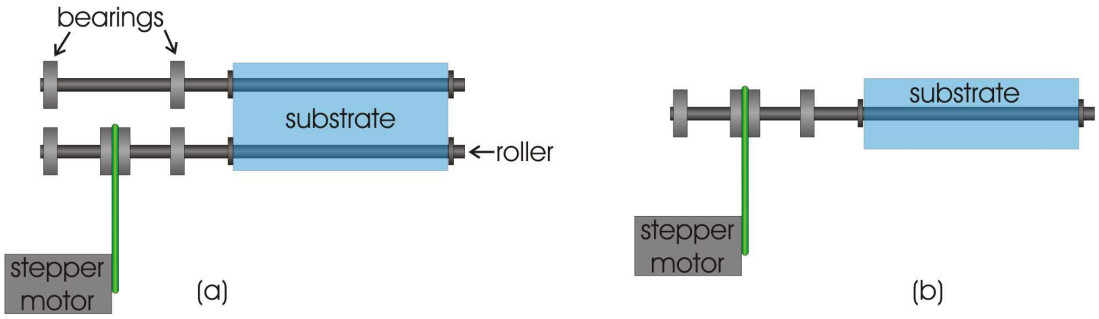

Figure 5.3: Configuration of the roller system for the cylindrical Direct UV writing system, (a) larger diameter cylinders with two rollers inside the tube supporting it, (b) smaller tubes, single roller acting as a spindle.

The translation stage system was fully computer controlled. A program was written to operate under MS-DOS to control the stepper motor boards via output pulses from the parallel port of the computer. A script array of linear and rotational steps was pre-calculated before the writing process. During the writing process the script was executed at a predetermined rate with minimum computing overhead. The triggering pulses from the parallel port drove the two independent stepper motor boards running in half step mode. The stepper motors were powered through ballast resistors to improve the stepping torque. The control software could also trigger the AOM to switch the power of the laser on/off as needed. An example of a summary report for the pre-calculation of the spiral waveguides is included in Appendix B

During operation, the rotational stage was only driven in one direction to avoid backlash effects, whilst the linear stage was run off the sample and reversed direction at the end of every translation of minimise the backlash. The laser was focused using a lens on a manual translation stage, with a resultant beam waist of 6μm. Alignment and focussing of the writing spot was aided through use of a video camera monitoring of the writing spot.

5.5 Cylindrical layer deposition

5.5.1 FHD based deposition

Initially, it was felt that a planar layer deposited on the outside of a cylinder would offer the best candidate for the waveguide geometry. To deposit such a layer it was decided to modify a flame hydrolysis system to operate in a manner between a FHD and OVD technique. The advantages of this process was that the layer deposition and composition should be very similar to planar FHD layers, relatively large 40mm diameter substrates can be used to minimise the bend loss and the layer on the exterior of the cylinder simplifies the channel deposition process.

The FHD system in this process is based upon a custom system designed and built within the ORC primarily by Dr Sam Watts and Dr Richard Williams. However, after the midpoint of construction the author was involved in the completion of the building of the system

providing prime experience for the subsequent modification to cylindrical geometries. Initially the whole planar FHD system will be described before concentrating on the modifications to deposit on cylinders. Most CVD based systems can be separated into two key components, the reagent delivery system and the deposition system. The reagent delivery system is described in some detail as the principle is relevant to all the deposition processes in this chapter.

5.5.1.1 Reagent delivery system

At the heart of the reagent delivery system there are four bubblers, containing the precursors $SiCl_4$, $POCl_3$, BBr_3 and $GeCl_4$ (figure 5.4). These components are in a liquid state at room temperature, but are delivered to the deposition system in the form of a vapour. A carrier gas (either dry oxygen or dry nitrogen) is bubbled through the liquid precursor forming a vapour rich supply gas, the density of the vapour dependent on the temperature of the precursor. Each bubbler is independently temperature controlled allowing the precursors to be maintained at a set bubbling temperature, while all four of the bubblers are set in a cooled silicone oil bath. Whilst somewhat inefficient, this configuration provides repeatable thermal response of each of the bubblers regardless of the environmental temperature. Each of the four bubblers have independent supply lines with the outputs mixing into a common feed, either to vent (during bubbler stabilisation) or to the burner (during deposition). The gas flow to each of the bubblers was determined via computer controlled mass flow controllers allowing the relative ratios of the dopants to be controlled throughout the deposition process.

The bubbler set was contained within a sealed glove box, maintained at a constant positive pressure of 5 mbar by a continual dry N_2 gas flow (~2 $lmin^{-1}$). The glove box was maintained at a positive pressure to ensure the atmosphere was dry and the temperature maintained at 40°C. The elevated temperature helps to prevent the reagents from condensing in the pipe-work within the glove box. It was critical to ensure that the pipe work was kept dry at all times, as the reagents transported throughout this system react with any water creating solid particles. If a reaction occurred within the transport system, it could result in a partial blockage of the pipes and thus the flow rates and relative dopant levels could be displaced.

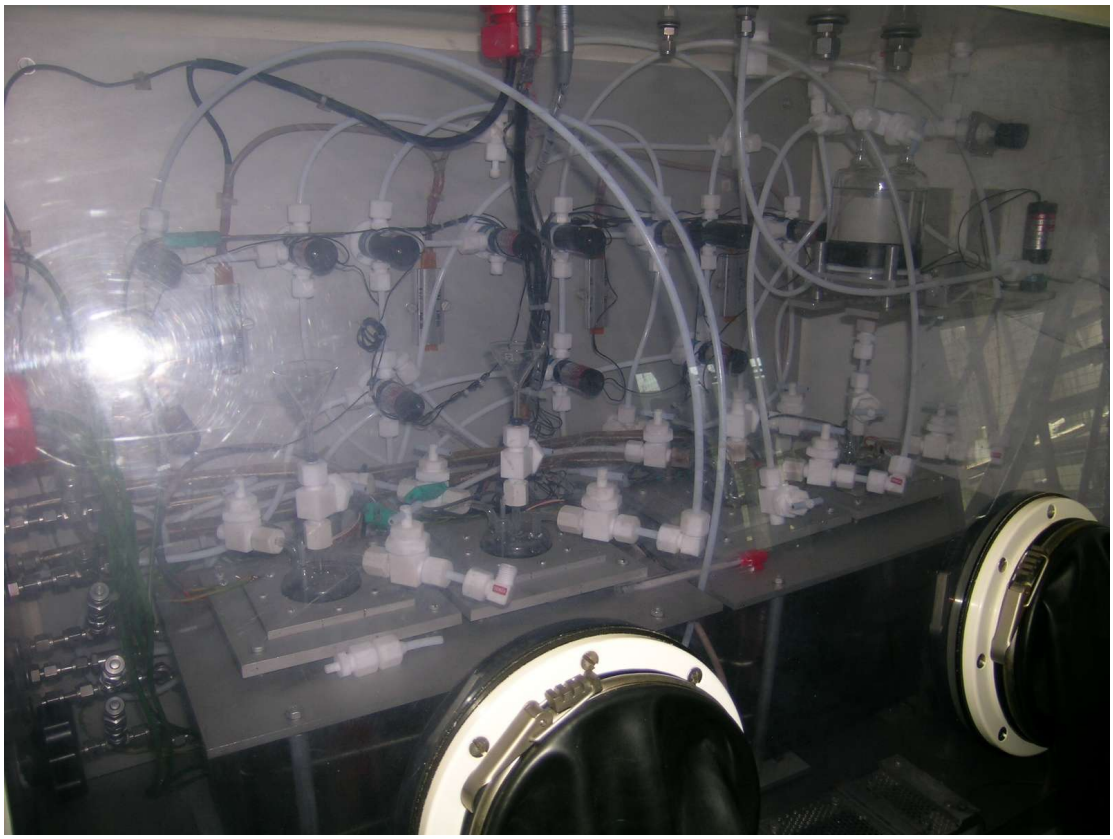

Figure 5.4: Picture of the reagent delivery system for the FHD system.

5.5.1.2 Deposition system

The deposition unit is where an oxy-hydrogen flame forms oxide particulates in the form of soot via hydrolysis (or oxidation – see section 4.2.5). The deposition chamber is split into two sections via a sliding seal, the top half is the reaction section while the bottom houses the pipe work and translation stages for the burner. This separation protects the mechanically sensitive components from the aggressive conditions within the deposition region. The burner assembly, in a variation from other FHD systems, is mounted vertically with the flame and soot deposition in the 'up' direction. The burner itself is mounted on a 2-dimensional translation system controlled via the same computer system as the bubbler unit.

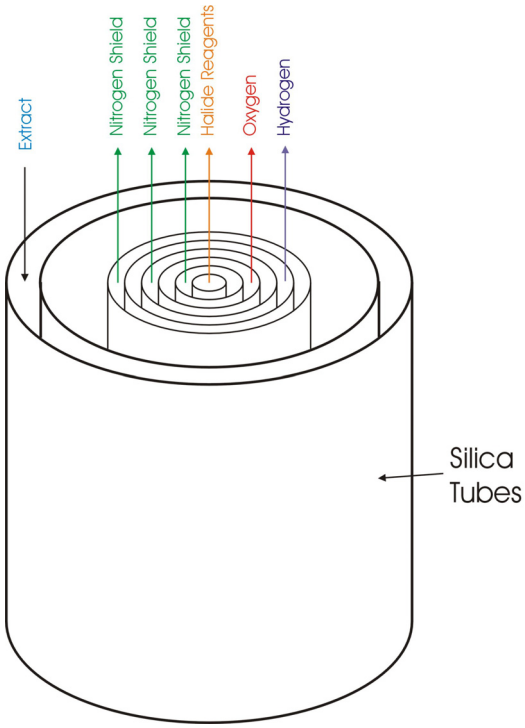

Figure 5.5: FHD burner configuration

The burner assembly has a six-ring burner in a concentric circle formation and two silica cylinders surrounding the burner (see figures 5.5 and 5.6). The silica tubes form a symmetrical extraction 'ring' around the burner. The extract removes the soot that does not bond to the substrate immediately after ejection from the burner, preventing it from producing larger soot particles that would interfere with the uniformity of the soot layer deposited. The nitrogen shields prevent any reaction at the head of the burner that could result in blocking of the rings and dilutes the flame as required.

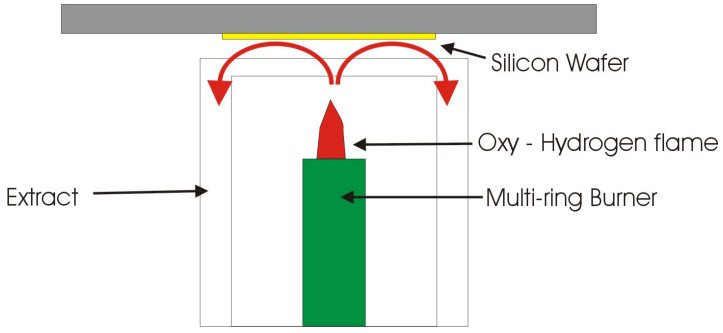

Figure 5.6: Burner configuration illustrating extract flow.

The wafer is mounted upside down over the burner, held in position via a vacuum system. The substrate is heated through a resistive element behind a large plate of silicon carbide,

conductively heating the sample. The high thermal conductivity and very large thermal mass of the silicon carbide plate reduced any variations of the substrate temperature. Heating of the substrate aided the deposition processes of soot bonding and prevented GeO_2 from depositing in a crystalline phase. It has been shown that the temperature of the substrate is critical in the phase of the Germanium oxide, below 400°C crystalline Germanium has been detected within the soot, above 500°C only amorphous Germanium was detected (Kawachi, Sudo et al. 1980).

5.5.2.3 Consolidation

The soot requires subsequent consolidation to form a glassy layer. Consolidation is the sintering of the discrete soot particles into a uniform glassy layer. It occurs at temperatures below the melting point of the material and is driven through a reduction of the free energy of the system. The process occurs when the soot particles are sufficiently softened by heating that the surface energy is sufficient to pull the particles together, reducing the extent of the air-silica interfaces and hence the free energy of the system as a whole.

The samples are consolidated in an Elite box furnace with a maximum temperature of 1550°C, although consolidation of silica-on-silicon samples is always carried out below 1400°C due to the melting point of silicon. The exact temperature of the consolidation process is a function of the composition of the soot, both the physical size and the molecular composition. Small particles coalesce in a shorter time (Rabinovich 1985) and the dopants GeO_2, P_2O_5 and B_2O_3 have lower melting points, thus reducing the consolidation temperature (Sakaguchi 1994).

5.5.2.4 Cylindrical modifications

For cylindrical deposition the only section of the system that needed to be changed is the structure for substrate mounting. In the planar FHD configuration the sample vacuum mount and heater all form part of the lid of the deposition chamber. The lid was designed to be removable allowing various alternative lids to be bolted onto the FHD system. This function allowed the construction of a lid specifically implemented for the deposition onto

40mm cylinders whilst maintaining virtually identical deposition conditions to the planar samples.

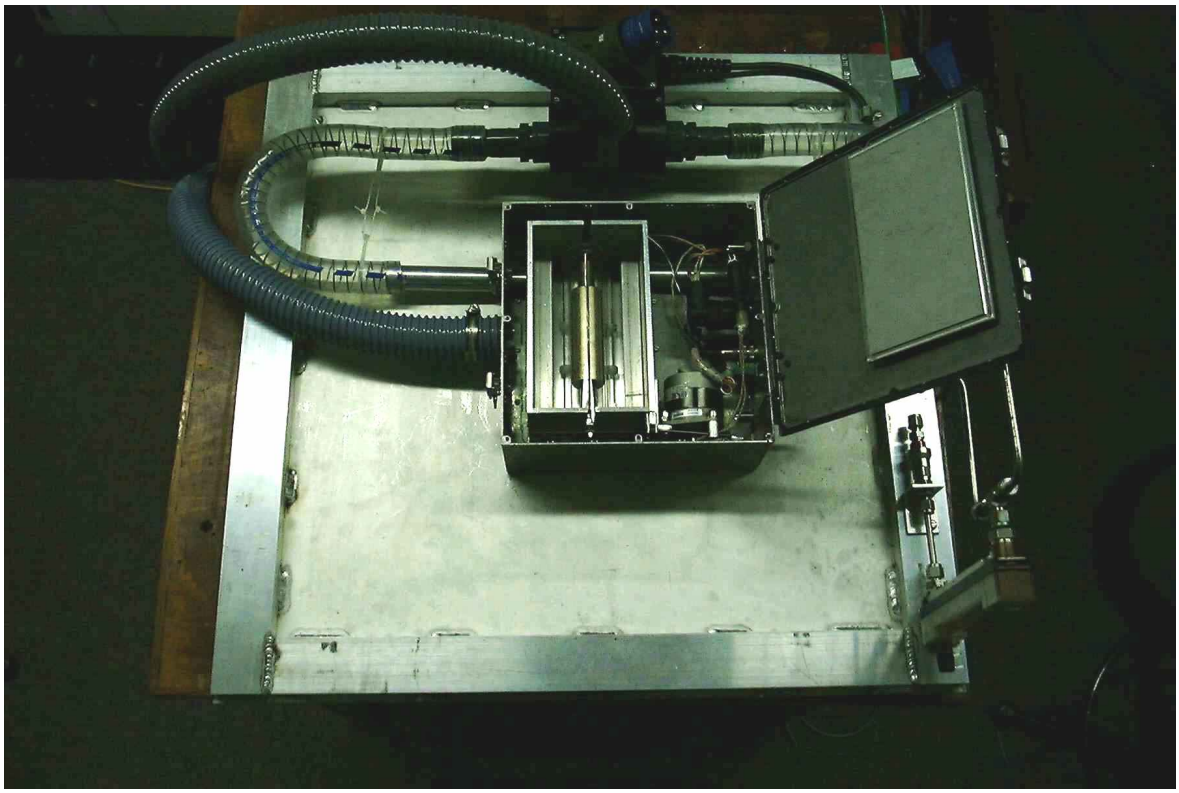

Figure 5.7: Overhead view of the cylindrical FHD system lid.

A picture of the lid is presented in figure 5.7. The system was designed to accept silica tubes with a diameter of 18mm to 80mm, although 40mm tubes were used throughout the experiment due to their availability as soot-tubes from the MCVD process. The set-up could accommodate samples up to 15cm long, although approximately 3cm of either end of the sample suffered from edge effects. Directly beneath the sample a rectangular slot was cut into the lid. The burner was linearly translated under the slot while the cylinder was rotated, depositing an even layer of soot over the perimeter of the tube. An extra extract was installed in addition to the circular extract of the burner, in the form of long parallel slots in the sides of the deposition slot (figure 5.8). The extra extract prevented un-deposited soot from by-passing the cylinder, clumping together and resettling back onto the substrate. The deposition box was positively pressurised to promote the general extracted air flow.

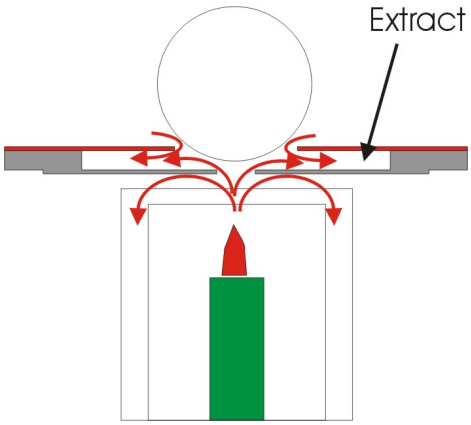

Figure 5.8: Schematic of the additional extract implemented in the cylindrical FHD lid.

The cylindrical substrate was heated through a conductive heater mounted through the axis of the tube. Rotation of the substrate was via four point contract rollers, two at each end of the tube outside of the deposition region. The rollers were driven from a single stepper motor linked to the main deposition control system. The deposition chamber was contained within a secondary box to aid the heating of the substrate and protect the operator of the system from any leakages from the deposition process.

The system differs only slightly from an OVD system, the main difference being in the deposition rate and burner function of the two systems. In general, the deposition rate from an OVD system is much greater, designed to produce thick glass layers that are subsequently drawn down to fibres. Thus, there is a significant difference in burner size and deposition flow rates when compared to the FHD based system which has to produce 5µm thick uniform layers. The second difference in an OVD system, the burner is also used to consolidate the soot. However in the cylindrical process that is not an option as the temperatures involved would melt the deposition equipment.

In order to allow the experimentation of the various processing parameters the cylinder substrates were pre-cut in to lengths of 30mm. The tubes were then cleaned in an ultrasonic bath in Acetone, IPA, Micro-clean and DI water before being ‘stuck’ together to form a single substrate 90mm long with Alumina cement. The adhesive withstood the deposition conditions but could easily be parted with the layers still in soot form to allow subsequent individual processing.

The samples were deposited in much the same process that planar silica-on-silicon structures were built up (Watts 2002). Each layer, the under-clad, core and over-clad were deposited individually and consolidated before the next layer was deposited. The consolidation parameters were translated directly from the planar work, thus the initial thermal cycle was 1400°C for 3hrs. Whilst these parameters resulted in a fully consolidated layer the silica tube started to crystallise (figure 5.9).

Figure 5.9: Cylindrical silica substrate crystallised after 1400°C consolidation process.

To reduce the crystallisation during the consolidation process the temperature was increased to the maximum that the furnace could control (1550°C) and the cooling rate enhanced through forced air convection. The samples were removed from the furnace at temperature, into ambient conditions and placed onto a fan box blowing air around and through the cylinder to aid the dissipation of thermal energy. With the increase in the consolidation temperature the duration of the consolidation process needed to be re-optimised. Thus, several samples were deposited at the same time using the above 'cut and shut' technique, but consolidated at 1550°C for different durations. The results are presented as a series of transmission images of the soot for the different processing times (figure 5.10).

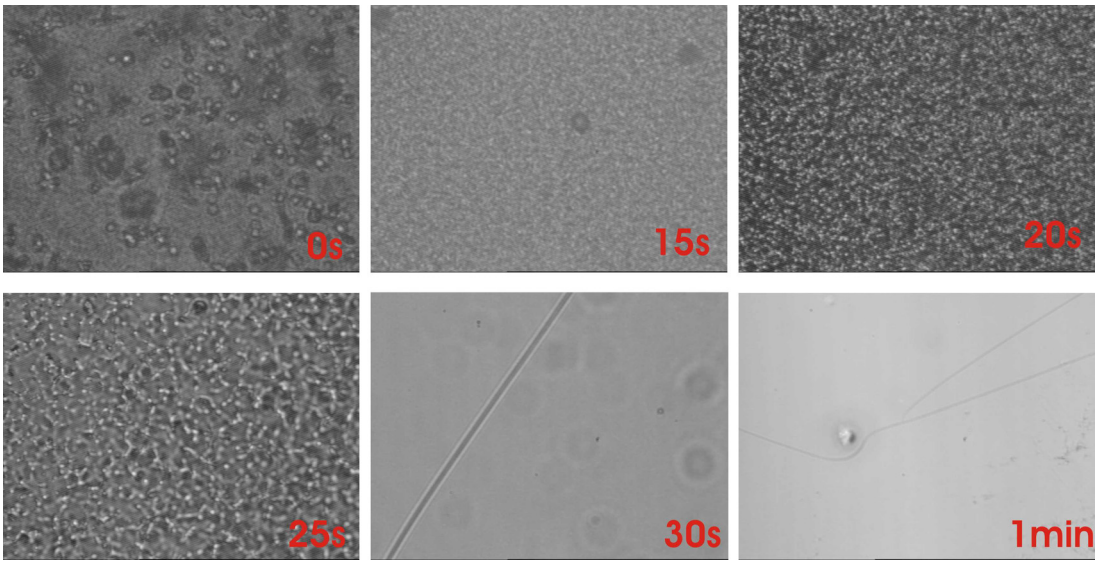

Figure 5.10: Effect of consolidation time at 1550C. Images at 50x magnification except for '1min' at 5x.

Consolidation of the samples for ~45s allows the full consolidation of the soot layer with minimal crystallization of the substrate (figure 5.11). Note however, that the glass layers in figure 5.10 have both cracked. The layers produced on the cylindrical substrates are susceptible to cracking. This is believed to be due to the larger thermal expansion coefficient of the doped layers (Miller and Chynoweth 1979) relative to the silica substrate. The relatively high levels of doping allow the consolidation of the soot into a glass at 'low temperatures' for silica, but ultimately result in a stressed glass layer. As the layers are on the outside of the silica substrate after consolidation they are under tensile stress. It is known that glasses under tensile stress are more susceptible to crack propagation and it is believed that this is the primary mechanism of the failure of the samples (Tomozawa 1996).

Figure 5.11: Fully consolidated planar layer on the outside of a cylindrical substrate deposited through the FHD process.

It is this cracking that appears to be the primary limiting factor for this technique of deposition. Samples can be produced without cracks, however after a couple of days cracks appear along the entire slab waveguide layer. It is believed that this is caused by moisture in the ambient environment promoting the formation of stress points, these subsequently form the initiator for crack propagation promoted through the tensile stress of the layer.

This cracking effect has prevented the fabrication of waveguide layers with a lifetime great enough for the definition of channel waveguides. Thus, alternative processes that allow the high temperature deposition and consolidation of the waveguide layers were investigated.

5.5.2 External MCVD

Given the limitations found using the FHD process and the current fabrication equipment an alternative fabrication process was undertaken using a MCVD fibre lathe but attempting to deposit material onto the outside of a cylinder. The MCVD process has several advantages over the OVD style technique; leading to it becoming a popular technique in fibre preform manufacture. The reaction occurs within the deposition tube, an environment that is sealed away from the burner. The burner plays against the exterior of the deposition tube, the heat diffuses through the glass to the inside of the tube providing the thermal energy required for the thermal oxidation of the reagents. As described in section 4.3.2.1 the temperature is enough to promote the generation of particulates in the form of soot, this soot travels ‘down stream’ of the burner before depositing onto the wall of the tube. As the torch traverses past the deposited soot it is consolidated into a glassy layer. Throughout this entire process the interior of the tube is exposed only to the reagent and the carrier gas, thus there is little contamination or water incorporation from the burner.

For the MCVD lathes the reagents are again supplied as a vapour in a carrier gas. The delivery system is essentially the same as that described in section 5.5.1.1. However the system is commercially built and as such is not quite so flexible in the various temperatures of the liquid precursors. The other difference is that the flow rates involved in the MCVD process are much greater than those of the FHD system.

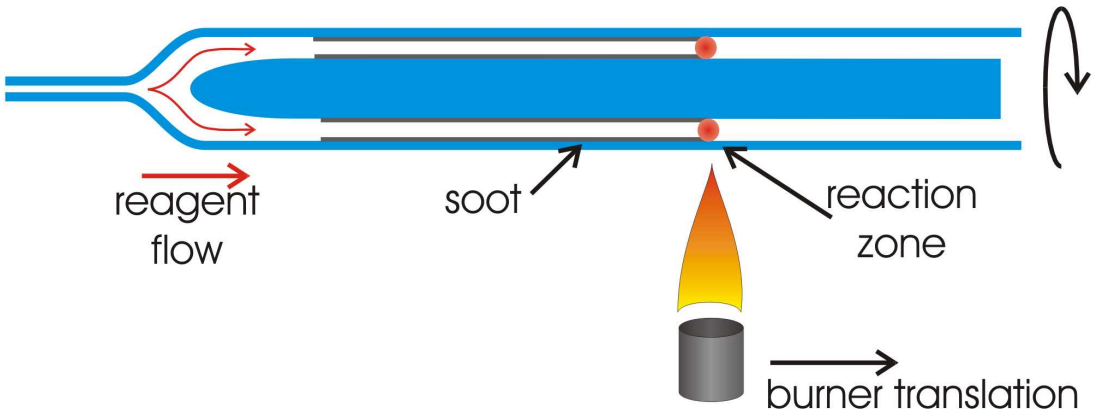

Figure 5.12: External MCVD process, a technique developed for the position of thin film silica layers on the outside of a cylinder based on the MCVD process

The MCVD technique deposits the glass layer on the inside of the tube. Ideally, the intention is to deposit the glass layer on the outside of the tube. One of the mechanisms in deposition processes, which includes the down stream deposition of the soot particles, can be attributed to thermophoresis, the force experienced by a particle in a temperature gradient in the direction of decreasing energy (Cho, Kim et al. 1998). By inserting a secondary tube within the deposition tube with the reagents flowing between the two structures, as the inner tube wall will be cooler than the outer tube in the reaction zone there will be a temperature gradient towards the inner tube, and hence deposition of soot (figure 5.12).

As the substrate tube is not directly heated at any point it is not possible to consolidate the soot into a glassy layer, but the temperature induced is enough to partially consolidate, producing a mechanically stable layer. The inner tube is then removed and consolidated directly by passing the burner over it, whilst this process induces water and burner contamination into the glass, it does result in the high temperatures required to consolidate un-doped silica. As the cladding layers can be produced using pure silica the expansion coefficient closely matches that of the tube substrate, and as such the cladding layer is not stressed. Since the cladding layer is not in tensile stress as in the cylindrical FHD samples, the outer cladding is much more resistant to the defect formation and crack propagation.

Several configurations of mounting the inner tube into the outer tube were applied as it was discovered that the process is very sensitive. Throughout the experiments the inner tube was sealed at the end facing the gas flow. This was to prevent the reagent from by-passing the reaction zone. The back end was always left open to prevent the tube exploding as it

was heated. The finalised configuration was constructed entirely from silica as this is one of the few materials that can resist the gases and temperature of the deposition process (and reduced contamination).

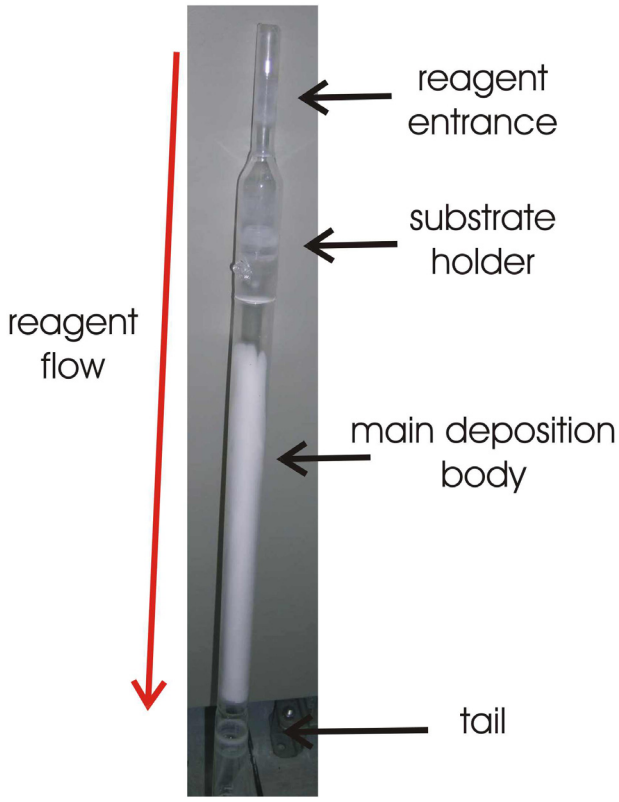

Figure 5.13: Out-side MCVD deposition tube (not the substrate tube). The three main sections are identified and the reagent flow. The main body contains a soot layer due to the incomplete nature of the consolidation process.

The outer tube consisted of 3 sections, the 'holder', the 'body' and the 'tail' (figure 5.13). The 'holder' is the section that holds the front end of the substrate tube whilst allowing the reagent to flow around the side of the substrate but within the outer tube (figure 5.14). The substrate was supported for the first 50mm in a friction fit sleeve, without the long support the softening of the tube during the deposition process causes it to droop. The main body is thick walled (5mm) 40mm diameter tube Although tube of this diameter is very hard to thermally control with the burners fitted to the fibre lathe, it has the strength to reach the deposition temperature and not collapse. The spacing between the two tubes is of the order 5mm, so any significant collapsing causes variations in the reaction temperature and can interfere with the soot flow. In the tail of the structure the substrate is attached to a soot tube that is a friction fit for the soot tube of the outer tube, vent holes in the substrate tube

allow gas flow through into the extract. For consolidation the substrate was slid out of the outer tube, mounted on the lathe and consolidated directly with the burner.

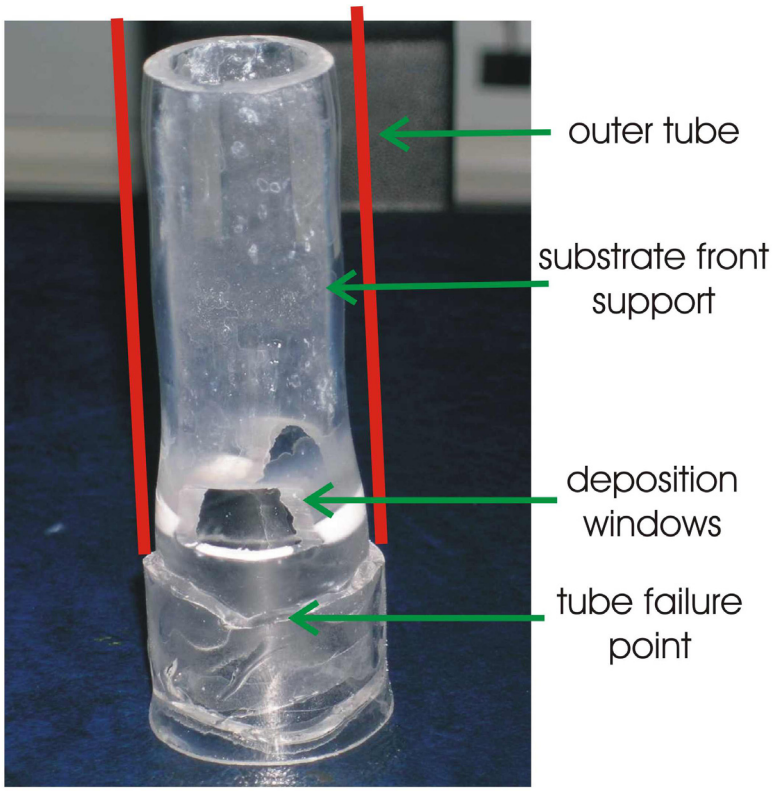

Figure 5.14: Holder assembly for the front of the substrate tube. In operation, the entire assembly is encased in an outer tube, fractured off as indicated in the picture allowing the interior sleeve to be visible.

Several deposition runs were performed using this process. As this was the first time the system had been implemented in this style it took several depositions to achieve a suitable layer. The deposition temperature was lower than standard ~1900°C to minimise the collapse of the outer tube (hence the soot build up in figure 5.13) with a thinner layer of soot deposited with each pass. However, this corresponds to the need to reduce the layer deposition rate as layer of the order millimetres are typically deposited in a fibre preform. The core layer was doped with a relatively low level of Germanium to minimise the thermal expansion issue as much as possible in these initial samples. Before removal from the deposition tube the soot was partially consolidated by translating a 2000°C burner slowly (10mm/min) over the length of the deposition region. This provided sufficient sintering such that the burner could be directly played over the deposited layers without blowing the soot off. An example of a cylindrical substrate produced in this manner is illustrated in figure 5.15 after being diced and polished.

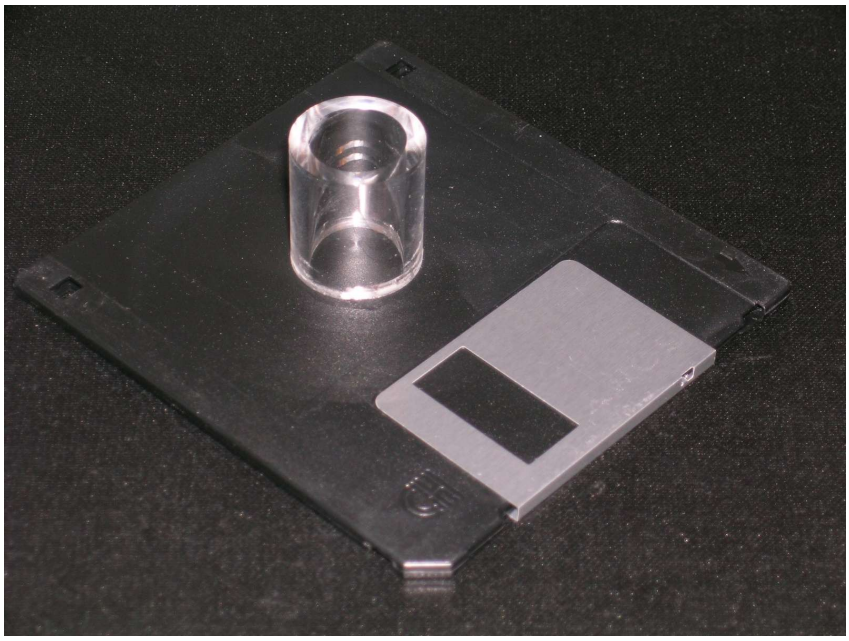

Figure 5.15: Section of substrate tube deposited via the external-MCVD process. A 1.44" floppy disc is included for scale.

The significant result with this fabrication technique is that the wave-guiding layers no longer cracked after a couple of days. There are two possible causes of the greater stability of the samples, the smaller size reduces the magnitude of the stress due to the thermal expansion and the deposition of the pure silica cladding. It is the authors' belief that the pure silica cladding layers play a significant roll in the strength of the waveguide. The composition of the cladding is very close to that of the silica substrate and as such will have a very similar thermal expansion. Thus there is little stress induced in the layer from the consolidation process, resulting in a significantly reduced chance of cracking.

For Direct UV writing the samples were Deuterium loaded in a pressure vessel for a week at 150Bar to ensure saturation of the glass before exposure. Several writing fluences were used during the writing process, with both straight channels defined along the axis of the cylinder and spiralled waveguides coiling two-thirds of the circumference of the cylinder. An end view of some of the induced channel structures, both straight and spiralled is provided in figure 5.16.

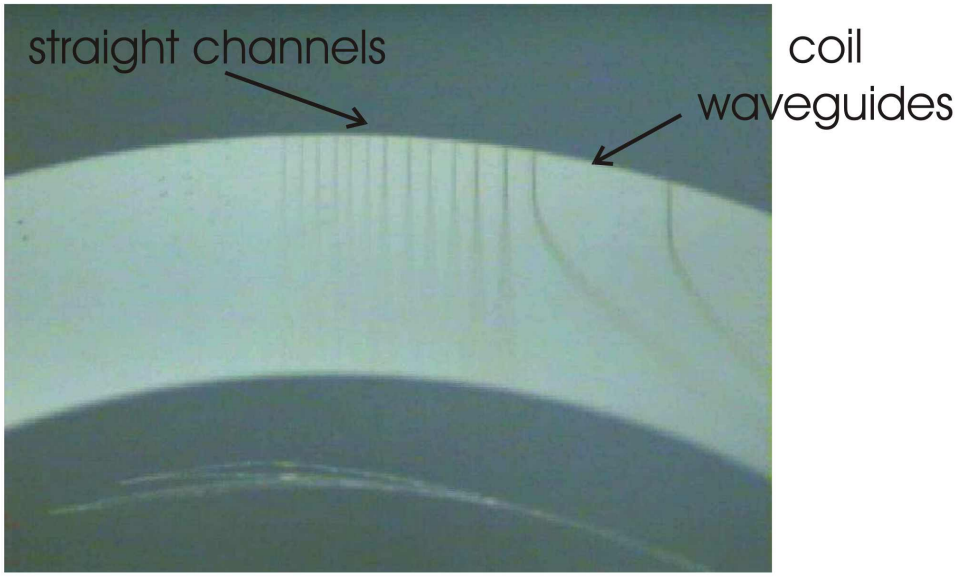

Figure 5.16: Off-axis view of Direct UV-written channel waveguides on the outside of a cylindrical substrate.

The NA of the waveguides was measured using the far-field mode size technique described in detail in section 8.1. The results for the horizontal NA is presented in figure 5.17, showing relatively low channel strength even for high fluences. A typical single mode 633nm profile is presented in figure 5.18. The cause attributed to this low index change is the relatively low doping levels of the slab core layer. Vertical NA's of the layers are measured between 0.03 to 0.05, still very weak wave-guiding structures, resultant from the low material refractive index. Due to the low levels of the doping the absorption levels of the glass are minimal preventing large index changes observed in the second half of this thesis (chapters 8 & 9). The very low index change results in very large bend losses in the coiled waveguide structures, thus the propagation properties of the structures were not able to be determined.

A second substrate was deposited using this technique with a greater concentration of Germanium in the core, however the deposition processing conditions were found to be radically different. It was later discovered that the external deposition tube had softened and deformed during the initial deposition processes. The subsequent change in spacing resulted in different temperatures involved in the reaction zone and hence different deposition rates. The deformation occurred as the external deposition tube was on the maximum size of what the burner could control, due to this the tube temperature was not fully controlled resulting

in the overheating and softening of the material. This concluded with the breaking of the deposition tube at the substrate 'holder' due to the stresses involved (figure 5.14).

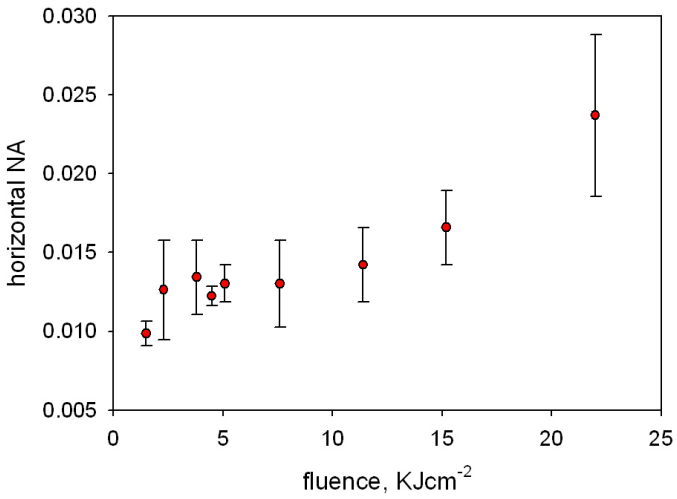

Figure 5.17: Horizontal (UV induced NA) of the straight channel waveguides written into the cylindrical substrates.

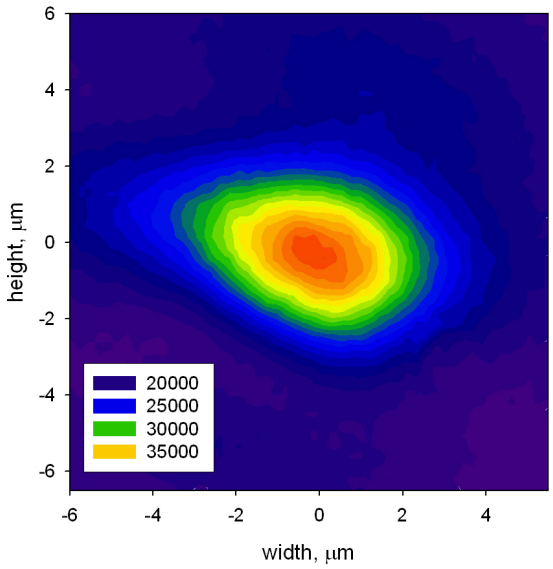

Figure 5.18: Typical mode profile at 633nm from a straight channel written on a cylindrical substrate deposited using the external-MCVD process

Thus, it was concluded that while the process was successful in the deposition of planar layers on the exterior of the cylinder, in this instance there was not sufficient control of the process. The indirect nature of the heating of the reaction zone coupled with the burner inability to control the heating of the cylinder made the process unstable. However there is

no obvious reason why the process could not be employed to deposit high quality planar layers through the use of a larger burner, better able to control the temperature of the reaction zone

5.5.3 MCVD

The alternative configuration, of depositing the layer onto the inside wall of the deposition tube was implemented through using the MCVD deposition technique. The deposition process was essentially the same as that described in section 4.3.2.1, however the precursor flow rates were significantly lower than in typical fibre fabrication processes.

Due to the size of the lathe and the burner configuration the maximum size tube that a controlled deposition process could be controlled had an internal diameter of 20mm and a wall thickness of 2.5mm. Unfortunately, this results in a high bend loss limiting the use of such fabricated structures. However, the tube size limitations arise only from the physical dimensions of the burner assembly, it is assumed that to realise such a structure that the use of a larger burner would be possible. The definition of channels on small diameter tubes allows the investigation of the Direct UV writing viability.

A typical deposition procedure for a creating a planar layer in the deposition tube is described by the following steps. Initially, the interior of the tube was prepared using a fluorine etch, and then subsequently flame polished. Then typically two under-clad layers were deposited of pure silica. The core layer was deposited onto the clad layer in a single pass comprising of Germanium doped silica (no other dopants), with a range of doping levels. The over-clad layers were again deposited as pure silica before a final polishing pass with the burner. This resulted in a fully consolidated layer within the tube.

5.5.3.2 Layer thickness

The MCVD deposition process is critically sensitive to the deposition conditions, both of the materials used and the particular machine. This has been experimentally encountered, in the production of the thin film layers. The size of fibre deposition tube used in the fibre fabrication process typically has an external diameter of 20mm. For the cylindrical

substrate purposes, the internal diameter before any substrate collapsing (~15mm) results in a very high bend loss (~50dBcm^{-1}), as such, these tube would make exceptionally poor curved waveguides.

To avoid the limitations of small curvature larger diameter tubes than normal were used in the fabrication process, however in changing the size and mass of the deposition tube the deposition rates for the layers were shifted from the prior calibrated rates. In order to investigate the deposition rates of the modified system samples were produced with a number of cores layers deposited concentrically with varying compositions (figure 5.19).

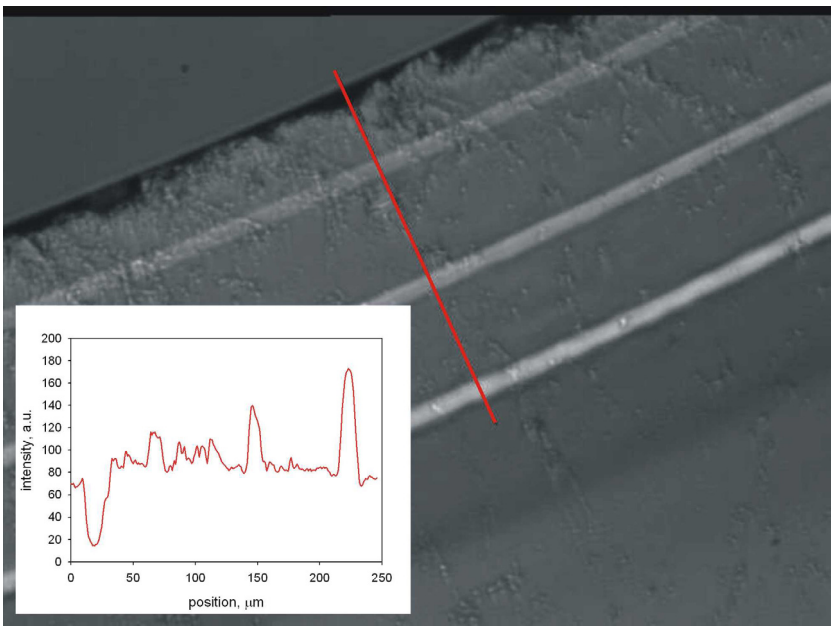

Figure 5.19: Three core layer sample calibrating the deposition rates for the different mass substrate tubes.

A method for measuring the thickness of the layer in the substrates is to collapse the cylinder into a solid rod, as in the fibre fabrication process. The collapsing is performed through multiple passes of the burner, heating the cylinder to the softening point of silica. Surface tension pulls the tube down with each pass, reducing the diameter of the cylinder until the air/silica interface in the cylinder is removed (figure 5.20). Through conservation of mass, as the diameter of each layer reduces the corresponding thickness increases.

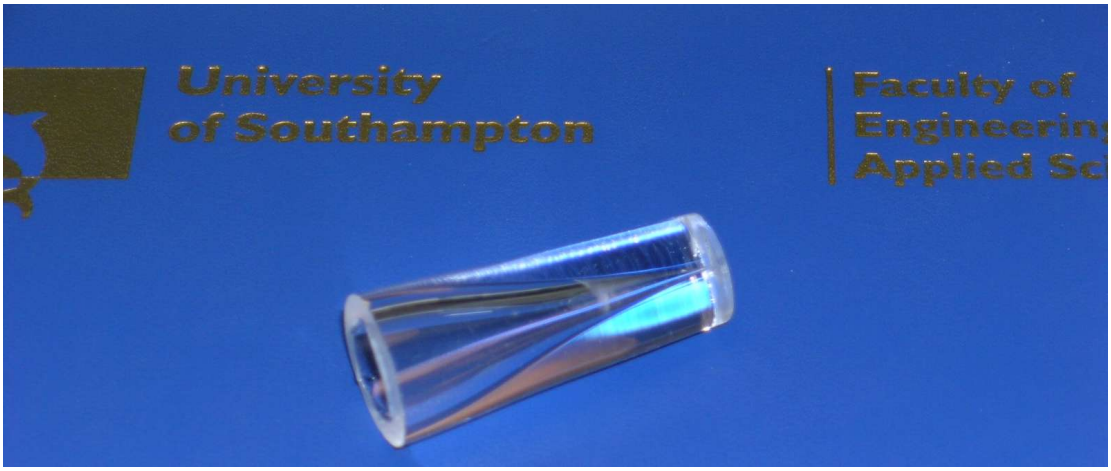

Figure 5.20: Tapered sample, scaling from the cylinder substrate to the collapsed core for refractive index profiling.

The typical thickness increase can result in a 5μm layer becoming a 120μm wide band of material, a structure subsequently profiled using a York Technology P104 laser profiler. The system scans a focused laser axially across a rod, measuring the refraction of the laser beam and associating it to a refractive index change (figure 5.21). This provides an alternative direct measurement of the refractive index profile rather than the measurement of guided white-light as in the transmission microscope images (figure 5.22).

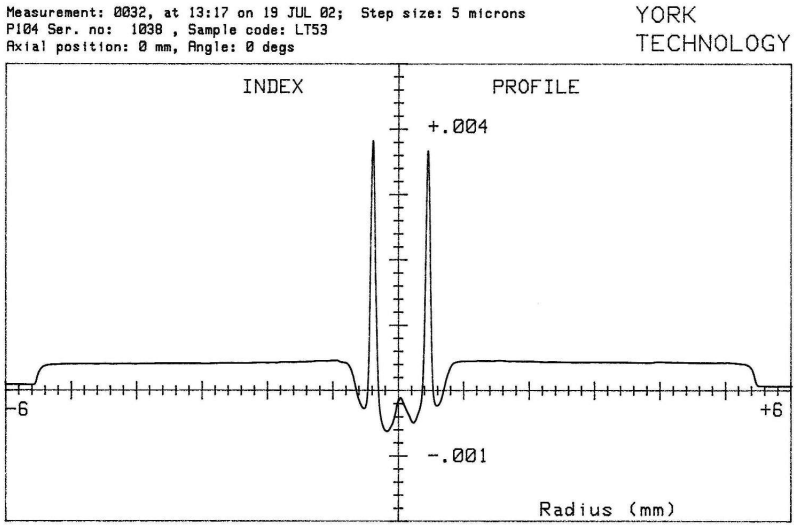

Figure 5.21: Refractive index profile of a collapsed substrate showing the 'core' layer surrounded by an under-clad and over-clad.

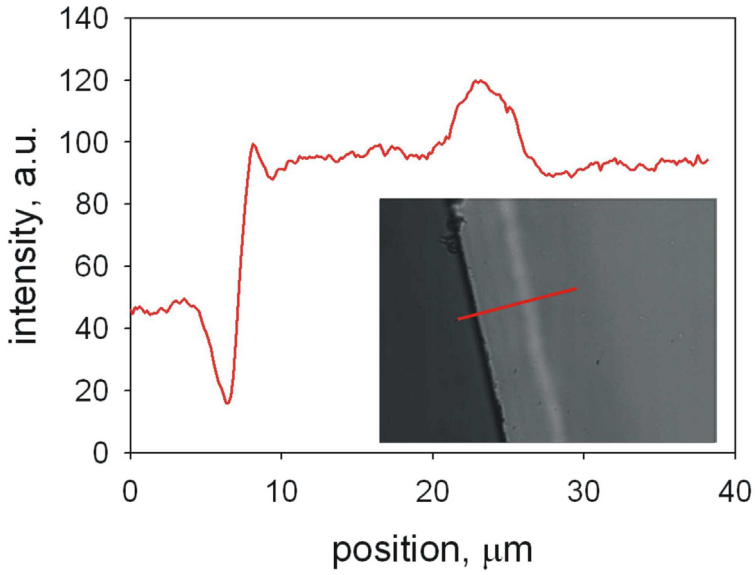

Figure 5.22: Line scan of the white-light transmission of the un-collapsed substrate profiled in figure 5.21.

In the attempt to define channel structures, due to the narrow nature of the cylinder the UV writing was performed from the outside surface focused through the bulk of the substrate into the core layer in the inside of the cylinder. This resulted in a relatively large beam diameter (>50μm radius) at the air/silica interface appearing to cause significant disruption to the writing spot. Thus, channels in these samples were not successfully defined. The limitation is not with the concept of fabrication, layers with a thickness of 5μm and a distinct boundary have been produced using this technique, rather the current mechanical limitations to the size of the tubes that can be deposited this way.

A possible solution was considered, after the thin-film layer is deposited the substrate is heated to temperatures required to collapse the tube, but the tube is pressurised causing it to expand. This would allow samples with a greater diameter to be produced in the lathe, whilst reducing the thickness of bulk glass that the UV writing beam is required to penetrate. Such a sample was produced by Andy Webb to test the concept, however it was discovered that control over the process was very limited and the variation in the tube diameter made it unsuitable for UV writing.

If larger tubes could be deposited then it would be conceivable to define the channel structures from inside the cylinder. Such an implementation would involve the writing

beam focused and reflected via a mirror on an arm on the inside of the tube. Whilst the channel structures could be defined in this manner the grating writing technique described in sections 7, 8 and 9 would be harder to implement in this geometry.

5.6 Summary

This chapter described the fabrication process used in the attempt in the fabrication of cylindrical waveguides. Descriptions of the equipment, process, characterisation techniques and results have been covered. The channel definition process used for these structures is the Direct UV-writing technique. To implement this, a set of prototype stages and control system were implemented to allow both linear and rotational channel definition.

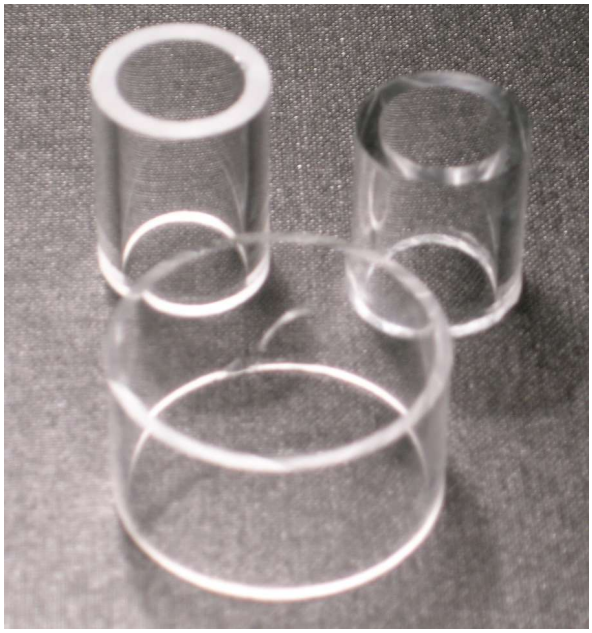

Figure 5.23: Range of cylindrical samples produced using FHD, exterior MCVD and MVD processes

A range of deposition techniques have been implemented to produce the thin film waveguide layers (figure 5.23). The techniques have resulted in layers being deposited on the outside of the cylinder (FHD and external-MCVD), although the FHD process was limited by material stress. Channels were defined in the external-MCVD process but the waveguides were relatively weak. Waveguide layers were deposited in the inside of a cylinder using the MCVD process to demonstrate that the process could be used as a

fabrication technique for ‘planar’ layers, although the tubes diameter was too small for practical waveguide definition.

Although there was no fully coiled waveguide defined in these samples, at no point was there a fundamental limitation to the process. While the doping levels in the FHD technique are prone to stress induced cracking it was shown that pure silica cladding does not suffer from such limitations. Thus, in the future by combining the advantageous steps of the deposition techniques presented (FHD deposition, pure silica cladding and high temperature consolidation) structures for cylindrical definition should be possible.

Chapter 6: Grating Structures

6.1 Abstract

Fundamental aspects of Bragg grating are introduced in this chapter, with a description of the structure and the wavelength response. Coupled mode theory is introduced to provide a model for the structures wavelength and group delay response, with the well known weak-grating equations presented. Common variations on the uniform Bragg grating structure are presented with a description of the resultant spectral responses. The chapter concludes with a description of some of the applications that Bragg gratings have been applied to illustrating the range of functions possible.

6.2 Introduction

The advent of the fibre Bragg grating has opened up a vast field of applications that were previously either cumbersome or impossible to implement(Othonos and Kalli 1999). Bragg gratings are devices with a periodic variation in the effective refractive index of a guided mode allowing coupling between specific and separate guided modes. The cross-coupling of power between modes results in a discrete wavelength dependent spectral response of the device.

The two key types of grating structures commonly encountered in wave-guiding components are distinguished by the magnitude of the grating period and the resultant modes coupled by those structures. Although both structures function through the same principle, the implementation and operation of these devices are classified as coupling into counter-propagating modes (Bragg gratings) and co-propagating modes (Transmission gratings).

6.2.1 Bragg Gratings

Bragg gratings or 'short period' grating structures couple power between two counter propagating modes within the refractive index perturbation. That is, when a guided wave incident to the index perturbation satisfies the *Bragg condition,* the power is coupled into a counter propagating mode with the opposite wavevector (i.e. reflected) (figure 6.1). The Bragg condition arises from the laws of conservation of energy and momentum; conservation of energy demands that the energy of the incident and reflected photons are the same. while conservation of momentum requires that the wavevector of the incident wave (k_i) coupled with the wavevector of the grating section (K) must equal the wavevector of the co-propagating wave (k_r). This is expressed in relation (6.1):

$$k_i + \mathrm{K} = k_r \qquad [6.1]$$

The magnitude of the grating wavevector is $\frac{2\pi}{\Lambda}$, where Λ is the period of the refractive index perturbation. In the case of waveguides where the power is coupled into a counter propagating mode the wavevectors are of equal magnitude but opposite sign $(k_i = -k_r)$. Hence the conservation of momentum condition is expressed as:

$$2\left(\frac{2\pi n_{eff}}{\lambda_B}\right) = \frac{2\pi}{\Lambda} \qquad [6.2]$$

where n_{eff} is the effective index of the guided mode and λ_B is the *Bragg wavelength,* the free-space wavelength of the light reflected by the grating structure. Equation (6.2) reduces down to the well known Bragg condition:

$$\lambda_B = 2n_{eff}\Lambda \qquad [6.3]$$

Thus the Bragg condition can be expressed as a simple relation between the effective index of a guided mode and the resultant peak spectral response for a given uniform index perturbation. However, it is also worth noting that Bragg gratings can also couple into counter propagating cladding modes where the wavelength response is defined by:

$$\lambda_{counter-clad} = \left[n_{eff,co} + n_{eff,cl}\right]\Lambda \qquad [6.4]$$

Where $\lambda_{counter-clad}$ is the peak response wavelength for the coupling between the core and clad modes. This coupling into the cladding modes is usually undesirable, as the

transmission profile will include additional dips at wavelengths shorter the main grating response.

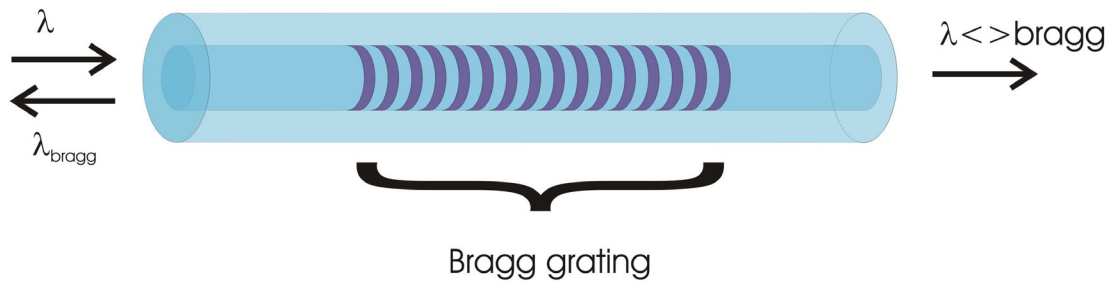

Figure 6.1: Schematic of a Bragg grating in a fibre geometry coupling power into a counter propagating mode.

6.2.2 Transmission Gratings

The second class of grating structure is the *transmission* grating or *long-period grating* (Erdogan 1997; Rastogi and Chiang 2002). A transmission grating couples power from the incident wave into a different wavevector propagating in the same direction (co-propagating) (figure 6.2). These structures are again a periodic refractive index perturbation, but as the name implies with periods much greater than in the counter propagation case due to the very small difference between the two modes. Typically the power is coupled into higher order or cladding modes (guided modes supported within the cladding layer) within the guiding structure. In an analogous manner to the Bragg grating, the phase matching condition for transmission gratings can be expressed as:

$$\lambda_{trans} = \left(n_{eff,core} - n_{eff,clad}\right)\Lambda \qquad [6.5]$$

where $n_{eff,clad}$ is the effective index of the cladding mode. As modes propagating in the cladding of a structure are generally higher loss, transmission gratings are often used as wavelength dependent attenuators(Othonos and Kalli 1999).

The work in this thesis is based on the short period Bragg grating structures although awareness of the long period structures demonstrates that in future work these structures can be incorporated into the existing geometry.

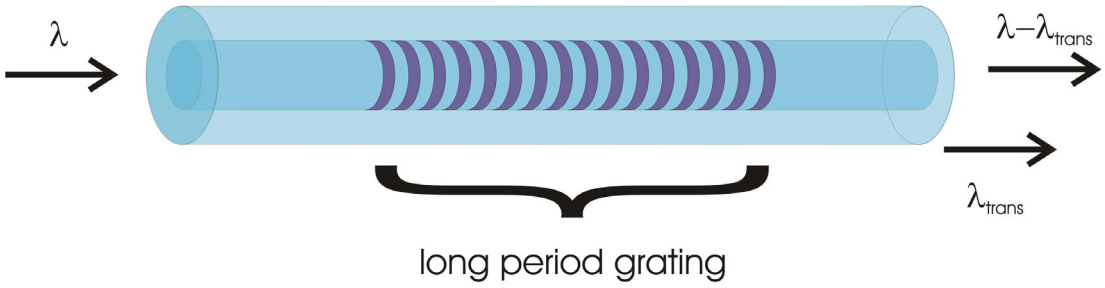

Figure 6.2: Schematic of a fibre based long-period grating demonstrating coupling power into a co-propagating cladding mode

6.3 Bragg grating response

The theoretical prediction of the spectral response arising from Bragg grating structures is an extensive topic with many numerical and analytical techniques targeted at a wide range of situations. Many of these techniques are well covered in literature and are beyond the scope of the material described in this thesis. However, an understanding of the wavelength response of the structures is provided through simple coupled mode theory. A summary of the coupled mode analysis of these structures is provided below, but for a more detailed description readers are directed towards (Yariv 1973)and (Ghatak and Thyagarajan 1998).

A simple structure that coupled mode theory can be applied to is a 'weak' Bragg grating of uniform structure (constant period and amplitude). By 'weak', it is assumed that the index perturbation is small compared to the strength of the waveguide and the incident wave penetrates to the end of the grating length. The refractive index profile of such a structure can be expressed as:

$$n(z) = n_0 + \Delta n \cos\left(\frac{2\pi z}{\Lambda}\right) \qquad [6.6]$$

where n_0 is the average refractive index, Δn is refractive index contrast, and z is the distance along the grating axis. One of the most common techniques used to describe such a structure is referred to as the *coupled mode* technique due to its simplicity and accuracy at the weak grating limit.

6.3.1 Coupled Mode Theory

Bragg grating structures couple power from an incident mode to a second reflected mode within the structure. Therefore coupled mode theory is often used to describe the power transfer between the two counter-propagating modes over the length of a uniform index modulation structure. The derivation of coupled mode theory will not be provided here as it is well covered in many publications [(Kogelnik and Shank 1972),(Yariv 1973)] with the description in this section closely following the work of [(Erdogan 1997) and (Othonos and Kalli 1999)].

In the case of Bragg gratings where the coupling is between two modes counter-propagating relative to each other the coupling equations describing the evolution of power along the *z* direction can be expressed as;

$$\frac{dA}{dz} = i\delta_d A(z) + i\kappa B(z) \qquad [6.7]$$

$$\frac{dB}{dz} = -i\delta_d B(z) - i\kappa^* A(z) \qquad [6.8]$$

$$A(z) = A(0)\exp\left(i\delta_d z - \frac{\varphi}{2}\right) \qquad [6.9]$$

$$B(z) = B(0)\exp\left(i\delta_d z - \frac{\varphi}{2}\right) \qquad [6.10]$$

where *A(z)* is the amplitude of the incident mode, *B(z)* is the amplitude of the co-propagating mode and φ is the phase of the grating. The detuning coefficient δ_d, refers to the difference between the incident wavelength and the peak Bragg response λ_b of the periodic perturbations and is given by:

$$\delta_d = 2\pi n_{eff}\left(\frac{1}{\lambda} - \frac{1}{\lambda_{bragg}}\right) \qquad [6.11]$$

It is assumed in this case that the refractive index perturbations are very small $(\delta n_{eff} \to 0)$, producing a weak grating with the assumption of no power loss within the structure. The coupling coefficient κ is given by:

$$\kappa = \kappa^* = \frac{\pi}{\lambda}\Delta n_{eff} \qquad [6.12]$$

The structure described in equation (6.6) is a uniform grating in both contrast and period therefore $\overline{\delta n_{eff}}$, $\frac{d\varphi}{dz} = 0$, and κ are all constant. In this simple case, equations (6.7) and (6.8) then become coupled first order differential equations, a closed form solution of which can be achieved by applying boundary conditions at the at the start and end of the grating structure (i.e. the backward propagating wave does not exist at the end of the grating). The amplitude reflection coefficient of the grating ρ, and the power reflection coefficient $R = |\rho|^2$ can then be shown to follow:

$$\rho = \frac{B(0)}{A(0)} = \frac{-\kappa \sinh(\gamma l)}{\delta_d \sinh(\gamma l) + i\gamma \cosh(\gamma l)} \qquad [6.13]$$

$$R = \frac{\sinh^2(\gamma l)}{\cosh^2(\gamma l) - \frac{\delta_d}{\kappa^2}} \qquad [6.14]$$

$$\gamma = \sqrt{\kappa^2 - \delta_d{}^2} \qquad [6.15]$$

Where l is the length of the grating structure. The reflection from a Bragg grating is plotted in figure 6.3 demonstrating the dependence of the magnitude and bandwidth of the spectral response with respect to the magnitude of the index perturbation in a cross coupling structure.

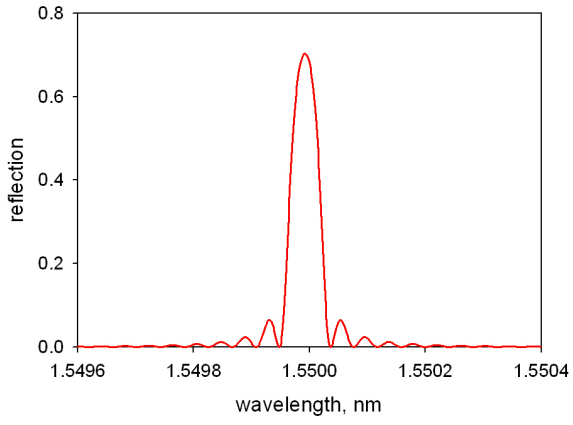

Figure 6.3: Theoretical spectral response of a Bragg grating structure 20mm long, with a core index of 1.45 and an index perturbation of 3×10^{-5}.

The peak reflectivity of this structure is by definition at the Bragg wavelength $(\delta = 0)$, and therefore equation (6.14) reduces to:

$$R_{\max} = \tanh^2(\kappa l) \qquad [6.16]$$

A bandwidth of the uniform grating can be defined as the spacing between the first minimum either side of the central, peak response, and is usually described as:

$$\frac{\Delta\lambda}{\lambda} = \frac{\Delta n_{eff}}{n_{eff}} \sqrt{1 + \left(\frac{\lambda_{bragg}}{\Delta n_{eff} l} \right)^2} \qquad [6.17]$$

It is worth noting that in the weak grating case, with very small index perturbations where $\left(\Delta n_{eff} << \frac{\lambda_{bragg}}{L} \right)$ then (6.17) reduces to:

$$\frac{\Delta\lambda}{\lambda} \rightarrow \frac{\lambda_{bragg}}{n_{eff} L} = \frac{2}{N} \qquad [6.18]$$

where N is the number of grating periods $\left(N = \frac{L}{\Lambda} \right)$. Thus, in the weak case the bandwidth is directly related to the grating length. In the strong grating limit the bandwidth reduces to:

$$\frac{\Delta\lambda}{\lambda} \rightarrow \frac{\Delta n_{eff}}{n_{eff}} \qquad [6.19]$$

Where the bandwidth is no longer dependent on the total length of the grating, as arises from the case of the guided mode not penetrating the full length of the grating structure.

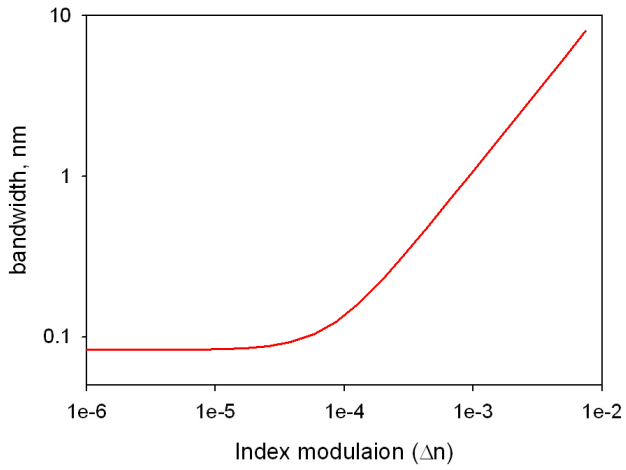

Figure 6.4: Bandwidth of a grating vs. the index modulation contrast for a fixed 20mm long Bragg grating. In the weak case the bandwidth is a function of grating length, in the strong case it is a function of index modulation contrast.

Thus for strong grating structures the bandwidth is proportional to the contrast of the index modulation. The effect of the weak and strong grating responses is illustrated in figure 6.4 with the difference in the bandwidth evident were the entire length of the grating structure is 'sampled' or where all the power is coupled before the end of the grating structure.

Bragg grating structures have dispersive properties above that of the native waveguide structure, an effect which can be either beneficial or detrimental depending on the application. The group delay is often used to describe the dispersive qualities of a Bragg grating structure and can be obtained from the derivative of phase (ψ) of the complex amplitude reflection coefficient (ρ) from equation (6.13) with respect to frequency. Therefore the group delay (τ) of a uniform Bragg grating structure can be expressed as:

$$\tau = \frac{d\psi}{d\omega} = \left(-\frac{\lambda^2}{2\pi c}\right)\left(\frac{d\psi}{d\lambda}\right) \qquad [6.20]$$

The theoretical profile of which is shown in figure 6.5 along with the simulated reflection profile of a strong uniform Bragg grating structure. The use of equation (6.20) allows us to imfer the group delay of the structure, even though for such strong gratings the coupled mode theory becomes unreliable.

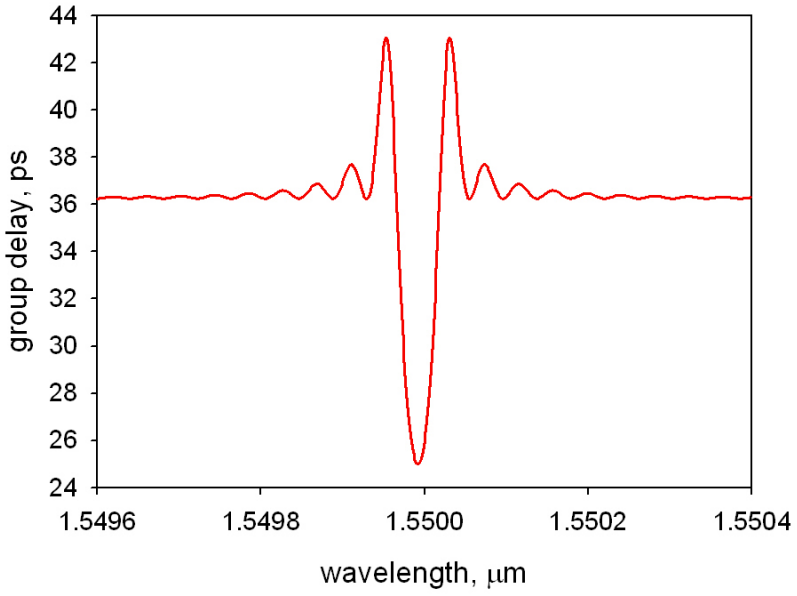

Figure 6.5: Theoretical group delay from coupled mode theory for the grating in figure 6.3.

The theoretical group delay of a uniform grating is demonstrated in figure 6.5. As can be seen at wavelengths from within the band gap (main reflection) of the grating structures the

light is predominantly reflected effectively from the front of the grating structure, with the peaks at the edges of the grating structure corresponding to vanishinlyg small reflections and the light effectively being 'trapped' in the grating structure.

Although the coupled mode theory has been covered in some detail above it is only valid for the simplest of grating structures. Bragg gratings comprising of more sophisticated position dependent profiles require more complicated analysis. Whilst most complicated structures are simulated using commercial software often the techniques employed are based on the fundamental approach described above.

6.3.2 Transfer Matrix Approach

The transfer matrix approach is mentioned as it is essentially a sophisticated form of the coupled mode equations commonly used to solve more complicated structures. The transfer matrix approach, or piecewise-uniform approach, is based upon identifying uniform sections for an overall non-uniform grating structure (Yamada and Sakuda 1987). These uniform sections are then combined to describe the entire grating structure. Each section of the grating is identified as a 2 by 2 matrix and by multiplying each unit in a cascade fashion, it is possible to subsequently describe the response of the entire grating structure.

As for the uniform grating case in the following analysis there are two modes, with the field amplitudes A_k and B_k representing the field strengths after propagating grating section *k*. Applying the boundary condition at the start of the grating $A_0 = 1$ and describing the propagation through each grating section using a matrix $\mathbf{T_k}$ it can be shown that (Othonos and Kalli 1999):

$$\begin{bmatrix} A_k \\ B_k \end{bmatrix} = \mathrm{T_k} \begin{bmatrix} A_{k-1} \\ B_{k-1} \end{bmatrix} \qquad [6.21]$$

where:

$$T_k = \begin{bmatrix} \cosh(\gamma dz) - i\frac{\delta_d}{\gamma}\sinh(\gamma dz) & -i\frac{\kappa}{\gamma}\sinh(\gamma dz) \\ i\frac{\kappa}{\gamma}\sinh(\gamma dz) & \cosh(\gamma dz) + i\frac{\delta_d}{\gamma}\sinh(\gamma dz) \end{bmatrix} \qquad [6.22]$$

The coupling components refer to the individual section from which the matrix is describing, with the definitions as above. However it is worth noting in this technique that the number of transverse matrices cannot be made arbitrarily large as the coupled mode theory only holds true for $dz >> \Lambda$.

6.4 Types of Bragg grating structure

Within the families of structures defined as Bragg gratings there are several 'classes' dependent on the spatial profile of the refractive index perturbations. Unlike the grating structure described in (6.6), the amplitude, period and phase of the grating can be dependent on position, thus giving a wide range of spectral responses. The more commonly encountered structures can be classed as uniform, apodised, chirped, phase-shifted and superstructure gratings. Each structure has specific spectral response characteristics, and therefore function. In this thesis the emphasis of the work is based on the definition of uniform Bragg gratings, however the other classes of structures are described due to their necessity in current devices and direct applicability to our fabrication technique.

6.4.1 Uniform Bragg Gratings

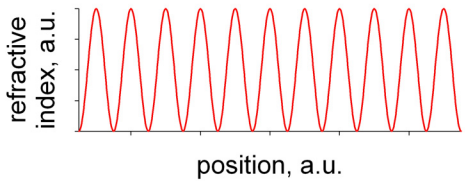

Figure 6.6: Schematic of the refractive index profile of a uniform Bragg grating

For the uniform Bragg grating (or Common Bragg Reflector) defined in equation (6.6), the period and contrast of the index modulation remain constant throughout the device length (figure 6.6), the spectral response of which is described in detail in the previous section. Uniform grating structures are often used as filters with the design directed towards a single wavelength response corresponding to the Bragg wavelength. Depending on the grating parameters such gratings can function as a narrowband transmission or reflection filter or a wide band filter (figure 6.7). Filter applications can include the reflection of a specific wavelength out of a WDM system, or the removal/reflection of a designated wavelength from a continuum of wavelengths.

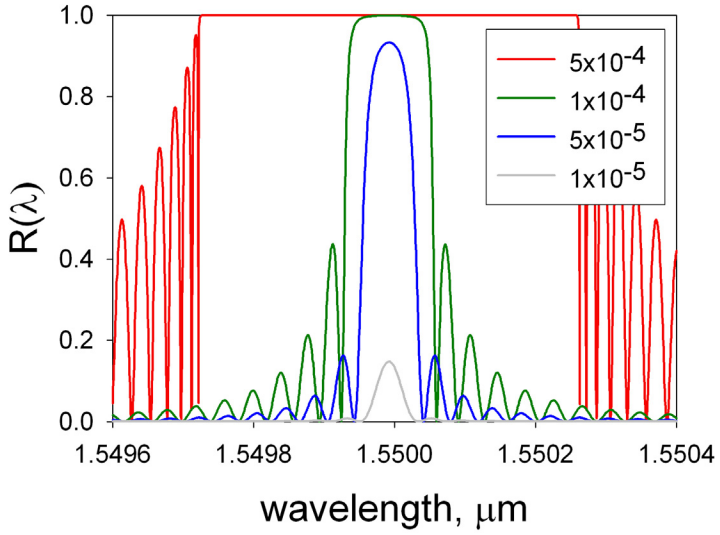

Figure 6.7: Range of spectral responses from an uniform Bragg grating demonstrating narrow bandwidth reflection of broad-band filtering and the associated side-lobes. Each plot represents a grating index perturbation strength for gratings of the same length.

Although a simple Bragg grating is efficient for wavelength selection, it also has significant side-bands, or secondary peaks either side of primary spectral response. These side-bands have well defined magnitudes and spacing, with the intensity decreasing as wavelength becomes more removed from the Bragg wavelength, an effect arising from the finite nature of the grating structure.

6.4.2 Apodised grating structures

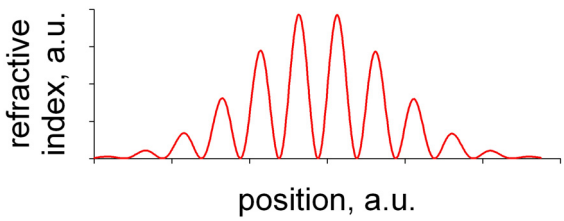

Figure 6.8: Schematic of refractive index profile for an apodised grating structure.

One of the significant drawbacks to the uniform Bragg grating structures is the side lobe structure arising at wavelengths away from the Bragg wavelength. In current WDM (and specifically DWDM) telecom systems crosstalk between adjacent channels can be a significant limiting factor in the overall performance. The tolerance of the filtering of adjacent channels for WDM systems is at least 30dB and preferably >40dB. The existence

of significant side lobes in the spectral response of the uniform Bragg grating result in a very wide spectral spacing of the channels, resulting in inefficient use of the available spectral window. Reduction of the side lobes allows denser channel spacing, therefore increasing the channel density for a given window.

Apodisation is a variation of the magnitude of the index perturbation along the grating length such that at the limits of the grating the contrast is reduced. The effect of apodisation is to 'smooth' out the discrete edges of the grating profile resulting in the suppression of the side lobs theoretically up to 60dB (Othonos and Kalli 1999), although in practice the suppression is often less and dependent on the apodisation profile applied. Suppression of the side-lobes comes with an associated reduction of the strength and bandwidth of the grating and significantly alters the group delay of the grating structure.

There are many profiles that are used for apodisation, from the Gaussian (commonly resulting from to the Gaussian structure of UV beam used to define the grating), the 'raised sine' and the Blackman profile as expressed in (6.23), (6.24) and (6.25) respectively (Ennser, Zervas et al. 1998) with the envelope functions of these profiles plotted in figure 6.9, although it is worth noting that a Gaussian with a wider FWHM but truncated at the edges is often used. The raised sine profile is an apodisation profile with zero dc index change, i.e. the average index of the structure is the same over the length of the grating keeping uniform waveguide strength.

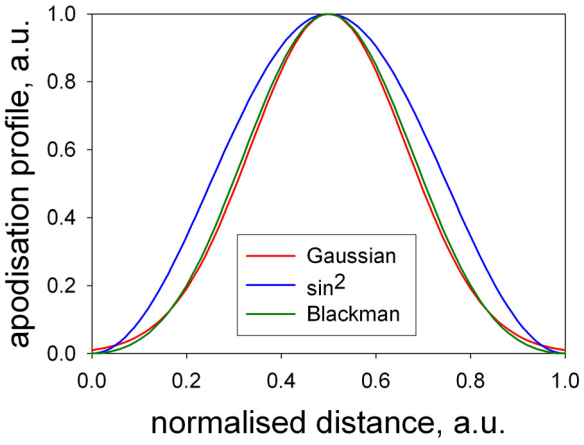

Figure 6.9: Refractive index contrast of common apodisation profiles

$$\Delta n = \Delta n_{\max} \exp\left(-\frac{1}{2}\left(\frac{z-a_0}{a_1}\right)^2\right) \quad [6.23]$$

$$\Delta n = \frac{\Delta n_{\max}}{2}\left(\sin^2\left(\frac{\pi z}{L}\right)\right) \quad [6.24]$$

$$\Delta n = \frac{\Delta n_{\max}}{2.38}\left(1+1.19\cos(x)+0.19\cos(2x)\right) \qquad x = \frac{\pi(2z-L:)}{L} \quad [6.25]$$

6.4.3 Chirped Fibre Bragg Gratings

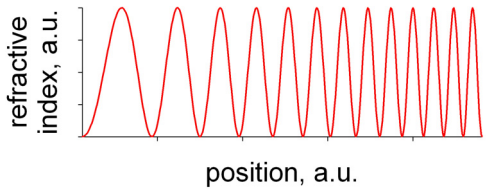

Figure 6.10: Schematic of the refractive index profile for a chirped Bragg grating structure

Uniform and the apodised gratings offer essentially the same functionality in the reflection or attenuation of specific wavelength signals in reflection or transmission modes respectively. By introducing a spatially varying period into the grating structure (figure 6.10), both the spectral and group delay response can be controlled allowing structures to be defined with a very specific response.

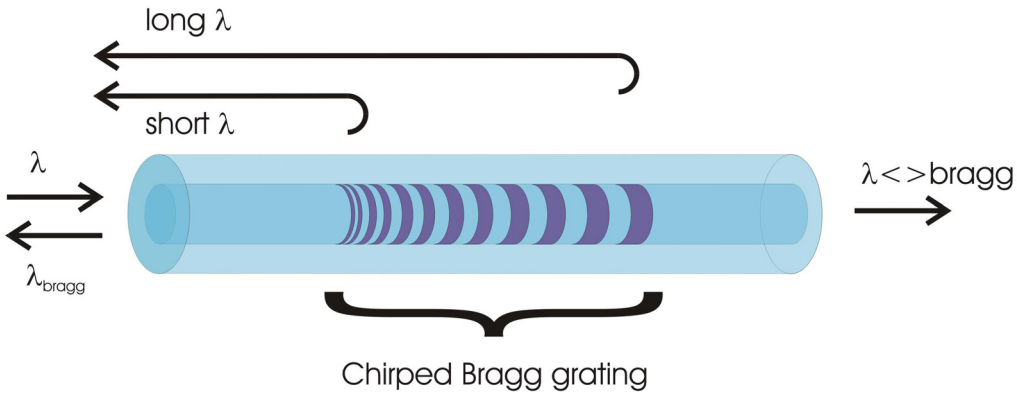

Figure 6.11: schematic of a chirped Bragg grating structure

Variation of the period of the Bragg grating over the length of the grating structure distributes the phase matching condition over the grating length with respect to the precise wavelength of the signal. Thus, with the spatial dependence of the phase matching

condition, the penetration depth of the incident light into the structure is wavelength dependent and therefore the group delay is wavelength dependent (figure 6.11). Through careful selection of the chirp of the grating structures the spectral and group delay response of a grating structure can readily be controlled. The application of this technique has been extensive, however one of the most noticeable is dispersion compensation(Ouellette 1987; Kashyap, Froelich et al. 1996; Dong, Cole et al. 1997).

In telecoms, long haul communication systems are limited through chromatic dispersion resulting in pulse broadening. Traditionally for single channel systems, this broadening is corrected through use of sections of negative dispersion fibre. Negative dispersion fibre (or Dispersion Compensating Fibre DCF) is designed to have a very high negative dispersion coefficient. These fibres are inserted into transmission lines periodically to compensate for the dispersion of standard communication fibre. Dispersion compensating fibre typically has a negative dispersion of ~30 times that of standard telecoms fibre thus after 50km of transmission around 1.4km of DCF is required to re-compress the pulse. The DCF normally comprises of a very small core structure, in single wavelength systems the only problem arises from the modal-miss match and associated loss due to the high doping levels. In WDM systems the intensity of the light in the core allows non-linear properties of silica to occur, allowing four-wave mixing and coupling of the signals at various wavelengths.

The group delay resulting from dispersion can be expressed as a Taylor series expansion about the central frequency of the pulse (Buck 1995). This results in a series of the terms (quadratic etc) that influence the dispersion properties. These higher order dispersion terms have the effect of varying the dispersion over relatively short wavelength ranges. In WDM systems these short scale wavelength variations affect the individual channels individually and can result in pulse broadening of the individual channels themselves. In general it is very hard to design DCF to compensate for these effects.

Using a chirped fibre Bragg gratings the temporal broadening of the pulse can be compressed without the associated disadvantages of loss or high power densities. It is worth noting that in general the grating structures are not only chirped, but apodised to combine the advantages of side-lobe suppression with controllable group delay properties to produce structures suitable for the DWDM systems of today.

6.4.4 Phase shifted gratings

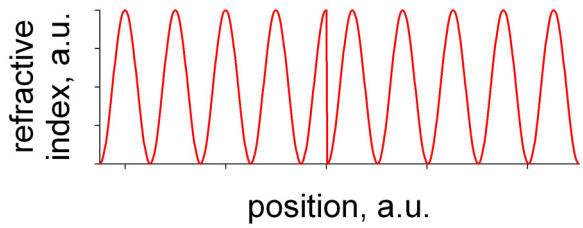

Figure 6.12: Schematic of the refractive index profile of a phase-shifted Bragg grating

Phase shifted gratings (figure 6.12) are commonly used in the fabrication of DFB semiconductor lasers. For this application, Bragg gratings are typically employed as narrow-band reflection filters centred around the Bragg wavelength. However, many applications benefit from functionality as a narrow band transmission filter, such as channel selection in a DWDM system. Whilst there are devices providing that functionally based on Michelson or Fabry-Perot interferometers they often involve multiple gratings and splitters and increase the cost and loss of a system(Othonos and Kalli 1999).

A single Bragg grating device can often offer the same functionality, by inserting an intentional phase shift across the grating length with the location and magnitude defining the exact spectral response of the structure. Essentially the phase-shift separates the structure into two gratings out of phase with each other acting as a wavelength selective Fabry-Perot resonator of which light satisfying the resonance condition can penetrate the band-gap effect of the original grating structure with resonant frequency dependent on the magnitude of the phase change.

These structures are often used as narrow-band transmission filters due to their wavelength selectivity. The other use for such structures is in the fabrication of distributed feedback laser devices. The presence of a phase-shifted grating within the gain media allows lasing only at the Bragg condition, a structure utilised in optical fibre lasers and semiconductor lasers alike.

6.4.5 Superstructure Bragg Gratings

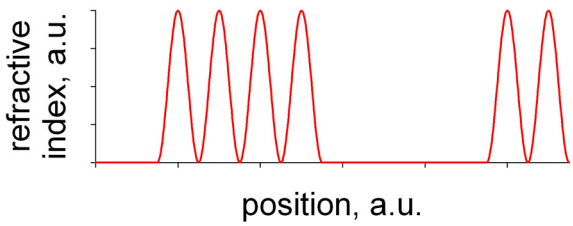

Figure 6.13: Schematic of the refractive index profile of a super structure Bragg grating

Superstructure gratings (figure 6.13) are Bragg gratings with a spatially periodic modulation of the amplitude of the grating contrast. This amplitude modulation is superimposed onto the Bragg grating structure along the length of the grating, resulting in a position dependent coupling coefficient. The earliest use of these structures is to produce a multi-channel response from a single Bragg grating. The period of the 'super-envelope' defines the spacing of the multiple Bragg reflections. A demonstration of the comb-like response of these devices is shown in figure 6.14.

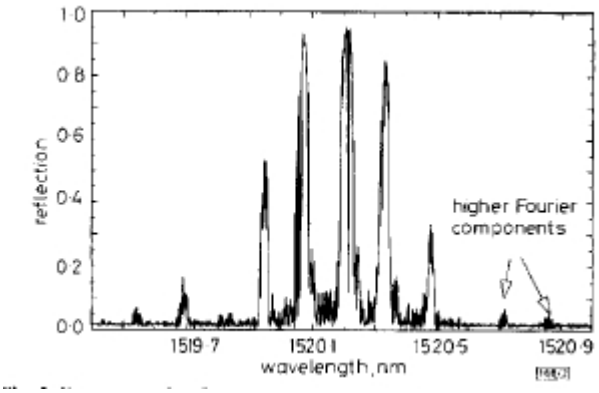

Figure 6.14: Spectral response of a superstructure grating with a constant grating period within a constant period super-envelope (Eggleton, Krug et al. 1994).

While the fabrication of superstructure Bragg gratings is beyond the scope of the work described in this thesis, the discrete local nature of the Direct Grating Writing technique described in chapter 8 should be ideal for the production of these structures.

6.5 Applications of Bragg gratings in devices

Fibre Bragg gratings have developed into an important technology in the field of optical communications, finding applications in a wide range of devices. The development of these components has primarily been driven by the rapid capacity increase of wavelength division multiplexing systems, of which Bragg gratings form a constituent part of many of the components used. Unique customisable filtering properties combined with in-line low-loss operation allow them to be combined with a wide range of structure to provide a wide range of functions. Examples of such functions and their applications are shown below to emphasise the flexibility of these structures.

6.5.1 Fibre Lasers

To date, the majority of fibre laser research has been directed towards erbium doped fibre lasers. There are many configurations possible but in general these fibres consist of the optical gain media of the erbium doped fibre (typically 2 m) configured into a cavity through the use of two reflecting Bragg gratings at either end (Reekie, Mears et al. 1986; Ball and Glenn 1992; Mizrahi, DiGiovanni et al. 1993). The gratings consist of a broadband mirror (~4nm) and a narrow bandwidth output coupler (~0.12nm). Below lasing threshold the broadband gain profile is dominant; at powers where the loss of the system is overcome lasing occurs, with the laser peak defined by the spectral response of the narrow output coupler grating.

6.5.2 Wavelength stabilisation of lasers

Semiconductor laser diodes offer cheap and mass produced laser sources available to the industry but they are not ideal components on their own. Commonly used structures are distributed feedback (DFB) or distributed Bragg reflector (DBR) architectures, however whilst these structures are relatively cheap and easy to manufacture the selection of the lasing wavelength has to be made at the point of design and accurate repeatable control of the lasing wavelength to less than 1nm is not always possible. An alternative technique is the use of fibre Bragg gratings as the output coupler. The output facet of the laser diode is coated with an anti-reflection coating and by pig-tailing a single-mode fibre with a Bragg

grating (of which the spectral response is readily controlled) a lasing wavelength from the gain spectrum can be selected. These devices are frequently referred to as *hybrid laser diodes*.

There are several modes of operation these devices can operate (Tkach and Chraplyvy 1986); two of the more common ones are single-mode and coherence collapsed. Single-mode operation requires the Bragg reflector to operate within the coherence length of the laser and acts as a high quality mirror (Brinkmeyer, Brennecke et al. 1986; Park, Rowe et al. 1986; Morton, Mizrahi et al. 1994). One of the advantages of these sources is a much greater temperature stability of the laser, typically DFB and DBR structures are highly sensitive to changes in the temperature of the device and the drive current resulting in a wavelength shift of the output spectrum. This wavelength shift results from the change in optical path-length of the cavity relative to the whole cavity length. Since hybrid devices are longer, but much of the length is silica fibre (much less temperature sensitive than semiconductor materials) the device as a whole is much more stable. The other type of device is the coherence-collapsed laser, which is differentiated by the Bragg grating located outside the coherence length of the laser. The reflection from this grating forces the diode to operate with broader modes and a strong reduction in the coherence length of the laser (Giles, Erdogan et al. 1994; Ventrudo, Rogers et al. 1994). This mode of operation forces the diode to operate within the bandwidth of the Bragg grating, stabilising the frequency, but the large number of beating modes leads to some high-frequency noise. However, this high frequency noise averages out the low-frequency fluctuations typically resultant from mode hopping. The low frequency stability is essential for the low speed applications, such as the 980nm pumping of erbium-doped fibre amplifiers.

6.5.3 Reflectors in fibre amplifiers

Fibre amplifier performance can be substantially enhanced through the use of Bragg gratings to reflect a range of wavelengths within the gain media. A wide range of reflector configurations are possible (Giles 1997), placing a broadband reflector centred around 1550nm provides the signal a second pass through the gain medium, in the case of small-signals this can result in up to a doubling of the amplified signal strength. Alternatively, the pump signal can be reflected for a double pass, in this configuration, with the signal still in a

single pass mode, yields approximately 1-3dB improvement. Other configurations are, in general, combinations of both techniques in a variety of coupling schemes.

6.5.4 Fibre amplifier gain equalisers

An alternative use of Bragg gratings is to control the gain spectrum from erbium-doped fibre. Typically erbium based amplifiers have gain spectra with peaks at 1530nm and 1560nm, with the fluctuation of the gain spectra limiting the useful 'level' bandwidth to approximately 10nm. Through employing grating structures to couple the incident light into radiative cladding modes with a wavelength dependence inverse to that of the gain spectra the wavelength region of uniform response can significantly enhanced. The gratings structures can either be tilted Bragg gratings (Kashyap, Wyatt et al. 1993) coupling the unwanted light into counter propagating cladding modes or multiple long period transmission gratings (Kashyap, Wyatt et al. 1993; Vengsarkar, Pedrazzani et al. 1996) coupling into forward cladding modes. These structures can result in gain flatness within 1dB over a greater than 40nm span.

6.5.6 WDM multiplexers/demultiplexers

Add/drop filters are essential for the operation of the wavelength division multiplexing systems, and there are a wide range of devices designed to fulfil the task. Of the simpler devices Bragg gating structures often form the specific wavelength selectivity required to add and drop a channel. A simple implementation is the use of a Bragg grating with a circulator (figure 5.15). A multi-wavelength signal is incident onto the fibre grating, with the Bragg resonance matched to one of the channels. The Bragg wavelength is reflected back and routed to an output by the circulator. Channels with wavelengths off the Bragg condition are transmitted by the grating structure.

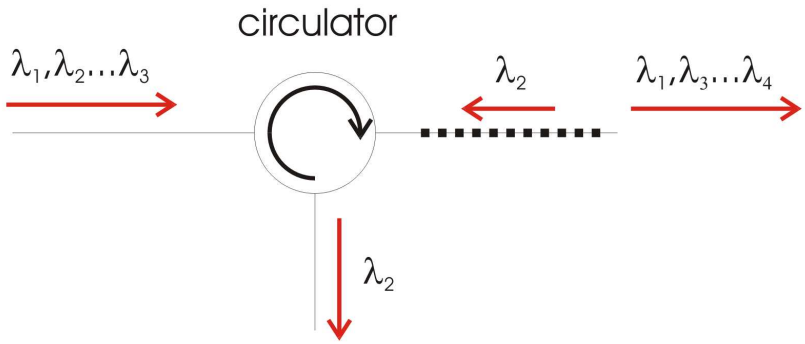

Figure 5.15: Schematic of a Bragg grating dropping a specific channel out of a WDM system

6.5.7 Variable wavelength response

One of the primary advantages of the Bragg grating structure is a well defined wavelength response. The Bragg resonance condition depends entirely on the period of the grating and the refractive index of the material defining the structure and with these parameters fixed the response is very stable. If either of the parameters is induced to change then the wavelength response of the grating is shifted, allowing the structure to respond as a sensor to the external environment (Othonos and Kalli 1999). For example, the period of a fibre grating, can readily be changed by placing the fibre under strain. Strain can change both the refractive index and the physical length of the grating, and therefore the period and spectral response of the grating. If the behaviour of the material is understood, this can provide highly accurate information on the stress of the fibre. Likewise, temperature will cause the material of the waveguide to expand and contract, also changing the period of the grating. Given that the spectral response is readily controlled by the strain of the fibre, the output of the Fabry-Perot style resonators allow for continuous tuning without mode hopping (Bell and Morely 1994) or can be used as diode laser stabiliser (Hillmer, Zhu et al. 1994; Maxwell, Kashyap et al. 1994).

6.6 Summary

In this chapter the background of Bragg grating reflectors was introduced. Initially the concept of a Bragg grating structure was described as a periodic modulation of the effective refractive index seen by a guided mode. The index perturbation allows power coupling between the incident guided mode and a counter propagating mode. The power coupling

only occurs at specific wavelengths that match the Bragg condition, where the periodic index perturbation provides the phase matching condition to satisfy the conservation of momentum and thus allow power transfer.

The wavelength response of Bragg grating structures was described using basic coupled mode theory. Although this technique is only applicable for uniform, weak grating structures it can be used to demonstrate the fundamental wavelength dependence of the reflection and group delay characteristics of Bragg grating structures. Having introduced the common Bragg reflector, several variants of grating structure were described, including apodised, chirped, phase shifted and superstructure gratings.

This chapter concluded with descriptions of some of the wide range of the application of Bragg gratings. It was shown that while the primary function of the Bragg grating structure is a wavelength selective reflector such devices can be used in a wide range of systems and applications. For example, Bragg gratings can be used as reflectors for laser devices, reflectors for fibre amplifiers, band-pass filters and add/drop filters for components in WDM systems.

Chapter 7: Bragg Grating Manufacture

7.1 Abstract

Over the course of fibre Bragg grating development, several key techniques have been used to inscribe index perturbations into fibres. To date, each technique has been based on the generation of an interference pattern with ultra-violet light and side exposure of a waveguide. The incremental developments up to the continuous fabrication techniques, used today, which allow the definition of grating structures different to that of the interference pattern used to inscribe them both in period and length are presented.

The concept of defining both the channel waveguide and the grating index modulation in the same fabrication technique is presented for the definition of planar structures. The advantages and disadvantages of the process are compared with current planar fabrication techniques. The proposed simultaneous method is a combination of the Direct UV writing process for the definition of planar channel structures and the continuous grating formation technique allowing the introduction of grating structure with a small writing spot.

Implementation of this simultaneous fabrication technique is described, a process referred to as Direct Grating Writing throughout the remainder of this thesis. The Direct Grating writing technique generates a tightly focused near circular writing spot through the intersection of two coherent laser beams, resulting in an interference pattern allowing grating structure to be defined. Through modulation of the writing spot as the sample is translated, the interference pattern structure is imprinted into the refractive index of the material. As the inference pattern is also the writing spot for channel waveguides, the imprinting of the grating structure defines the channel waveguide at the same time.

One of the primary advantages of this technique is that theoretically, the contrast of the grating structure can be varied between the total index change induced by the exposure, to null grating contrast. The grating period is defined though the period of writing spot modulation, not the period of the interference pattern. Such formation processes are investigated through the use of a simple simulation providing insight into the structures produced.

7.2 Introduction

In this section an overview of the key historical developments of the fabrication techniques of fibre and planar Bragg gratings is described. The early manufacturing processes described here were developed for the fabrication of fibre Bragg gratings due to the low loss of fibre and its extensive use. However, these techniques are also highly relevant to the fabrication of planar channel Bragg gratings as they are based on the inscription of a periodic index onto an existing channel waveguide, a similar process for both the planar or fibre geometry. Typically in the planar case there are far fewer fabrication techniques employed as the majority of the development work was performed on the more mature fibre Bragg gratings before planar channel waveguides were seen as a viable structure. Thus only the most popular techniques were transferred between the two technologies. As such, a brief overview of the development of various key fibre grating inscription techniques is presented below.

7.3 Fibre grating fabrication techniques

7.3.1 Self-organised grating formation

The first grating was produced accidentally in 1979 by Hill et al. The discovery is described in detail in chapter 2, but it is a process where an intense incident wave formed a standing wave with the end reflection off the end of the fibre. .

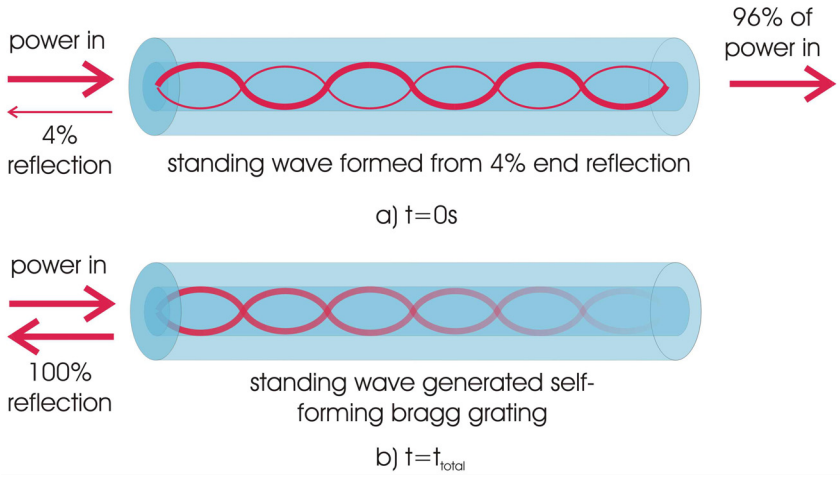

Figure 7.1: Schematic of the self-organising process in the formation of a Bragg grating

The intense fields at the anti-nodes of the standing wave induced a refractive index increase in the material. The period of the refractive index increase automatically matched the Bragg condition and thus coupled mode power into the reflected mode. As the reflected intensity increased, so did the intensity of the standing wave and hence, the index change.

These structures became known as 'Hill gratings' although they were initially viewed with little interest as the period of the grating structure is fixed to the wavelength of the writing radiation and the photosensitive effect was only observed at 488nm (and at high power).

7.3.2 One photon reaction

The true realisation of the potential of fibre Bragg gratings arose from combination of two developments. The first was the discovery that the refractive index increase process observed in the Hill gratings was a result of a two-photon reaction, and could be triggered directly through the more efficient single photon process. When stimulated thus, the refractive index increase was found to be orders of magnitude greater, therefore bringing the refractive index increase to lower and more achievable beam powers. However, it was the combination of the single photon process with the development of the side-exposure technique that turned the fibre Bragg grating from intellectual curiosity to a realisable device.

7.3.3 Side exposure

Virtually all techniques used today to define fibre Bragg gratings are variants of the side exposure technique. In 1989 Meltz et al. demonstrated the inscription of an interference pattern generated by the intersection of two UV beams through the side of germanium doped optical fibre. The period of the interference pattern, and hence the grating structure, was defined by a combination of the intersection angle of the two beams and the wavelength of light. Thus the gratings could be written using light around the ~240nm absorption band but produce interference patterns for wavelengths in the low-loss window of silica. The use of single photon interaction allowed viable refractive index changes to be induced from a relatively large diameter interference pattern exposed through the side cladding of the fibre (figure 7.2).

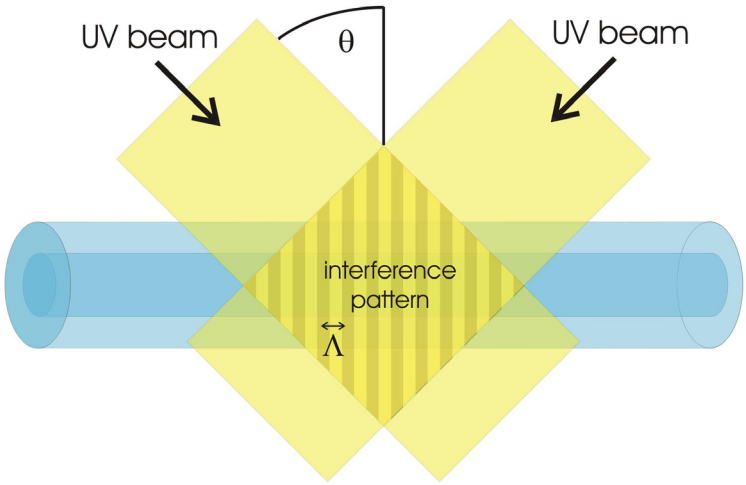

Figure 7.2: Schematic of the concept of side exposure in the manufacturing of fibre Bragg gratings

The interference pattern was generated by intersecting two coherent beams, generated from the same source laser, but split via amplitude splitting and then recombined at a pre-determined intersection angle such that the period of the interference pattern generated is;

$$\Lambda = \frac{\lambda_{uv}}{2\sin\left(\frac{\theta}{2}\right)} \qquad [7.1]$$

where both the wavelength and angle are to be considered in air and correspond to the arrangement in figure 7.2. The strongest advantage to this approach is the flexibility presented by the intersection angle of the two beams; this angle is not fixed by any component and as such can readily be varied to provide a range of interference patterns, and therefore grating periods from a single setup.

There are two disadvantages associated with the crossed-beams interference technique, arising from the dependence on the coherence of the laser source and the stability of the interferometer. Interferometric techniques require laser sources with a high degree of coherence to allow the fabrication of interference patterns with good fringe visibility, severely limiting the type of laser that can be used as a beam source. Post-splitting, the beam-path is critical to the contrast of the interference pattern, and any difference in the length of the two interferometer 'arms' must be significantly shorter than the coherence length of the laser. Spatial coherence of the writing beam is also of critical importance, frequently requiring the correct orientation of the writing beam (e.g. beam splitters result in spatial inversion of the reflected arm) and requiring precise symmetry of the optical components in each arm to avoid unnecessary contrast reduction (e.g. defects on the

mirrors). The biggest disadvantage is susceptibility of interferometers to mechanical vibrations and air currents. Any variation in the mechanical alignment from vibrations or density of the gas in the beam path can affect the phase of the two arms independently and thus shift the position of the interference pattern, reducing or extinguishing the uniformity of the structure inscribed into the fibre.

7.3.4 Phase-Mask

One of the most significant developments in the technique of Bragg grating inscription is the application of the phase mask. The phase mask is a diffractive optical element composed of a material transparent to the wavelength of operation with a two-dimensional surface relief structure etched or machined into one face of the component. The profile of the relief structure is chosen such that the 0^{th} order transmitted beam is suppressed as much as possible (less than 3%) whilst maximising the power contained within the ±1 order diffracted beams. The period of the surface relief defines the angle of diffraction between the two beams, providing control over the period of the interference pattern at the time of manufacture. The interference pattern is generated in the region of intersection of the phase mask with a period half that of the surface relief pattern. It is this interference pattern that is normally used to inscribe an index modulation into the host material.

7.3.5 Direct mask exposure

By far and away the most commonly used and possibly simplest technique of grating inscription is the direct phase mask exposure (Hill, Malo et al. 1993). Here the phase mask is placed in stationary, near-contact with an optical fibre (figure 7.3) such that the interference pattern from the 1^{st} order interfering beams coincides with the photosensitive core of the fibre.

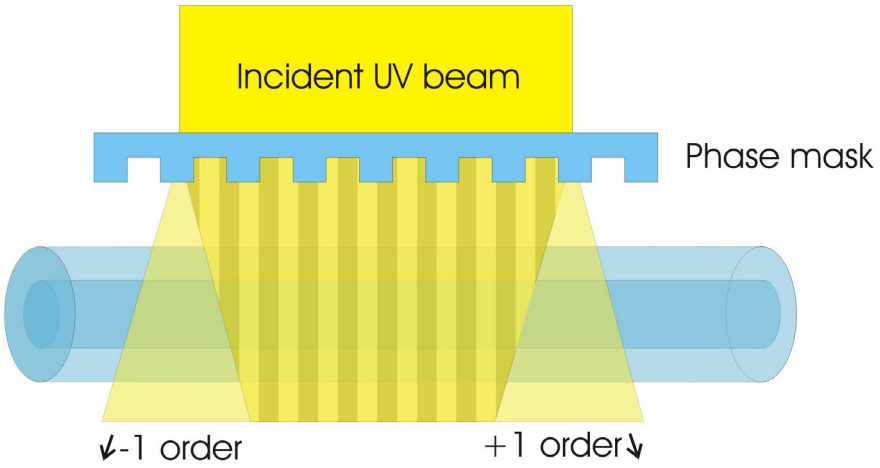

Figure 7.3: Direct phase mask exposure

The strengths of the phase mask technique are based around the stability offered in comparison to amplitude splitting interferometers. Here, the beam is not split until the diffractive element, with the interference occurring immediately after the phase mask to minimise the propagation length of the beams while they are susceptible to beam path errors. Overall the distance the beams require to stay coherent is of the order of 100μm as this is typically the distance between the core of the fibre and the phase mask. Not only does this minimal interference path reduce the instability of the interference pattern, it greatly reduces the coherence requirements of the UV source, allowing more powerful and yet cheaper sources to be used.

Phase mask based fabrication techniques do however have limitations prompting the continued development of more complicated fabrication processes. For example, the displacement between the phase mask and the photosensitive core of the fibre is critical for the fabrication of high quality structures. Also, while power is preferentially diffracted into the 1^{st} orders, there is always residual power contained within the higher diffracted orders (Dyer, Farley et al. 1995). At distances where the higher order diffracted beams are still overlapping, the interference pattern can become corrupted. The optimal distance is just greater than the point at which the 2^{nd} order beams are no-longer intersecting, however this does reduce the useable area of the interference pattern for a given beam diameter. Overall the quality of the interference pattern is always affected by the 0^{th} order beam because, although suppressed it is never fully extinguished, and thus interferes with the 1^{st} order beams to create additional periodic index fluctuations.

It is important to note the main feature of direct phase mask exposure is both its greatest advantage and disadvantage. It is a stable and repeatable system for generating a known, fixed interference pattern as the period depends only on the wavelength of light and the period of the phase mask. This allows for an extremely simple fabrication infrastructure to produce high quality, repeatable Bragg grating structures, however there is no flexibility in the grating structure defined by a single mask. Even the slightest change of the structure of the grating requires a different phase mask, increasing cost and fabrication time. Any error in the phase mask, as is common from e-beam stitching errors, is translated through inscription into errors in the grating structure.

7.3.6 Non-contact phase mask exposure

An alternative use of phase masks is to generate two spatially symmetric diffracted beams that are subsequently manipulated through extra optical components to reposition or re-shape the interference pattern. This technique is often referred to as non-contact exposure (a misleading term as it implies the direct exposure is in physical contact with the fibre, which is normally not the case). However, the distances between the mask and fibre in these techniques are much greater than in the direct write comparison.

By placing a UV transparent prism (Kashyap, Armitage et al. 1993) after the diffractive element the $\pm 1^{st}$ orders are internally reflected within the prism avoiding the disadvantages of beam propagation in a turbulent atmosphere, before being re-combined at the photosensitive core. Alternatively, using mirrors after the diffractive element allows selection of the different order of beams to be recombined (ie 1^{st} and 1^{st} or 1^{st} and 0^{th})(Dyer, Farley et al. 1996) whilst still retaining the same spatial orientation of the interferometer arms but providing control over the angle of recombination (figure 7.4). However, this technique is once again susceptible to the environmental changes and the quality of the reflecting mirrors.

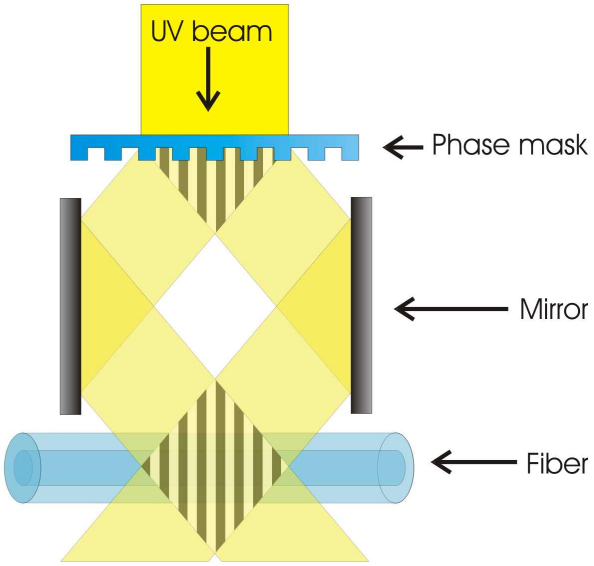

Figure 7.4: Non-contact grating inscription using two mirrors to redirect the diffracted beams from a phase mask.

7.3.7 Point-by-point fabrication of Bragg gratings

One of the most conceptually versatile techniques to overcome the disadvantages associated with interferometric based system is the point-by-point technique (Malo, Hill et al. 1993). In this technique the Bragg grating is formed by increasing the refractive index of the material in a single plane per exposure. Multiple exposures coupled with translation build up the grating structure a plane at a time up to the full length of the grating. In the implementation by Malo et. al. the writing laser was incident on a narrow slit that was in turn imaged onto the fibre, with a single pulse of the beam generating the local refractive index change to form a grating plane (figure 7.5). The fibre was then translated one grating period before the next exposure. However, the minimum size of the refractive index change in the material using this technique was 0.7μm, preventing the writing of a first order Bragg grating in the silica fibre and requiring the 2^{nd} or 3^{rd} order grating structures to achieve ~1550nm responses.

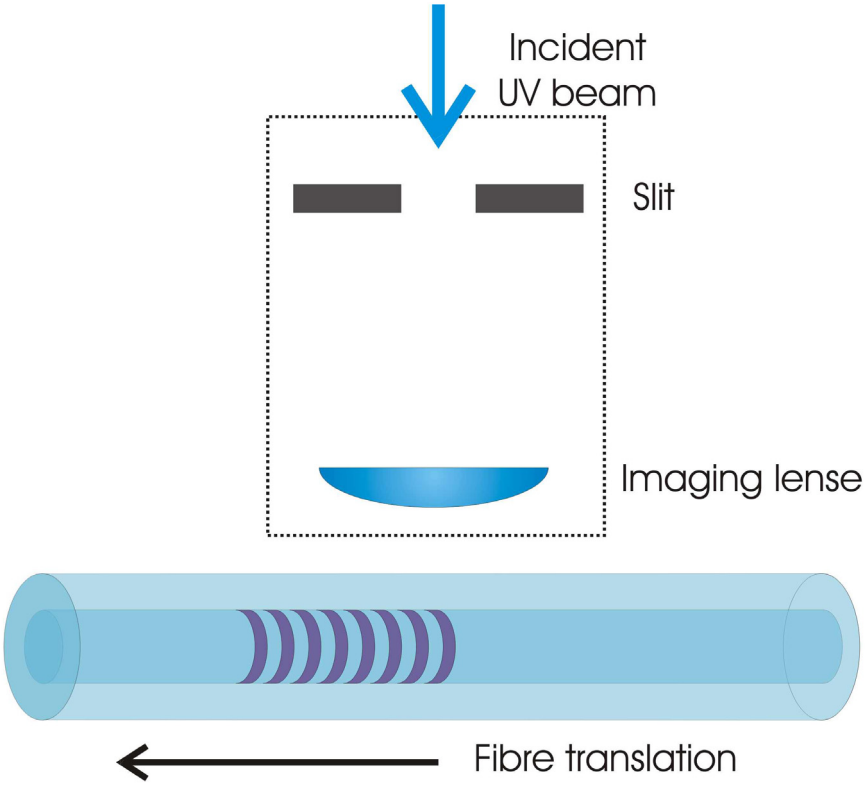

Figure 7.5: Point-by-point grating inscription

There are two key advantages with the point-by-point technique; namely the lack of an interference pattern and flexibility. As there is no interference pattern the technique does not set requirments on the coherence of the laser source and is not subject to environmental turbulence. Process flexibility results from the ability to define virtually any refractive index modulation of a period greater than the inherent writing spot by adjusting the distance translated between exposures and the power used to define each plane. As such, this technique is ideally suited for fabrication of structures with varying grating length, contrast, period and phase. Disadvantages include long fabrication times and errors in the grating period caused by thermal drift and variations in the strain on the fibre. The fact that these errors ultimately limit the length of the structures that can be written, coupled with the difficulty in focusing a writing spot tightly enough to produce a 1st order grating, curtailed the direct application of this technique.

7.3.8 Mask image projection

A variant of the imaging technique utilises a transmission mask with a multitude of 'grating planes' (UV absorbing lines) deposited on a transmitting substrate with periods ranging

from 5μm to 120μm (Mihailov and Gower 1994). The transmission mask was imaged with a 10:1 reduction and grating structures with periods >1μm were inscribed. Due to the size of the features that can be defined using this technique the gratings were again operated in the higher-order mode for responses below 3μm.

The advantage of this technique is the relative simplicity of the setup and the low fluence exposed to the mask (due to the subsequent image reduction) when compared to the direct phase mask systems. The drawback is the inability to define fine grating structure, although this technique is well suited to defining long period gratings.

7.3.9 Non-stationary grating writing

A significant enhancement in the flexibility of fibre Bragg grating definition arises from the relative motion of the fibre, phase mask or writing beam relative to each other. By introducing a small velocity difference between the scan rate of the phase mask to the fibre an index perturbation is defined with a period 'detuned' from the interference pattern generated from the phase mask (Cole, Loh et al. 1995; Loh, Cole et al. 1995). This allows Bragg gratings with a period and response different to that of the native interference pattern to be created. By varying the relative velocity of the phase mask a Bragg grating with a position varying period can be produced allowing chirped structures to be produced from a uniform phase mask (Loh, Laming et al. 1995). The detuning process and limits are described in more detail in section 7.5.1, however in general the detuning range possible with this phase mask technique is approximately 10-15nm.

The same research group demonstrated that by dithering the relative position of the fibre/phase mask the local contrast of the index perturbation can be reduced without altering the overall exposure, thus allowing apodised grating structures to be produced with a constant average index over the region of UV irradiation.

7.3.10 Long grating structures

Many of the complex Bragg grating structures needed for modern applications have sophisticated grating profiles. These profiles often require structures of the order 10's of

mm, much longer than is typically achieved in the stationary exposures. A simple and stable solution is to fix both the fibre and phase mask together with a stationary relative position and translate the entire structure relative to the writing laser (Hill, Malo et al. 1993; Martin and Ouellette 1994). This technique requires long phase masks with the associated risk of stitching errors (Williams, Liu et al. 1997) but does offer a technique for varying the strength of the grating structure through altering the translation velocity (Kashyap, McKee et al. 1994).

Extending the length of a grating beyond that of a phase mask can be achieved by moving the fibre relative to the phase mask a significant distance between each exposure. This effectively joins together multiple grating sections to act as a single long grating structure. However, Bragg gratings are highly sensitive to any errors in the grating structure, particularly the phase of the index perturbation. A single phase shift between two co-incident gratings significantly affects the performance of the grating (see section 6.4.4). One technique used to minimise this effect is to phase-trim the regions between the connecting gratings through exposure to additional irradiation after grating inscription, whilst observing the grating response (Kashyap, Froehlich et al. 1996). However, this process can be time consuming, lead to un-optimal grating response, and suffer from differential ageing of the regions exposed to different fluences.

A more reliable technique used to reduce phase errors monitors the fluorescence of the grating inscription process during the writing process (Rourke, Pugh et al. 2000). Overlapping short successive sections of a longer grating structure was achieved by monitoring the florescence of a low probe signal as the position of the next grating was shifted. The observed florescence altered in intensity due to the prior grating exposure allowing correlation with the previous inscription.

7.3.11 Continuous grating definition

Continuous grating definition techniques build up the grating structure through many exposures of the interference pattern spatially separated by the period (or multiples thereof) between each exposure. Using this technique, gratings much longer than the writing beam or phase mask can be generated in a continuous run.

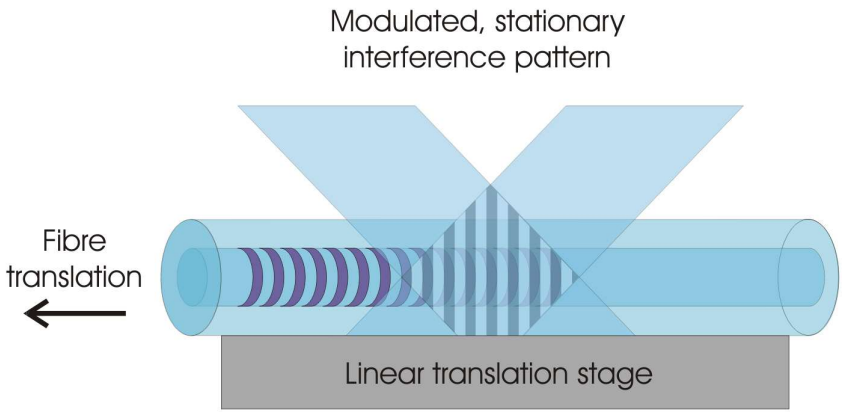

Figure 7.6: Continuous grating definition

The first implementation of this technique utilised a free-space interferometer to generate an interference pattern, through which the fibre was translated with a constant velocity (Asseh, Storoy et al. 1997). The fibre was mounted on a linear air bearing stage with the position was monitored by an interferometer. As the stage was translated with a constant velocity a UV laser pulse triggered for each exposure of the interference pattern. In this case the duration of each pulse was 10ns, due to the relatively slow translation velocity, each exposure results in an virtually stationary exposure of the interference pattern. As the laser pulse is triggered under the control of the interferometer it is readily trivial to insert phase shifts between exposures, and thus the grating structure (Asseh, Storoy et al. 1995).

7.4 Planar Techniques

7.4.1 Traditional planar grating inscription techniques

7.4.1.1 Physical relief gratings

In the fabrication of planar Bragg grating structures there are typically two techniques that can be applied, material relief gratings or superimposed gratings. Both fabrication processes have associated characteristics that, whilst resulting in devices with similar functionality, provide significant distinction between the final structures.

In planar processing the definition of a corrugated waveguide is, conceptually, a simple processing step utilising the same fabrication techniques as described for channel fabrication in section 4.4.1. The index modulation can be induced in several applications, all based on the permanent structuring of the material in or surrounding, the channel waveguide. Bragg grating structures can be defined through periodic modulation of the channel waveguide thickness, a grating structure in contact with the waveguide or a buried refractive index based structure in the cladding layer (figure 7.7).

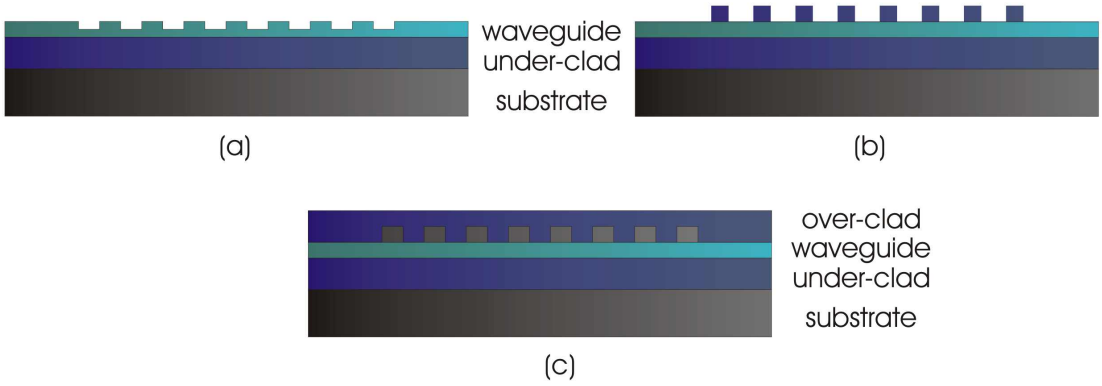

Figure 7.7: Material based corrugated waveguide planar Grating structures, (a) surface relief in the waveguide, (b) grating structure in contact with the waveguide and (c) buried grating in contact with the waveguide.

Advantages of such structure definition techniques are the well developed processes transferred from microelectronics, common applicability to many different materials and bulk manufacture once the mask design is finalised. Disadvantages include fabrication limitations, there are many fabrication steps, and accurate exposure of the grating period is often difficult with the reliable etching of the grating structure subject to inconsistency over large areas. Devices fabricated using this technique are associated with a higher propagation loss along with birefringence. Physical relief grating structures are difficult to fabricate uniformly with errors increasing the loss of the structure or corrupting the grating response. Apodisation profiles are difficult to implement when using this technique, severely limiting the spectral performance of the structures.

7.4.1.2 UV inscription

The other dominant technique for grating fabrication in planar substrates is the inscription of refractive index perturbation through the exposure to a UV interference pattern. Such processes are similar to the fibre techniques outlined in section 7.3, where the interference pattern is over-laid onto an existing channel waveguide (figure 7.8).

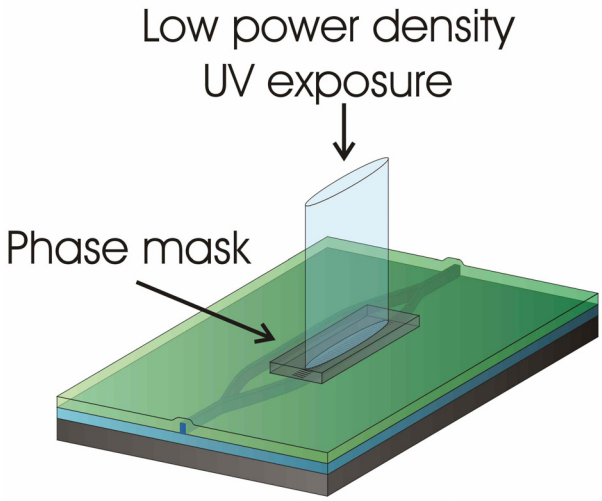

Figure 7.8: Planar implementation of Bragg grating inscription in an existing channel waveguide

Advantages of UV inscription processes in planar substrates are generally the same as those for fibre, allowing high quality low loss grating structures with complex refractive index profiles. One disadvantage is that changes in the average index of the channel waveguide can occur with exposure, altering the channel properties. As the grating structure is critically dependent on the quality and coherence of the interference pattern, any errors are transcribed into the index perturbation, and the refractive index change of the material can degrade with time and temperature. The range of techniques described in 7.3 all have individual strengths and weaknesses, but the most commonly employed technique for Bragg grating fabrication is direct exposure through a phase mask (figure 7.8). This technique has proven to be stable and easily applied; however, it is somewhat inflexible requiring an individual phase mask for each grating structure.

7.4.2 Two-step processing characteristics

Planar grating structures defined through the two-step processing described above have several characteristics resulting from the processing techniques. The UV exposure superimposes the intensity pattern of the interference structure on the existing index structure defining the channel waveguide (figure 7.9).

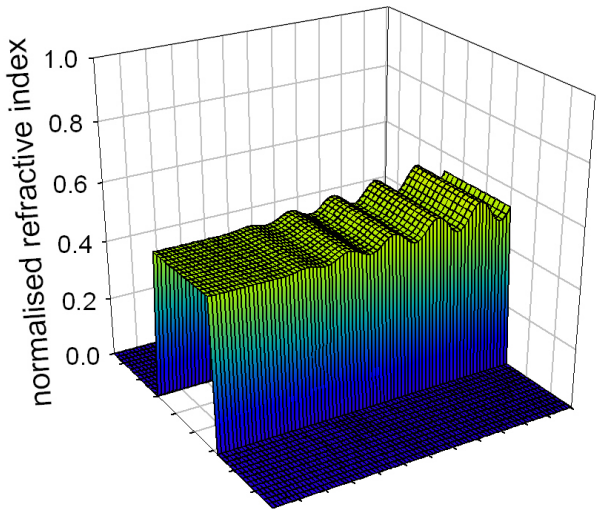

Figure 7.9: Schematic of a conceptual structure resulting from the superposition of a UV interference pattern onto a photosensitive RIE channel waveguide.

The overall increase in average refractive index arising from UV exposure limits the total power that the channel waveguide can receive before severe modification to the strength, and therefore the guiding properties, of the structure. However, limiting the overall fluence used to write the grating restricts the maximum contrast of the index perturbation and prevents the fabrication of short, strong band-pass structures. Typically in these two-step processes the size of the interference pattern is very large, often the size of the entire grating structure. As stated earlier, in the case of direct phase mask exposure there is no flexibility in the structure defined, whereas by applying the continuous fabrication techniques (section 7.3.11) the parameters of the grating can be varied as the structure is written. However, the maximum local rate of change of the grating structure is determined by the width of the interference pattern, which is severely limiting in planar devices due to the small lengths involved in the samples.

7.4.3 Simultaneous definition of channel and grating structures

Conceptually, if the channel and the grating structures are defined at the same time using the same low-loss process, there is potential for a high degree of control over the grating form. As both grating inscription and Direct UV writing are based on the same material response from exposure to UV irradiation, the two techniques are ideally suited for combining into a single fabrication process.

One limitation of existing planar grating fabrication techniques is the quality of the initial channel waveguide. As described in chapter 4, the most commonly used technique for the definition of channel waveguides is reactive ion etching. The structures that this technique produces are very good (relatively low loss, strong index change) but as described previously, the channel structures can suffer from rough channel walls. An additional drawback is the requirement for etch uniformity. In general for channel waveguides small magnitude, long scale (mm) variations of the channel structure do not affect the overall performance of the channel. However, Bragg grating devices demand very good uniformity in the properties of the host channel waveguide, and are often of the order 10's millimetres long, corresponding to length scales across which uniformity is hard to control in etched structures.

The ability to define both channel waveguides and grating structures places severe requirements on the form of the UV writing beam. To define channel waveguides through relative translation (allowing both straight lines and curves to be defined) the writing spot must be tightly focused to a circular spot approximately as wide as the channel structure to be defined. A linear (1-dimensional) intensity modulation is needed to define the grating structure as in all the inscription cases, by incorporating the interference pattern into the writing spot any refractive index modulation inscribed, will be as wide as the channel waveguide. The average index increase of the grating defines the channel structure (figure 7.10).

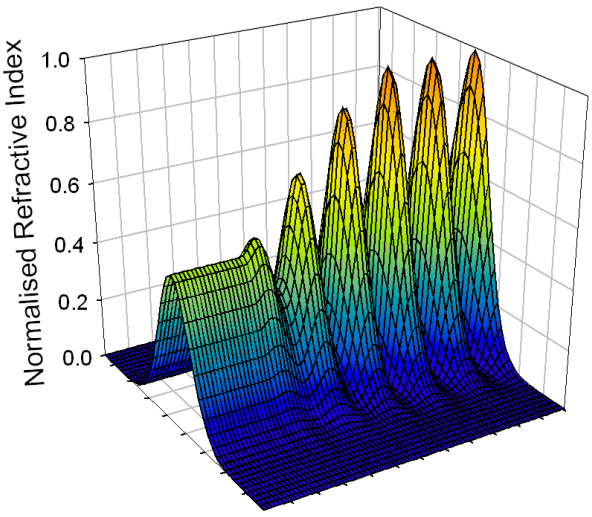

Figure 7.10: Schematic of the structure resulting from the all-UV definition in a single step of Bragg grating index modulation and channel waveguide, highlighted in the rapid transition between zero grating contrast and maximum grating contrast.

Devices defined in this manner would have the full photosensitive response of the material for both gratings and waveguide structures and the average index of the channel section can be made independent of the contrast of the refractive index perturbation. As the UV writing spot is very small, the grating structure is built up in a technique analogous to the continuous definition of fibre Bragg gratings. The very small interference pattern allows highly accurate placement of the grating structures and very rapid alterations of the grating structure.

From a device production consideration, combining the two processes of channel waveguide definition and grating inscription minimises the number of processing steps. Once the 3-layer photosensitive sample is produced a structure is programmed in computer code as for Direct UV writing and then written in a single step. There is no need for subsequent clean-room processing, or custom mask/phase-mask manufacture, as all structuring is performed by the single set-up. All structures are defined in computer software, and therefore the system is ideal for one-off prototyping, whilst still retaining the ability to fabricate multiple structures as required.

In concept the combination of a focused writing spot with an interference pattern is an ideal solution to the two-step problems. The difficulty is in the generation of such a structure. The conventional fibre fabrication techniques for generating interference patterns were considered (table 7.1) before the adoption of the free-space interferometer.

Technique	**Advantages**	**Disadvantages**
Direct mask exposure	Very stable interference pattern	Would not work due to the size of the writing spot relative to the phase mask
Non-contact mask exposure	Spatially symmetric coherent beams	Stray diffraction orders and the introduction of focusing lenses
Point-by-point	No interference pattern	Not a circular writing spot for curved channel definition
Image Projection	No interference pattern	Required optics impractical, if not impossible
Two-beam interference	Simple implementation of focussing optics. Robust.	Susceptibility to turbulence, thermal drift and source laser coherence

Table 7.1: Methods of generating a small scale writing spot with inherent intensity modulation for simultaneous definition of channel and grating structure.

7.5 Direct Grating Writing

7.5.1 Concept

Direct Grating Writing (DGW) is a technique for UV inducing channel waveguides and Bragg grating structures in a single fabrication step. This concept has several advantages in terms of fabrication processing and devices that can be manufactured. These include the following:

- The same spot defines both the channel waveguides and the Bragg channel waveguides, with no alteration of equipment for either structure, allowing complex planar lightwave circuits to be written in a single run.
- The small interference pattern provides large flexibility in the period of the grating structure defined without the need for changing the period of the interference pattern.
- For planar Bragg gratings both the channel and the grating are defined using the same material response to irradiation, therefore the Bragg structure has the potential to utilize the full UV index change possible in the glass.
- The contrast of the grating structures is independent (up to a limit) of the average index (strength) of the channel waveguide, with the theoretical contrast ranging from total extinction to almost twice the average index increase of the channel.
- The average index of the channels and grating can be matched for optimal coupling.
- All of the associated design and prototyping advantages of Direct UV writing.

7.5.2 Principle of Operation

The fundamental principles behind the Direct Grating Writing process developed during the course of this project appear similar to those of the continuous grating writing techniques in section 7.3.11, although several distinct differences exist in the experimental implementation. In our process a UV interference pattern is generated by intersecting two tightly focused coherent UV beams at a fixed point in space. A ‘blank’ photosensitive sample is then aligned with this interference spot and translated relative to it. With the

power to the spot continuously on the effect of the interference pattern is averaged out through the motion of the stages, resulting in the equivalent of a Direct UV writing process for channel waveguides. As in Direct UV writing, the size of the spot defines the width of the channel waveguide, while the beam power exposed to the material (fluence) controls the strength of the refractive index change, and the relative motion of the writing spot to the sample directs the path for each waveguide. If the writing laser is modulated during sample translation, with a frequency such that between subsequent exposures the sample has translated approximately the distance of the period of the interference pattern, then after multiple exposures an interference pattern is built-up. As this Bragg grating structure is written using the same writing spot as the channel waveguide, the width of the average index increase is exactly the same as the continuous exposure case, i.e. the channel waveguide structure is defined automatically by the average index increase resulting from the fluence of the writing process (figure 7.11). Appropriately modulating the laser power as the sample is translated results in the grating structure extending much greater lengths than the writing spot. Once the full grating structure has been written, switching to continuous exposure allows the definition of subsequent waveguide structures such as s-bends and couplers.

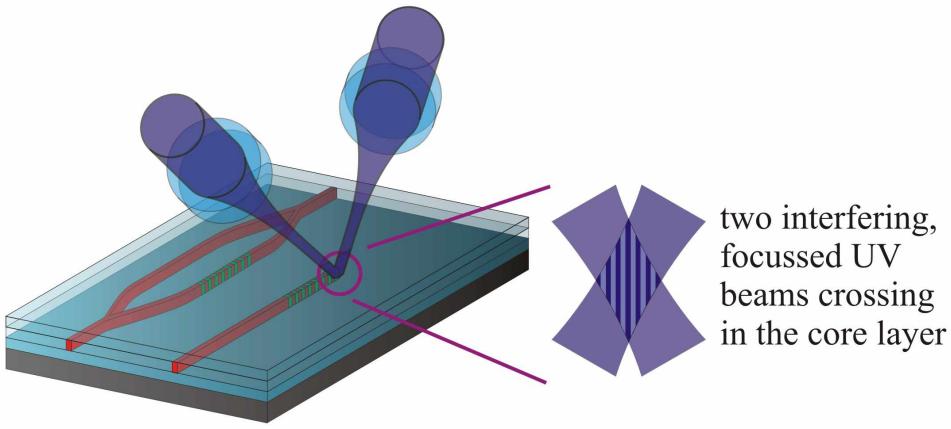

Figure 7.11: Direct Grating Writing concept for defining PLC with grating structures in a single step.

7.5.3 Experimental Arrangement for Direct Grating Writing

The Direct Grating Writing setup is a combination of high precision translation stages, stable UV beam path and a rapid, flexible computer control system. The experimental requirements are stringent due to the combination of a Direct UV writing setup with a

continuous Bragg inscription setup, both of which have requirements in separate areas. Direct UV writing requires 3-d translation stages with micron positional control and a tightly focused, stable, good quality UV writing spot. Grating inscription requires a nm-resolution translation system, a rapid programmable control system for beam modulation and a stable interference pattern. The following sections describes the work undertaken during this project to create the Direct Grating System, a technique for the simultaneous definition of the channel and grating structure, suitable for non-flat planar samples.

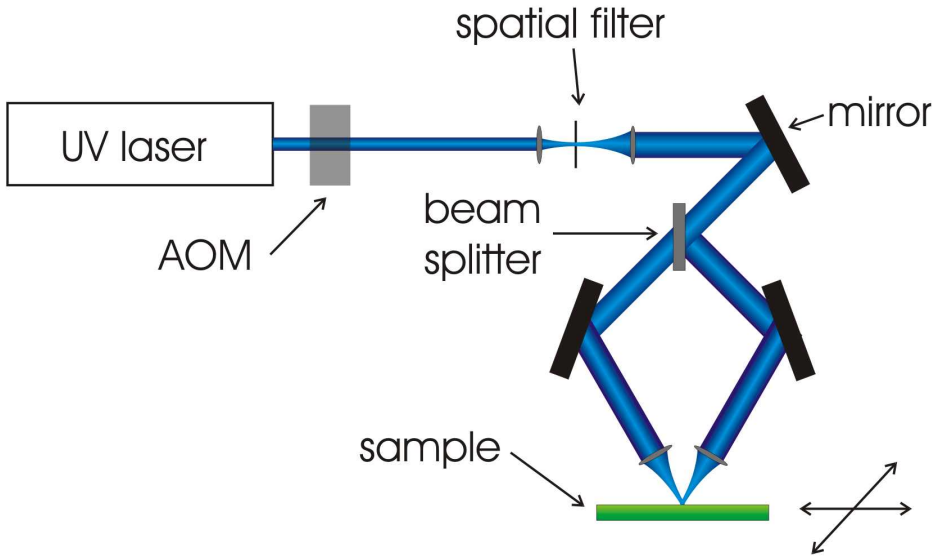

Figure 7.12: Schematic of the Direct Grating Writing system

7.5.4 UV Beam Path

The UV source used in these experiments is a Coherent Sabre Fred CW frequency doubled Ar-ion laser. This laser was chosen as it offers good spatial and temporal coherence (coherence length ~2cm), with a continuous output, resulting in less damage to the photosensitive material and yet sufficient power to induce significant refractive index change. Frequency doubling is performed via a Beta-Barium Borate (BBO) crystal, doubling the 488nm fundamental frequency to 244nm, with a resultant maximum output of ~500mW. The output of the laser is controlled/modulated by a fused-silica acousto-optic modulator (AOM) that, like the BBO crystal is Brewster angled to reduce back-reflections (the high intensities would cause conventional AR coatings to degrade with time). The AOM is aligned to give preferential diffraction into the first diffracted order (~80% max) to which the subsequent beam path is aligned. Although there is an associated power loss with utilising the 1st order, the extinction ratio of the first order is unity as opposed to ~20% of

fundamental mode. The diffraction efficiency is controlled through an analogue 110MHz RF generator controlled via a 0-1v drive signal.

The first order diffracted beam is isolated from the fundamental beam path through use of an aperture before being directed to a spatial filter. The spatial filter is operated with a small aperture resulting in partial clipping of the optimal beam waist as well as functioning as a 3x beam expander. By clipping the beam waist the spatial filter functions to some degree as a beam pointing stabiliser, converting beam pointing fluctuations into intensity variations, not as critical in an interferometer setup as pointing drift. After the AOM and the spatial filter the maximum beam power available for UV writing is ~150mW, a reduction in absolute power from the 500mW, however the beam quality and stability is significantly enhanced.

Once filtered, the beam can be steered to either a conventional single beam path Direct UV writing setup, or to the Direct Grating Writing setup. The DGW beam path undergoes several 90˚ reflections to ensure maximum efficiency of the mirrors whilst orientating the beam until incident on a fused silica beam-splitter. The reflected and transmitted beams generated from the splitter form the two paths of the interferometer. The beam splitter is 5mm thick to displace any cavity reflections from the subsequent beam path of the transmitted arm. In this case the transmitted arm does not have an extra inverting mirror to correct for the differing number of reflections in the beam paths due to the symmetrical nature of the beam from the spatial filter.

The two interferometer arms intersect with a half angle of 13˚ at the writing position. Before intersection the two beams are focused down to ~3μm spots via two independent lenses mounted on 3-d miniature translation stages allowing fine control over focal position of the two beam waists (figure 7.13). The focal points are then aligned to ensure crossing at the correct height at the beam waists of both arms of the interferometer.

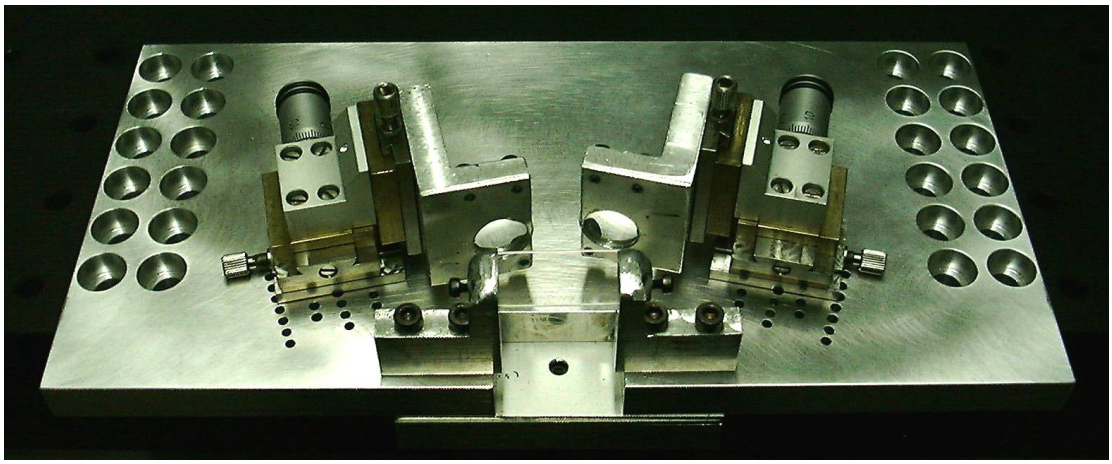

Figure 7.13: Lens mounts allowing independent alignment of the two 3um writing spots.

The optical arrangement was enclosed in a Perspex box to minimise room-wide air currents and thermal fluctuations, with the interferometer beam path contained in a secondary structure to minimise air currents from the translation stages. The Perspex has a secondary effect of isolating any scattered UV radiation from the operators.

7.4.5 Translation stage set-up

During the DGW process the sample is translated relative to the fixed position interference writing spot through use of computer controlled translation stages. The translation stages consist of cross mounted Aerotech air-bearing stages with a translation span 50cm x 50cm. The stages are non-contact linear stages with air bearing support, supplied from liquid nitrogen boil-off with integral non-contact optical encoders (500nm resolution) driven by brushless linear servo-motors. The combination of non-contact translation system with the large base of the translation stages provides a stable, smooth translation system.

The height of the sample is controlled through a manual linear translation stage. Alternative closed loop systems were investigated but for the initial implementation of the system using relatively small planar samples (less than 30mm in length) a passive system was found to be sufficient. To ensure the photosensitive layer remains in the plane of the crossing beams the sample has a low profile levelling stage that in combination with the height control allows for compensation of tapered thickness samples or particulate contamination between the stage and the sample. The planar sample is mounted on an anodised aluminium vacuum chuck with a reference flat for rapid secure mounting and alignment.

The motion of the stages is operated through an extended computer numerical control process based on the Aerotech U600 control system. This process allows for waveguide structures to be defined directly in a g-code programming language providing dynamic control over the UV writing parameters.

7.5.6 Modulation Control

The modulation of the writing beam for the grating definition process is controlled by a separate system from the stage control software. The system is a modification of the original control system developed by M. Cole, M. Durkin and M. Ibsen at the ORC for continuous definition of fibre gratings (Durkin 1999).

The 'x' axis position of the translation stage is continuously monitored by a secondary double-pass He-Ne interferometer. The axis of motion monitored is aligned to coincide with the plane of intersection of the two interferometer arms (therefore normal to the interference pattern). The interferometer used is a Zygo ZMI-1000 measurement system with a resulting resolution of 1.24nm (1 Zygo unit). Positional data is outputted from the interferometer via the parallel port as a 32-bit number in Zygo units updated at 2MHz. To minimise the overhead of the control computer in-situ the parameters of the grating structure are calculated prior to the writing translation. The profile of the grating structure is stored as an array of 32-bit numbers corresponding to the position of the modulation change-of-state positions in Zygo units with the most significant bit of the number replaced with the state of the writing beam.

The 32-bit number is outputted via a 32-bit digital I/O card to a hardware comparator board built by A.Fu monitoring the digital output of the Zygo interferometer. When the output of the interferometer is equal or greater than that in the comparator buffer (less the most significant bit) the state of the writing beam is switched to the state defined by the most significant bit and subsequently triggers the comparator to download the next 32-bit address from the computer.

7.6 A question of duty

As described in section 7.3.11 the definition of Bragg grating sections requires the laser to be modulated as the sample is translated relative to the writing spot. In the fibre implementation of continuous grating definition a pulsed laser source was used. This technique delivered high power densities over very short time periods, resulting in approximately stationary exposures as the fibre is translated. However, the power levels involved in this process have frequently been observed to create additional loss in the material, a critical effect when defining the entire structure through UV exposure. To keep the UV induced loss to a minimum, a CW laser source is used and modulated through an AOM, allowing the duration of each exposure to be much longer than that associated with pulsed sources.

In the DGW process the external modulation of the laser is therefore controlled by an astable control signal, modulating between a high and low state. For a uniform grating with constant period and contrast written with a uniform translation velocity the control signal is an oscillating signal of fixed frequency. However, the overall exposure and contrast of the structure is defined by the duration the laser write pulse for each modulation. Applying commonly used definitions from electronics field, the *duty cycle* of the signal is the percentage of the period that the signal is 'high'. For example when defining channel waveguides with the beams constantly on the effective duty cycle is 100% while with the beam off it is 0%, with values in between independent of the modulation frequency (figure 7.14).

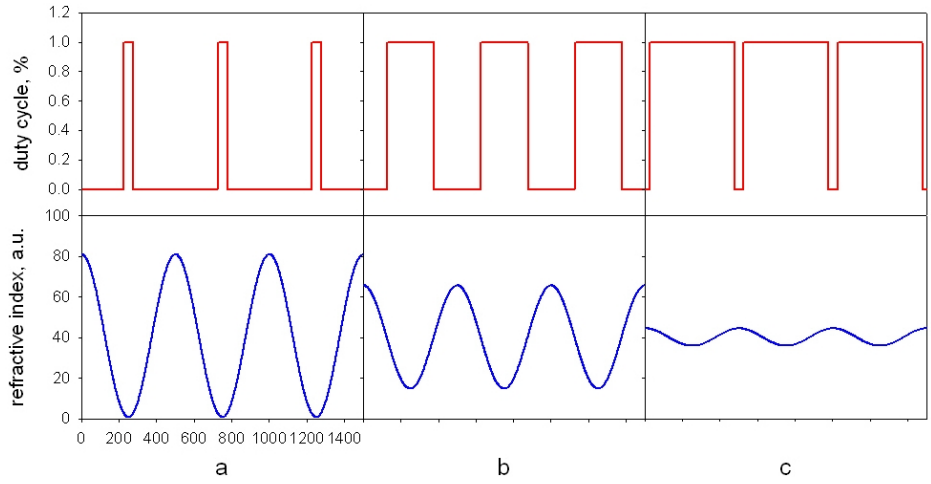

Figure 7.14: Illustration of effect of duty cycle on fluence matched structures with the same modulation frequency. Duty cycle values of (a) 10%, (b) 50% and (c) 90%.

In fibre fabrication techniques, there is always a balance between the exposure levels used to induce large refractive index perturbations and the overall increase of the average index of the channel waveguide due to exposure. Increasing the average index of the structure can adversely affect the device that is produced, or long tapered sections either side of the gratings are written to increase the strength of the channels before and after the grating structures. Particularly in techniques using CW writing sources there is a very narrow range of duty cycles that provide maximum grating contrast with minimum average index reduction, with values around ~35% typically providing the best results.

However, this no longer applies when defining the channel waveguide structure and Bragg grating structure independently. This is because the average index increase defines the channel waveguide structure, and as such is selected through writing conditions as for the classical Direct UV written channel waveguide. As such, variations in the beam power/writing speed can be used to compensate for the reduction of beam power due to the less than 100% duty cycle. These balanced writing conditions, subsequently referred to as *fluence matched*, result in the duty cycle defining only the index perturbation contrast. The effect of duty cycle on grating contrast is demonstrated in figure 7.15, although writing time tends to infinity when writing a 100% contrast grating.

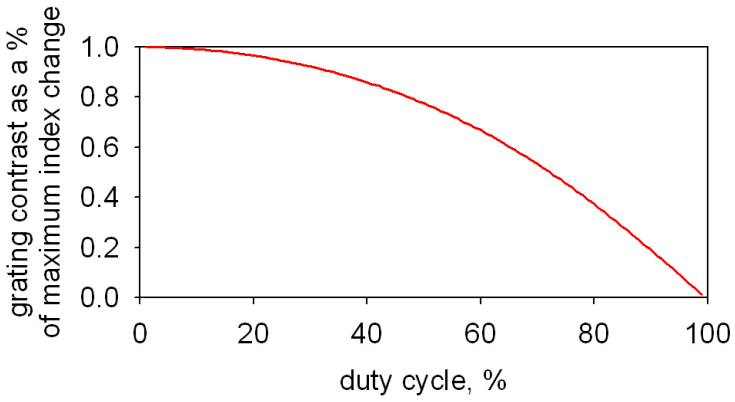

Figure 7.15: Grating contrast (% of channel strength) as a function of duty cycle.

Whilst intrinsically there is little use of grating structures that have the very large grating contrast as demonstrated in figure 7.14a (other than short, broad band filters) the ability to define such large index perturbations is extremely advantageous when combined with other fabrication techniques, such as centre-wavelength detuning.

7.5.1 Centre wavelength detuning

Centre wavelength detuning (more simply referred to as detuning) is the process of introducing a differential in the distance between each stepped exposure of an interference pattern and the inherent period of said pattern (Cole, et. al. 1995). If the difference between the interference pattern period and the spacing of each exposure is small, then the resulting index perturbation built up after the summation of all the exposures has a period corresponding to the stepping period. The build up of the resulting index structure for a simplified case of the detuning regime is demonstrated in figure 7.16, where the structure is defined by a series of stationary exposures each subsequently offset from the previous one by the period of the interference pattern plus 100nm. As is evident in the figure there is a 'run in' and 'out' period across the width of the writing spot where the exposures of the spot build up. Once the sample has translated beyond the width of the spot the refractive index structure induced in the material is in a steady-state, such that the period of the index modulation is defined by the stepping period of the writing spot exposures. The effect of using the 'incorrect' interference pattern to write the structure is a reduction in the contrast of the induced refractive index perturbation.

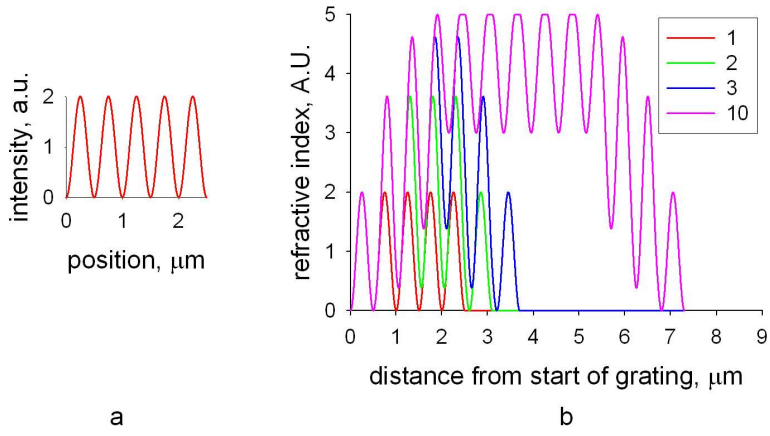

Figure 7.16: Demonstration of refractive index build up through the detuning process, (a) is the intensity of the writing spot, (b) is the resulting index pattern after multiple 100nm detuned exposures.

The contrast of the grating perturbation that is induced is dependent on several factors, most notably the number of grating planes contained within the writing spot, and the magnitude of the difference between the interference period and the duty cycle used to define the

structure. The range of detuning that can be achieved for a particular setup is of particular interest, as it directly defines the flexibility of fabrication process.

From a geometrical consideration an expression for the maximum detuning range for a given writing spot can be obtained. In the fluence matched DGW method, the overall exposure is defined through the total fluence, as the exposure level is balanced through translation velocity and beam power for the applied duty cycle. As such any value of duty cycle can theoretically be used (not 0%). Of interest is the maximum range of detuning possible, requiring the minimum limit of the duty cycle, which can be approximated to the stationary exposure case. The point of refractive index perturbation extinction occurs when the first fringe 'peak' of the n^{th} exposure overlaps with the last minima of the first exposure, i.e. π out of phase as shown in figure 7.17. If the difference between the interference pattern period (Λ) and the stepping period is a constant function(Δ), then the maximum limit of detuning can be expressed as:

$$\Delta = \frac{\Lambda}{N} \qquad [7.1]$$

where N is the number of interference periods contained in the writing spot.

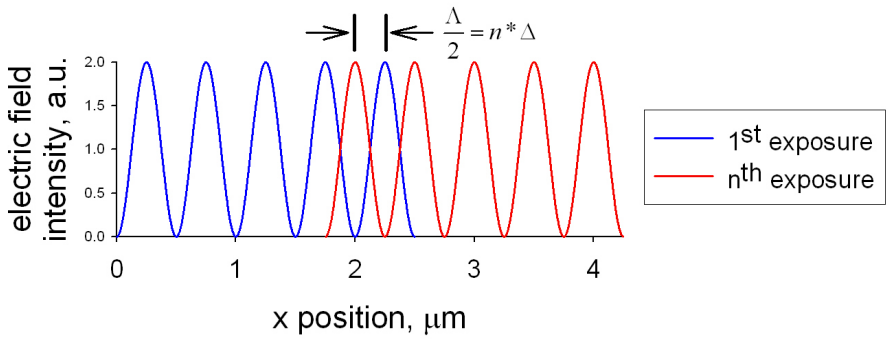

Figure 7.17: Point of null grating contrast in detuning process

As the period of the interference pattern used in the DGW technique is fixed (for a given intersection angle), the maximum detuning span can be expressed in terms of the size of the writing spot as shown in figure 7.18. Thus it is evident that the inversely proportional relationship between the width of the spot and the detuning range severely limits the flexibility of phase mask generated interference patterns. In phase mask implementations, the writing spot is typically at least 100μm wide, limiting the variation in grating period that can be defined to ~5nm. However, in the case of defining the grating period with the same

size spot as used in Direct UV writing (<5μm in diameter), the detuning span is increased to >100nm, a flexibility of ~20% of the period of the interference pattern itself.

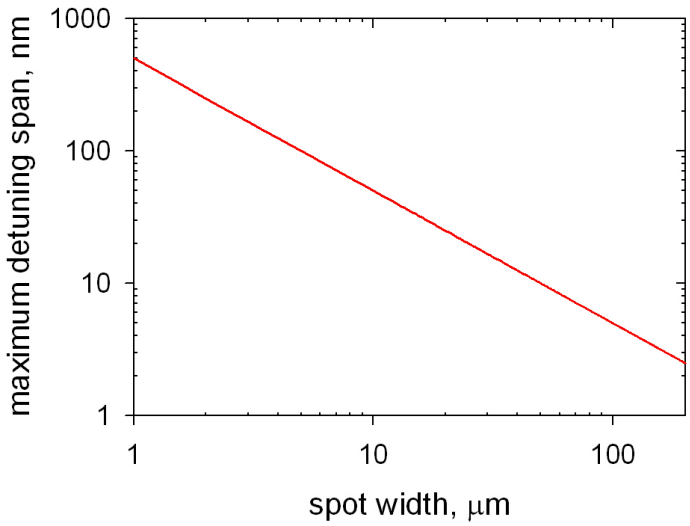

Figure 7.18: Maximum detuning range vs. spot size for a 500nm interference pattern.

Throughout the detuning range the contrast of the grating ranges from 0% to the maximum contrast possible, at the point of zero detuning. In reality the period of the grating structure will, in most cases, be detuned from the native interference pattern, thus not only does the magnitude of the detuning and the duty cycle define the contrast, but the size of the writing spot, the profile of the writing spot, photosensitive response of the material and noise in the system, all contribute to the resulting index contrast. To this end, a simulation was programmed to investigate the contrast of fluence matched channel Bragg grating structures under various conditions.

For the purpose of this simulation the physical variable of the DGW process were considered as diligently as possible. The writing spot is formed by overlapping two coherent laser beams, and as such will have a more complicated profile that the simplified case of figure 7.16 (a). Although the focused beam waists are approximately 3μm in diameter, to account for the slight overlap and mismatch between the beams the writing spot is approximated to a 4μm spot with a cosine envelope function as shown in figure 7.19 (a). The simulation is based on a fluence matched summation for a given duty cycle in a 'blank photosensitive' sample as it is translated relative to the spot. Although relatively crude the

simulation allows for the imposition of various factors including all the relative writing parameters and external effects, such as noise in the phase of the interference pattern and material saturation. One flaw in this process is the assumption of a linear summation of exposure, which ignores threshold effects (section 8.6.4). It is almost certain that both threshold effects and saturation occur, however the model still provides a useful first-order guide to predicted performance.

By using the described simulation with a duty cycle of 50% throughout the detuning span, the contrast of the index perturbation over this range is demonstrated in figure 7.19. The bell shaped behaviour of the grating contrast is as intuitively expected, with the greatest contrast centred at the native interference pattern of the writing spot. The period of the index perturbation is also plotted, and follows the period of the exposures as anticipated.

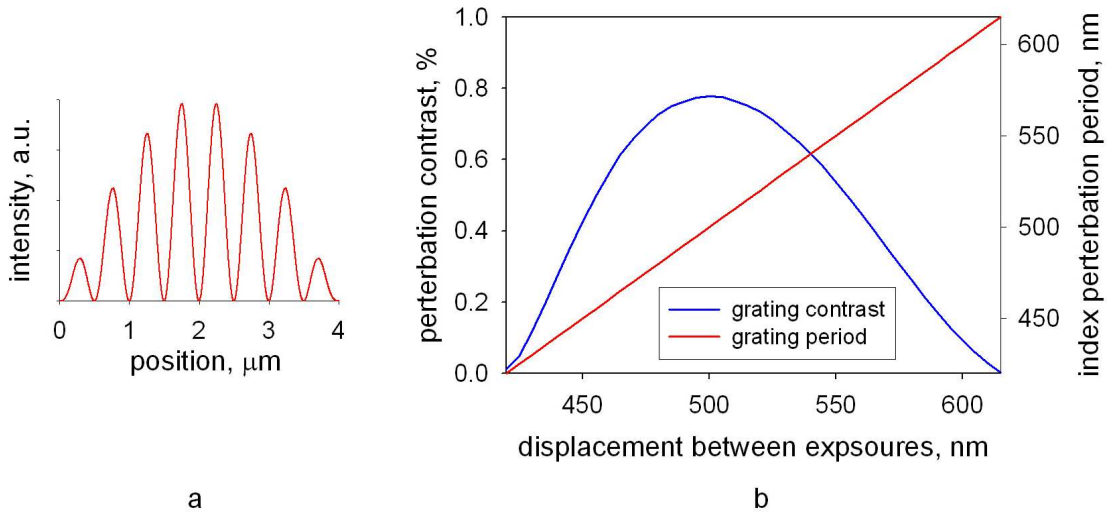

Figure 7.19: Contrast variation during detuning process for 4um writing spot (a) running at 50% duty cycle (b)

One of the issues to be considered with using a writing spot that contains only 8 grating planes is the risk of errors in the writing process. If the phase of the interference pattern is shifted during the process of inscribing the grating this can be translated into a phase shift or error in the grating structure itself. Given the inherent sensitivity to environmental conditions associated with interferometers, it was necessary to investigate the effect and nature of the instability.

A study of the interferometer was performed using the back plate in figure 7.13 using a He-Ne laser with the back reflected beams offset such that an interference pattern could be

imaged on a CCD array (figure 7.20). The spatial position of the interference pattern was monitored over time to establish the long term stability of the arrangement, with the fringe position remaining stable to within 10% over 400s (1 frame every 30s), a duration far greater than any likely grating inscription time. There was a long term drift in average position of 20% over 1000s, ascribed to thermal fluctuations in the setup. However this does not establish any effect from short scale effects of drift. To establish this, the writing process was further simulated with varying degrees of random shift in the absolute position of the interference pattern as the writing progresses. The contrast and the period of a sample grating was subsequently monitored with respect to the magnitude of the constraints on the dithering of the position.

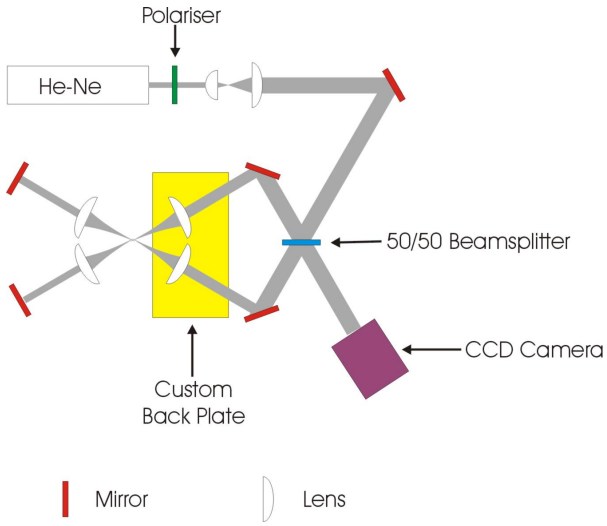

Figure 7.20: Interferometer test rig observing the stability of the interference pattern of the system over long time periods

The results of the turbulence simulation are shown in figure 7.21, and as expected random fluctuations in the phase of the writing spot have minimal effect of the period of the index modulation and only a relatively small effect in the contrast, providing the period of the duty cycle is accurately triggered, which is a fair assumption given the resolution of the Zygo interferometer. This is an artefact of the writing process, after the summation of the total 'high' time for each exposure. It should also be noted that the index structure is not an image of the interference pattern in the writing spot but a composite, with the structure defined by the linear 'lines' of the interference pattern perpendicular to the waveguide creating the index difference.

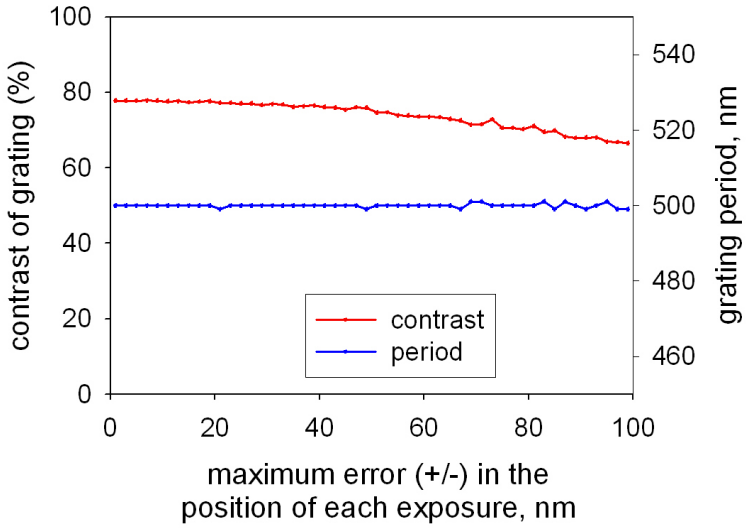

Figure 7.21: Effect of random noise on the phase of the inference pattern on the grating contrast and pattern

From these assessments it is clear that while the interferometer is not optimally stabilised, for a proof-of-principle DGW system it should be sufficiently stable. Subsequent enhancements to the system could include a system for actively locking the interference pattern in place to ensure the phase of the writing spot at all times.

7.6 Summary

In this chapter main elements of Bragg grating fabrication are described. Initially described is the discovery of the Bragg grating along with photosensitivity in 1978, followed by key development stages historical fabrication techniques that ultimately result in the Direct Grating Technique.

The concept of using a variant of Direct UV writing to define both the channel waveguide and the Bragg grating structure at the same time was presented. This technique has all the advantages of the flexible Direct UV writing system; the structures are written in a single fabrication step with no need for subsequent processing whilst adding to it the ability to define Bragg grating structures at the same time. By combining the two structures into the same fabrication step, maximum use of photosensitivity can be employed and the fabrication process is much simpler with no other fabrication steps or alignments.

The various parameters that control the nature of the structures written were explained, and a computer simulation of the DGW process developed. This simulation allowed investigation into the various writing conditions to be used for grating fabrication, providing an insight into the contrast and periods of the grating structures. The theory behind the DGW technique was found to be flexible, and should allow grating contrasts from almost unity to no grating structure at all, i.e. channel structures. It was also determined that the process should be relatively insensitive to small scale instability of the interference pattern, as long the duty cycle modulation is accurately triggered with respect to position within the sample.

Chapter 8:
Basic planar Bragg grating structures via DGW

8.1 Abstract

The results for the first demonstration of simultaneously defined channel waveguide and Bragg grating structures are presented. The structures were written into a range of samples including unloaded in-house fabricated FHD samples, Deuterium loaded and thermally locked samples. The various writing conditions were investigated both for the channel waveguide response and the grating structure response. The unexpected result that lower beam powers for a fixed overall fluence result in stronger channel waveguides and greater grating contrast was observed for both the thermally locked samples and freshly loaded samples.

Control over the grating structure in both the index modulation contrast via the duty cycle and the grating period were both demonstrated. Gratings with null index modulations up to a maximum of 1.5×10^{-3} were demonstrated. Bragg structures with wavelength responses over a span of 488nm, covering the entire O, E, S, C, L and U bands in the ITU spectrum were produced using the computer controlled detuning technique.

8.2 Introduction

Throughout the course of this project a wide range of Direct Grating Writing (DGW) experiments were performed to investigate the process of simultaneous channel and grating definition. In this section the initial results are presented, with the definition of basic Bragg grating structures. The material in this chapter demonstrates the very first simultaneous definition of channel waveguides and gratings, and the response of various samples to the writing conditions.

8.3 Characterisation techniques

The planar Bragg gratings described in this thesis were characterised in terms of modal confinement, NA and spectral response using two experimental arrangements based on visible (HeNe 633nm) and telecoms (1.3-1.7μm) wavelengths. The author implemented both characterisation setups as a fundamental part of this project allowing the development and optimisation of the DGW process.

8.3.1 Visible characterisation

Interrogation of the DGW channel waveguide structures at a wavelength of 633nm provides essential insight into the channel dimensions and strength, and allows more flexible imaging than in infra-red characterization.

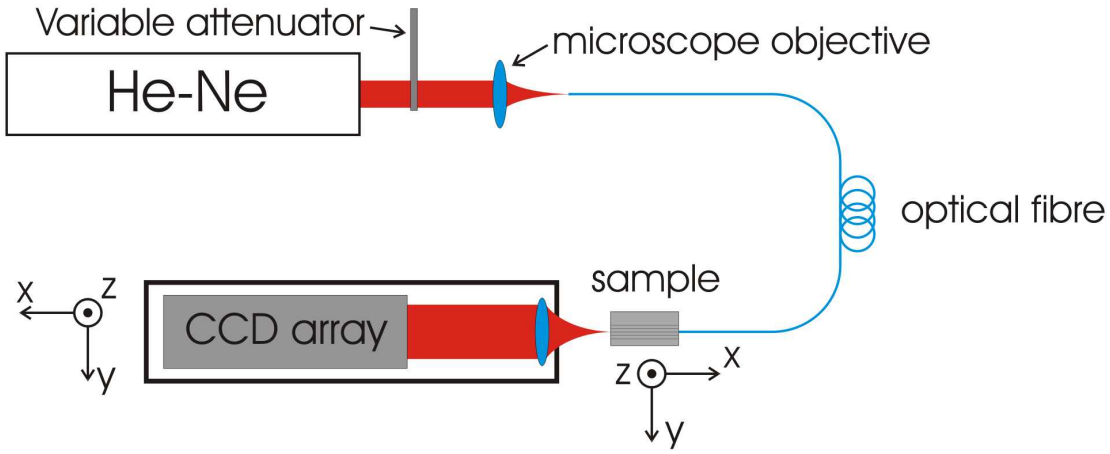

Figure 8.1: 633nm characterisation setup for imaging near- and far-field modal intensities.

The experimental arrangement used for measuring the NA and modal characteristics of the devices is based on a frequency stabilised He-Ne laser (632.8nm). Power regulation of the laser is via a manual variable intensity attenuator before launch into optical fibre. Selection of the correct fibre depends on the exact use of the setup and the strength of the waveguide (see later), typical choices being single mode 633nm or SMF28. The fibre is then facet-coupled into the channel (or slab) waveguide with the launch position monitored through use of an overhead camera allowing accurate discrimination between channels. The special feature of the characterisation setup in figure 8.1 is the characterisation camera. The

imaging lens and the CCD array are securely fixed onto a single mounting system that has translation in all three primary axes, with the displacement between the two components fixed. Focussing of the image is via translation of the entire camera system, thus the magnification for any given lens is constant if the image is focussed regardless of any alignment translation relative to the sample. Prior calibration of the CCD pixel size for each imaging lens (microscope objectives for repeatable mounting) allows rapid, accurate dimensioning of the images captured. The CCD array is part of a digital camera system, which unlike most video systems undergoes no digital-analogue-digital conversion; the data is continuously handled as 12-bit integers with a resolution of 500 x 290 pixels. Custom software converts the output data into formatted, scaled tables for analysis or direct input into graphing programs.

This HeNe based system is used to measure both near-field mode profiles and the far-field mode profile. To capture the far-field intensity distribution of a mode, the translation stage is fitted with a digital micrometer (resolution ~5μm), that when zeroed with the camera image focused onto the output facet of the waveguide allows accurate determination of the distance between the image plane and the output of the waveguide. The signal incident on the CCD array will be dominated by the light at the imaging plane of the system, thus allowing the rapid mapping of the far field intensity. By applying this information to the analogous technique for the measurement of fibre numerical aperature (NA) (Ghatak and Thyagarajan 2000) an approximation for the channel NA can be obtained. The NA can be approximated as the sine of the half angle between the 5% intensity points of the field intensity distribution. The distance between the output facet and the image plane (d) must be significantly greater than the ratio;

$$\frac{d^2}{\lambda} \qquad [8.1]$$

for operation in the far field. As these measurements are notoriously noisy the use of the high precision translation stages allow multiple measurements to be taken at varying distances and the output cone plotted. From a best-fit line an average NA can be obtained.

Care must be taken with this technique as the method is very dependent on the overfilling of the launch, the stripping of modes that cannot propagate, and the index structure of the channel. Particularly critical is the short propagation length involved in most of the

structures as, unlike fibre analysis with interaction lengths >2m, planar channels are typically of the length ≤3cm.

8.3.2 Infra-red characterisation

The planar Bragg grating structures produced during this project were primarily designed for operation around 1.5μm. To characterise these structures, an independent setup was developed to allow waveguide imaging along with spectral analysis of the Bragg gratings (figure 8.2). The IR sources available for this setup include an EDFA based ASE source and a LED based broadband source (low power) with an output spectrum ~1.3-1.7μm. When using the ASE source there is sufficient incident power to use a 3dB coupler as a signal splitter and monitor any back-reflected spectra from the channel waveguide. The output of either source can be polarised using a fibre polarizer, with the final orientation aligned relative to the TE or TM states using a manual polarisation controller.

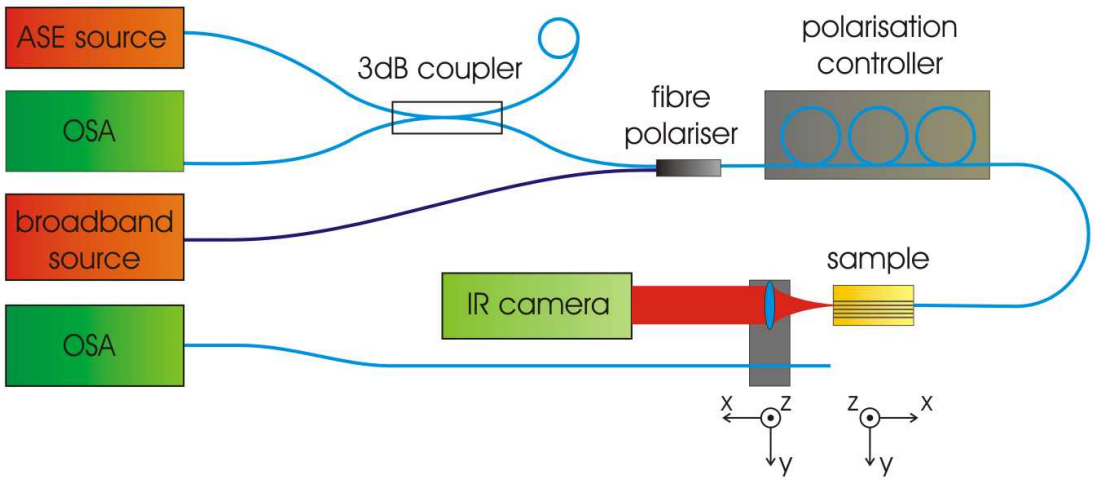

Figure 8.2: IR/grating characterisation setup. The source can be switched between a wide band LED source or high power ASE source. The channel waveguide output can be imaged onto a IR camera or fibre coupled to an optical spectrum analyser

Flat cleaved facet launching is used to couple light into the waveguide structures, with index matching fluid suppressing any air-silica reflections. The position of each channel/fibre is monitored through use of an overhead camera allowing rapid channel discrimination. The sample position is translated via a 3-dimensional piezo translation stage with ~10mm coarse travel and ~0.2μm fine resolution. The output stage is a matched type, with the option of mounting a microscope objective to image the output facet onto an IR camera or couple the

light into a fibre for analysis via an optical spectrum analyser. Due to the size of the IR camera, it is not possible to mount the imaging lens at fixed distance, so relative pixel size must be recalibrated for each sample alignment. The signal from the camera is captured using an analogue card before conversion using a second custom programme allowing the pixel calibration to be set before outputting the data as an ACSII table.

This versatile setup was created to facilitate the imaging of the waveguide mode, interrogation of planar Bragg grating reflection/transmission, and also analysis of broadband waveguide behaviour. All samples were flat polished before characterisation (often before writing) but due to the relative simplicity of facet coupling, extinction ratios of ~30dB are repeatable but this does allow for rapid characterisation of each sample.

8.4 Every journey starts with a step…

The first samples to be used for Direct Grating Writing were produced within the ORC using the custom built flame hydrolysis deposition (FHD) system developed (section 5.51). In previous Direct UV writing experiments strong photosensitive responses in excess of 10^{-2} were observed in these samples (Watts 2002) providing a good basis for the fabrication of planar Bragg grating structures.

The samples used in this experiment were three layer, silica-on-silicon samples with a under/over cladding index of 1.47 and a core index of 1.48. The core thickness was 5μm and photosensitivity was introduced by co-doping with Phosphorus, Boron and Germanium (approximately 2%). The cladding layers also contained the same three co-dopants, although much lower levels of Germanium (~0.8%) were used to minimise photosensitivity in the cladding layers. To replicate the writing conditions of the prior Direct UV writing channel definition experiments, the sample was Deuterium loaded at 150bar and the same fluence were used in the DGW attempt.

Initial investigation of the sample revealed clear channel waveguide structures, but no grating structure with a response in the wavelength range of the ASE source used to interrogate the structure. There was some suspicion as to the exact nature of the index change induced in these structures with the possible belief that a strong thermal process

could induce large average index difference but limit the ability of the writing process to create small scale grating structure. Thus, the experiment was repeated with the same sample but without the pre-sensitisation of Deuterium loading.

8.4.1 …and many index steps make a grating

A second set of simultaneous channel and grating writing was performed using the sample's intrinsic photosensitivity, avoiding any risk of saturation effects. In these experiments the writing spot had a 6μm diameter to ensure overlap between the two beams, a duty cycle of 25% and grating period of 531nm were applied. Under these conditions a simultaneous channel and grating structure was formed in the material, yielding the reflection response illustrated in figure 8.3.

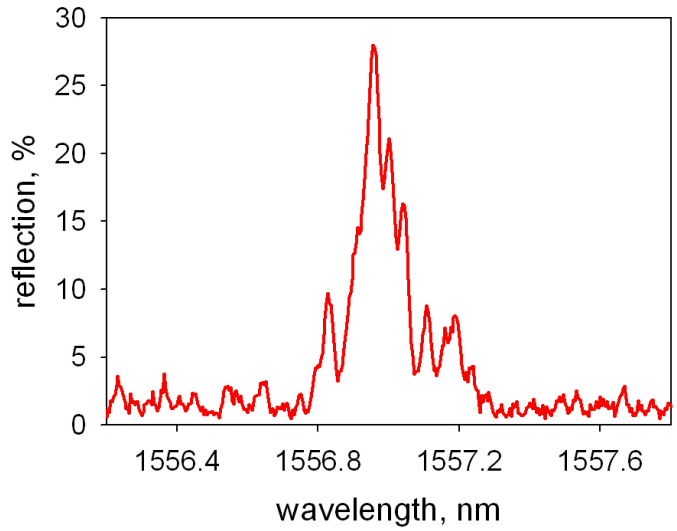

Figure 8.3: Reflection spectra from the first demonstration of simultaneous definition of channel and Bragg grating using the DGW technique

For the non-Deuterium loaded FHD samples the channel strength was significantly weaker than the loaded samples due to the lack of photosensitisation, however they were sufficiently strong to guide a mode and allow the coupling between the incident and reflected wave. The simultaneously written channel waveguide and Bragg structure was 14mm long, with a reflectivity of ~28% and bandwidth of 0.132nm. The grating strength is relatively weak, due to a combination of the low contrast of the grating from the small index change and the poor modal confinement of the guided mode to the channel region. This is because the grating structure is primarily confined to the channel waveguide, poor

confinement results in the smaller modal overlap with the grating structure, and thus the coupling strength reduced.

In further experiments the grating writing process was repeated, to produce several grating structures of the same length, the same waveguide strength but different grating periods using the *centre wavelength detuning* technique (section 7.5.1) producing a range of graphs with differing periods, the peak responses of which are demonstrated in figure 8.4. Through interrogation of the grating structures with both TE and TM polarisation, the combined birefringence of the channel and grating structure can be revealed. Fitting a linear function to the grating period vs. Bragg wavelength provides a value for the effective index for the guided mode, giving 1.46597 and 1.46594 for the TE and TM polarisations respectively. The difference between these two values gives the birefringence of the structure to be $3x10^{-5}$, a low value ascribed to the intense thermal cycle involved in the sample processing.

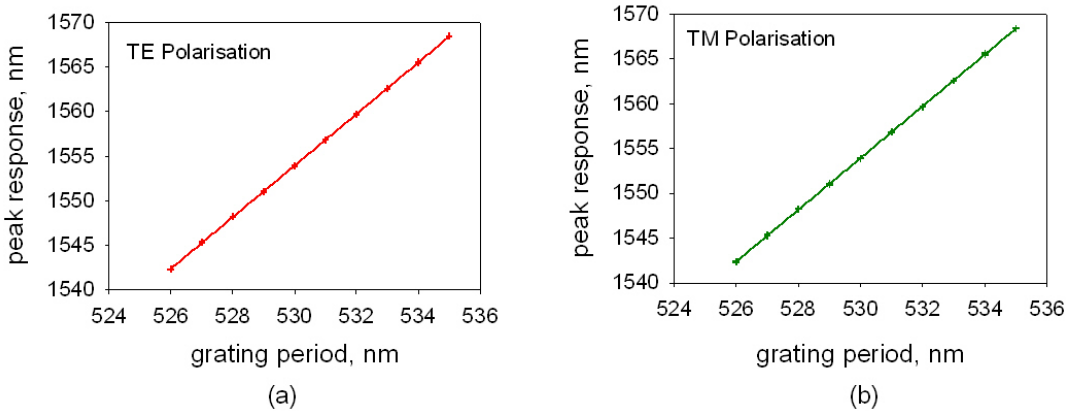

Figure 8.4: Demonstration of Bragg wavelength against grating period, with the period defined using centre wavelength detuning. (a) TE polarised, (b) TM polarised.

Of particular interest in the processing of these structures is the response of the material with respect to fluence, and interrogation of the Bragg wavelength for a known grating period, hence the effective index is a very accurate technique to monitor the change in a material with irradiation. A range of channels, each grating spanning the sample length and period of 532nm were written with a range of fluences spanning 0.7kJcm^{-2} to 6kJcm^{-2} (figure 8.5).

For the graph it is apparent that as the UV writing fluence increases, the index increase of the material is not a simple linear increase, but instead rapidly reaches a saturation level at

~2kJcm^{-2}. This is not entirely surprising given the un-loaded nature of the sample, it is not unreasonable to expect a limiting effect of the lower number of Germanium Oxygen Deficiency Centres (GODC's) very rapidly. At powers greater than the total limiting point there are no more defect centres to trigger and there is not enough absorption in the material to trigger a thermal index change.

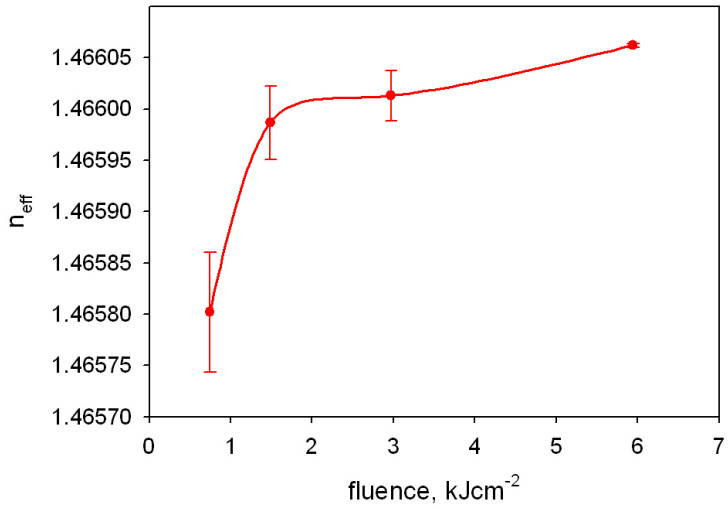

Figure 8.5: Effective index of the guided mode with respect to writing fluence

In general, the use of samples from the in-house FHD facility, while demonstrating the concept of DGW as a functioning process, are not ideally suited for the development of the system. This is because the FHD equipment is essentially designed as a prototyping facility, allowing customisation or modification of the deposition at various points in the process, and as such is not suitable for production runs of identical samples. As such, further development work was undertaken using commercially available 3-layer silica-on-silicon wafers designed for use with etched planar waveguides provided by Alcatel Optronics UK.

8.4.2 Commercial samples

Given that the above grating and channel structures were not written in conditions that typify Direct UV writing, and as such were weak structures, the same experiments were performed using the commercial quality samples provided by Alcatel. The samples had core and cladding layers designed for reactive ion etching, as such are relatively standard composition. In these substrates the core layer was doped with Germanium to increase the

index of the layer and provide the host sites for the photosensitive reaction. Each sample was photosensitised through Deuterium loading at 130bar for a week before *thermally locking* (Riziotis, Fu et al. 2001). Thermal locking is a photosensitivity stabilising technique whereby the generation of the UV absorbing defects in the glass is triggered by the bulk heating of the sample. Once locked, the photosensitivity enhancement, although reduced, has a lifetime measured in years (see chapter 2). The thermal locking process used for these samples was 1400°C for 5s, a value from initial research at the ORC known to provide substantial enhancement compared to an unloaded sample.

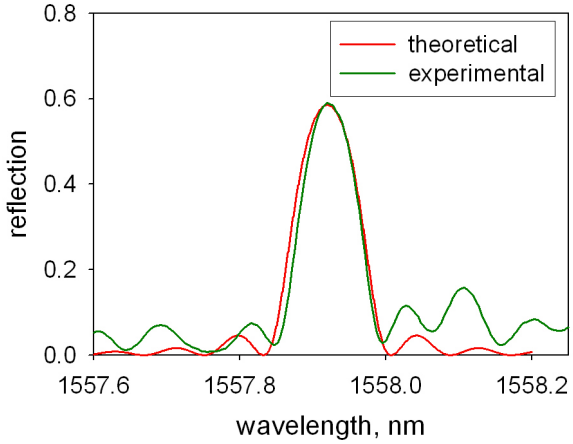

Figure 8.6: Reflection spectra for a 10mm long grating in a thermally locked commercial wafer. Green – experimental data, Red – Simulation for an index perturbation $5x10^{-5}$.

A typical spectra from the thermally locked samples is shown in figure 8.6, where the green trace corresponds to the measured data and the red trace to a theoretical response for a 10mm long grating with an index perturbation of $5x10^{-5}$. The correlation between the two traces is quite good, especially as there is no compensation for the ASE source profile. As is evident from the graph, the grating response is cleaner and stronger in the commercial quality wafers compared to our own FHD samples, clearly indicating the viability of this process for various photosensitive samples.

A similar analysis of the Bragg response vs. grating period yields the same information about the sample wafer as that measured for our own FHD substrates, a result shown in figure 8.7. Fitting the best fit line through the data points yielded an effective index of 1.45645 (TE) and a birefringence of $4x10^{-5}$. Note that the reflection wavelength of the gratings written using this technique span the entire C-band of the telecommunication window, with no need to alter the experimental configuration of the system.

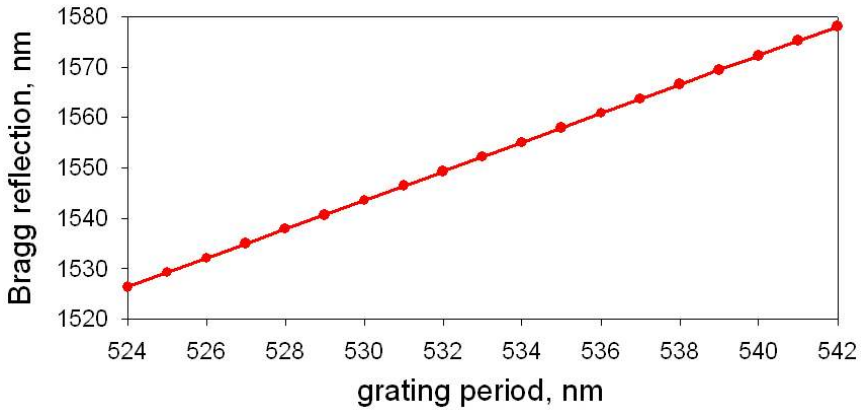

Figure 8.7: Bragg reflection vs. grating period, spanning the entire 'C-band' with all the gratings fabricated using the same fixed intersection angle between the laser beams for a thermally locked sample.

On a similar sample the peak grating reflected strength was monitored vs. the length of the grating structure. Arrays of channel waveguides were written containing grating sections of various lengths and each reflection spectra analysed once writing was complete. The reflected strength measurement is very sensitive to damage or contamination on the end facets, however it does approximately follow the $\tanh^2$ function (equation 6.16) as expected. Fitting the equation relating the reflection strength to grating length yields a grating index modulation of 4.9×10^{-5}, a result in good agreement with the value estimated from figure 8.6.

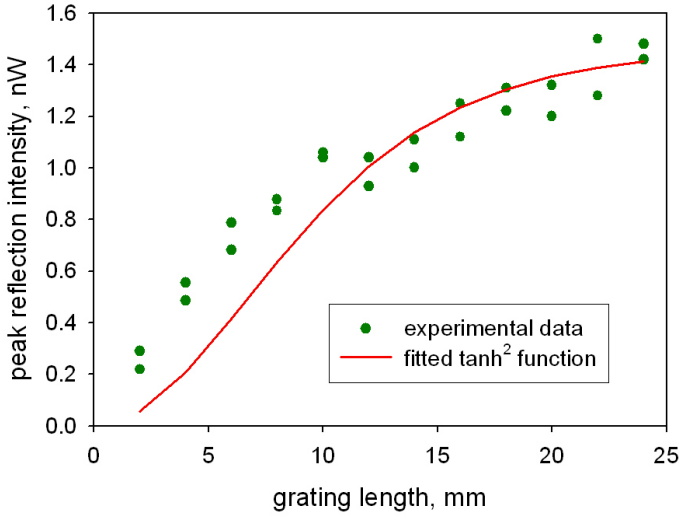

Figure 8.8: Variation of peak Bragg reflection strength vs. grating length. Green spots - experimental data, Red line - fitted $\tanh^2$ curve.

8.5 Optimisation for thermally locked samples

So far, the DGW results described in this chapter were the first proof-of-principle of this new grating fabrication technique. However, the writing conditions chosen were selected through the results of traditional Direct UV writing known to produce guiding channels. However, one of the difficulties with UV induced structures, in particular buried structures, is an intrinsic inability to fully characterise the refractive index properties of the resultant channel waveguide. The width of the channel is often not the same as that of the writing spot, it is often dependent on the mechanism of the index change and other properties of the material (absorption, melting point etc.). In addition, the channel waveguide cannot be prism coupled into due to the over-clad, and comparisons cannot be drawn with identical 2-layer structures that have been processed with the same conditions, as the presence of the over-clad has been shown to significantly influence the writing process (Watts 2002).

While the mode profile of such a buried waveguide structure can reliably be imaged, the resulting mode size is a function of both the channel strength and size, the absolute values of which are both unknown. The far-field mode profile is often used to approximate the numerical aperture of the waveguide, and then the NA related to the index change. Care must be taken when using this technique however, as the 5% far field distribution is merely an estimate of the NA of a structure and its relation to index change makes several assumptions, including a step-index profile of the waveguide. In UV induced waveguides the index profile is not a step given the Gaussian nature of the beam, and as such the NA makes a useful comparison to the relative strength of a waveguide but absolute values cannot be rigorously extracted.

By contrast, the analysis of the response of an internal grating structure is a very accurate and simple technique for investigation of both the channel and grating properties. This technique has been applied to waveguides created by a traditional two step process, increasing fabrication time and introducing the possibility of changing the structure investigated (Faerch and Svalgaard 2002).

From these first results it was apparent that the 6μm diameter writing spots result in wide mode structures, thus the focusing lenses were replaced with lenses focusing down to a

beam waist diameter of approximately 3μm. Using the smaller writing spot a range of writing conditions were applied to investigate the relationship between total fluence, beam power and translation velocity on the simultaneously written channel and grating structures. The writing velocity spanned from 15mm/min to 480mm/min with beam powers of 80, 40 and 20mW, of fixed length 25mm and a duty cycle of 25%.

Upon inspecting the results it is clear that the full UV writing procedure is not entirely explained through the concept of overall fluence (exposure). The channel structures written using a lower beam power and lower translation velocity demonstrate behaviour associated with stronger guides than those written with greater beam powers but the same fluence. The mode profile was asymmetric for all channels, but structures written with lower beam powers demonstrated greater confinement of the light. A typical thermally locked mode profile is presented in figure 8.9.

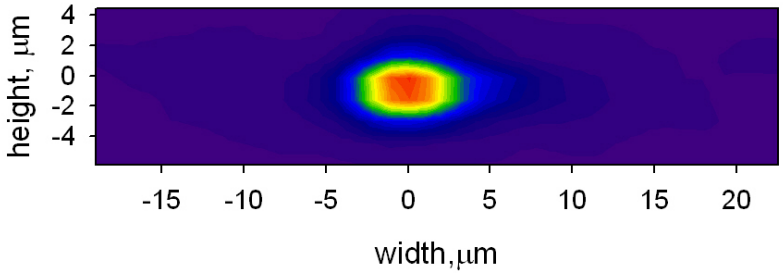

Figure 8.9: Mode profile in a thermal locked sample.

The variation of NA with fluence is plotted in figure 8.10. Only the weakest and strongest channel for each beam power is plotted due to the relative insensitivity of the technique. Each data point shown takes the average value from two channels written under identical conditions, with each NA value taken in the procedure described in section 8.3.1, and as such represents the best fit to the far-field mode distribution at 7 distances.

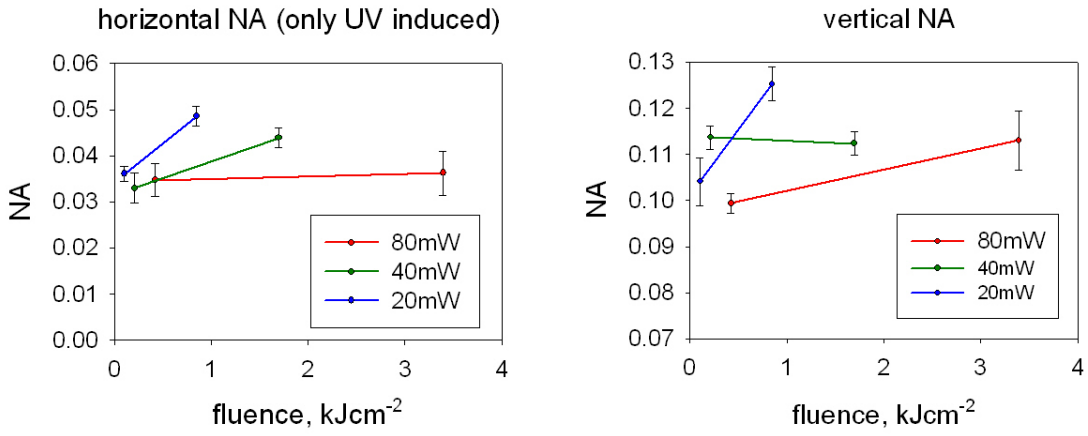

Figure 8.10: Channel NA vs. writing conditions for channel structures. Note the lower beam power for the same exposure results in greater index change. The horizontal NA is dependent only on the index change while the vertical is dominated by the slab index structure.

The NA data given in figure 8.10 correlates to the effect found from the mode profiles, and demonstrates that the greater index change arises from slower translation with a weaker beam power. This effect is not expected when compared to index changes in pulsed laser systems where the index difference is more dependent on peak beam power than translation speed. However the NA is noisy and can be corrupted by damage or contamination to the end facets of the sample.

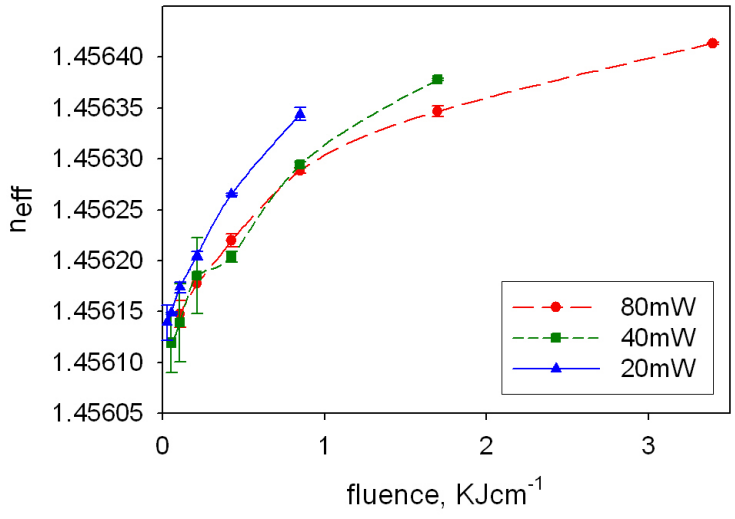

Figure 8.11: Effective index of thermally locked channel structure vs. UV writing conditions.

Interrogation of the grating structures confirms the UV exposure trend indicated by the NA measurements. As the reflected signal is dependent only on the Bragg condition in the

grating region it is not affected by launch errors. The variation of effective index with writing power is plotted in figure 8.11. From the graph it is evident the effective index of the channel is greater for structures written with the same fluence if the translation is slower. Here, the data is far less susceptible to launch conditions than that of the NA technique and clearly indicates that the maximum refractive index increase occurs at the maximum fluence, a result in contrast to figure 8.10. If the NA data is extrapolated to maximum index change, then values of $4x10^{-5}$, $2.9x10^{-4}$ and $3.6x10^{-4}$ were obtained for 80, 40 and 20mW respectively. From the grating data, changes in the effective index of 3.1, 2.5 and $1.4x10^{-4}$ were observed. Interestingly, observing the strength of the grating from the maximum intensity of the Bragg reflection also indicates how the strength of the grating structures vary with UV writing conditions (figure 8.12).

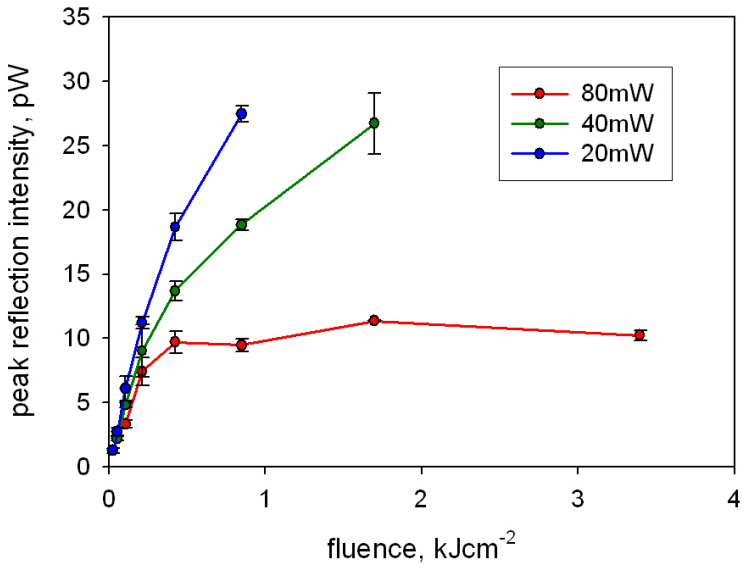

Figure 8.12: Bragg reflection strength vs. fluence for different writing conditions. All gratings have the same length and period.

From the graph it is clear that the intensity of the grating response varies significantly, implying a variation in the contrast of the grating structures with changing writing conditions. Of particular note is the apparent saturation of the reflection strength for the 80mW channels at fluences greater than $0.6kJcm^{-2}$. The maximum grating contrast for the beam powers extrapolated from the bandwidth of the gratings and is displayed in table 8.1. The structures written using 80mW peak beam power, although demonstrating the greatest effective index increase, clearly have the weakest grating structure, correlating with the saturation of grating reflection strength in figure 8.12. The gratings written with lower

beam powers undergo no such saturation, with similar grating contrasts. It is believed that the small grating contrast increase for gratings written with 40mW relative to those written at 20mW is due to the slightly larger index change from the higher fluence (figure 8.11) providing slightly better confinement to the index perturbation. This grating saturation is an interesting effect, possibly caused through thermal limiting of the type I effect (chapter 2), sensitivity to scattered UV light within the waveguide bleaching out the index modulation or a slow thermal effect allowing the combination of multiple processes.

Beam power, mW	Fluence, $kJcm^{-2}$	Δn
80	1.7	$2.26\pm0.04 \times 10^{-4}$
40	0.8	$3.23\pm0.03 \times 10^{-4}$
20	0.4	$3.01\pm0.02 \times 10^{-4}$

Table 8.1: Maximum obtained values of grating index perturbation with different writing conditions.

This data clearly indicates that the optimum processing conditions of these samples do not include high beam powers, rather lower beam powers and slower translation velocity. In reality there is a trade off between the low beam power and the associated extended fabrication time associated with that, for similar changes in effective index. For the sample in figure 8.12, 25mm long with translation speeds spanning between $0.25mms^{-1}$ and $8mms^{-1}$ corresponds to writing times 100s and 3.1s respectively. Clearly, it is not feasible to produce long structures using the slowest translation speed, so a compromise between fabrication time and grating quality has to be made. However, there is no doubt that the unique insight provided through the incorporation of Bragg grating structures into channel waveguides offers new and enhanced understanding of the Direct UV writing process.

8.6 Deuterium loaded vs. thermally locked

8.6.1 Deuterium mobility

As a technique for prolonging photosensitivity thermal locking is relatively unrefined, it has been shown to enhance the intrinsic photosensitivity of Germanium doped silica but the technique is as yet un-optimised for maximum photosensitivity response for minimum

material effect. It is well known that for freshly loaded samples, Deuterium or Hydrogen loading significantly enhances the photosensitive response of a material, with defect formation only in the UV exposed regions. After writing any unexposed regions the sensitizer out-diffuses leaving the host material unchanged. While in optical fibres the mobility of the photosenitiser is not a drawback, and concentrations within the core remain approximately constant through the writing period. Due to the 'thin' over-cladding in planar samples the mobility of Hydrogen is a significant disadvantage, with appreciable out-diffusion occurring within timescales typically associated with the UV writing. To investigate this effect a range of gratings were written with the same writing conditions but over 2 hrs after Deuterium loading at room temperature (figure 8.13).

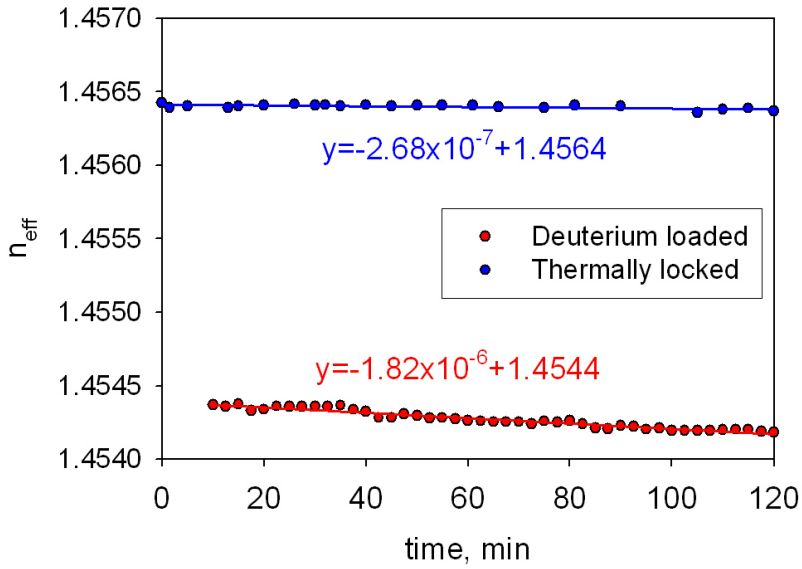

Figure 8.13: Effect of Deuterium out-diffusion on effective index of channel strength.

From the diagram it is clear that the Deuterium is mobile enough to modify the UV absorbing defect density as time increases. There are several interesting points about this result, most notably the reduction of n_{eff} with time for the thermally locked samples (an order of magnitude less than that of the unlocked samples) can be attributed to a drop in the output power of the laser throughout the duration of the experiment, while no such drift was observed during the unlocked experiment. The samples were not written immediately upon removal from the Deuterium cell, for safety considerations sample removal was at a remote location to the writing set-up. With time an obvious critical factor to the final DGW parameters, to minimise out-diffusion before the writing time the samples are stored in

liquid nitrogen (chapter 2). The data for the loaded samples starts 10 minutes after removal from storage, representing the alignment time required to ensure the writing beams are over lapping in the core of the sample. There is no such delay associated with the locked sample as there are no special storage conditions after thermal locking due to the stable nature of the photosensitivity.

8.6.2 Sample alignment and threshold

One of the significant differences between the behaviour of the locked and unlocked samples is observed during the alignment process. As the thermal locking is believed to promote the generation of UV absorbing defects before exposure to the UV radiation, the observed fluorescence is immediate, and at low irradiation levels remains constant over time (high exposures deplete the photosensitivity, resulting in a diminishing of the intensity of the fluorescence). This fluorescence exhibits no threshold effect, with the intensity scaling with the exposure power. This is in direct contrast to the freshly Deuterium loaded samples which exhibit threshold and exposure time dependent effects. Powers below threshold (powers that produce clear fluorescence in locked samples) have no visible effects on the sample. Powers on the cusp of the threshold have a time dependent response - initially there is no fluorescent response, then after approximately 2s there is a diffuse glow before coalescing into a focused fluorescent response in less than half a second. This observation provides interesting insight into the difference between the two types of material processing (figure 8.14). In discussions with other research groups using UV writing technique (Svalgaard 2003) a threshold effect has been observed in the writing conditions and is proposed to be the result of a cascade absorption from the creation of extra defects. Initially there is little absorption of the UV power, creating low levels of defects, then the defects created during the exposure increase the absorption of the laser, in-turn allowing more power to be coupled into the material structure. As such, once there is enough power to create the initial defects, the time for the saturation of defect creation results from the overall exposure fluence. Although not observed in this manner before, this corresponds well with threshold effects in the writing powers used to define channel waveguides by this author and others.

(a) (b)

Figure 8.14: Imaging of writing spot, (a) full writing power in freshly Deuterium loaded sample, (b) low power spot in thermally locked sample

Figure 8.15 illustrates the effect of the threshold when defining channel structures. For these structures, the fluence used to define the channels was on the cusp of threshold, thus initially the writing conditions are not quite enough to trigger the cascade effect. Throughout the writing process the energy of the laser is transferred into thermal energy around the writing spot, and as the sample is translated the temperature increase in the direction of motion from prior exposure is added to the energy from the UV irradiation. Once sufficient thermal energy is present, the cascade absorption is triggered causing a discrete step in the waveguide strength.

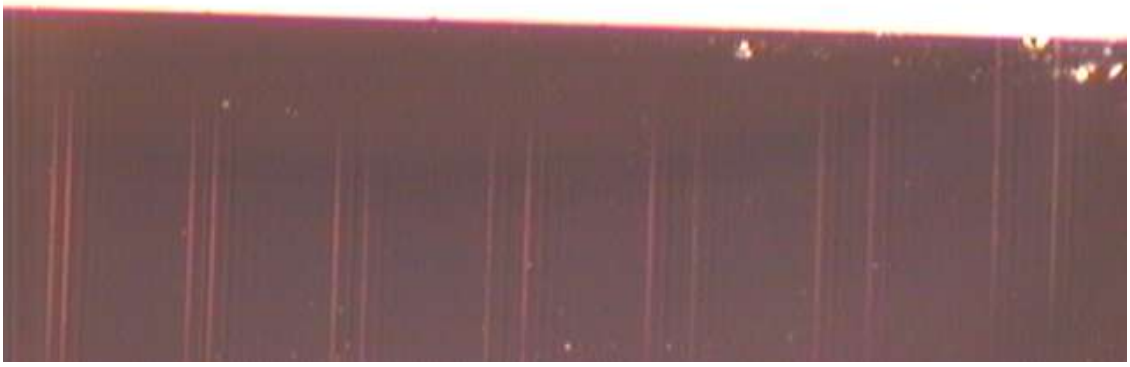

Figure 8.15: View of channel structures written on the cusp of threshold. The channel definition process does not occur until sufficient energy triggers the cascade absorption of the energy resulting in a discrete step in the strength of the waveguide.

8.6.3 Strength of channel waveguides

As indicated in figure 8.13, there is a significant difference in the effective index of channel waveguide structures written with the same UV conditions but different photosensitivity enhancement processes. In contrast to the effective index data, channel waveguides in thermally processed samples are not visible from overhead imaging, whilst those written

into freshly loaded samples are clearly visible. This implies that the channels in the freshly loaded samples have a greater, or better defined index difference in the channel structure.

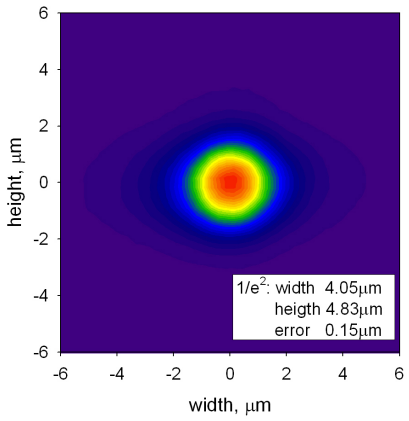

Figure 8.16: 633nm mode profile (single mode launch) of freshly Deuterium loaded sample.

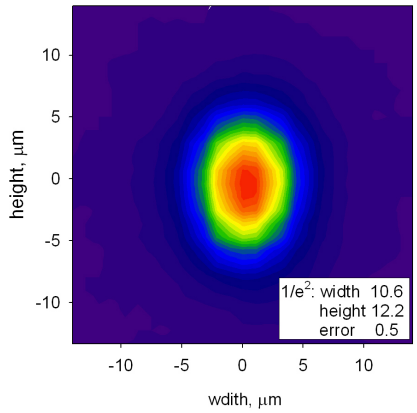

Figure 8.17: 1.55um mode profile of freshly Deuterium loaded channel waveguide

Comparison of the near field guide mode profile confirms the visual analysis (figure 8.16 and 8.17).The vertical NA@633nm is ~0.17±0.015, and the horizontal is ~0.18±0.04. Although the NA measurement is prone to noise with waveguides of this strength, it does however, give an indication of the strength of the waveguides in both the horizontal and vertical profile.

It is known that the rapid thermal cycling involved in the thermal locking process changes the index of the over-clad layer on the samples. Through critical-angle prism coupling data the over-clad refractive index is 1.4605±0.0002 and after the thermal locking process is 1.4564±0.0002 thus clearly significantly changing the index profile of the structure.

8.6.4 Un-locked writing conditions

From the results already described in this chapter it is apparent that similar silica-on-silicon samples demonstrate radically different responses to Direct UV writing dependent on the processing history of the sample. Thus in order to optimise the DGW process for the strong channel structures it is necessary to again investigate the response of the sample to the UV writing conditions, in particular to the dependence on beam power.

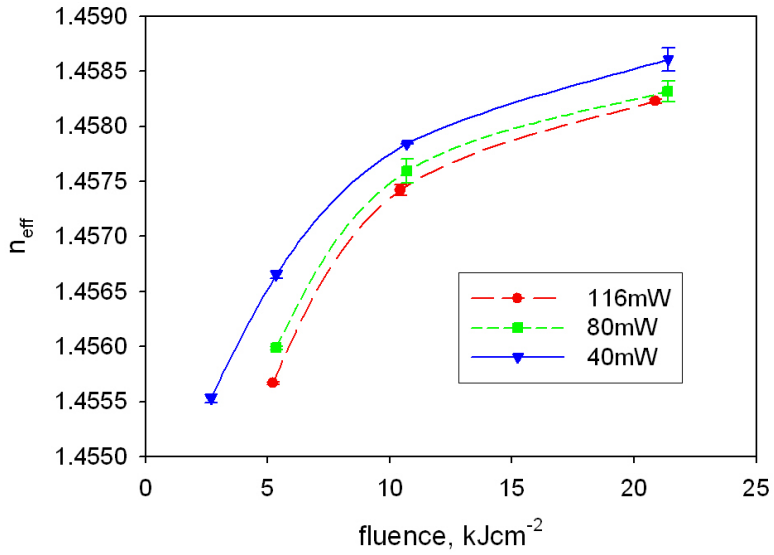

Figure 8.18: Effective index vs. writing conditions for a freshly Deuterium loaded sample.

As a general rule, the writing conditions for the freshly loaded samples are significantly different to those used for the thermally locked samples. For example, the exposure levels that result in a plateau of the index change in the thermally locked samples are below the threshold effect in the unlocked samples. Below this threshold there are no discernable waveguides written into the unlocked samples, providing anecdotal evidence to suggest that the thermal locking promotes the generation of defects equivalent of a fluence of at least 3kJcm^{-2}. From figure 8.18 it is evident that the same trend of the balance between beam power and translation velocity is displayed by the freshly loaded samples, where lower beam powers result in stronger changes in refractive index for a given fluence. However, unlike the locked samples there is no dramatic saturation effect for any of the beam powers, and instead they all tend towards the same index change. The relationship between slower translation speeds and stronger refractive index change is reflected in the threshold effect, with a 40mW beam power defining channels at lower fluences where greater beam powers fell under the threshold level failing to form channel waveguides.

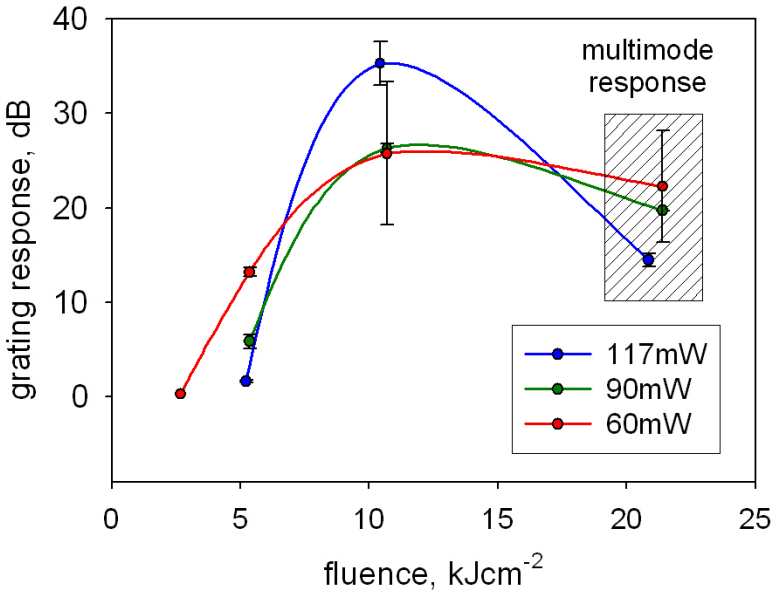

Figure 8.19: Grating response vs. writing conditions. Note that for higher fluences multimode response was observed from the grating structure

The strength of the grating response appears to follow the same general trend as the refractive index increase. However, the data is confused by the waveguide becoming multimode at the higher writing fluences (shaded box figure 8.19, example spectra figure 8.20). This is a clear indication of the strength of the refractive index change although this effect is dominated by the existing slab waveguide structure within the sample, with the vertical refractive index difference always greater than that of the horizontal (only UV induced) index difference.

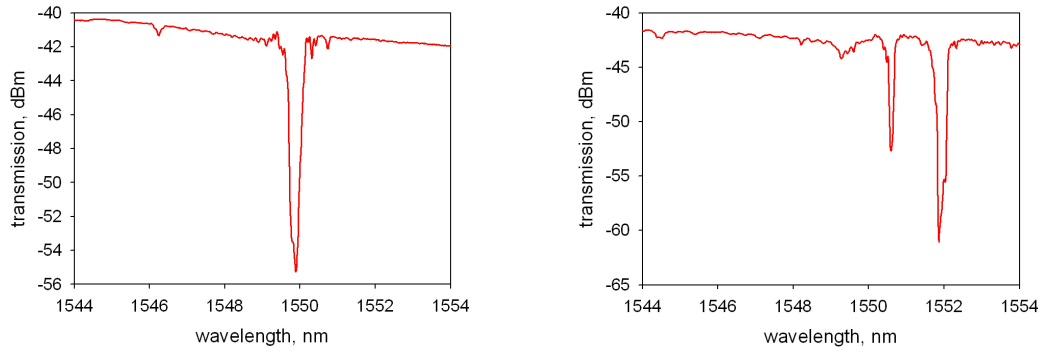

(a) (b)

Figure 8.20: Transmission spectra from two gratings written with 60mW beam power, (a) fluence of 5kJcm^{-2} and (b) fluence of 21kJcm^{-2} demonstrating multi-mode response.

In conditions with strong coupling between the forward and backward propagating modes, significant cladding modes can occur. The spectral structure of the cladding modes arise as a combination of the vertical and horizontal states, due to the finite thickness of the over-cladding structure there are discrete cladding modes, while the effect of the horizontal slab waveguide structure permits a continuum of spectral responses.

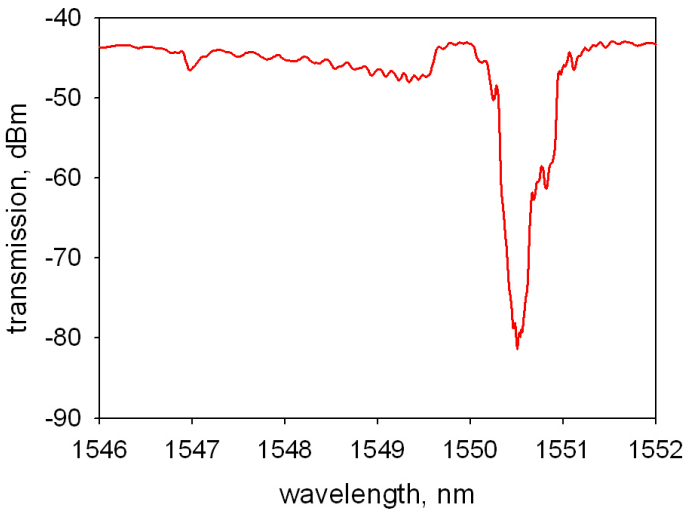

Figure 8.21: Spectral response from a strong planar grating in an unlocked Deuterium loaded sample (117mW, 10kJcm^{-2}) with associated cladding mode structure

Due to the strong channel and grating responses that can readily be achieved using Deuterium loading and cryo-storage, the experiments following in this thesis were all performed using the technique. Thermal locking is a promising technique for future development of time independent photosensitivity enhanced samples, however the required optimisation is a task beyond the scope of the work described in this thesis. In addition it should be noted the following experiments were all performed using Hydrogen loading, and not Deuterium. The use of Deuterium to increase photosensitivity has been demonstrated, but for economy during the development of this technique Hydrogen is far more attractive.

8.7 Grating strength vs. duty cycle

Section 7.6 describes the control of the Direct Grating Writing process through the duty cycle of the writing beam. A duty cycle of 100% results in the writing beam continually on through translation. As expected, the continual exposure through the translation averages out the interference pattern resulting in a channel waveguide structure with no index

perturbation. Such structures do not exhibit any modal coupling, and demonstrate the same spectral response as a structure written with a conventional Direct UV setup.

In order to incorporate channel waveguides and Bragg grating structures simultaneously, modulation of the writing spot is used to define the grating structure. To ensure the interference pattern is the element defining the index modulation and not just the on/off modulation of the writing spot, channels were written using a single beam to generate a writing spot without an interference pattern. During this single-beam experiment, the same writing conditions and modulation conditions were used to define the structure as would normally be used to create a Bragg grating and resulted in no spectral grating response.

The effect of duty cycle on the grating bandwidth is demonstrated in figure 8.22. All the channels were written with a fluence of 9.7kJcm^{-2}, with a grating period of 531.8nm, and a length of 8mm. From grating to grating the duty cycle was varied from 10% to 90% with the effective index varying over 4x10^{-5} over the duration of the experiment. The experiment was arranged such that the effect of the Hydrogen out-diffusing was approximately compensated by the increase in writing strength associated with going to lower powers by fluence matching.

In the subsequent set of channel Bragg waveguides, the grating contrast responded approximately as expected with the duty cycle clearly demonstrating the ability of the DGW technique to allow the control of the refractive index perturbation in the Bragg structure without affecting the channel structure itself (figure 8.22). However, there is a disagreement between the modelled grating response and the observed response for duty cycles <30%, this is believed to be due to the dispersive thermal process involved in the photosensitive index increase.

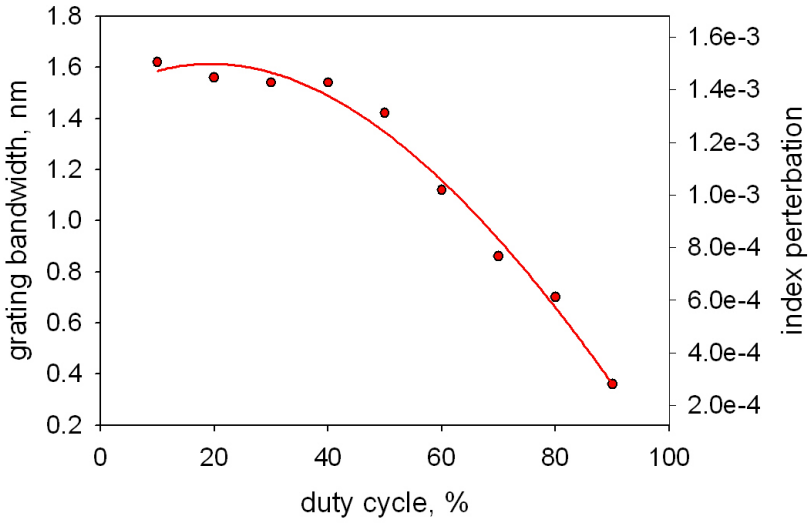

Figure 8.22: Effect of duty cycle on grating bandwidth. Right axis - calculated minimum index modulation from coupled mode equation 6.17. Note, the line is only for indicative purposes only.

Thus, the contrast of the grating modulation can readily be controlled though use of the duty cycle whilst maintaining the same channel strength. The full scale of grating contrasts from null, wash-out producing a channel waveguide structure to a full grating contrast ~1.5×10^{-3} is demonstrated. This demonstrates that the technique can scale the contrast of the grating structure and as such, ideal for producing apodised grating structures. This function has not been implemented yet as it requires more sophisticated control software, but the principle is successfully demonstrated.

8.7 Ultra-wide detuning span

In section 7.5 the numerous advantages of a grating fabrication technique using a small interference pattern were described in relation to the flexibility of centre wavelength detuning. This is born out experimentally in figure 8.7 in which range of grating periods were defined over the C-band with virtually no difference of grating contrast. The range of grating periods defined in that experiment demonstrated the ability to define grating structures that have periods varying not only in the sub-nm scale for producing chirped structures but can be used to fabricate entire grating structures of significantly varying response.

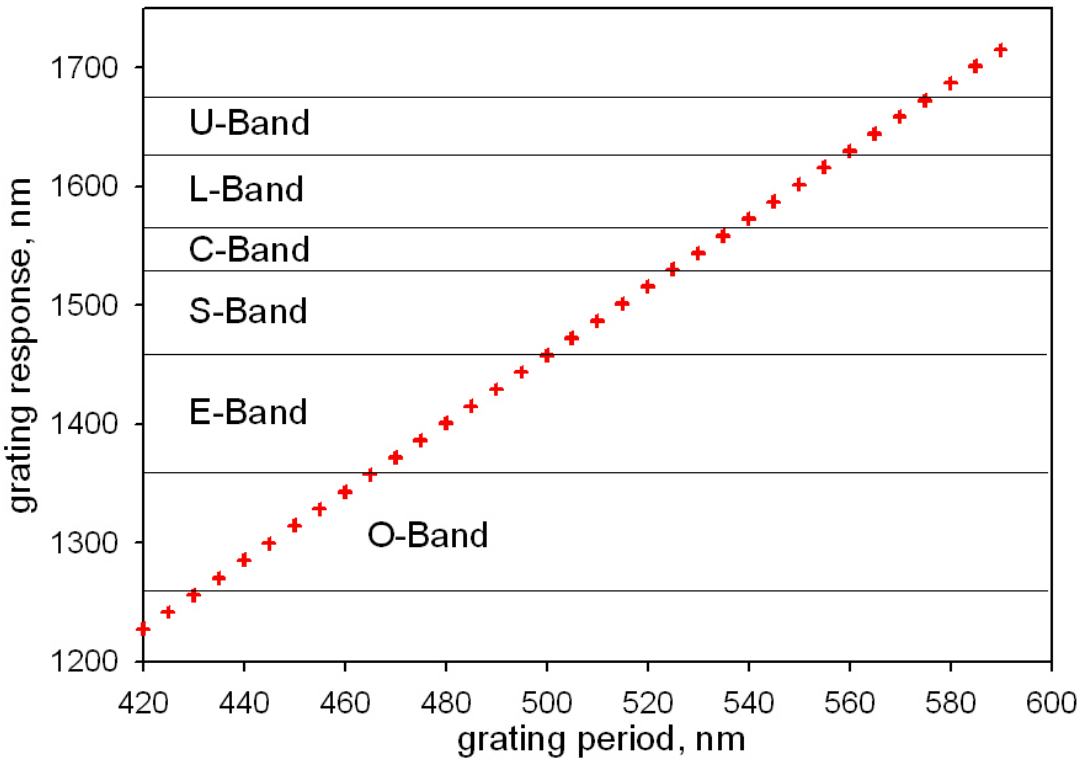

Figure 8.23: Range of Bragg grating periods defined through Direct Grating Writing with a fixed intersection angle of the writing beams. Grating responses ranging from 1.23um to 1.71um were observed, with the span limited by the characterisation source.

However, from the theory of the writing process, the use of a significantly smaller writing spot allows a much greater range of detuning to be performed. Figure 8.23 illustrates the range of grating periods that can be defined from a fixed intersection angle set-up, it is evident that the use of such a small writing spot to produce the interference pattern provides the system with an almost unparalleled flexibility for the definition of Bragg grating structures. It is the author's belief that this represents the widest range of first-order Bragg grating structures written consecutively in a single fabrication run without changing any elements of hardware.

This result demonstrates that not only can the detuning process be used to change the period of the grating as it is written for chirp and dispersion compensation, but that the DGW fabrication technique as a whole realises the potential of a rapid-prototyping concept. Structures can be designed that incorporate any grating response within the entire ITU spectrum (from the bottom of O-band @1260nm to the top of the U-band @1675nm) with

the grating period controlled entirely via software, circumventing the limitations of fabricating phase masks of an exact period fabricated (Tanaka, Hibino et al. 2002). In addition, any combination of any number of gratings can be incorporated into the same device with minimal impact of fabrication time and complexity.

It should be noted that all of the gratings in figure 8.23 have responses greater than 4dB, and were all written with a duty cycle of 25%. However, unlike the C-band grating span in figure 8.7, there is significant variation of the grating contrast over this 488nm wavelength range arising from the detuning process, although these effects can be compensated and controlled via the use of the duty cycle, a process described in detail in section 9.3. It is also worth noting that while these results cover a significant range of the grating periods that can theoretically be defined through this technique, they do not represent the entire span as the measurements were limited by the bandwidth of the broadband source.

8.8 Summary

The first ever demonstrations of the Direct Grating Writing process, defining both channel waveguides and Bragg grating structures were presented. The samples were produced on in-house fabricated silica-on-silicon samples and as such were not ideally suited to the writing process. However, grating structures were written, in relatively weak channel structures with reflectivity's up to 28% and bandwidths of 0.132nm proving the concept of the process.

Subsequent sections dealt with the optimisation of the writing process using silica-on-silicon samples produced by Alcatel Optronics UK. The samples were produced using flame hydrolysis deposition and consisted of a buried, Germanium doped core layer. To avoid time associated effects the samples used initially were thermally locked, providing a weaker but virtually permanent enhanced photosensitivity. Again, channel structures with grating responses were produced in this alternative material system with index perturbation contrast in the order of $5x10^{-5}$.

Subsequent investigation into the writing conditions revealed dependence not only on the total fluence, but the intensity of the beam. For a given fluence, slower translation resulted

in a stronger channel structure. This observation was confirmed by both NA measurements and effective refractive index measurements.

Direct Grating Writing was performed into freshly Deuterium loaded samples. These produced very strong channel waveguides and grating structures (transmission dips >30dB). The freshly loaded samples exhibited a distinct threshold effect, powers below a certain level result in no waveguide structure being defined, powers above result in a relatively strong waveguide. Like the thermally locked samples, lower beam powers for a given fluence resulted in a stronger channel waveguide, with the same relationship applying for the threshold, the lower the beam power, the lower the threshold.

The effect on the grating writing duty cycle and period were investigated. The effect of the duty cycle on the overall contrast of the grating structure was found to follow as expected with the theory for DC values >30%. At 100% no grating structure was defined, defining a channel waveguide only. At below 30% duty cycle the grating contrast appeared to saturate, a response thought to be from the diffuse nature of parts of the photosensitive mechanism. The full extent of the detuning possible using the small spot interference was demonstrated by the fabrication of grating structures with Bragg responses spanning over 488nm, covering the O, E, S, C, L and U bands of the ITU spectrum. This is believed to be the first demonstration ever of gratings formed over the entire spectrum from a single non-modified grating writing set-up.

Chapter 9: Functions and applications of DGW structures

9.1 Abstract

In the following sections the structures and devices that have been fabricated using the Direct Grating Writing technique are presented. These functions include the demonstration of grating contrast control over a detuning range of 488nm, the measurement of the total channel dispersion of a waveguide and measurement of local photosensitive responses. The ability of the technique to define more complicated components commonly encountered in Planar Lightwave Circuits (PLC) such as y-splitters and power couplers are demonstrated as well as an ability to selectively and accurately change the strength of channel waveguides produced through reactive ion etching. Finally, the promise of these structures as easily manufactured sensors for refractive index change, either thermally or through a 'sampling' structure is demonstrated.

9.2 Introduction

In the previous chapter the techniques and processing considerations for producing channel waveguides with integral Bragg gratings structures was extensively described. In the following material the use of the Direct Grating written structures are presented for a range of applications, with functions more sophisticated than in chapter 8. These applications range from power splitting/coupling components with potential for inclusion in PLC, the investigation of the proximity of components on a substrate, and the potential of these devices as sensors. Whilst this is not an exhaustive list of the potential of devices available from this fabrication technique, it illustrates the range of possible applications for which this fabrication process could be used.

9.3 Contrast compensated Ultra-wide detuning

9.3.1 A tale of two techniques

In the previous chapter the centre wavelength detuning results covering a 488nm grating response span were presented. When detuning by this range there is a significant effect on the grating contrast resulting from the detuning technique (section 7.5.1). While in section 8.7 control over the index perturbation contrast via the duty cycle used to write the structure was demonstrated. By combining detuning and the effects of duty cycle control to balance the grating contrast, gratings of uniform response can be produced over the entire 488nm detuning range. The contrast for periods close to that of the interference pattern can be reduced and for grating periods at the limits of the detuning process the contrast can be enhanced from normal writing conditions. The ability to produce a normalised grating response over the detuning range is essential for producing structures with broad-band performance.

The bandwidth for a range of gratings produced throughout the centre wavelength detuning experiment is illustrated in figure 9.1. The bandwidth responds approximately as expected through the detuning process, with a relatively good agreement between the simulation of the contrast (section 7.5) and the experimentally observed bandwidth. The gratings in this experiment are all 8mm long and written in sets of 3 gratings per channel. Note that below 1.3μm, there is a theoretical increase in the grating contrast in a region defined as 'over-tuned'. This region is a section beyond the point of minimum contrast where a grating the correct period can be defined on the wrong side of the detuning window, an effect possible due to the low number of grating planes defined in a single exposure. The relative contrast of the grating structures around the null are controlled through use of the duty cycle whilst maintaining the same overall fluence.

Offsetting the contrast shift due to detuning, through the use of the duty cycle (as illustrated in section 8.7) allows the very wide range of grating periods with similar bandwidths to be written with the same strength channel waveguide (figure 9.2).

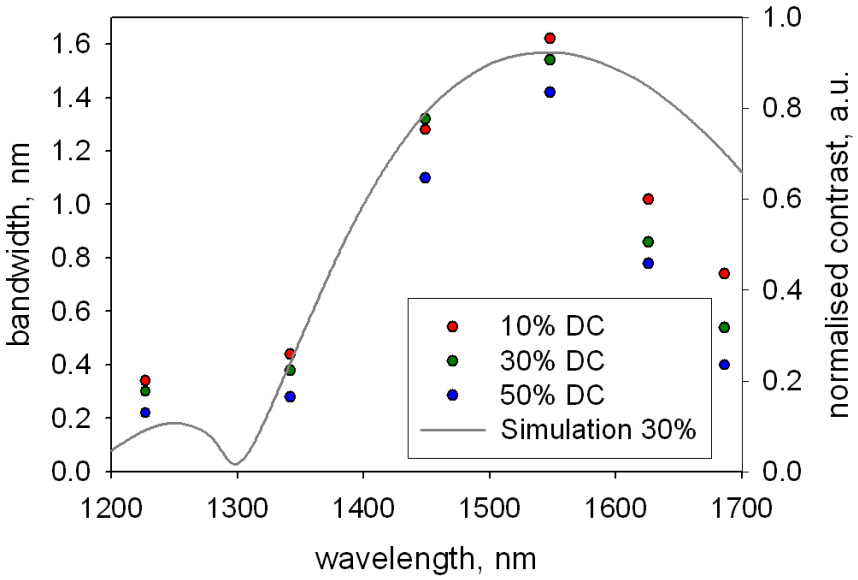

Figure 9.1: Grating bandwidth vs. grating Bragg wavelength for various duty cycles. The grey line represents the simulated response from simulation in section 7.5.

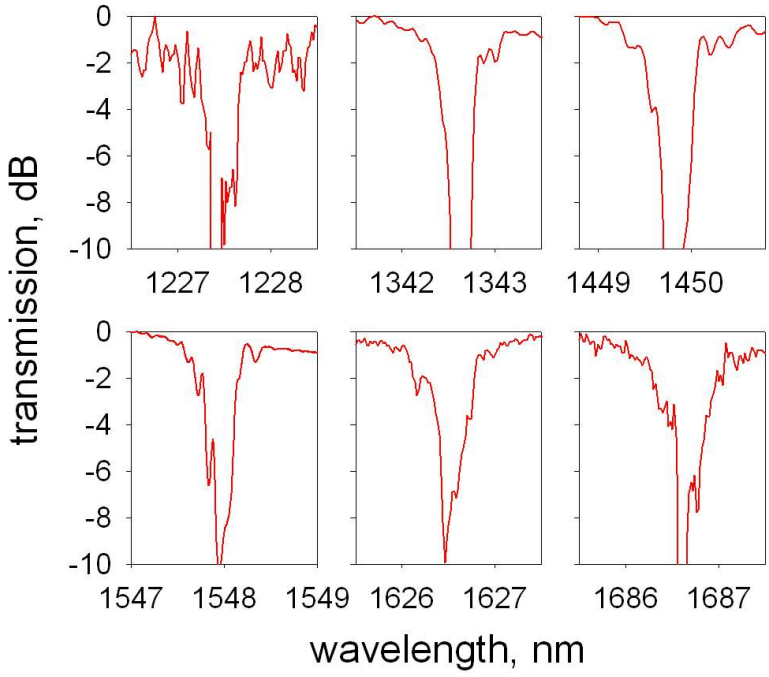

Figure 9.2: Range of gratings spanning from below O-band to above U-band with approximately normalised grating bandwidth. Noise on the traces is a combination of low signal-to-noise ratio and a surface contaminated sample.

The graphs in figure 9.2 are indicative of the grating spectral response and the parameter control through the DGW process, all the grating bandwidths (3dB) are ~0.4nm with transmission dips of the order 10dB. The noise in each trace is due to the low signal-to-noise ratio when using a very broad band source and a high resolution OSA to profile the

grating response. Further noise was introduced during the writing process due to partial contamination of the sample surface during cyro-storage. However, the results clearly indicate the principle of the technique for controlling the contrast of the grating structures allowing the production of arrays of grating structures with normalised spectral responses within a very wide spectral window.

9.4 Dispersion analysis

9.4.1 Dispersion

The ability to readily and simply define Bragg grating structures over a wide spectral range is not only useful from a fabrication perspective, but offers insight into the material and device properties.

Waveguides are known to be dispersive, and single mode waveguides have a total dispersion that is a combination of both the material dispersion and the waveguide dispersion. Material dispersion is a result of the wavelength dependent refractive index $n(\lambda)$, such that different wavelengths of light experience a difference refractive index. It can be shown that the group velocity of a pulse of light can be expressed as (Ghatak and Thyagarajan 1998):

$$\frac{1}{v_g} = \frac{1}{c}\left[n(\lambda_0) - \lambda_0 \frac{d^2 n}{d\lambda_0^{\,2}} \right] \qquad [9.1]$$

where v_g is the group velocity, λ_0 is the free-space wavelength and c is the velocity of light. The time for a pulse to propagate though a length of material L is expressed as:

$$\tau(\lambda_0) = \frac{L}{v_g} = \frac{L}{c}\left[n(\lambda_0) - \lambda_0 \frac{dn}{d\lambda_0} \right] \qquad [9.2]$$

This means that if the source has a spectral width $\Delta\lambda_0$ then each wavelength component will have a different group delay, and therefore a different propagation time, thus broadening the pulse. This broadening can be expressed as:

$$\Delta\tau = \frac{d\tau}{d\lambda_0}\Delta\lambda_0 = -\frac{L}{c}\left(\lambda_0^{\,2} \frac{d^2 n}{d\lambda^2} \right)\left(\frac{\Delta\lambda_0}{\lambda_0} \right) \qquad [9.3]$$

The broadening in equation (9.3) is proportional to the length of the sample and spectral width of the pulse. To apply a more general value the *material dispersion* is expressed as the temporal broadening per length per spectral width:

$$D_m = \frac{\Delta\tau}{L\Delta\lambda_0} = -\frac{1}{\lambda_0 c}\left(\lambda_0{}^2 \frac{d^2 n}{d\lambda_0{}^2}\right) x10^9 \qquad [9.4]$$

with the units (ps $km^{-1}nm^{-1}$), wavelength in micrometers and speed of light in kms^{-1}.

Equation (9.4) gives the dispersion for a wave propagating through any dispersive material. The second component to the total dispersion arises from the modal confinement from the waveguide structure. Even if the material forming the core and cladding layers is free from material dispersion, confinement of the guided mode into a channel structure results in a wavelength dependent response. In section 3.4.1 the normalised waveguide parameters are defined, the *normalised frequency* is a function of the free-space wave-number, and *b* is a function of the effective refractive index for a structure. Thus for different wavelengths the strength of the confinement varies, resulting in a variation in the effective index and group delay, giving rise to waveguide dispersion.

9.4.2 Measurement of total dispersion

The results in section 8.7 are presented demonstrating the span of Bragg gratings that can readily be defined using the Direct Gating Writing set-up. The span is considerable, covering 488nm with the grating periods defined though periodic modulations of the laser beam. As each grating structure is defined through a process controlled though the position of the writing spot, the period is accurately known. Through interrogation of Bragg structure and knowledge of the grating period the effective index of the guided mode can accurately be determined to the resolution of the OSA. From this data the function of the effective index with wavelength can be obtained, and hence the total dispersion of the channel waveguide. The effective index against wavelength is plotted in figure 9.3.

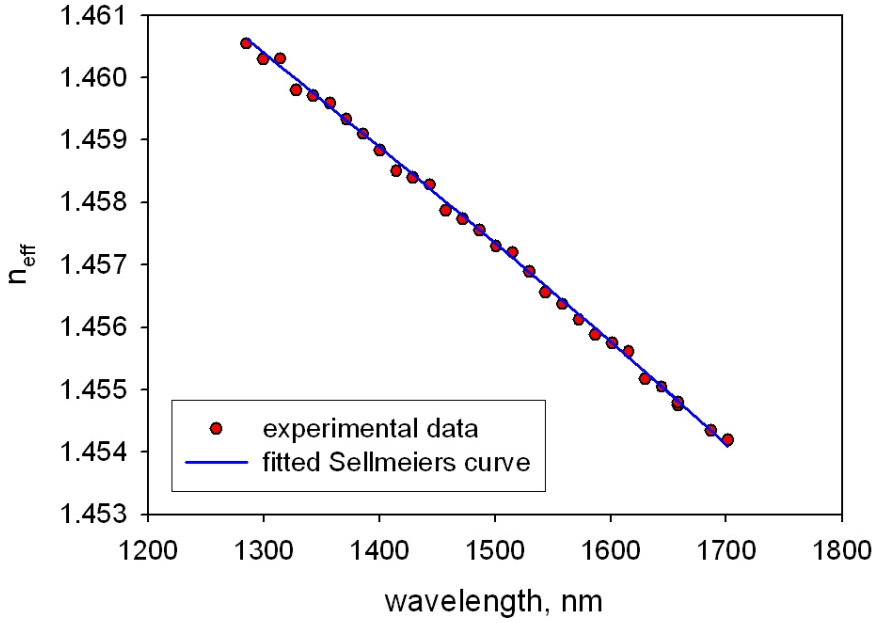

Figure 9.3: Effective index as a function of wavelength determined though the Bragg response of grating structures over a wide span. The blue line is the fitted Sellmeier's equation.

The data in figure 9.3 has approximately been compensated for the out-diffusion of hydrogen for the duration of the experiment from the results in figure 8.13. The refractive index of pure and doped silica can be represented by Sellmeier's equation as a function of wavelength (Ghatak and Thyagarajan 1998);

$$n^2(\lambda_0) - 1 = \frac{b_1 \lambda_0^{\,2}}{\lambda_0^{\,2} - a_1} + \frac{b_2 \lambda_0^{\,2}}{\lambda_0^{\,2} - a_2} + \frac{b_3 \lambda_0^{\,2}}{\lambda_0^{\,2} - a_3} \qquad [9.5]$$

The fitted constants to the data are present in table 9.1, as obtained from the fitted curve in figure 9.3.

	a	***b***
1	0.006169	0.714171
2	0.018372	0.432036
3	97.93111	1.184613

Table 9.1: Best fit Sellmeier's coefficients to the experimental data in figure 9.3.

The second derivative of the Sellmeier curve is obtained and with equation 9.4, to be plotted as the total dispersion of the material and the channel combined in figure 9.4. For reference, the dispersion of bulk silica is plotted along with a simulation of the dispersion of the waveguide and hence an estimate of the material dispersion. In order to account for the non-symmetrical nature of the channel waveguide, when estimating the dispersion due to

the waveguide structure the simulation described in section 3.5.1 was used to plot the second order differential of refractive index with wavelength. The structure had a vertical index step of $1x10^{-2}$ and a horizontal index difference of $4x10^{-3}$ to emphasise the asymmetric nature of these waveguides.

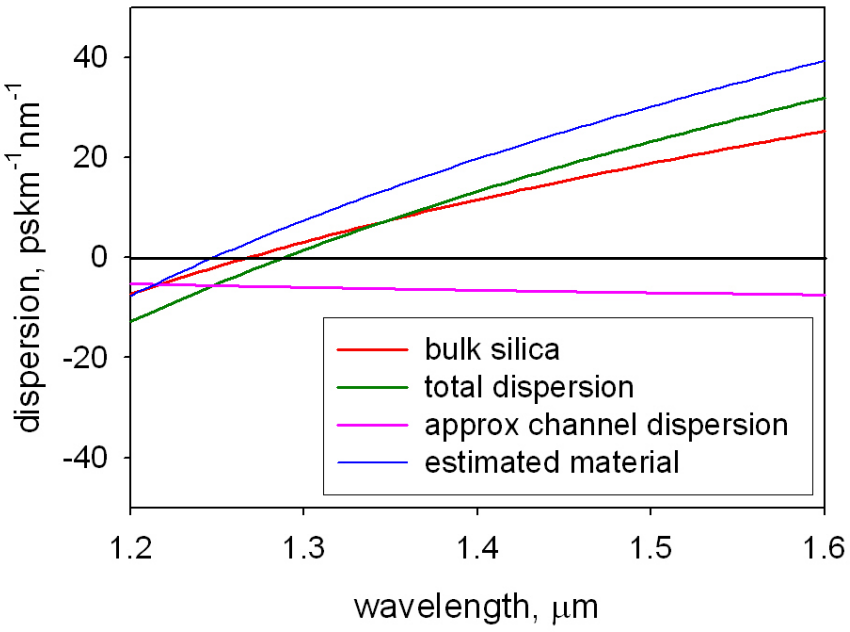

Figure 9.4: Dispersion as measured through use of the wide detuning range possible via the DGW technique. Red - Bulk silica for reference, green - measured total dispersion for both the waveguide and material, pink - estimated channel dispersion and blue – estimated material dispersion.

The zero material dispersion point (ZMDW) is defined as the wavelength with minimal dispersion, which for the total channel waveguide is 1.283μm. Taking into account the estimated dispersion for the channel waveguide alone this results in an estimated ZMDM wavelength for the material is ~1.247μm.

It is worth noting that while in principle the above technique provides a simple way to determine the dispersion of a waveguide, it is critical on an accurate fit for the Sellmeier equation. Error in experimental points of the effective index at the stage of fitting the Sellmeier equation can have significant consequences when taking the second derivative of the equation. While the effective refractive index of planar Bragg gratings written spectral responses spanning >400nm can accurately be measured, in this experiment the effects of out-diffusion of the Hydrogen were only approximately compensated for. The structures were written in channels containing sets of three gratings, and there is still structure

implying a grouped response of the sets of gratings with effective index in figure 9.3. This indicates that there is still some error in the strength of the channel waveguides and thus the effective refractive indices. While the Sellmeier equation can be accurately fitted to the effective index data, deviation of the data points will significantly affect the coefficients. As the dispersion is related to the 2nd derivative of the effective index with respect to wavelength and the terms in equation 9.5 all contribute, a small deviation has a significant effect on the dispersion. By defining the structures in a process minimising this systematic error, this technique represents a very simple process for the direct measurement of the total dispersion of the channel.

9.5 Proximity characterisation

The ability to define a grating at the same time as the channel structure for use as a diagnostic tool has been presented in section 7. In the previous situation, the various writing parameters were investigated by interrogating the grating structure and measuring the bandwidth and Bragg wavelength of the structure. The incorporation of grating structure through Direct Grating Writing with minimal changes to the writing parameters of the waveguide, allowed the subsequent interrogation of the channel structure, a process not possible without changing the properties of the surrounding medium. There is a second advantage with this technique for the investigation of material response, due to the very local nature of the grating structure. Both the grating and guided mode are contained to an area of the order 10μm's, this allowing very specific investigations of local effects surrounding the UV defined waveguides.

Of particular interest is the effect of UV writing in the proximity to existing written channel waveguides. In previous publications it has been reported (Faerch and Svalgaard 2002) that Direct UV writing depletes the photosensitivity of a material in the region surrounding the exposed waveguide. This effect is particularly important given the serial nature of defining 2-dimensional multi-channelled structures (couplers, splitters, etc.) where one arm is written after the other. In the joining regions, if the second waveguide is of a *v*-number then the coupling strength and ratios would be different to the intended performance. Using the DGW technique, an array of channels and channels with gratings were written to investigate this proximity effect. Initially a plain channel structure was written, and then parallel to it a

second channel with a grating structure contained was written with the same fluence (figure 9.5). This process was repeated with a range of channel spacings and the subsequent Bragg response recorded for each set.

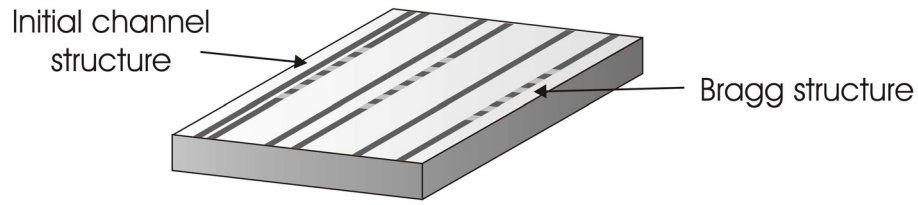

Figure 9.5: Structure of proximity experiment investigation the effect of proximity to an existing waveguide in the Direct Grating Writing process.

The spacing between the channels and channel Bragg gratings ranged from 10μm to 400μm, with the fluence matched for all structures and the effective index compensated for the out-diffusion of Deuterium with time. The variation of the effective index with separation distance is illustrated in figure 9.6. It should be noted that the effect of the first exposure on the local material photosensitivity is slightly more complicated in this case than the photosensitivity depletion effect previously reported. With large separation distances, >280μm there appears to be no effect on the strength of the second waveguide. However, as the separation reduces with spacing to less than 200μm there is a detrimental effect on the strength of the induced index change, with a minima in photosensitivity occurring at approximately 60-80μm separation. As the channels get closer together, the strength of the effective index increases back to expected levels. At ~10μm away from the initial exposure there is a sharp increase in the strength of the channel. It was observed that while data for closer spacing was taken, the structure acts as a single wide waveguide structure obscuring the level of photosensitivity.

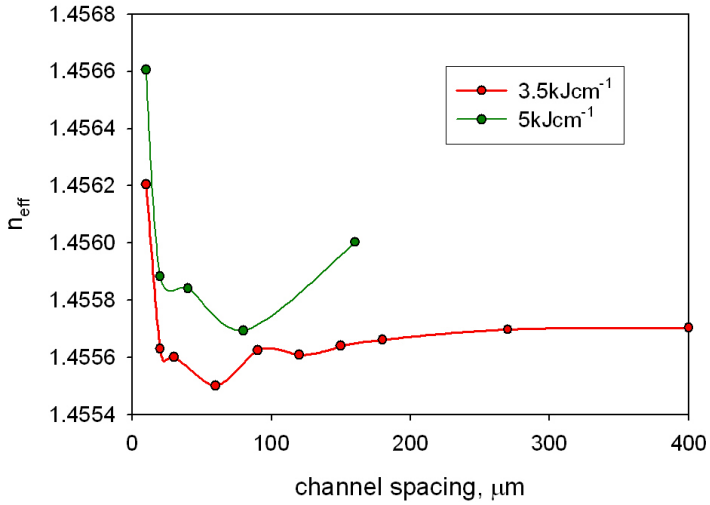

Figure 9.6: Effect of varying proximity to a prior exposed waveguide on the effective index of the '2nd' channel.

From these results it can be theorised that at the close proximity to the existing waveguide the initial exposure diffused enough thermal energy into the surrounding material to activate bonding of Deuterium into the silica matrix, creating the UV absorbing defects. In the second 'close' exposure the defects have already been activated so the cascade absorption occurs immediately, coupling more energy into defect creation using any remaining Deuterium in the material. Although there is likely to be significantly less free Deuterium in the sample at this time, the combination of the already present defects and the immediate cascade absorption allows the definition of a stronger waveguide. As the spacing is increased, the amount of energy coupled into the structure from the initial exposure consequently decreases, significantly reducing the density of these pre-bound defects (although some will remain) but thermally encouraging the migration of free Deuterium from the sample. It is further assumed that in the 'depletion' region the energy was not sufficient to initiate defect formation but diffused heat is sufficient to increase the rate of thermal diffusion. At distances greater than this, the thermal diffusion effect decreases until a separation of approximately 200μm is reached after which the sample is unaffected by local UV writing proximity effects.

This experiment highlights the complex effect that, as the distance between waveguides varies, the strength of the waveguide will initially decrease before increasing significantly. This is of particular relevance to coupler structures with s-bend structures, which taper into the parallel waveguides with typically around 10μm spacing (section 9.9).

9.6 Pre-locking

The proximity based photosensitivity modification results in section 9.5 indicate a local generation of defect centres in the UV writing process in regions where there was not sufficient energy to significantly raise the refractive index. This suggests a technique for the stabilisation of Deuterium or Hydrogen out-diffusion with respect to time could be achieved by using an initial rapid translation with the beam power on the threshold, creating the initial defects in the structure but not creating any significant index increase. This 'pre'-exposure technique would require a rapid translation with the beam power continuously on for both the channel and grating structures. In this way the entire structure could be 'pre-mapped' with a time independent enhanced photosensitivity during the initial high levels of Deuterium loading. Subsequent channel structures (and Bragg gratings) would then be defined in a second writing step of greater power after the surrounding Deuterium has depleted. This could minimise any out-diffusion of the Deuterium photsensitiser and allow greater refractive index contrast between the channel and the surrounding core layer.

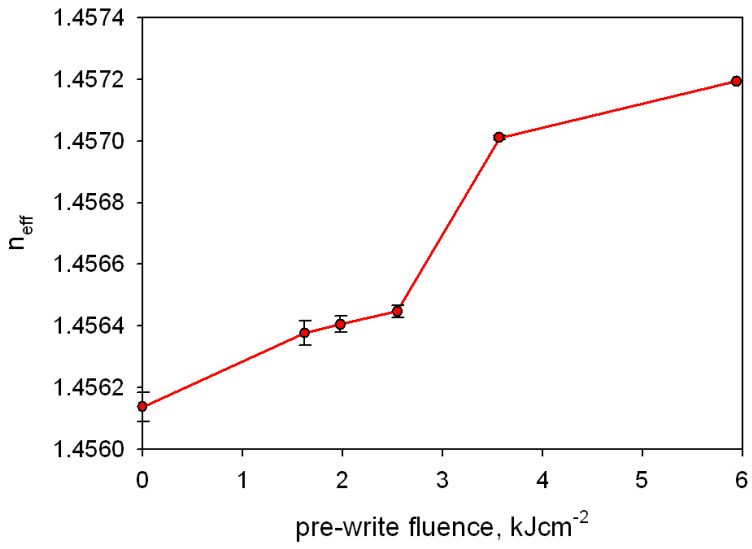

Figure 9.7: Effect of pre-write fluence on the effective index of a Bragg grating channel with the 'overlay' fluence kept at 4.1kJcm^{-2}.

Investigation of this potential UV photosensitising pre-locking technique was based on two processes, the first of which was the pre-writing of the channels followed immediately by the 'overlay' writing. The initial results of this experiment are shown in figure 9.7. As expected from the normal channel writing process (section 8.6.4), the pre-exposure values

have a distinct fluence threshold around the 3kJcm^{-2} level. With fluences greater than this there is a significant step in the resulting strength of the channel, although these powers are effectively writing a weak waveguide in the initial pass. The second overwriting exposure adds to the overall strength of the channel and incorporates the grating structure.

In the second process of the experiment, pre-written channels were written, and then held stationary for 4hours at ~30°C to allow the mobile Deuterium to diffuse out. Whilst not completely depleted of mobile Deuterium, there should be a significant drop in the photosensitive response of the sample when the 'overlay' channels have been written (figure 9.8). As can be seen from the graph, channels were successfully written into the pre-exposed areas of the sample, albeit with a significantly reduced index change when compared to the channels written before the out diffusion of the Deuterium. This implies that a significant factor in the results in figure 9.7 is due to unbound Deuterium within the sample, significantly adding to the strength of the channel waveguide during the writing process.

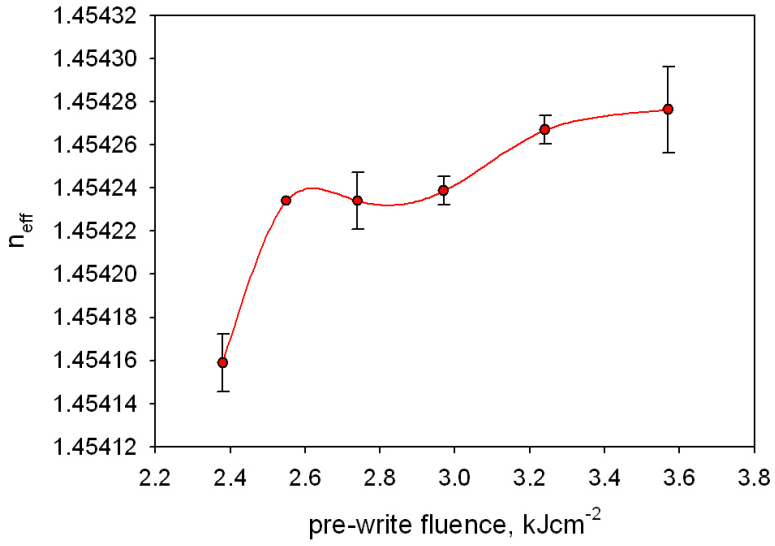

Figure 9.8: Pre-write experiment with the mobile Deuterium allowed to out diffuse for 4 hours between pre-write and over-write.

Interestingly, there is a distinct variation of the effective index of the channel waveguide for the different strength pre-locking structures occurring around 2.6kJcm^{-2}. This implies there is a definite incorporation of defects in the pre-writing process that is dependent on the overall power; although once past the threshold point the effect does not significantly vary

with power. The other interesting point is the effective index of these channels is less than has been observed before, the freshly loaded samples rarely demonstrating an effective index below, 1.455. Such low index channels were previously observed in the out-diffusion experiment (8.6.1), thus it is likely that, like the overall strength of the channel waveguide is related to the availability of the Deuterium, as is the threshold level observed in the writing experiment. Due to the lower level of free Deuterium, and the already incorporated level of defects, the threshold for subsequent writing is lower.

9.7 Multiple overlay gratings

A device that appears particularly interesting for optical integrated technology is based on the superposition of multiple grating structures into a waveguide at the same location (Othonos, Lee et al. 1994). Such devices could be used to function as a comb-filter, with the grating responses functioning individually from within the same waveguide. Comb-structure devices are applicable for multiplex/de-multiplexing functions or any device where discrete wavelengths need to be selected from a continuum. The advantage of such a structure is its compact size, as all the gratings are superimposed across the same channel section and thus, the device length is the same as a single grating. This simplified structure results in no need for splitting or routing of the structure into individual grating arms, and even with no temperature control all the grating structures experience the same ambient conditions and thus change together.

In this experiment the initial channel and Bragg grating is defined in a single exposure. The subsequent grating structures were over-written on top of the existing channel and grating with the same writing fluence but different grating period. Thermally locked samples were used for the process to avoid complications arising from the Deuterium depletion from the prior exposures. Figure 9.9 contains the evolution of the spectral response for channels with 1 to 4 gratings superimposed.

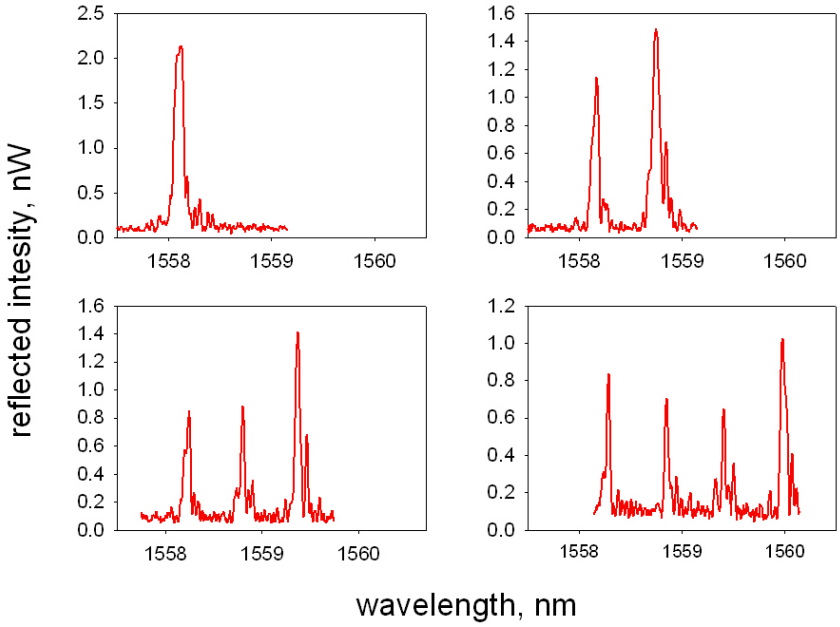

Figure 9.9: Evolution of grating spectra as each grating spectra is overwritten the previous section. Not only are extra spectral responses induced but the average index of the structure is increased with each exposure.

From the graphs it is evident that with each additional overwritten grating structure the distinct spectral response from that structure is evident in the spectral profile. It should be noted that as the number of structures increase, and therefore the overall exposure of the material, the effective refractive index of the entire structure is also increased. As the contrast of the index perturbation is to a limit independent of the strength of the channel, unlike in the case of inscribing the gratings into existing waveguide structures, the overall resultant index from multiple exposures can be tailored to the average index of the lead-in/out channel structures.

It is worth noting the relative strengths of the grating structures, while consistently the last grating to be overlaid has the strongest response (for constant writing conditions) the second strongest is in general the first grating exposure. Thus, for the case of overwritten grating structures, it can be stated that as the n^{th} grating is overlaid the *n-1* becomes the weakest structure. This implies that the index change for the overwritten gratings may be of a different photosensitivity mechanism and as such have implications for the lifetime of such devices.

9.8 2-D structures

There has been much emphasis on the advantages of combining the Direct UV writing process with planar grating writing in order to create a flexible, rapid planar lightwave circuit prototype system. One of the key aspects of such a fabrication process would be ability to define structures throughout a plane, such as y-splitters and s-bends. On of the most fundamental structures for splitting power and coupling light into various waveguides is the y-splitter. The y-splitter structure was the first multi-channel structure implemented on the Direct Grating Writing technique to ensure that the added complexity of the composite writing did not hinder the definition of curved waveguide structures. The mode profile in figure 9.10 was a y-splitter fabricated to test the technique.

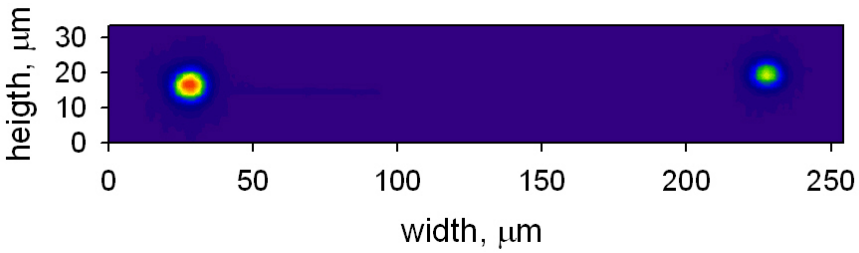

Figure 9.10: Mode profile of a 1x2 y-splitter structure. Output arm spacing of 200um and a power splitting ratio of approximately 3:2 due to the proximity of the first waveguide when writing the second arm.

For a more complex structure fabricated by the DGW technique an overhead view of a cascaded 1x8 splitter (3x(1x2)) is included in figure 9.11 with the associated mode profile in figure 9.12. The entire device length is 30mm and the output port spacing is 28.5μm per channel. This device illustrates the ability of the technique to produce long structures composed of multiple waveguide intersections and curves, however the output mode profile also highlights the need to compensate for the proximity of the neighbouring channels during the writing process. There is a significant division of power between the first and last port, with the weakest channel 20% of the strongest.

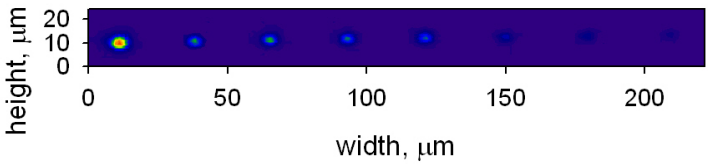

Figure 9.12: Mode profile from the 1x8 device picture in figure 9.11, note the weakest channel ~20% of the power of the strongest.

To incorporate Bragg gratings into the DGW fabrication of 2-dimensional structures, a Mach-Zehnder device was fabricated using the format illustrated in figure 9.13. The two separated arms of the structure were spaced 200μm apart and the gratings written with a period difference of 0.4nm, and the entire device taking approximately 2 minutes to write. The subsequent reflected spectral response is provided in figure 9.14.

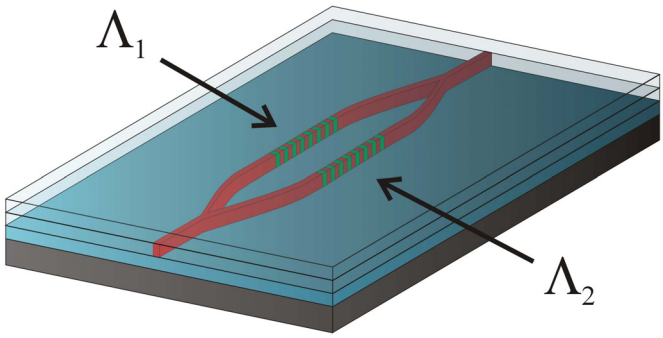

Figure 9.13: DGW structure incorporating both y-splitters and Bragg grating structures

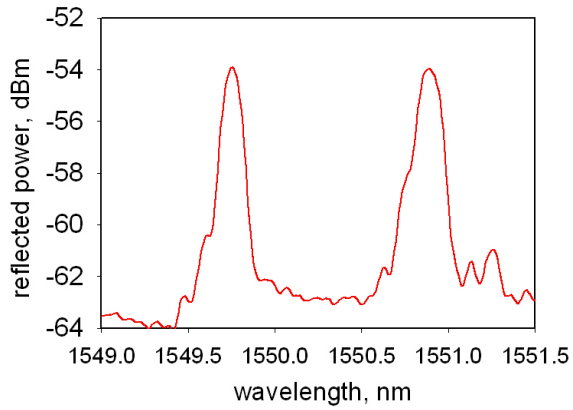

Figure 9.14: Reflection spectra from the Mach-Zehnder style structure defined in figure 9.13

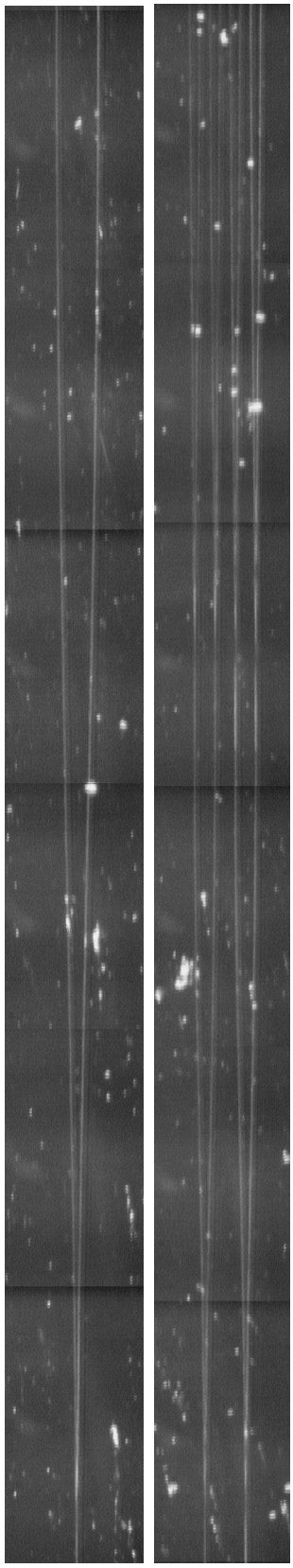

Figure 9.11: Composite picture of an overhead view of 3 cascaded 1x2 splitters

The two reflection peaks evident in the reflection spectrum of figure 9.14, demonstrate that there is no difficulty in combining the simultaneous writing of grating and channel waveguides into the structures of more complicated 2-dimensonal devices, thus allowing applications of this technique to include more sophisticated components.

9.9 Directional couplers

Directional couplers are devices ideally suited to a planar geometry, forming the guided wave equivalent of a beam splitter. Such devices rely on the extension of the evanescent field from guided modes extending into the cladding structure surrounding the waveguide. If there is a second waveguide close enough that the evanescent fields interact then power can be coupled between the two structures. The structures can be used for power splitting, coarse wavelength splitting, sensors etc.

In a planar geometry cross coupled directional coupler devices generally (Ghatak and Thyagarajan 1998) comprise of two channel waveguide structures brought very close together (typically of the order 10μm) for a fixed interaction length before separation (figure 9.15). In the coupling region the power oscillates back and forth between the two channel waveguides.

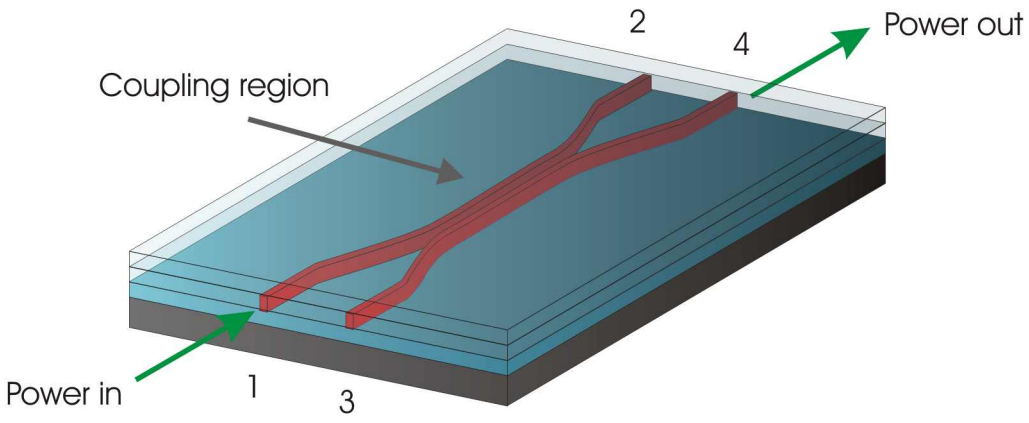

Figure 9.15: Concept of a directional coupler in planar geometry

The directional coupler system (figure 9.15) can be considered as a waveguide with two cores and two modes (symmetric and asymmetric). Within the coupling region the two modes will have different propagation constants and therefore propagate with different

velocities. When light is incident in one of the input arms of the coupler it excites both the symmetric and asymmetric modes, which either constructively or destructively interfere with each other resulting in a distribution of power between the two modes. As the modes have different propagation constants, the balance of the interference, and thus the power distribution, is a function of distance in the coupling region. When the phase difference between the two modes is π then a cancellation of fields occurs in the input waveguide and all the power is transferred to the second waveguide. Further propagation along the coupling region results in power transfer back to the input waveguide, and so forth in an oscillating function throughout the coupling region. If the propagation constant of the two channel waveguides are the same, then the case is known as phase matched and total power can be transferred between the two waveguide structures. Any imbalance between the two waveguide propagation constants results in non-total transfer of energy. The power coupled from an incident waveguide (1) to an adjacent waveguide can expressed as:

$$\frac{P_2(z)}{P_1(0)} = \frac{\kappa^2}{\gamma^2}\sin^2 \gamma z \qquad [9.6]$$

$$\gamma^2 = \kappa^2 + \frac{(\beta_1 - \beta_2)^2}{4} \qquad [9.7]$$

Where $P(z)$ is the power in the respective waveguide distance z from the start of the coupling region, κ is the coupling coefficient and β is the propagation constant for the two waveguides. The power in the launch guide is defined simply as the power not in channel 2.

Based on the crossed coupler architecture, the inclusion of a Bragg grating structure in the coupling region allows the coupling of power into a counter-propagating mode. Coupler structures designed in this manner were produced with an over-head view of half the structure shown in figure 9.16. The other half of the structure is a symmetrical image. In the coupling region, the waveguide spacing is 10μm with various coupling lengths ranging from 8mm to 8.9mm and the power slitting ratio between the two arms for a given coupling length was monitored. A typical broadband output profile of the two output ports is shown in figure 9.17.

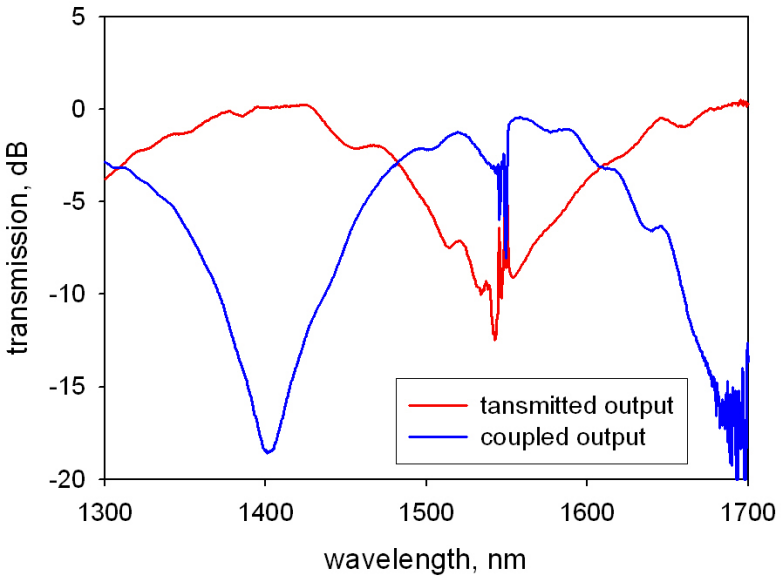

Figure 9.17: Power transmission spectra of a coupler structure with a Bragg grating response at 1550nm.

The coupler structure with the wavelength output profile illustrated in figure 9.17 has a coupling section of 8mm, resulting in maximum coupling into the second waveguide at ~1550nm. The power division between the two sections is not total, with approximately a 10dB difference between the two channels. This implies a miss-match between the propagation constants of the two channels, as expected from the proximity effect described in section 9.5. The spacing of the two channels in the coupling region is 10μm, a distance with significant pre-exposure from the first channel definition (9.5).

By expressing the data taken for the range of structures as the ratio of power between the two output arms for a given wavelength against the coupling section lengths the data should follow the trend defined in equation 9.6. The experimental data, along with the best fit of equation 9.6 is presented in figure 9.18, the coupling coefficient κ was fitted with a value of 0.994mm^{-1} and the difference between the propagation constants for the two waveguides is 0.716mm^{-1}.

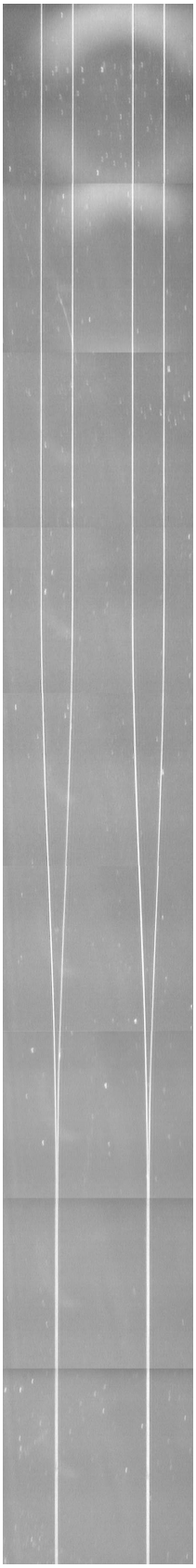

Figure 9.16: Overhead view of half a directional coupler structure

The coupling coefficient is a little higher than would typically be expected in fibre couplers or etched structures as the horizontal index change (the orientation of the coupling evanescent fields) is UV defined and therefore weaker than the vertical material induced index difference. Thus, the evanescent field has greater penetration of the cladding and greater interaction with the evanescent field of the second waveguide when compared to structures with symmetrical index profiles.

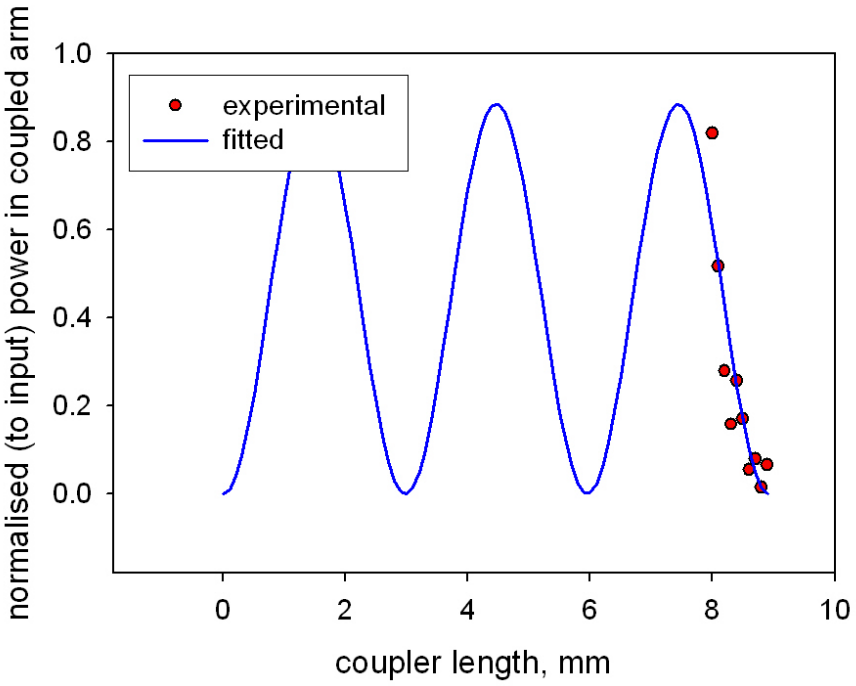

Figure 9.18: Coupling into output arm at 1591nm vs. coupler length. Fitted is the theoretical response from equation 9.6.

The difference of the two propagation constants of the two waveguides can be expressed as the difference in the effective indices of the two channels:

$$\beta_1 - \beta_2 = \frac{2\pi}{\lambda_0}\left(n_{eff1} - n_{eff2}\right) \qquad [9.8]$$

From the fitted data using the values given above the difference between the two effective indices between the two channel waveguides is $2\text{x}10^{-4}$, similar to the values obtained from the proximity experiment, although the writing conditions were significantly different. The coupling length is the minimum distance required for the maximum transfer of power between the two channels and in the above example is 1.58mm. Based on these promising initial results a series of future experiments are planned to optimise these structures for use in planar lightwave circuits including cascaded structures with integral Bragg reflectors for WDM add/drop functioning.

9.10 Overlay onto etched channels

Whilst the main thrust of the work in this thesis has been directed towards the definition of channel structures and Bragg gratings at the same time, thereby avoiding the need for any subsequent processing, there is a readily apparent second implementation of the fabrication system. The Direct Grating Writing system is essentially a very tightly focused interference pattern, combined with very accurate translation system. This has the potential for not only writing structures in virgin substrates but to pick out structures defined though other techniques and modify the feature. The key advantage of this process is the ability to select exclusively a single channel waveguide and uniformly change the properties, for example, increasing the refractive index change as in UV trimming or inserting a channel specific grating without alteration to the surrounding structures. This is very similar to existing grating fabrication techniques, but the ability to selectively and yet uniformly change channel structures of an existing sample provides an added level of control over the processing conditions.

The samples used for this experiment were etched silica-on-silicon samples provided by JDS Uniphase. The refractive indices of the channels were uniformly changed along the entire length of the structure, and a grating structure inscribed to allow the characterisation of the effective index of the channel. Sets of two channels per fluence level were exposed, with the power controlled by varying translation velocities throughout the UV exposure. Each channel was specifically targeted for individual writing fluence with the resulting graph of effective index vs. fluence given in figure 9.19.

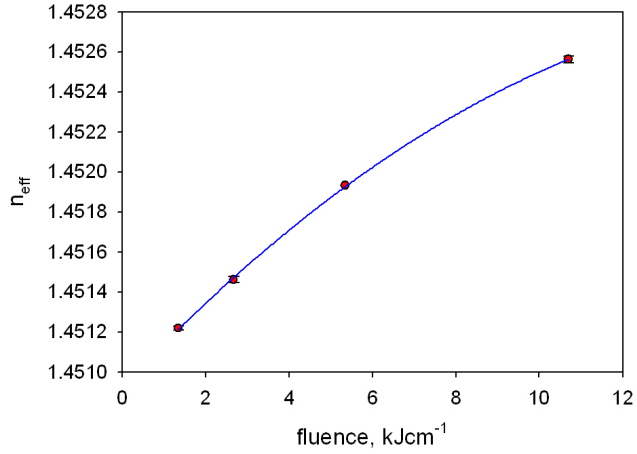

Figure 9.19: A graph of effective index vs. fluence, changing the effective index of an existing etched channel waveguide by uniformly exposing it throughout the entire translation and adding Bragg grating structures for characterisation.

From these results it is clear that the DGW set-up can readily target and expose specific channel structures and uniformly increase the refractive index of the relevant section of the channel through translation of the writing spot. High quality Bragg grating structures were written into buried etched channel sections with a resulting sample transmission spectra illustrated in figure 9.20. There was no apparent detriment to the writing process from the tightly focused writing beams, offering an accurate method for the evaluation of the exposure levels used when UV trimming existing structures. The etched structure provided a well matched mode for the collection fibre and the lack of a slab layer allowed for good signal collection of the guided mode only.

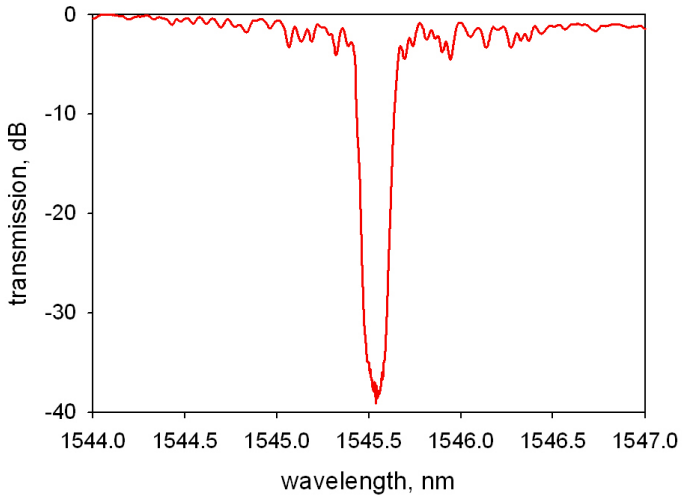

Figure 9.20: Transmission spectra from an etched channel waveguide with a grating structure inscribed using the DGW setup.

The potential for this DGW technique for subsequent UV trimming or grating inscription into existing channels is high. Clearly the technique works, and although the initial alignment is more of an issue then traditional bulk exposure techniques the local nature of the index change provides more control of the changes induced into the structure. Not only can individual channels be selected without affecting neighbouring structures the exposure over a channel can be spatially dependent and very accurately controlled. For example, the index of a curved waveguide could be increased to reduce the loss in the bend section, with the index increase tapering with radius of curvature.

9.11 Thermal tuning

One of the advantages of planar structures is their compact size and the associated implication of thermal uniformity across integrated structures on the device. Unlike fibre systems with individual component lengths of tens of centimetres (or longer) the possibility of a thermal gradient across the components readily exists. There are of course solutions for packaging such structures to have an athermal response, however these tend to significantly increase the cost and bulk of a system.

For requirements with less absolute thermal requirements, relative stability is offered in the planar geometry. The waveguides themselves are physically very close together, and the planar geometry readily allows for simple mechanical attachments to insulators or heaters as required. As the waveguides are close together, the response between them to temperature changes tend to be uniform and thus for structures with reference arms like Mach-Zehnder interferometers with a sensing window crude thermal stability can be achieved. However, the thermal response of the grating structures is of interest both in stability and as use as a temperature sensor.

The thermal response of an 8dB reflection grating was measured using a heated sample plate. The control system was open looped with the temperature measured in the copper heating plate the sample was mounted on 1mm directly below the sample. Reflection spectra of the Bragg grating were taken using the normal grating characterisation setup

(section 8.3.2) once the temperature had stabilised to within 1 degree per 2 minutes. The temperature tuning curve of the sample is plotted in figure 9.21.

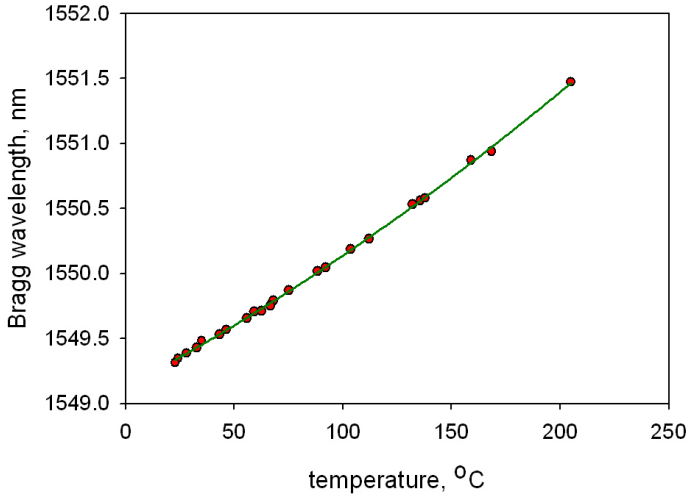

Figure 9.21: Bragg response as a function of temperature. The response deviates from linear at high temperatures, although below 150°C the thermal sensitivity is 10.8 pm°C^{-1}.

The grating exhibited linear response up to approximately 150°C, at temperatures greater than that there is a deviation for the linear trend, although this could be due to experimental error due to the open-loop nature of the control system. The linear fit provided a sensitivity of 10.8 pm°C^{-1}, approximately 3pm°C^{-1} less than is often observed in fibre Bragg gratings. There has been no assessment about the strain of the structure due to the different expansion coefficients between the silica and the silicon of the sample.

9.12 Etched sensors

The thermal response of the structures is shown in section 9.11, a combination of the thermal-optic response and expansion of the material changing the period of the material. This function has potential for use as a relatively crude temperature sensor, however there is large field of research dedicated to applying Bragg gratings as targeted sensors for specific functions. There are several reasons why Bragg gratings make attractive sensor devices, they are accurate, mechanically robust (no moving components), they can be formed out of passive materials (silica) and they can be very remote from the decoding equipment (i.e. can be used in explosive atmospheres). There are a wide range of triggers that the sensors can

detect including; gasses, strain and magnetic fields, but they are all based on the change of effective index of the guided mode or the mechanical change of period of the grating.

While mechanically changing the period of a Bragg grating can function as the basis of a sensor, it is relatively limited in application except for strain measurements. In contrast, the change of the effective index of the structure can be triggered by a wide range of effects, which can either affect the waveguide material directly or a material in contact with the guiding structure. As long as the change in the refractive index of a material occurs within range of the evanescent field then the effective index of the guided mode is changed, signified by a change in the Bragg response from a grating structure. The resolution of such a structure is limited by the ability to accurately determine the change in the Bragg response, however the degree of the wavelength shift does depend on the design of the structure. The electric field distribution within a slab waveguide is described in section 3.4, however an illustration of the field penetration with the variation of over-clad index is illustrated in figure 9.22.

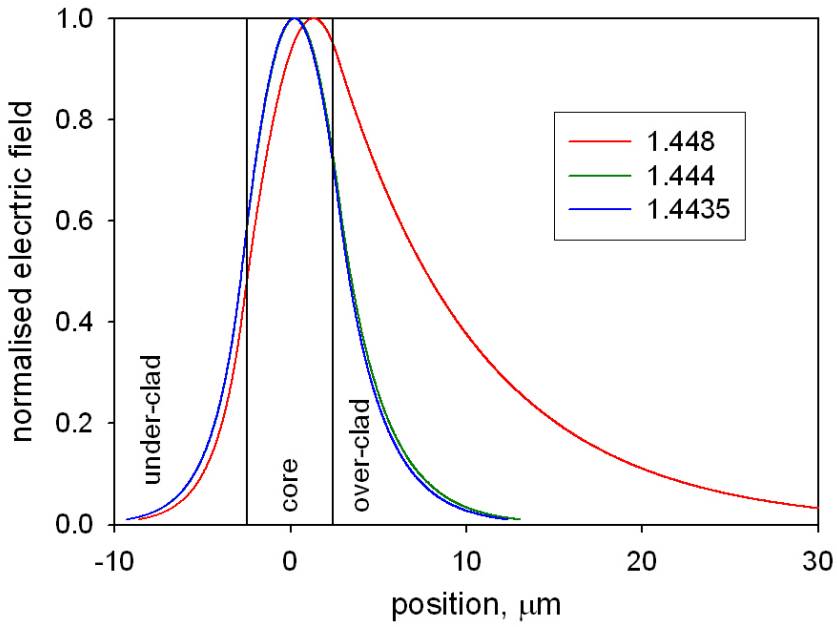

Figure 9.22: Illustration of the evanescent field penetration for a slab waveguide with an under-clad index of 1.44, core index of 1.45 and a range of over-clad indices. Clearly the penetration depth of the guided mode is dependent on the strength of the guide, it is clear that a significant part of the mode is contained within the clad but the amount does vary significantly with index.

The aim of the following experiment is to use UV written grating structures as sensors of refractive index of a medium placed in contact with the top surface of the sample. As

described above, the guided mode will penetrate into the cladding of the layer, with the degree of penetration dependent of the index difference. With the samples currently used, the confinement of the mode is such that the cladding layer is sufficiently deep that the evanescent field intensity has diminished to zero before encountering the end of the cladding layer. For a telecom structure this is ideal as the guided mode does not encounter surface roughness inducing extra loss or is affected by packaging environments. However, this buried structure is not compatible with a sensor structure. To get around this we are using a process ideally suited for planar structures, namely etching a window into the over-clad. The removal of some of the over-clad material has no mechanical strength issues (as would be the case for fibre structures), it is easily done and retains the flat surface topography of the planar sample.

9.12.1 Thin clad-sensor

For the sensing experiment there were two attempts at producing the etched window structures, the first attempt was to partially remove the cladding to a thickness of approximately 7μm, allowing only a small percentage of the guided mode to extend into the sensor window.

Etching of the cladding layer was performed using a wet-etch of hydrofluoric acid (48%) with the sensor window drawn out through using baked photo-resist. Although it would be possible to photo-lithographically define a window structure and reactive-ion etch the window the wet-etch approach was preferred for a number of reasons. It was simpler to implement, faster, and the boundary of the sensor window only had to be larger than the Bragg grating structure within the channel waveguide as that is the interrogative element. Once sufficient etch depth was obtained the sample was immersed in water to stop the etching process.

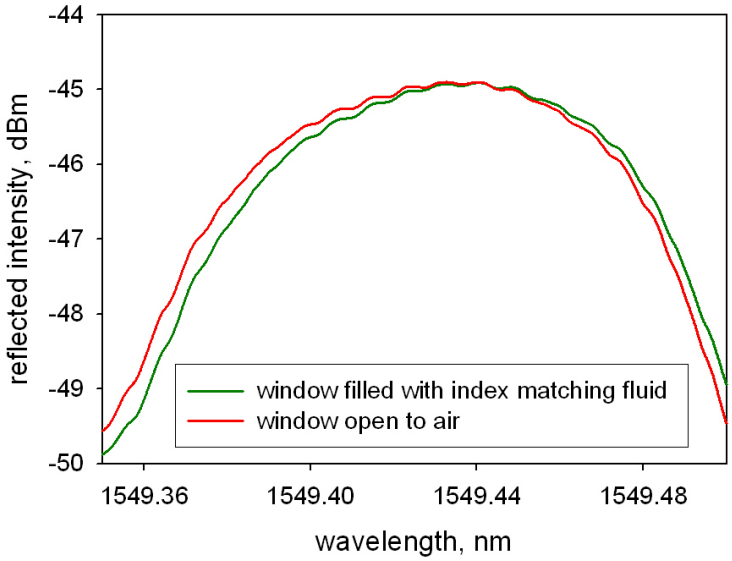

Figure 9.23: Effect of a sensor structure with an etched window with a resulting over-cladding thickness of 7um. The two curves represent the window open to air and filled with index matching fluid (n=1.45), with a 3pm average wavelength shift between the two materials.

The advantage of this configuration is the structure remains relatively low loss, as only a small part of the mode encounters the etched surface. However, the material within the sample window is not directly sampled, but rather effects the field distribution within the three layer sample subtly changing the effective index. The response of such a sensor structure is illustrated in figure 9.23. Clearly even with a very large index change in the window the effective index shift is minimal, 3pm for a $\Delta n = 0.45$, although the difference was detectable. However, to increase the sensitivity of the sensor it was decided to etch the window down.

9.12.2 Etching down to the core

The second approach was to etch the sensor window down to reveal the core layer of the waveguide. The material would then have a direct impact on the waveguide structure and hence, a greater effect on the effective index on the guided mode. However such structures can be expected to be relatively high loss, due to surface roughness at the core/window interface and attenuation through the 'sample'.

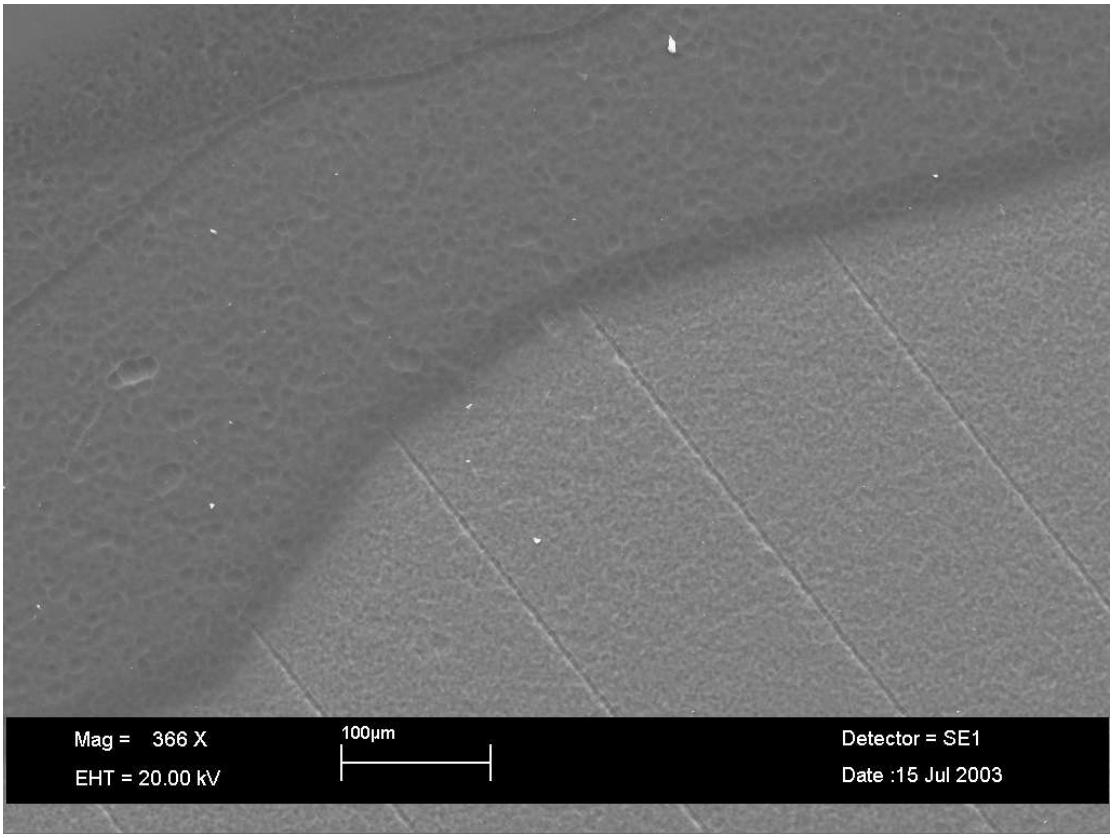

Figure 9.24: Edge of the etched window. Top left is the previously etched 7um clad layer with no channel structure evident. Bottom left of the window shows the revealed core layer with channel waveguides. The UV written channels etch faster the unexposed core material indicating refractive difference through surface relief.

In the etching process the UV exposed material has a greater etch rate, therefore the channel structures can clearly be seen on the SEM surface scan (figure 9.24). In the figure, the top left corner the structure is the cladding layer left from the initial etch and it is important to note that there is no evidence of any accelerated etch rate in the regions above the channel waveguides, regions through which the writing beams have also propagated. The contrast with the core layer is dramatic, in the boundary between the second etch window down to the core layer the evidence of the channel structures is discrete, with no gradual fade in.

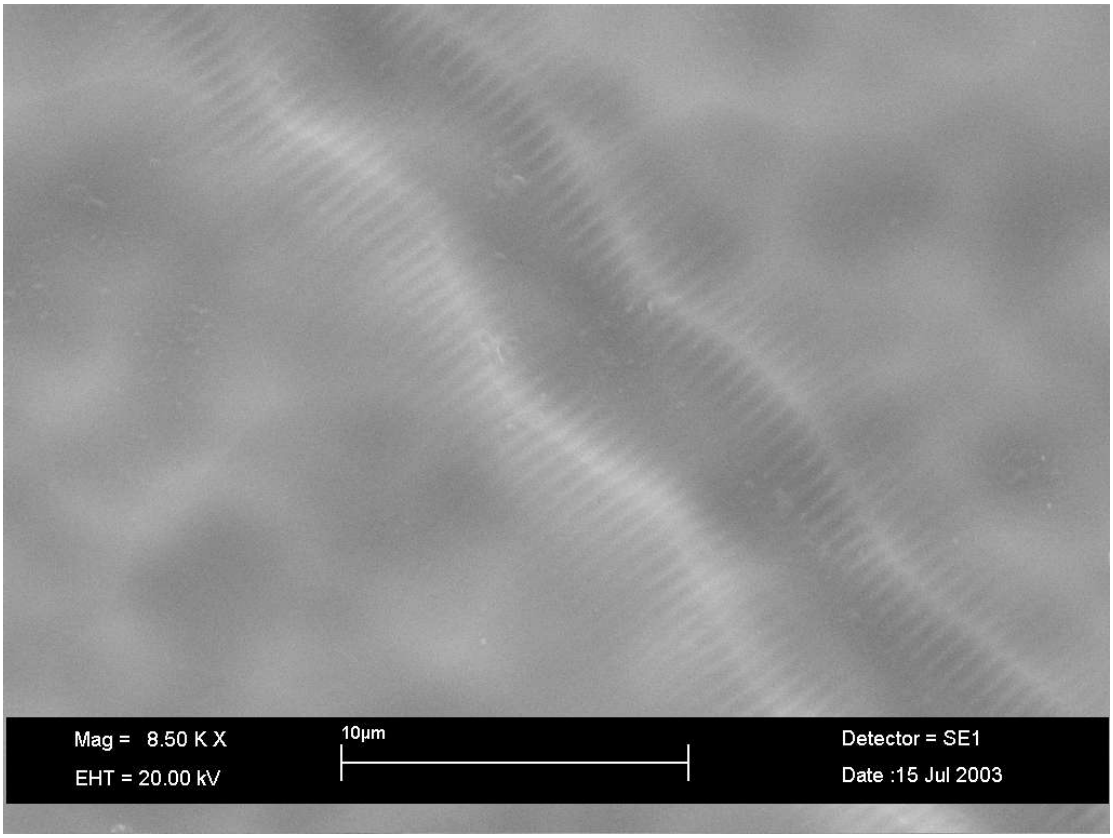

Figure 9.25: SEM image of a channel waveguide and Bragg grating structure after etching. The first direct observation of the structure induced through the Direct Grating Writing. The wave-nature of the channel waveguide is thought to arise from the wet-etch process as it follows closely to the surface texture observed on unexposed material.

Within the core layer the exposed channel waveguide etched faster than the unexposed material, while the grating structure also had a differential etch rate revealing the index perturbation to be observed directly (figure 9.24). The surface relief index structure is dramatically apparent and allows the extent of grating structure to be seen, extending either side of the channel waveguide structure. This is because during the Direct Grating Writing process there is a weak UV exposures surrounding the peak intensity of the writing spot without enough power to define the channel structure. Because both writing beams have similar 'weak field' intensities the contrast of the interference pattern in this region surrounding the writing spot is high, even though the overall intensity is low. It is believed that due to the proximity of the interference pattern on the edge of the writing spot, to the channel defining intensities at the centre, the diffusion of the thermal energy in surrounding material permits the weak inscription of the interference pattern even with very low powers and negligible average index change. This process is very similar to the proximity effect described earlier in section 9.5.

The exact cause of the accelerated etch rate in the UV exposed channel waveguides has not been fully identified, and is most likely due to a combination of the mechanisms arising from the grating definition regime. Accelerated etch rates tend to be associated with photosensitivity mechanisms based on a damaged regime rather than the weaker type 1 effect, although it would be expected that due to the defect density in the exposed regions the etch rate would vary. Thermal expansion/stress processes where the index change increase is due to the densification related stress, are well known to change the etch rates and it is likely that this process is occurring to some degree. However, the presence of features on a 500nm scale and the lack of differential etch rate in the cladding would make this process unlikely to be the only mechanism.

9.12.3 Theoretical response

The theoretical response of such an etched sample is illustrated in figure 9.24. The standard effective index simulation from chapter 3 was run with the cladding index layer replaced with the 'sample', a liquid with varying refractive index. The two-layer sample theoretically has a much greater sensitivity to variations of refractive index, however the structure ceases to act as a waveguide as the index of the sample tends towards that of the channel. As can be seen from the simulation the predicted shift in effective refractive index is much larger for smaller sample index changes. Even with low refractive indices there is a significant shift in the Bragg grating response for a small index change. It is clear that there could be two forms of sensor; the first type being a general 'broad' sensor operating in the less sensitive span (1.3-1.4 in figure 9.26) but capable accepting a wide range of refractive index samples. The second type would be 'sensitive' operating only with refractive indices within 0.015 of the core (1.442-1.457 in figure 9.26) providing a much more sensitive response but far more limited operation range.

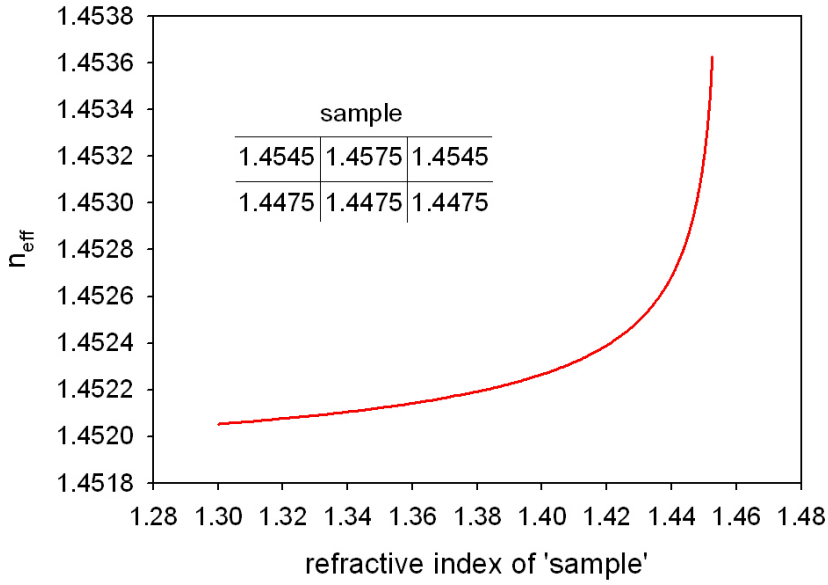

Figure 9.26: Simulated response of a two layer UV written Bragg grating sensor. The sample is in the form of a liquid with a given refractive index, the resultant effective index is plotted for the reflected mode.

9.12.4 Sensor response

The response of the sensor structure is illustrated in figure 9.27. Various index matching fluids of known refractive indices were placed on the sample and the corresponding Bragg response monitored from the back-reflected signal, and the effective index of the structure determined. The response of the sensor fits very well with the predicted trend in figure 9.26. Subsequent liquids of unknown refractive index commonly found near laboratories were fitted to absolute index by the effective index induced on the structure. While the absolute refractive indices of the substances are unknown the index of the sugar drink is higher than that of the sugar-free as expected. The structure also works on substances such as milk, which is a suspension not a solution offering a good indication that it could work with other, more commercially interesting substances.

The discrimination of these liquids occurred in the 'broad' sensor window, with the lower sensitivity. Even in this regime the difference between the different substances were apparent on a normal OSA. The sensitivity of such devices in the 'sensitive' regime should offer much potential in the detection of weak index changes targeted towards non-telecoms use of such structures.

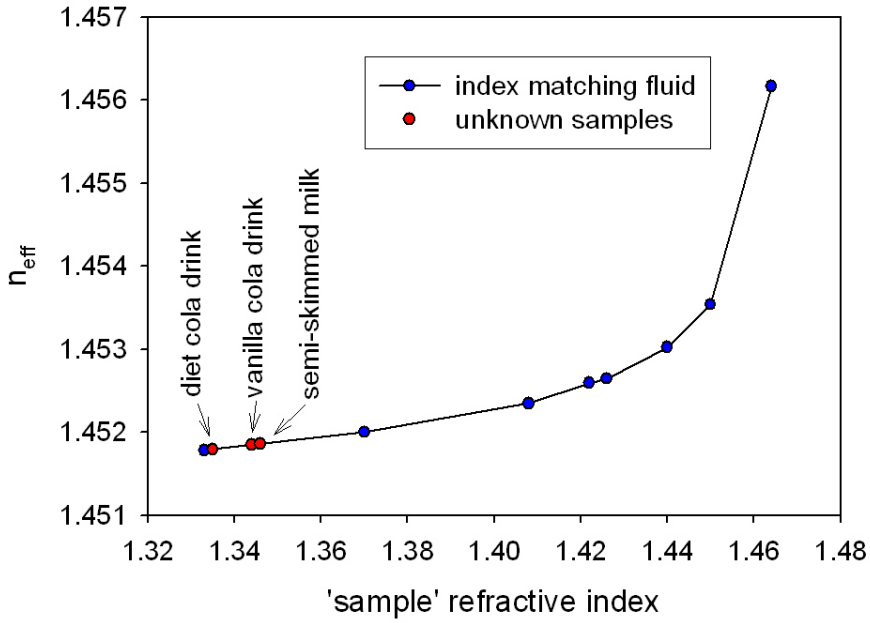

Figure 9.27: Experimental sensor response. Effective index vs. known index matching fluid, with additional liquids of unknown index fitted by the induced effective index of the structure.

The ability of the Direct Grating Writing technique to define planar coupler structures with a range of grating periods offers huge potential for the production of arrays of sensor. Each sensor could operate on a different wavelength with a separate window, all coupled to a single launch fibre with all components on the same substrate with all channel and grating structures defined in the same single process.

9.13 Summary

In this chapter the applications of the grating structures were discussed and demonstrated in a range of specific cases. Initially, the combination of the duty cycle and detuning control was demonstrated allowing the definition of grating structure covering 488nm, all with the same bandwidth response and channel strength. The ability to define such a wide range of grating periods was then applied to investigate the total dispersion characteristics of the channel waveguide. Through knowledge of the grating period, the effective index as a function of wavelength could be obtained. The second derivative of this function provided the total dispersion of the channel waveguide, with the zero dispersion point found to be 1.283μm.

The technique was then applied to investigate the effect of defining channels close to existing UV written channel waveguides. It was found that not only is the photosensitivity reduced in a band spanning around 30μm to 150μm next to a channel but that closer than 30μm the photosensitivity increases, a previously unknown effect only visible through the local nature of the Direct Grating Writing process.

The ability to accurately position channel waveguides and structures easily allows the location of previously exposed channels. The overlay of up to 4 grating structures was demonstrated with no significant disruption of the grating responses. The ability to track and expose existing etched channel structures was demonstrated, with fine control over the index change.

The applicability of Direct Grating Writing for the fabrication of planar lightwave components was demonstrated through the definition of multi-channelled structures. Both the fabrication of three cascaded 1x2 y-splitters (1x8) and directional couplers were demonstrated

Bragg grating structures are ideal structures for sensing the environment around them. The thermal sensitivity of our planar Bragg grating is demonstrated to be 10.8pm°C^{-1}. However planar structures are ideal for the production of devices with sensor 'windows', we have demonstrated a cheap, easy technique for producing such structures and demonstrated the ability to distinguish between liquids without sugar, with sugar and milk, offering huge potential in the field of possible sensors.

Chapter 10: Conclusions

There were two aims of this project, both based on different applications of Direct UV writing. The first project was the combination of the advantages of Planar Lightwave Circuits with the benefits of long channel waveguide structures. The route of integration was through the use of a cylinder as a substrate. By producing effectively 'planar' layers in the form of a cylinder, there is the ability to define both PLC devices, and long path-length channel structures in the form of a helix around the perimeter of the cylinder.

The second aim was to develop a Direct UV writing technique that allows the definition of Bragg grating structures at the same time as the channel waveguide. Such a process would allow the definition of wavelength specific devices in a single fabrication step, adding to the versatility of the Direct UV writing technique.

10.1 Cylindrical Substrate

In traditional planar devices all the structures are produced upon a two-dimensional plane. Due to processing constraints substrates are typically of the order 4-6 inches in diameter, with a single substrate used to produce several components. This restriction forces planar structures to have limited path lengths.

Structures associated with PLC, such as cascaded power splitters, directional couplers and band-pass filters could all be integrated onto a cylindrical substrate as on the scale of the components the substrate is effectively planar. Devices that require long interaction lengths, for example rear-earth doped gain media, poled silica or dispersion compensating gratings could be produced with very long path-lengths, tightly coiled around the cylinder and integrated with the PLC components.

The proof of the concept of production of cylindrical substrates was a key section of the work presented in this thesis. Although there are several fabrication techniques that appear ideal for the fabrication of thin, waveguide quality layers of the surface of a cylinder, as in virtually all cases of fabrication there are limitations with the implementation. To this end,

three fabrication processes were used to produce sample substrates. Two of the techniques involved depositing layers on the perimeter of a cylinder whilst the other deposited on the inside of the cylinder. Modified Chemical Vapour Deposition was used in the fabrication of the layer in the inside of the cylinder. However, although the layers were robust, the radius of curvature of the tube induced excessive loss into the waveguides and channels were hard to define in this geometry.

The deposition of the thin-film layers on the outside of the cylinder were produced using fabrication equipment modified specifically for this project. The first technique, based on Flame Hydrolysis Deposition, applied the same principles of planar fabrication to the cylindrical implementation. As a result, exceptional control over the thickness and composition of the layer was observed, however due to the need for consolidation in a furnace, the high doping levels in the deposited layers left the glass prone to cracking. An alternative technique was a modification of the MCVD process to allow the deposition of layers on the outside of the cylinder. This process was capable of much greater temperatures and thus cladding layers of pure silica were used. These samples showed no susceptibility to cracking, however, the deposition process was hard to control, with variation between depositions. Waveguides were successfully Direct UV written along the axis of the cylinders. Helical waveguides were also written, however the strength of the waveguide was not sufficient to overcome the loss due to the bend radius (although the waveguide structures could be seen). The channels were weak due to the low level of Germanium in the core layer of the waveguide structure. Subsequent depositions were not possible due to damage of the deposition glasswork, however the principle of producing photosensitive layers on the outside surface of a cylinder was demonstrated and so the focus of the work was directed towards the grating writing techniques.

In conclusion, cylindrical substrates were produced in a variety of fabrication processes. All of these processes produced layers suitable for waveguiding, however each technique had a limitation, resulting from the fabrication resources available. It can be expected that a combination of the FHD deposition process with the high temperature consolidation of the MCVD technique would produce stable, controllable cylindrical substrates suitable for Direct UV writing. The process of Direct UV writing channels waveguides onto the cylinder substrates was successfully demonstrated along the axis of the structures.

10.2 Direct Grating Writing

The second aim of the work in this thesis was the development of a variation of the Direct UV writing system capable of inscribing Bragg gratings structure with the same flexibility as channel waveguides. The result, and the primary achievement presented in this thesis is the development of a system allowing definition of both channel waveguides and Bragg grating structures at the same time, with the entire process under computer control. The resultant technique was named as Direct Grating Writing, due to its basis on Direct UV writing and grating writing techniques.

Direct Grating Writing is a fabrication process with several advantages over traditional planar Bragg grating definition. There are three main advantages to the system as a whole:

- Simultaneous definition of channel waveguides and Bragg gratings
- Computer controlled single step fabrication
- Small-spot grating definition

Simultaneous definition of the channel and Bragg grating structure has several advantages over common two-step techniques. From an infrastructure point of view, only one piece of processing equipment is required for both structures and only one fabrication run is required per device. There is no need to align the interference pattern to an existing channel waveguide so the alignment is always correct and the full photosensitivity of the structure can be used for both the grating and channel structure.

The fabrication process is computer controlled, with the channel structures and devices to be produced existing only in computer code. As the system writes the structures directly from that code, there is no need for time and cost intensive mask design/fabrication or subsequent clean room processing. The grating structure is likewise controlled by the processing computer, with the grating structure tailored individually for each device, with no need for phase masks.

As the writing spot is very small, containing less than 10 interference fringes the system has an almost unparalleled flexibility in the grating structures that can be defined. The ability to

produced grating structures with the Bragg centre wavelength responses spanning 488nm (the entire ITU spectrum) from a single fabrication run has been presented. Control over the grating contrast has been demonstrated through normalising the response over the 488nm span to a single value.

These grating structures have been incorporated into 2-dimensional devices, used to measure the dispersion of a channel waveguide, to characterise the writing process itself, to measure the index change in existing etched structures with exposure and to act as sensors for temperature or refractive index changes. These applications cover only a small part of the possible structures that can be defined simply and cheaply using this process, but give an indication of the potential of the technique as a 'multi-tool' of Planar Lightwave Circuit fabrication.

10.3 Future Work

Both aims of the project have reached definite conclusions, with the proof-of-principle in the cylindrical work, and the innovation of the Direct Grating Writing technique. However, there are areas of development for both these processes that would prove very interesting. These include:

- Production of channels and gratings in active rare-earth doped glasses to form laser structures
- Realisation of Direct Grating Writing on cylindrical substrates
- Extend the DGW technique to allow the fabrication of apodised and chirped structures
- Development of Bragg grating based sensors

The production of lasing structures in rare earth doped layers is particularly appealing due to the shortage of planar laser devices. Of particular interest is the production of tapered coupling regions for diode bars, coupling to a gain region with DFB or DBR reflectors. Direct Grating Writing would be an ideal technique for such structures as it is capable of defining both the channel taper structure and the grating structure.

Or particular interest is the definition of the channel and grating structures onto the cylindrical substrates. The limitation of the fabrication of the cylindrical samples could probably be overcome through use of the FHD system to deposit the layers and the use of a wide-bore fibre-pulling tower furnace for consolidation. However, even with a suitable substrate the prototype cylindrical UV writing set-up would have to be upgraded to perform Direct Grating Writing. However, if combined, the possibilities of combining the long path length structures, gratings and rare-earth doped materials would have the potential for structures such as multi-channel optically pumped DFB arrays.

In the work presented in this thesis the grating structures are relatively crude in that the grating structure does not vary with position. The ground work of demonstrating that the contrast and the period can be varied has been presented, however for the production of advanced devices the inclusion of apodisation and chirp is essential.

Sensor structures are interesting as they are the application of well developed telecoms technology into a non-telecoms field. Although grating based sensors are already a rapidly developing field, the simplicity of the DGW technique in combining wavelength selective Bragg gratings with coupler structures offers vast potential for interesting devices.

The above suggestions only cover a tiny range of the possible future work that could be done with both the cylindrical and DGW techniques. The Direct Grating Writing technique in particular has generated much interest in the both the academic and industrial field (Appendix A).

References

Abe, M., Takada, K., et al. (2002). "Reduction in dispersion of silica-based AWG using photosensitive phase trimming technique." Electronics Letters **38**(25): 1673-1675.

Asseh, A., Storoy, H., et al. (1995). "10cm Yb3+ Dfb Fiber Laser with Permanent Phase-Shifted Grating." Electronics Letters **31**(12): 969-970.

Asseh, A., Storoy, H., et al. (1997). "A writing technique for long fiber Bragg gratings with complex reflectivity profiles." Journal of Lightwave Technology **15**(8): 1419-1423.

Ball, G. A. and Glenn, W. H. (1992). "Design of a single-mode linear-cavity erbium fibre laser utilizing Bragg reflectors." Journal of Lightwave Technology **10**(10): 1338-1343.

Bautista, J. R. and Atkins, R. M. (1991). "The Formation and Deposition of Sio2 Aerosols in Optical Fiber Manufacturing Torches." Journal of Aerosol Science **22**(5): 667-675.

Bell, B. A. and Morely, W. W. (1994). "Continously tunable single-mode erbium fiber laser." Optics Letters **17**: 2841-2846.

Bilodeau, F., Hill, K. O., et al. (1994). "High-Return-Loss Narrow-Band All-Fiber Bandpass Bragg Transmission Filter." Ieee Photonics Technology Letters **6**(1): 80-82.

Brinkmeyer, E., Brennecke, W., et al. (1986). "Fiber Bragg Reflector for Mode Selection and Line-Narrowing of Injection-Lasers." Electronics Letters **22**(3): 134-135.

Buck, J. A. (1995). "Fundermentals of Optical Fibers." John Wiley & Sons.

Cho, J., Kim, J., et al. (1998). "An experimental study of heat transfer and particle deposition during the outside vapor deposition process." International Journal of Heat and Mass Transfer **41**(2): 435-445.

Cole, M. J., Loh, W. H., et al. (1995). "Moving Fibre/Phase Mask-Scanning Beam Technique for Enhanced Flexibility in Producing Fiber Gratings with Uniform Phase Mask." Electronics Letters **31**(17): 1488-1490.

Contardi, C., Taylor, E. R., et al. (2001). "Study of UV-written channels in lead silicate glasses." Journal of Non-Crystalline Solids **291**(1-2): 113-120.

Cullen, T. J., Rourke, H. N., et al. (1994). "Compact All-Fiber Wavelength Drop and Insert Filter." Electronics Letters **30**(25): 2160-2162.

Dong, L., Cole, M. J., et al. (1997). 40 Gbit/s 1.55um transmission over 109km of nobn-dispersion shifted fibre with long continously chirped fibre gratings. OFC, Dallas, U.S.A.

Douay, M., Xie, W. X., et al. (1997). "Densification involved in the UV-based photosensitivity of silica glasses and optical fibers." Journal of Lightwave Technology **15**: 1329-1342.

Durkin, M. (1999). "Advanced fibre Bragg gratings: Application to dispersion compensation." Optoelectronics Research Centre. University of Southampton.

Dyer, P. E., Farley, R. J., et al. (1995). "Analysis of Grating Formation with Excimer-Laser Irradiated Phase Masks." Optics Communications **115**(3-4): 327-334.

Dyer, P. E., Farley, R. J., et al. (1996). "Analysis and application of a 0/1 order Talbot interferometer for 193 nm laser grating formation." Optics Communications **129**(1-2): 98-108.

Eggleton, B. J., Krug, P. A., et al. (1994). "Long periodic superstructure Bragg gratings in optical fibres." Electronics Letters **30**(19): 1620-1622.

Emmerson, G. D., Gawith, C. B. E., et al. (2003). "Photosensitivity locking technique applied to UV written planar Bragg gratings." Electronics Letters **39**(6): 517-518.

Ennser, K., Zervas, M. N., et al. (1998). "Optimization of apodized linearly chirped fiber gratings for optical communications." Ieee Journal of Quantum Electronics **34**(5): 770-778.

Erdogan, T. (1997). "Fibre grating spectra." IEEE Journal of Lightwave Technology **15**: 1277-1294.

Faerch, K. and Svalgaard, M. (2002). "Symmetrical waveguide devices fabricated by direct UV writing." Ieee Photonics Technology Letters **14**(2): 173-175.

Ghatak, A. and Thyagarajan, K. (2000). "Introduction to fibre optics." Cambridge University Press.

Giles, C. R. (1997). "Lightwave applications of fiber Bragg gratings." Journal of Lightwave Technology **15**(8): 1391-1404.

Giles, C. R., Erdogan, T., et al. (1994). "Simultaneous Wavelength-Stabilization of 980-Nm Pump Lasers." Ieee Photonics Technology Letters **6**(8): 907-909.

Hibino, Y., Maruno, T., et al. (2001). "Recent progress on large-scale PLC technologies with advanced functions." Ntt Review **13**(5): 4-9.

Hill, K. O., Fujii, Y., et al. (1978). "Photosensitivity in optical fiber waveguides: Application to reflection filter fabrication." Applied Physics Letters **32**: 647-649.

Hill, K. O., Malo, B., et al. (1993). "Bragg Gratings Fabricated in Monomode Photosensitive Optical Fiber by Uv Exposure through a Phase Mask." Applied Physics Letters **62**(10): 1035-1037.

Hillmer, H., Zhu, H. L., et al. (1994). "Nowel tunable semiconductor lasers using contiously chirped distributed feedback gratings with ultra high spatial prescision." Applied Physics Letters **65**: 2130-2132.

Hoffmann, M., Kopka, P., et al. (1997). "Low-loss fiber-matched low-temperature PECVD waveguides with small-core dimensions for optical communication systems." Ieee Photonics Technology Letters **9**(9): 1238-1240.

Johnson, D. C., Hill, K. O., et al. (1987). "New Design Concept for a Narrow-Band Wavelength-Selective Optical Tap and Combiner." Electronics Letters **23**(13): 668-669.

Kashyap, R. (1999). "Fibre Bragg gratings." San Diego, CA, Academic Press.

Kashyap, R., Armitage, J. R., et al. (1993). "Light-Sensitive Optical Fibers and Planar Wave-Guides." Bt Technology Journal **11**(2): 150-158.

Kashyap, R., Froehlich, H. G., et al. (1996). "1.3m long super-step-chirped fibre Bragg grating with a continuous delay of 13.5ns and bandwidth 10nm for broadband dispersion compensation." Electronics Letters **32**(19): 1807-1809.

Kashyap, R., Froelich, H.-G., et al. (1996). "Super-step-chirped Fibre Bragg gratings." Electronics Letters **32**(15): 1394-1396.

Kashyap, R., McKee, P. F., et al. (1994). "Novel Method of Producing All-Fiber Photoinduced Chirped Gratings." Electronics Letters **30**(12): 996-998.

Kashyap, R., Payne, R. A., et al. (1994). "Wavelength-Uncommitted Lasers." Electronics Letters **30**(13): 1065-1067.

Kashyap, R., Wyatt, R., et al. (1993). "Wide-Band Gain Flattened Erbium Fiber Amplifier Using a Photosensitive Fiber Blazed Grating." Electronics Letters **29**(2): 154-156.

Kashyap, R., Wyatt, R., et al. (1993). "Wavelength Flattened Saturated Erbium Amplifier Using Multiple Side-Tap Bragg Gratings." Electronics Letters **29**(11): 1025-1026.

Kawachi, M., Sudo, S., et al. (1980). "Deposition properties of SiO2-GeO2 particles in the flame hydrolysis reaction for optical fibre fabrication." Japanese Journal of Applied Physics **19**(2): L69-L71.

Kogelnik, H. (1990). "Theory of optical waveguides." New York, Springer-Verlag.

Kogelnik, H. and Shank, C. W. (1972). "Coupled wave theory of distributed feedback lasers." Journal of Applied Physics **43**: 2327-2335.

Koo, J. S., Williams, R. B., et al. (2003). "UV written waveguide devices using crosslinkable PMMA-based copolymers." Electronics Letters **39**(4): 394-395.

Lam, D. K. W. and Garside, B. K. (1981). "Characterization of single-mode optical fiber filters." Applied Optics **20**: 440-445.

Lee, D. L. (1986). "Electromagnetic principles of integrated optics." John Wiley & Sons.

Lemaire, P. J. (1991). "Reliability of optical fibers exposed to hydrogen: prediction of long-term loss increases." Optical Engineering **30**(6): 780-788.

Li, Y. P. and Henry, C. H. (1996). "Silica-based optical integrated circuits." Iee Proceedings-Optoelectronics **143**(5): 263-280.

Loh, W. H., Cole, M. J., et al. (1995). "Complex Grating Structures with Uniform Phase Masks Based on the Moving Fiber-Scanning Beam Technique." Optics Letters **20**(20): 2051-2053.

Loh, W. H., Laming, R. I., et al. (1995). "10 cm chirped fibre Bragg grating for dispersion compensation at 10 Gbit/s over 400km of non-dispersion shifted fibre." Electronics Letters **31**(25): 2203-2204.

Loh, W. H., Laming, R. I., et al. (1995). "Single-Frequency Erbium Fiber External-Cavity Semiconductor- Laser." Applied Physics Letters **66**(25): 3422-3424.

Mailis, S., Riziotis, C., et al. (2003). "Direct ultraviolet writing of channel waveguides in congruent lithium niobate single crystals." Optics Letters **28**(16): 1433-1435.

Mairaj, A. K., Fu, A., et al. (2001). "Optical channel waveguide in chalcogenide (Ga : La : S) glass." Electronics Letters **37**(19): 1160-1161.

Malo, B., Hill, K. O., et al. (1993). "Point-by-Point Fabrication of Micro-Bragg Gratings in Photosensitive Fiber Using Single Excimer Pulse Refractive- Index Modification Techniques." Electronics Letters **29**(18): 1668-1669.

Martin, J. and Ouellette, F. (1994). "Novel Writing Technique of Long and Highly Reflective in-Fiber Gratings." Electronics Letters **30**(10): 811-812.

Maxwell, G. D., Kashyap, R., et al. (1994). "Demonstration of a Semiconductor External-Cavity Laser Using a Uv Written Grating in a Planar Silica Wave-Guide." Electronics Letters **30**(18): 1486-1487.

Meltz, G., Morey, W. W., et al. (1989). "Formation of Bragg gratings in optical fibre filters by a transverse holographic method." Optics Letters **14**: 823-825.

Mihailov, S. J. and Gower, M. C. (1994). "Recording of Efficient High-Order Bragg Reflectors in Optical Fibers by Mask Image Projection and Single-Pulse Exposure with an Excimer-Laser." Electronics Letters **30**(9): 707-709.

Miller, S. E. and Chynoweth, A. (1979). "Optical Fibre Telecomunications." Academic Press.

Mizrahi, Y., DiGiovanni, D. J., et al. (1993). "Stable Single-Mode Erbium Fiber-Grating Laser for Digital- Communication." Journal of Lightwave Technology **11**(12): 2021-2025.

Morton, P. A., Mizrahi, V., et al. (1994). "Stable Single-Mode Hybrid Laser with High-Power and Narrow- Linewidth." Applied Physics Letters **64**(20): 2634-2636.

Okamoto, K. (1999). "Recent progress of integrated optics planar lightwave circuits." Optical and Quantum Electronics **31**(2): 107-129.

Othonos, A. and Kalli, K. (1999). "Fibre Bragg Gratings: Fundermantals nd Applications in Telecommunication and Sensing." Artech House.

Othonos, A., Lee, X., et al. (1994). "Superimposed Multiple Bragg Gratings." Electronics Letters **30**(23): 1972-1974.

Ouellette, E. (1987). "Dispersion cancellation using linearly-chirped grating filters in optical waveguides." Optics Letters **12**(11): 847-849.

Park, C. A., Rowe, C. J., et al. (1986). "Single-Mode Behavior of a Multimode 1.55-Mu-M Laser with a Fiber Grating External Cavity." Electronics Letters **22**(21): 1132-1134.

Rabinovich, E. M. (1985). "Preparation of Glass by Sintering." Journal of Materials Science **20**(12): 4259-4297.

Rastogi, V. and Chiang, K. S. (2002). "Long-period gratings in planar optical waveguides." Applied Optics **41**(30): 6351-6355.

Reekie, L., Mears, R. J., et al. (1986). "Tunable single-mode fibre laser." Journal of Lightwave Technology **4**(7): 956-957.

Riziotis, C. (2002). "Advanced Bragg grating based integrated optical devices for wavelength division multiplexing systems." University of Southampton.

Riziotis, C., Fu, A., et al. (2001). Rapid heat treatment for photosensitivity locking in Deuterium-loaded planar optical waveguides. BGPP 2001, Streea, Italy.

Rourke, H., Pugh, B., et al. (2000). Fabrication of extremely long fibre gratings by phase matched concatenation of multiple short sections. Bragg Gratings, Photosensitivity and Poling in Glass Waveguides. **33**: 125-127.

Sakaguchi, S. (1994). "Consolidation of Geo2 Soot Body Prepared by Flame Hydrolysis Reaction." Journal of Non-Crystalline Solids **171**(3): 228-235.

Snyder, A. W. and Love, J. D. (1983). "Optical Waveguide Theory." Chapman and Hall.

Sulimov, V. B., Sokolov, V. O., et al. (1996). "Cluster modelling of the oxygen vacancy in SiO2-GeO2 system." physica status solidi(b) **196**(157): 175-192.

Svalgaard, M. (1997). "Ultraviolet induced refractive index structures in germanosilica." Technical University of Denmark.

Svalgaard, M. (1999). "Effect of D-2 outdiffusion on direct UV writing of optical waveguides." Electronics Letters **35**(21): 1840-1842.

Svalgaard, M. (2003). "Private communication."

Svalgaard, M. and Kristensen, M. (1997). "Directly UV written silica-on-silicon planar waveguides with low loss." Electronics Letters **33**(10): 861-863.

Sze, S. M. (1988). "VLSI Technology." McGraw-Hill.

Tanaka, T., Hibino, Y., et al. (2002). "100-GHz spacing eight-channel light source integrated with gratings and LDs on PLC platform." IEEE Photonics Technology Letters **14**(9): 1348-1350.

Tkach, R. W. and Chraplyvy, A. R. (1986). "Regimes of Feedback Effects in 1.5-Mu-M Distributed Feedback Lasers." Journal of Lightwave Technology **4**(11): 1655-1661.

Tomozawa, M. (1996). "Fracture of Glasses." Annual Review of Material Science **26**: 43-74.

Varshneya, A. K. (1994). "Fundamentals of Inorganic Glasses." Academic Press, Inc.

Vengsarkar, A. M., Pedrazzani, J. R., et al. (1996). "Long-period fiber-grating-based gain equalizers." Optics Letters **21**(5): 336-338.

Ventrudo, B. F., Rogers, G. A., et al. (1994). "Wavelength and Intensity Stabilization of 980 Nm Diode-Lasers Coupled to Fiber Bragg Gratings." Electronics Letters **30**(25): 2147-2149.

Watts, S. P. (2002). "Flame hydrolysis deposition of photosensitive silicate layers suitable for the definition of waveguiding structures through direct ultraviolet writing." Department of Electronics and Computer Science. Southampton, University of Southampton.

Williams, J. A. R., Liu, X., et al. (1997). The effects of phase steps in e-beam written phase-masks used for fibre grating fabrication by near-field holography. IOOC-ECOC 97, Vol **1**: 187-190.

Yamada, M. and Sakuda, K. (1987). "Analysis of almost-periodic distributed feedback slab waveguide via a fundermental matrix approach." Applied Optics **26**: 3474-3478.

Yariv, A. (1973). "Coupled mode theory for guided-wave optics." IEEE Journal of Quantum Electronics QE-**9**: 919-933.

Appendix A: Publications

A1.1 Invited talks

G.D.Emmerson, C.B.E.Gawith, R.B.Williams, P.G.R.Smith, S.G.McMeekin, J.R.Bonar, R.I.Laming, 'Ultra-wide planar Bragg grating detuning and 2D channel waveguide integration through direct grating writing', ECOC 2003, Rimini 21-25 Sep 2003

G.D.Emmerson, C.B.E.Gawith, R.B.Williams, P.G.R.Smith, 'Simultaneous direct UV-writing of channel and Bragg grating structures', Photonics West, San Jose 24-29 Jan 2004

A1.2 Prize winning talks

G.D.Emmerson, C.B.E.Gawith, R.B.Williams, P.G.R.Smith, 'Direct UV writing of channel waveguides and Bragg grating structures', Rank Prize Fund Mini-Symposium: Passive Optical Components, Grasmere 16-19 Jun 2003

A1.3: International conferences

G.D.Emmerson, C.B.E.Gawith, R.B.Williams, P.G.R.Smith, S.G.McMeekin, J.R.Bonar, R.I.Laming, 'Ultra-wide detuning through direct grating writing of planar Bragg structures', BGPP 2003 Monterey 1-3 Sep 2003

G.D.Emmerson, C.B.E.Gawith, S.P.Watts, I.J.G.Sparrow, V.Albanis, R.B.Williams, P.G.R.Smith, S.G.McMeekin, J.R.Bonar, R.I.Laming, 'Direct grating writing as a characterization technique for direct UV written waveguide structures' BGPP 2003 Monterey 1-3 Sep 2003

G.D.Emmerson, C.B.E.Gawith, S.P.Watts, R.B.Williams, P.G.R.Smith, S.G.McMeekin, J.R.Bonar, R.I.Laming, 'All-UV-written integrated planar Bragg gratings and channel waveguides with no phase mask', SIOE 2003 Cardiff 14-16 Apr 2003

G.D.Emmerson, C.B.E.Gawith, S.P.Watts, V.Albanis, R.B.Williams, P.G.R.Smith, S.G.McMeekin, J.R.Bonar, R.I.Laming, 'Direct UV writing of Bragg grating channel waveguides in a single step process', ECIO 2003 Prague 2-4 Apr 2003

J.-S.Koo, C.B.E.Gawith, V.Albanis, S.P.Watts, G.D.Emmerson, R.B.Williams, P.G.R.Smith, M.C.Grossel, 'Integrated optical structures written in a polymer film by UV-induced refractive index modification', ECIO 2003 Prague 2-4 Apr 2003

A.K.Sheridan, C.B.E.Gawith, G.D.Emmerson, P.G.R.Smith, J.S.Wilkinson, 'UV-written channel waveguides in ion-exchanged Pyrex', ECIO 2003 Prague 2-4 Apr 2003

C.B.E.Gawith, G.D.Emmerson, S.P.Watts, V.Albanis, M.Ibsen, R.B.Williams, P.G.R.Smith, S.G.McMeekin, J.R.Bonar, R.I.Laming, 'Single-step definition of channel waveguides with integral Bragg gratings in germanosilica-on-silicon wafers by direct UV writing', CLEO/Europe EQEC 2003 Munich 22-27 Jun 2003 CJ1-1-MON

G.D.Emmerson, S.P.Watts, C.B.E.Gawith, V.Albanis, C.Riziotis, A.Fu, M.Ibsen, R.B.Williams, P.G.R.Smith, 'Directly UV-written planar channel waveguides containing simultaneously defined Bragg gratings', OFC 2003 Atlanta 23-28 Mar 2003

A1.3 Submitted conferences

I.J.G.Sparrow, G.D.Emmerson, C.B.E.Gawith, S.P.Watts, V.Albanis, R.B.Williams, P.G.R.Smith, 'Direct grating writing for the characterisation of material properties used for UV written planar waveguides', OFC 2004 Los Angeles 22-27 Feb 2004

G.D.Emmerson, C.B.E.Gawith, R.B.Williams, P.G.R.Smith, 'Single step writing of equalised bandwidth Bragg gratings within planar light-wave circuits', OFC 2004 Los Angeles 22-27 Feb 2004

A1.4 Journal Publications

C.B.E.Gawith, G.D.Emmerson, S.G.McMeekin, J.R.Bonar, R.I.Laming, R.B.Williams, P.G.R.Smith, 'Small-spot interference pattern for single-step 2D integration and wide wavelength detuning of planar Bragg gratings', Electronics Letters 2003 Vol.39(14) pp.1050-1

G.D.Emmerson, C.B.E.Gawith, S.P.Watts, V.Albanis, R.B.Williams, S.G.McMeekin, J.R.Bonar, R.I.Laming, P.G.R.Smith, 'Photosensitivity locking technique applied to UV written planar Bragg gratings', Electronics Letters 2003 Vol.39(6) pp.517-8

J.Koo, R.B.Williams, C.B.E.Gawith, S.P.Watts, G.D.Emmerson, V.Albanis, P.G.R.Smith, M.C.Grossel, 'UV written waveguide devices using crosslinkable PMMA-based copolymers', Electronics Letters 2003 Vol.39(4) pp.394-5

G.D.Emmerson, S.P.Watts, C.B.E.Gawith, V.Albanis, M.Ibsen, R.B.Williams, P.G.R.Smith, 'Fabrication of directly UV-written channel waveguides with simultaneously defined integral Bragg gratings', Electronics Letters 2002 Vol.38(24) pp.1531-2

A1.4 Submitted journal publications

G.D.Emmerson, C.B.E.Gawith, R.B.Williams, P.G.R.Smith, 'Demonstration of computer controlled direct grating writing of planar Bragg gratings over a 488nm wavelength span', Photonics Technology Letters 2004

G.D.Emmerson, C.B.E.Gawith, S.P.Watts, R.B.Williams, P.G.R.Smith, 'All-UV-written integrated planar Bragg gratings and channel waveguides through single-step direct grating writing', IEE Proc. Optoelectronics: Special Issue *Semiconductor Optoelectronics* 2003

based HEMT technology'. 2002 IEEE Int. Solid-State Circuits Conf. Tech. Dig., San Francisco, CA, USA, 2002, pp. 192–193
5 ISHII, K., MURATA, K., IDA, M., KURISHIMA, K., ENOKI, T., SHIBATA, T., and SANO, E.: 'Very-high speed selector IC using InP/InGaAs heterjunction bipolar transistor', *Electron. Lett.*, 2002, **38**, (10), pp. 480–481
6 MURATA, K., OTSUJI, T., SANO, E., KIMURA, S., and YAMANE, Y.: '70-Gbit/s multiplexer and 50-Gbit/s decision IC modules using InAlAs/InGaAs/InP HEMTs', *IEICE Trans. Electron.*, 2000, **E83-C**, (7), pp. 1166–1169
7 ENOKI, T., ITO, H., IKUTA, K., and ISHII, Y.: '0.1 μm InAlAs/InGaAs HEMT with an InP-recess-etch stopper grown by MOCVD'. Int Conf. on Indium phosphide and related materials, 1995, pp. 81–88
8 SANO, K., MURATA, K., and YAMANE, Y.: '50-Gbit/s demultiplexer IC module using InAlAs/InGaAs/InP HEMTs', *IEICE Trans. Electron.*, 2000, **E83-C**, (11), pp. 1788–1790

Fabrication of directly UV-written channel waveguides with simultaneously defined integral Bragg gratings

G.D. Emmerson, S.P. Watts, C.B.E. Gawith, V. Albanis, M. Ibsen, R.B. Williams and P.G.R. Smith

A new technique for UV direct writing of Bragg gratings in planar silica is presented. In this method the Bragg gratings and the channels are defined simultaneously, conferring advantages in flexibility of design and grating performance. Photosensitive germanium-doped silica-on-silicon produced by flame hydrolysis deposition was used.

Introduction: Direct UV-writing is a fabrication process for planar waveguides based on the same permanent photoinduced refractive index change used in the fabrication of fibre Bragg gratings [1]. This UV induced refractive index change has recently been applied to the field of integrated optics, showing that an intense UV beam focused to form a writing spot and translated within the photosensitive core of a planar sample can form a low-loss channel waveguide [2]. Subsequent progress has demonstrated the suitability of direct writing to produce integrated optical components, including power splitters and directional couplers [3]. The integration of directly UV written waveguides and Bragg gratings within a planar geometry is of great significance, but to date directly written channels with Bragg gratings have been produced using a two-step process. In such cases, a primary exposure is often used to create a channel waveguide while a secondary exposure superimposes the grating structure. As the channel writing process often saturates the photosensitive response of the material a sequential process cannot be used to optimise both the grating strength and waveguide geometry in a single process. To this end we present a new method of directly writing a Bragg grating structure whilst simultaneously defining the channel waveguide, thus allowing the optimal use of the photosensitivity of the material.

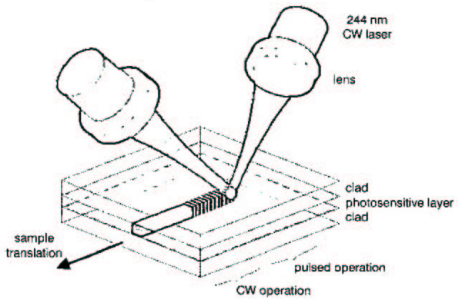

Fig. 1 *Simultaneous direct UV writing of channel and subsequent grating sections using focused beam interference within core of photosensitive planar FHD sample*

Experiment: For these initial experiments three-layer germanium-doped silica-on-silicon samples developed at the Optoelectronics Research Centre using flame hydrolysis deposition (FHD) were used as the writing media. Germanium doping of the middle layer introduces inherent photosensitivity to UV radiation [1], while all three layers were co-doped with phosphorus and boron facilitating independent control of refractive index and processing parameters.

Fig. 1 shows a schematic diagram of our approach. Direct UV writing into the buried germanosilicate layer was performed using a CW frequency doubled argon-ion laser operating at 244 nm. A beam splitter was used to create two separate beam paths at an intersection angle of 27° and each beam was individually focused to a spot size of 6 μm. The two focused beams are crossed within the photosensitive layer resulting in a writing spot with an inherent interference pattern. During writing this interference allows a channel waveguide containing a periodic refractive index modulation within the photosensitive layer to be written.

When the sample is translated under a constant writing spot the intra-spot intensity pattern is averaged out, resulting in a channel waveguide. However, if the laser beam intensity is modulated with a period close to the time taken for the sample to move one grating period through the intra-spot interference, then a channel waveguide is induced that has a periodic index modulation, thus forming a Bragg grating. In our system the laser beam is pulsed using an acoustic-optic modulator triggered by an interferometer monitoring the position of the sample. The formation of Bragg gratings within the core can be directly controlled by changing the spatial superposition of the interference pattern, as is utilised in the fabrication of continuous fibre Bragg gratings [4]. This technique allows different grating periods to be defined without the need to change the beam intersection angle. The period of the Bragg grating is defined by the laser modulation as the sample is translated, and not solely by the period of the interference pattern. The range of detuning allowed depends inversely upon the number of planes in the writing spot and so a small spot is advantageous in writing widely detuned gratings. In this Letter we are presenting preliminary results on Bragg gratings of varying period, length and strength.

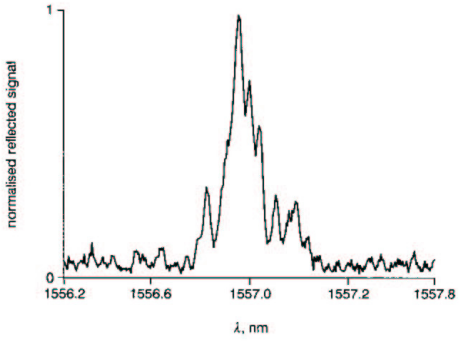

Fig. 2 *Typical reflection spectra for simultaneously defined planar Bragg grating*

Results: The gratings were analysed using an EDFA based ASE source, the output of which was transmitted and selectively orientated through a fibre polariser. Connected to the polariser was a 3 dB coupler to allow the back-reflected signal to be analysed using an OSA. Fabry-Perot resonances were partially suppressed through use of index matching fluid at the point of fibre launch.

An example of the back-reflected signal from a 14 mm-long grating is shown in Fig. 2 and exhibits a reflectivity of approximately 28% with a FWHM of 0.132 nm. As can be seen, the spectral response is not optimised and exhibits Fabry-Perot fringes due to stray reflections from the sample facets. Future devices are planned that will incorporate chirped and apodised grating structures with optimised UV induced index, thereby allowing higher reflectivity and tailored spectral response.

Fig. 3 shows the effect of the period of the grating written against the peak reflected wavelength. As expected from the Bragg condition the response is linear, allowing for n_{eff} of the channel and grating to be measured to a high degree of accuracy. Precise control of the polarisa-

tion state launched into the sample allowed the birefringence of the structure to be obtained, n_{eff} for TE and TM polarisation states were 1.46597 and 1.46594, respectively, implying a of birefringence of 3×10^{-5}. Fig. 4 shows n_{eff} for a range of different waveguides written at different fluences by varying the translation speed of the sample.

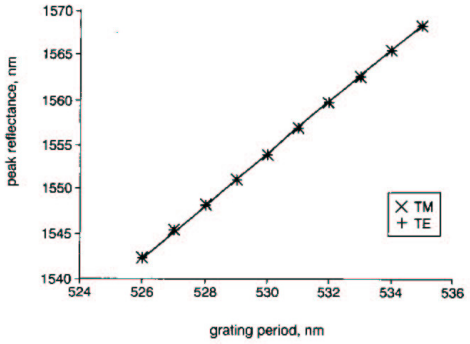

Fig. 3 *Range of grating periods and associated measured peak reflection wavelengths, allowing determination of n_{eff} for TE and TM polarisation*

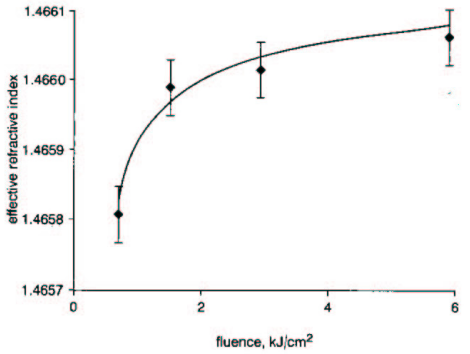

Fig. 4 *Variation of n_{eff} with writing fluence, varied by altering sample translation speed*

Discussion: We have demonstrated the first simultaneously written channels with integral Bragg gratings in a photosensitive planar media. We have shown that it is possible to write Bragg gratings over a large range of wavelengths by pulsing of the writing spot intensity during translation entirely under software control. Based on these initial results, future FHD samples will be optimised for UV writing and photosensitivity will be enhanced through the investigation of deuterium loading, selective dopant concentrations and other associated processes. The future development and optimisation of photosensitive materials and UV direct writing techniques will ultimately allow the realisation of high quality integrated Bragg grating and channel waveguiding structures suitable for application within telecomms devices.

25 September 2002
Electronics Letters Online No: 20021056
DOI: 10.1049/el:20021056

G.D. Emmerson, S.P. Watts, C.B.E. Gawith, V. Albanis, M. Ibsen, R.B. Williams and P.G.R. Smith (*Optoelectronics Research Centre, University of Southampton, SO17 1BJ, United Kingdom*)

E-mail: rbw@orc.soton.ac.uk

References

1 HILL, K.O., and MELTZ, G.: 'Fiber Bragg grating technology fundamentals and overview', *J. Lightwave. Technol.*, 1997, **15**, pp. 1263–1276
2 SVALGAARD, M., and KRISTENSEN, M.: 'Directly UV written silica-on-silicon planar waveguides with low loss', *Electron. Lett.*, 1997, **33**, (10), pp. 861–863
3 FAERCH, K., and SVALGAARD, M.: 'Symmetrical waveguide devices fabricated by direct UV writing', *IEEE Photonics Technol. Lett.*, 2002, **14**, (2), pp. 173–175
4 UK Patent Application: GB2316760A

Fabrication of low-cost planar wavelength-selective optical add-drop multiplexer by employing UV photosensitivity

Mahn Yong Park, Wonshik Yoon, Soowook Han and G. Hugh Song

A 2 × 2 optical add-drop multiplexer has been fabricated by exclusive use of the UV photosensitivity effect in defining the waveguide patterns and Bragg pattern without using any etching process on the multilayered slab structure prepared by a single session of flame hydrolysis deposition process. That is, the waveguide patterns were written by direct writing of a focused UV beam and, subsequently, the periodic grating was imprinted on the plate by a broad UV exposure over a phasemask. The add and drop efficiencies measured at the Bragg wavelength were 25 and 20 dB, respectively.

Introduction: The UV photosensitivity effect in Ge-doped silica fibres has attracted considerable attention since a large refractive-index increase of the order of $\sim 10^{-3}$ was obtained when the Ge-doped silica fibre was illuminated by an intense UV laser beam [1]. The effect has also been applied to fabricating various kinds of planar waveguide devices in addition to fibre optic devices. Designed patterns of waveguides have been drawn directly by exposing a focused UV laser beam on the Ge-doped silica plate [2–4]. It was also reported that Bragg grating filters and optical add-drop multiplexers (OADM) were fabricated on the photosensitised silica buried-channel waveguides that were already formed by the dry etching process of standard photolithography [5].

Here, we made an effort to reduce the production cost of OADMs based on established silica-on-silicon technology in two respects: First, we prepared a three-layered slab waveguide structure in one session of a flame hydrolysis deposition (FHD) process. Secondly, we made exclusive use of the UV photosensitivity effect in defining both the waveguide patterns and Bragg pattern on the multilayered slab structure, eliminating the need for photolithography process associated with dry etching. In this Letter, we report the measured spectrum of the fabricated optical add-drop multiplexer (OADM) evaluating the feasibility of our simplified approach.

Experimental setup: The FHD technique was used in preparing a three-layer silica structure on a silicon substrate for its low-cost mass-production operation. The underclad and overclad layers are borophosphosilicates, in which the dopant concentrations of B_2O_3 and P_2O_5 were around 20 and 6 mol%, respectively. In the core layer, about 10 mol% of GeO_2 was co-doped with about 20 mol% of B_2O_3. Such relatively high doping concentrations were chosen for the purpose of both enhancing the photosensitivity effect and simplifying the deposition/sintering procedure. The doping concentrations were measured by the electron-probe micro-analyser.

All three silica layers were prepared in one session of the deposition process (continuous deposition) and were sintered simultaneously in an electric furnace. The refractive indices of the clad and core layers of the sample, measured by the prism-coupling method at a wavelength of 1.55 μm, were 1.4480 and 1.4520, respectively. The prepared silica plates were then put into a hydrogen-loader of 100 atm for three days at 50°C.

The UV-writing setup for patterning optical waveguides consists of a frequency-doubled Ar-ion laser operating at the wavelength of 244 nm, several optical components (a beam-expander, an objective lens), and computer-controlled stages with movement accuracy of 50 nm [2].

By the focused spatially filtered beam from a frequency-doubled Ar-ion laser with optical output power of 80 mW, the designed waveguide patterns were directly UV-written with the scan speed of 30 μm/s. From

Measured results: The circuits were measured on wafer using 50 Ω coplanar probes. Fig. 4 shows the eye diagram of the output signal at 40 Gbit/s with a pseudorandom bit sequence (PRBS) of length $2^{31}-1$. A data bit rate of 40 Gbit/s with a large voltage of 3 V_{p-p} at each output was obtained for a single-ended input voltage of 0.5 V_{p-p}. The well-opened eye diagram was obtained at such data rate and output voltage swing. The added rms jitter of the driver is smaller than 0.5 ps compared with the input signal. The output driver delivers 100 mA through an effective load of 30 Ω formed by the on-chip 80 Ω resistor and an external 50 Ω load. The 20–80% rise/fall times as short as 8/10 ps were observed on both outputs. The crossing point control feature was tested and 30 to 70% was demonstrated. The output amplitude has an adjustment range of 2.3 to 3 V_{p-p}. The total power consumption of the circuit is 2.5 W using a single supply voltage of −5.8 V.

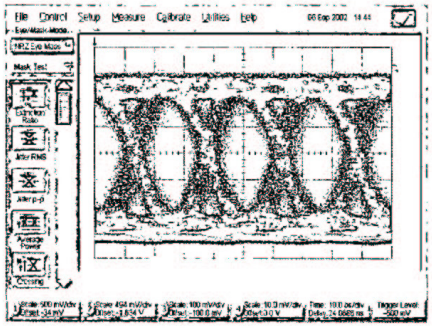

Fig. 4 *Measured 40 Gbit/s output eye diagram at 0.5 V_{p-p} input with PRBS = $2^{31}-1$*

Conclusion: A monolithic modulator driver IC for optical fibre links has been fabricated using a 0.15 μm GaAs pHEMT technology. The modulator driver can be operated up to 40 Gbit/s with an output voltage swing of 3 V_{p-p} at each output. Short rise/fall times of 8/10 ps were obtained using 6-inch industry manufacture GaAs pHEMT process with $f_T = 95$ GHz. The circuit has moderate power dissipation of 2.5 W using a single supply voltage of −5.8 V. This is the first reported 40 Gbit/s modulator driver IC in lumped-element configuration using depletion mode pHEMTs.

15 December 2002
Electronics Letters Online No: 20030305
DOI: 10.1049/el:20030305

Z. Lao, M.C. Ho and V. Radisic (*Advanced Product Development Center (APC), OpNext Inc, Thousand Oaks, California, USA*)

E-mail: sull@mpeg.korea.ac.kr

K. Guinn, S. Lee, M. Yu and M.L. Xu (*OpNext Inc, Eatontown, New Jersey, USA*)

Z. Lao: Now with (address for correspondence) Microelectronics Laboratory, HRL Laboratory, 3011 Malibu Canyon Road, Malibu, CA 90265-4797, USA

M.C. Ho and V. Radisc: Now with TRW Space and Electronics, Redondo Beach, California, USA

References

1 VIRK, R.S., CAMARGO, E., HAJJI, R., PARKER, S., BENELBAR, R., NOTOMI, S., and OHNISHI, H.: '40-GHz MMICs for optical modulator driver applications'. IEEE MTTS Int. Microw. Symp. Dig., 2002, pp. 91–94

2 SHIGERMATSU, H., SATO, M., HIROSE, T., and WATANABE, Y.: 'A 54-GHz distributed amplifier with 6-V_{pp} output for a 40 Gb/s $LiNbO_3$ modulator driver', *IEEE J. Solid-State Circuits*, 2002, **37**, (9), pp. 1100–1105

3 MOUZANNAR, W., JORGE, F., VUYE, S., DUTISSEUIL, E., and LEFEVRE, R.: '40 Gbit/s high performance pHEMT high voltage modulator driver for long haul optical fiber communications'. 2002 IEEE GaAs IC Symp., Monterey, CA, USA, October 2002

4 SCHMID, R., MEISTER, T.F., REST, M., and REIN, H.-M.: 'SiGe driver circuit with high output amplitude operating up to 23 Gb/s', *IEEE J. Solid-State Circuits*, 1999, **34**, (6), pp. 886–891

5 CHERTOUK, M., TU, D.W., MENG, P., YUAN, C.G., CHIANG, W.D., KUO, C.Y., CHANG, C.C., CHANG, A., CHEN, H.H., CHEN, C.H., and CHAO, P.C.: 'Manufacturable 0.15 um PHEMT process for high volume and low cost on 6" GaAs substrates: the first 0.15 μm PHEMT 6" GaAs foundry fab'. 2002 GaAs Mantech Conf., Dig. Ppr., San Diego, CA, USA, April 2002, pp. 138–141

Photosensitivity locking technique applied to UV written planar Bragg gratings

G.D. Emmerson, C.B.E. Gawith, S.P. Watts, V. Albanis, R.B. Williams, S.G. McMeekin, J.R. Bonar, R.I. Laming and P.G.R. Smith

A technique is presented for thermally processing deuterium loaded silica-on-silicon samples to provide an enhanced photosensitivity lifetime of at least one year at room temperature. Subsequent simultaneous writing of channel waveguides and Bragg gratings resulted in grating reflections of ~80% with a FWHM of 0.1 nm.

Introduction: Direct UV-writing is a planar lightwave circuit fabrication process based on the photosensitive refractive index increase occurring in specific materials in response to UV irradiation. This increase in index in silica has long been used to fabricate periodic index modulations in the core of photosensitive fibres to produce fibre Bragg gratings [1]. Photosensitivity in silica is achieved through adding dopants, typically germanium and further enhanced by diffusing hydrogen into the germanium doped core [2]. The loading of fibres with hydrogen or deuterium is now routinely employed to obtain greater UV induced refractive index change without the need for excessive dopant levels that would result in higher losses.

Recently, we reported the first demonstration of simultaneously defined channel waveguides and Bragg grating structures in germanium-doped silica-on-silicon samples [3] with an un-optimised peak reflectance of ~28%. Our single-step process is based on a writing spot with a periodic modulation and was developed to allow both the grating and channel to utilise the full photosensitivity of the material with no need for a phase mask. This is achieved using two writing beams, each individually focused to create a single writing spot with an intrinsic interference pattern defined by the wavelength and intersection angle of the two beams (Fig. 1).

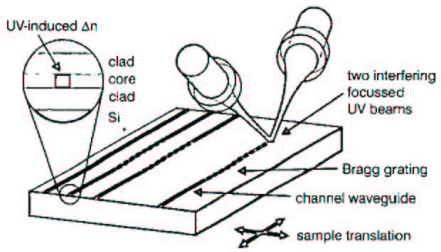

Fig. 1 *Simultaneous direct UV writing of channel waveguides and Bragg gratings using focused beam interference in core of three-layer silica-on-silicon sample*

As the sample is translated under the spot, the intensity of the laser is modulated with a period such that the fringe pattern in the writing spot overlaps in step with the previous exposures, inducing a channel waveguide with an inherent Bragg grating index modulation. This unique approach has significant advantages as Bragg gratings can be integrated into any channel structure at any point throughout the writing process. Software control of the modulation makes writing channels without gratings trivial and allows complete control of the grating parameters.

The conventional approach of deuterium loading used in fibres is problematic for planar samples, as the thin over-clad layer typical in silica-on-silicon samples (~20 μm) results in the deuterium diffusing rapidly out of the core. The rate of diffusion can be significantly reduced by lowering the temperature of the sample [4], extending the writing time available for more complicated structures to be written. However, the duration of the writing window is still finite, and due to the low temperatures involved the setup is susceptible to condensation reducing the fidelity of the writing spot. Purged enclosures [4] can reduce this problem but are difficult to implement with two-beam set-ups without introducing phase errors in the two paths that would result in grating washout.

To this end, we have developed a technique of thermally processing deuterium loaded samples to provide long term photosensitivity enhancement with a lifetime measured in months. It is likely that the 'photosensitivity lock' is due to thermally induced bonding of deuterium to the oxygen atoms present at the germanium sites, increasing the percentage of germanium oxygen deficient centres in the silica matrix.

Experiment: The samples used for this experiment were three-layer silica-on-silicon wafers manufactured by Alcatel Optronics UK using flame hydrolysis deposition. The core layers were doped with germanium to produce an initial intrinsic photosensitivity which was enhanced by deuterium loading at ~150 bar for >5 days. Upon removal from the cell the samples were immediately placed into a furnace at 1400°C for 5 seconds to initiate the thermal locking.

Direct UV writing into the deuterium-locked samples was performed using a CW frequency doubled Ar-ion laser (λ at 244 nm) and the beam power controlled via an acoustic optical modulator. To produce the intra-spot interference pattern the beam path was split to form two separate branches that were recombined at an angle of 29° in the plane of the sample. Each beam was individually aligned and focused to a spot size of 6 μm at the point of intersection (Fig. 1). The samples were mounted on a computer controlled 2D translation stage allowing translation relative to the writing spot.

Our gratings were analysed using an EDFA based ASE source coupled to a polarisation controller. An OSA was used to monitor both the reflected and transmitted spectra of the Bragg gratings.

Results: In our deuterium-locked samples a response of 80% with FWHM of 0.1 nm was achieved, an example spectral profile of which is shown in Fig. 2. As a way of confirming the lifetime of the deuterium locking process we went back to one of our earliest locked wafers, which was locked 18 months before, and confirmed that the photosensitivity persists and the resultant gratings were virtually identical for the same processing and UV writing conditions. As a control, an unlocked but deuterium loaded sample was left for 10 days and exhibited no photosensitive response.

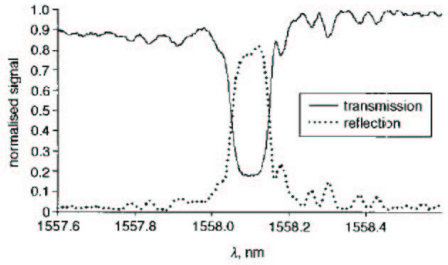

Fig. 2 *Reflection spectra for simultaneously written channel waveguide with integral Bragg grating*

To demonstrate one of the advantages of the simultaneous writing technique, centre-wavelength detuning [2] was used to produce a wide range of Bragg gratings of various pitches with the same interference pattern. Fig. 3 demonstrates such a range of gratings, all written with the same fluence. As shown by the graph, it is possible to write gratings covering the entire C-band with no change to our setup, the defined period of the grating controlled solely through software.

As the peak reflected wavelength of a given grating is dependent on the effective refractive index of the channel waveguide (as defined by the Bragg relation $\lambda_b = 2\Lambda n_{eff}$), writing gratings with the same period but different translation speeds allowed us to assess the variation in strength of the UV induced channel waveguides with fluence (Fig. 4). This writing process coupled with thermal locking provides an accurate and robust measurement of the photosensitivity of the sample independent of deuterium out-diffusion.

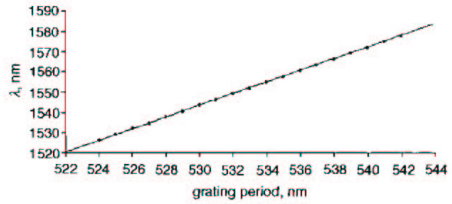

Fig. 3 *Range of grating periods achievable through centre wavelength detuning demonstrated across C-band*

Detuning range demonstrated is limited only by bandwidth of measurement (ASE) source, and not by technique

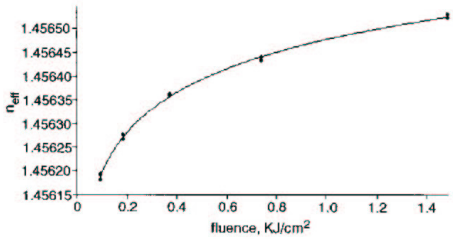

Fig. 4 *Variation of n_{eff} with UV writing fluence for deuterium locked sample*

Discussion: In conclusion, we have demonstrated a thermal process for deuterium locking in germanosilicate planar layers which results in an enhanced photosensitivity lifetime greater than one year. Using this process in conjunction with the simultaneous definition of channels and gratings superior devices with reflections >80% and FWHM of 0.1 nm were realised. These techniques will allow us to optimise the composition of future photosensitive host materials and subsequent thermal processing steps. Our locking process offers potential commercial advantages as sample photosensitivity becomes stable after the thermal step and thus requires no special handling or storage procedures.

20 December 2002
Electronics Letters Online No: 20030379
DOI: 10.1049/el:20030379

G.D. Emmerson, C.B.E. Gawith, S.P. Watts, V. Albanis, R.B. Williams and P.G.R. Smith (*Optoelectronics Research Centre, University of Southampton, SO17 1BJ, United Kingdom*)

E-mail: gdc@orc.soton.ac.uk

S.G. McMeekin, J.R. Bonar and R.I. Laming (*Alcatel Optronics UK, Starlow Park, Livingston, EH54 8SF, United Kingdom*)

References

1 HILL, K.O., and MELTZ, G.: 'Fiber Bragg grating technology fundamentals and overview', *J. Lightwave. Technol.*, **15**, pp. 1263–1276
2 LEMAIRE, P.J., ATKINS, R.M., MIZRAHI, V., and REED, W.A.: 'High pressure H_2 loading as a technique for achieving ultrahigh UV photosensitivity and thermal sensitivity in GeO_2 doped optical fibres', *Electron. Lett.*, 1993, **29**, (13), pp. 1191–1193
3 EMMERSON, G.D., WATTS, S.P., GAWITH, C.B.E., ALBANIS, V., IBSEN, M., WILLIAMS, R.B., and SMITH, P.G.R.: 'Fabrication of directly UV written channel waveguides with simultaneously defined integral Bragg gratings', *Electron. Lett.*, 2002, **38**, (24), pp. 1531–1532
4 SVALGAARD, M.: 'Effect of D_2 outdiffusion on direct UV writing of optical waveguides', *Electron. Lett.*, 1999, **35**, (21), pp. 1840–1842

After each measurement the insertion loss was determined and no change was found at a measurement accuracy of 0.3 dB.

To find possible long term degradation effects at space communication powers the irradiation time was extended up to 14 days at an output power of 300 mW. No noticeable changes of the ratio P_{out}/P_{in} could be determined.

The laser power was increased until the output power reached 2 W. It was held over 9 h. After a subsequent increase of the output power up to 2.7 W the input fibre core was destroyed, while the waveguide itself did not lose its transmission value.

Conclusion: We have shown the possibility of singlemode light guidance up to 2 W at 1064 nm in annealed proton exchanged waveguides for times much longer than the photorefractive time constants. Concerning the low amount of the index changes stable wave guidance should be possible for powers in the range of several 100 mW suitable for applications in space communication.

Acknowledgment: The authors acknowledge the German Aerospace Center (DLR) for supporting this work in the project MIOR (contract No. 50 YH 9901).

28 March 2003
Electronics Letters Online No: 20030703
DOI: 10.1049/el:20030703

J.-P. Ruske, B. Zeitner and A. Tünnermann (*Institute of Applied Physics, Friedrich-Schiller-Universität Jena, Max-Wien-Platz 1, D-07743 Jena, Germany*)

E-mail: ruske@iap.uni-jena.de

A.S. Rasch (*LITEF GmbH, P.O. Box 774, D-79007 Freiburg, Germany*)

References

1 WIESMANN, T., and ZECH, H.: 'Optical space communications systems', Proc. 26th. ECOC, Munich, Germany, 2000, Vol. 1, pp. 25–28
2 MCMICHAEL, I., CHRISTIAN, W., PLETCHER, D., CHANG, T.Y., and HONG, J.H.: 'Compact holographic storage demonstrator with rapid access', *Appl. Opt.*, 1996, **35**, pp. 2375–2379
3 PEITHMANN, K., WIEBROCK, A., and BUSE, K.: 'Photorefractive properties of highly-doped lithium niobate crystals in the visible and near-infrared', *Appl. Phys. B*, 1999, **68**, pp. 777–784
4 BRYAN, D.A., GERSON, R., and TOMASCHKE, H.E.: 'Increased optical damage resistance in lithium niobate', *Appl. Phys. Lett.*, 1984, **44**, pp. 847–849
5 RUSKE, J.-P., ROTTSCHALK, M., and STEINBERG, S.: 'Light induced refractive index changes in singlemode channel waveguides in $KTiOPO_4$', *Optics Commun.*, 1995, **120**, pp. 47–54
6 SARKISOV, S.S., CURLEA, M.J., KUKHTAREV, N.V., FIELDS, A., ADAMOVSKY, G., SMITH, C.C., and MOORE, L.E.: 'Holographic surface gratings in iron-doped lithium niobate', *Appl. Phys. Lett.*, 2001, **79**, pp. 901–903
7 FUJIWARA, T., CAO, X., SRIVASTAVA, R., and RAMASWAMY, R.V.: 'Photorefractive effect in annealed proton exchanged $LiNbO_3$ waveguides', *Appl. Phys. Lett.*, 1992, **61**, pp. 743–745
8 GLASS, A.M., VON DER LINDE, D., and NEGRAN, T.: 'High voltage bulk photorefractive effect and the photorefractive process in $LiNbO_3$', *Appl. Phys. Lett.*, 1974, **25**, pp. 233–235

Small-spot interference pattern for single-step 2D integration and wide wavelength detuning of planar Bragg gratings

C.B.E. Gawith, G.D. Emmerson, S.G. McMeekin, J.R. Bonar, R.I. Laming, R.B. Williams and P.G.R. Smith

A single-step technique for defining 2D channel waveguide structures with internal Bragg gratings in photosensitive germanosilica-on-silicon using two interfering focused UV beams is presented. Through software control, grating detuning across the S-, C-, and L-wavelength bands is also demonstrated.

Introduction: Direct UV writing provides an attractive route towards low-cost integrated optical components in photosensitive silica-on-silicon wafers [1]. Combining closely packed channel waveguides with a versatile Bragg grating tailored spectral response would allow the creation of compact systems for wavelength division multiplexing on a single optical chip. To this end we recently presented the first demonstration of simultaneously defined channel waveguides with integral Bragg gratings based on the interference of two focused UV-writing beams [2]. This single-step approach was developed to promote optimal use of sample photosensitivity for both the waveguide geometry and Bragg grating superstructure, with the potential for implementing many aspects of advanced grating design, such as chirp and apodisation, without the need for a phase mask. In this Letter we present two refinements unique to the small writing spot used during this process, extending the UV-written channel waveguide geometry to two dimensions, while also demonstrating a grating detuning response across the S-, C-, and L-wavelength bands, a technique controlled entirely through computer software and requiring no modifications to our experimental setup.

Direct grating writing: In our direct grating writing arrangement two focused beams are overlapped to give a micron-order near-circular spot with an inherent interference pattern in one dimension (Fig. 1). Exposure of this intensity pattern onto a suitable photosensitive sample results in a periodic change in refractive index that can be extended, plane by plane, into a long grating in the simultaneously defined channel by on/off modulation of the writing beam during sample translation. When the sample is translated under a constant writing beam, the intra-spot interference pattern is averaged out and the focused spot can be used to write standard channel waveguide structures, including the curves and junctions that form the basic building blocks of many larger integrated optical systems. The combination of these two techniques allows planar Bragg gratings to be inserted into complex UV-written devices in a single processing step, and is achievable as a direct result of the small writing spot fundamental to this process.

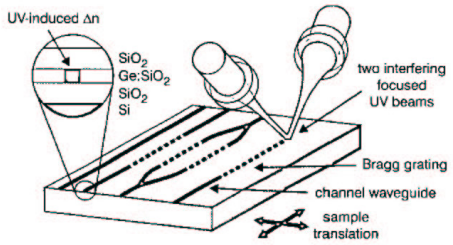

Fig. 1 *Single-step definition of channel waveguides and Bragg gratings*

Experiment: Fabrication of direct-written gratings was performed using a frequency-doubled 244 nm argon-ion laser, a high precision three-dimensional translation stage, and an interferometrically-controlled acousto-optic modulator. A beam splitter was used to create two separate beam paths at an intersection angle of 29°, and both beams were individually focused and aligned to give a single 4 μm interfering spot. Photosensitivity of the three-layer germanosilica-on-silicon substrates used during these experiments was enhanced by deuterium loading at 150bar for one week, following which the samples were UV-written immediately at room temperature. A range of planar Bragg gratings based on variations of period, length, channel waveguide structure, and UV-writing conditions (speed, power, etc.) have been written and subsequently characterised using an optical spectrum analyser. A typical transmission spectra from a straight channel waveguide (NA = 0.12) with a 10 mm-long integral Bragg grating section is shown in Fig. 2, demonstrating an unoptimised unapodised reflection peak of 98% with less than 0.3 nm bandwidth.

To demonstrate the 2D capabilities of our direct grating writing technique, Mach-Zender structures were written in a single-step based on the arrangement shown in Fig. 1. For each device two 5 mm-long cosine-style y-splitter sections were used to seperate the two central

arms of the structure by 200 μm, corresponding to s-bend radii of ~60 mm. For these initial experiments two 8 mm-long planar Bragg gratings with periods of 532 and 532.4 nm, respectively, were incorporated into the two arms of each device, resulting in dual-peak spectral responses typical of that shown in Fig. 3. From the graph the distinction between the two grating reflection responses is clear, and future work will be aimed at integrating such gratings into larger optical systems.

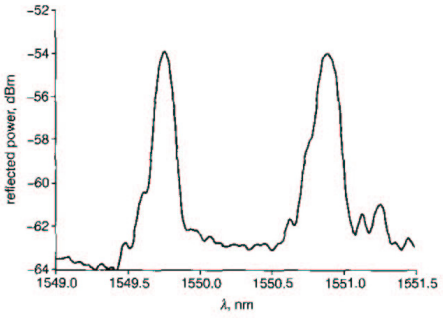

Fig. 3 *Reflection spectra for 2D Mach-Zender channel waveguide structure*

Grating detuning: With the absolute period of our small-spot interference pattern defined by the refractive index of the host material and intersection angle of the two focused beams, the process of centre-wavelength detuning [2] was applied to allow gratings of different periods to be defined via computer-controlled modulation of the writing beam, with no alteration to our optical arrangement. In this detuning process, each stepped exposure of the writing spot is slightly offset from the period of the original interference pattern by a predetermined amount, allowing a selectively different Bragg grating period to be defined in the photosensitive material. While this flexibility comes at an overall loss of grating contrast, an important feature for our direct grating writing process is that the effective wavelength range attainable by detuning is inversely proportional to the number of interference fringes present in the writing spot. In our system a spot diameter of 4 μm with a 532 nm period interference pattern results in approximately eight interference fringes written per exposure. Compared to phase-mask-based schemes, which generally rely on repeated exposures of hundreds of interference fringes, this extremely small writing spot allows a much greater range of detuning from the native interference pattern than traditionally possible. This effect is dramatically demonstrated in the graph of Fig. 4, where an effective detuning range of ~180 nm, encompassing the full S-, C-, and L-wavelength bands, is shown.

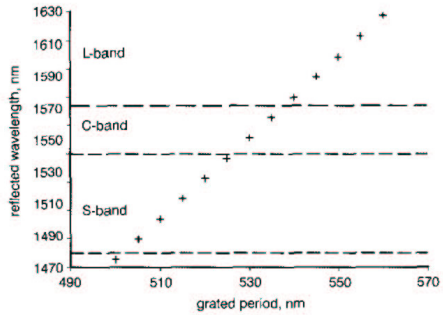

Fig. 4 *Demonstration of grating detuning across S-, C-, and L-wavelength bands*

Conclusion: We have presented two refinements to our recently reported direct grating writing process, each specifically derived from our unique use of a micron-order circular writing spot with an inherent interference pattern. Using these processes, we have demonstrated single-step integration of planar Bragg gratings into 2D Mach-Zender structures and an 180 nm-wide grating detuning response encompassing the S-, C-, and L-wavelength bands, a result achieved entirely through software control. Based on these early results it is hoped that further optimisation of channel waveguide and Bragg grating characteristics will lead to highly efficient integrated optical devices for use in wavelength-selective planar systems.

30 May 2003
Electronics Letters Online No: 20030699
DOI: 10.1049/el:20030699

C.B.E. Gawith, G.D. Emmerson, R.B. Williams and P.G.R. Smith (*Optoelectronics Research Centre, University of Southampton, Southampton, SO17 1BJ, United Kingdom*)

E-mail: cbeg@orc.soton.ac.uk

S.G. McMeekin, J.R. Bonar and R.I. Laming (*Alcatel Optronics UK, Starlaw Park, Livingston, EH45 8SF, United Kingdom*)

References

1 SVALGAARD, M., POULSEN, C.V., BJARKLEV, A., and POULSEN, O.: 'Direct UV writing of buried singlemode channel waveguides in Ge-doped silica films', *Electron. Lett.*, 1994, **30**, (17), pp. 1401–1402
2 EMMERSON, G.D., GAWITH, C.B.E., WATTS, S.P., ALBANIS, V., WILLIAMS, R.B., MCMEEKIN, S.G., BONAR, J.R., LAMING, R.I., and SMITH, P.G.R.: 'Photosensitivity locking technique applied to UV written planar Bragg gratings', *Electron. Lett.*, 2003, **39**, (6), pp. 517–518
3 IBSEN, M., DURKIN, M.K., COLE, M.J., and LAMING, R.I.: 'Sinc-sampled fiber Bragg gratings for identical multiple wavelength operation', *IEEE Photonics Technol. Lett.*, 1998, **10**, (6), pp. 842–844

High-speed modulation of 850 nm InGaAsP/InGaP strain-compensated VCSELs

H.C. Kuo, Y.S. Chang, F.Y. Lai, T.H. Hsueh, L.H. Laih and S.C. Wang

High performance 850 nm InGaAsP/InGaP strain-compensated vertical cavity surface emitting lasers (VCSELs) are demonstrated with superior output characteristics and modulation bandwidths up to 12.5 Gbit/s from 25 to 85°C.

Introduction: 850 nm vertical surface emitting lasers (VCSELs) have become a standard technology for application in local area networks (LANs) from 1.25 to 10 Gbit/s [1–4]. The main advantages of VCSELs are the low threshold current, low divergent angle, and circular beam, which lead to simpler packaging and low electrical power consumption. The surface emission from the VCSELs also makes easy the two-dimensional array integration and allows wafer-level testing, in turn leading to low fabrication cost. The use of an Al-free InGaAsP-based active region is an attractive alternative to the conventional (Al)GaAs active region for IR VCSELs; while edge emitting diode lasers with Al-free active regions have demonstrated performance and reliability surpassing AlGaAs-active devices [5]. In addition, theoretical calculations have predicted a lower transparency current density, high differential gain and better temperature performance in InGaAsP-strain active VCSELs compared to lattice-matched GaAs quantum well active devices [6]. These parameters are very important in high-speed and high-temperature applications because the relaxation resonance frequency of the laser depends on the square root of the differential gain as well as the difference of operation current and threshold current [4]. The use of tensile-strained barriers (InGaP) can provide strain compensation and reduce active region carrier leakage. Al-free materials are significantly less reactive to oxide level, which compared to AlGaAs materials makes them ideal for reliable manufacture [5]. Proton-implanted VCSELs using strain $In_{0.18}Ga_{0.82}As_{0.8}P_{0.2}$ active-region has demonstrated good performance [7]. In this Letter, we demonstrate the high-speed and high-

Appendix B: Programs

Throughout the work on the project presented in this thesis several computer programs have been written to aid the research undertaken. Of the programs, two are referenced directly in the body of the thesis, the effective index mode solver and the cylindrical Direct UV writing software. The programs were written in Visual Basic due to the availability of the software and ease of compatibility with other windows based programs.

B1.1 Effective index mode solver

The control panel for the software is illustrated in figure B1, in this instance the dynamic variable is the refractive index of the UV induced core, but it can be selected to be any parameter within the problem.

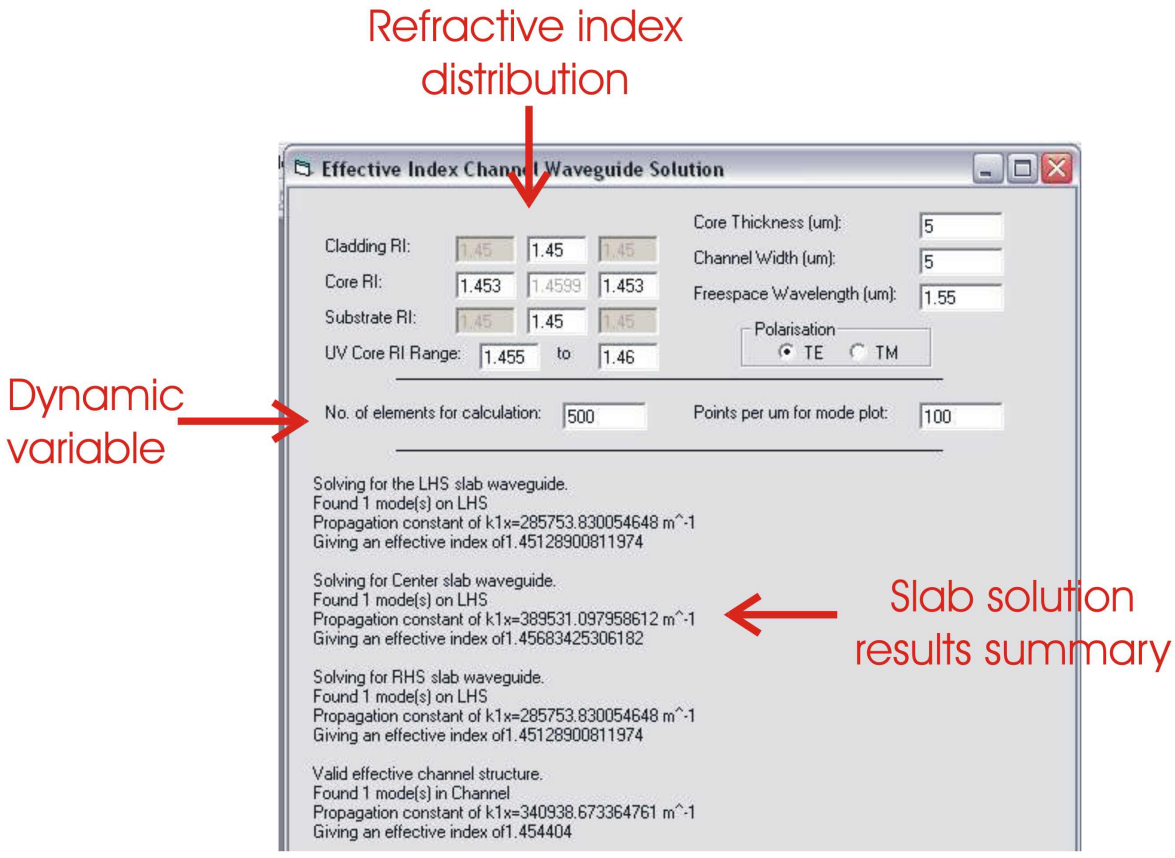

Figure B1: Front-end of the effective index mode solver

The solving process is illustrated in figure B2, the refractive index distribution is split into three vertical slab waveguides. These are individually solved using the slab mode solver below. The effective index for the three structures is then used to construct a 4th slab

waveguide (figure B2) problem, which is solved in a similar process, except using the other polarisation state for the guided wave. The effective index for this structure is an approximation for the effective index of the guided mode and is stored in a output file with the corresponding value of the dynamic variable. This allows a range of parameters to be varied is a systematic process, observing the effect on the guided mode.

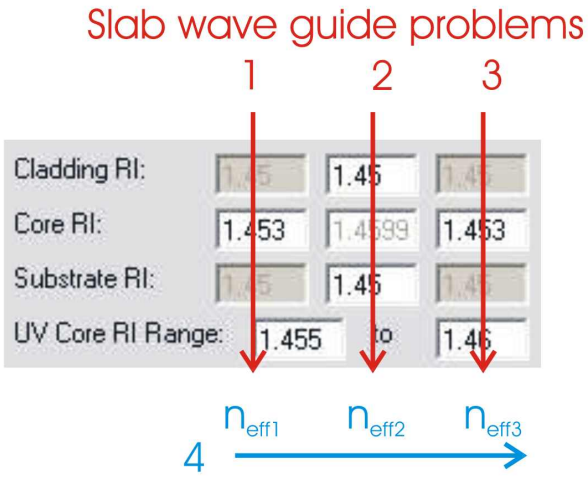

Figure B2: Slab waveguide solution order

Slab mode solving module (TE modes):

```
Public Sub TEModes()

'TE slab mode solver – by Greg Emmerson

Dim CladRI, CoreRI, SubRI, Wavelength, ccAngle, csAngle, PI As Single
Dim TEThiS(), TEThiC(), X(), F1(), TEF2(), TEk1x(), TEX(), TETheta() As Single
Dim NoElements As Integer

NoElements = frmMain.Elements
CladRI = frmMain.PassClad
CoreRI = frmMain.PassCore
SubRI = frmMain.PassSub
Wavelength = frmMain.Wavelength
PI = 3.141592654
d = frmMain.d
k0 = (2 * PI) / (Wavelength)

ReDim TEThiS(1 To NoElements)
ReDim TEThiC(1 To NoElements)
ReDim X(1 To NoElements)
ReDim F1(1 To NoElements)
ReDim TEF2(1 To NoElements)

'find the critical angle at which the wave will no longer propagate
'for the clad core interface
ccAngle = Atn((CladRI / CoreRI) / Sqr(-(CladRI / CoreRI) * (CladRI / CoreRI) + 1))
csAngle = Atn((SubRI / CoreRI) / Sqr(-(SubRI / CoreRI) * (SubRI / CoreRI) + 1))

If ccAngle > csAngle Then
   MaxX = 0.99 * Cos(ccAngle)
Else
   MaxX = 0.99 * Cos(csAngle)
End If

ccDeg = (180 / PI) * ccAngle
csDeg = (180 / PI) * csAngle
```

```
'so scale X
For i = 1 To NoElements
   X(i) = i * MaxX / NoElements
Next i

'TE Modes

For i = 1 To NoElements
   temp = (CoreRI ^ 2 - SubRI ^ 2 - (CoreRI ^ 2) * (X(i) ^ 2)) / ((CoreRI ^ 2) * X(i) ^ 2)
   TEThiS(i) = Atn(Sqr(temp))

   temp = (CoreRI ^ 2 - CladRI ^ 2 - (CoreRI ^ 2) * (X(i) ^ 2)) / ((CoreRI ^ 2) * X(i) ^ 2)
   TEThiC(i) = Atn(Sqr(temp))

   temp = CoreRI * k0 * d * X(i)
   F1(i) = Tan(temp)

   'if F1(i) is negative then it should be using n=1
   If F1(i) < 0 Then
      F1(i) = Tan(temp - PI / 2)
   End If

   TEF2(i) = Tan((TEThiS(i) + TEThiC(i)) / 2)

Next i

'now look through the table of results for the points where F1 and F2 cross

TEmodeNo = 0
For i = 1 To NoElements - 1
   If TEF2(i) > F1(i) And TEF2(i + 1) < F1(i + 1) Then ' found a crossing point
      TEmodeNo = TEmodeNo + 1
      ReDim Preserve TEk1x(0 To TEmodeNo)
      ReDim Preserve TEX(0 To TEmodeNo)
      ReDim Preserve TETheta(0 To TEmodeNo)

      TEX(TEmodeNo) = i
      TEk1x(TEmodeNo) = CoreRI * k0 * ((X(i) + X(i + 1)) / 2)
      TETheta(TEmodeNo) = Atn(-((X(i) + X(i + 1)) / 2) / Sqr(-((X(i) + X(i + 1)) / 2) * ((X(i) + X(i + 1)) / 2) + 1)) + 2 * Atn(1)
    End If
Next i

frmMain.k1x = TEk1x(1)
frmMain.NoModes = TEmodeNo

End Sub
```

B1.2 Helical waveguide programmer

For Direct UV writing of the helical structures in chapter 5, a program was defined for the generation of the scrip file. The structures to be defined were treated as a s-bend on an effectively infinitely wide substrate. An example of a typical helical waveguide summary file is provided below in figure B3, describing the structure to be defined.

Summary for waveguide generation file 21050301.pgm

Number of waveguides in batch = 3
Space between waveguides is = 1.000E-03m
Writing speed of the waveguide is = 5.000E-04m/s
Traversal speed of = 1.000E-03m/s
With the time parameter of =6.827E05 Loops/s

Diameter of waveguide substrate = 2.000E-02m
Length of the waveguide substrate = 3.000E-02m
Stage x-direction step size = 4.210E-07m
Stage rotational step size = 8.491E-05 Radians
Total length of the waveguide = 5.000E-02m
Lead in and out distance is = 2.000E-03m
Radius of the bends in the waveguide = 1.000E-02

Length of waveguide not straight down the x axis = 4.600E-02m
Angle of arc of the waveguide bends = 8.605E-01 radians
Length of each bend in waveguide is = 8.605E-03m
Distance of the diagonal of the waveguide is= 2.879E-02m
Distance between diagonal waveguides is= 6.521E-04m
Waveguide entrance to exit displacement = 1.956E-02m

Waveguide quantised into 43858 procedures of which consisted of 35629 steps in the x direction and 11518 radial steps

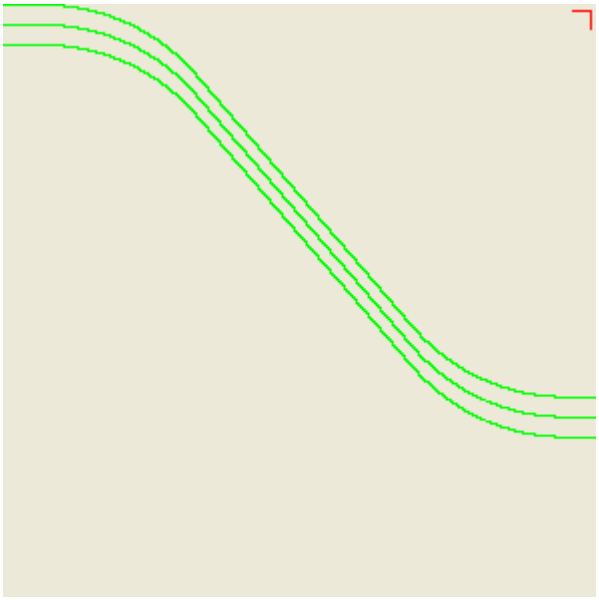

Figure B3: Summary file for the Direct UV writing of helical waveguides. The green line in the picture is the path of the channel and the red lines are a 1mm scale.